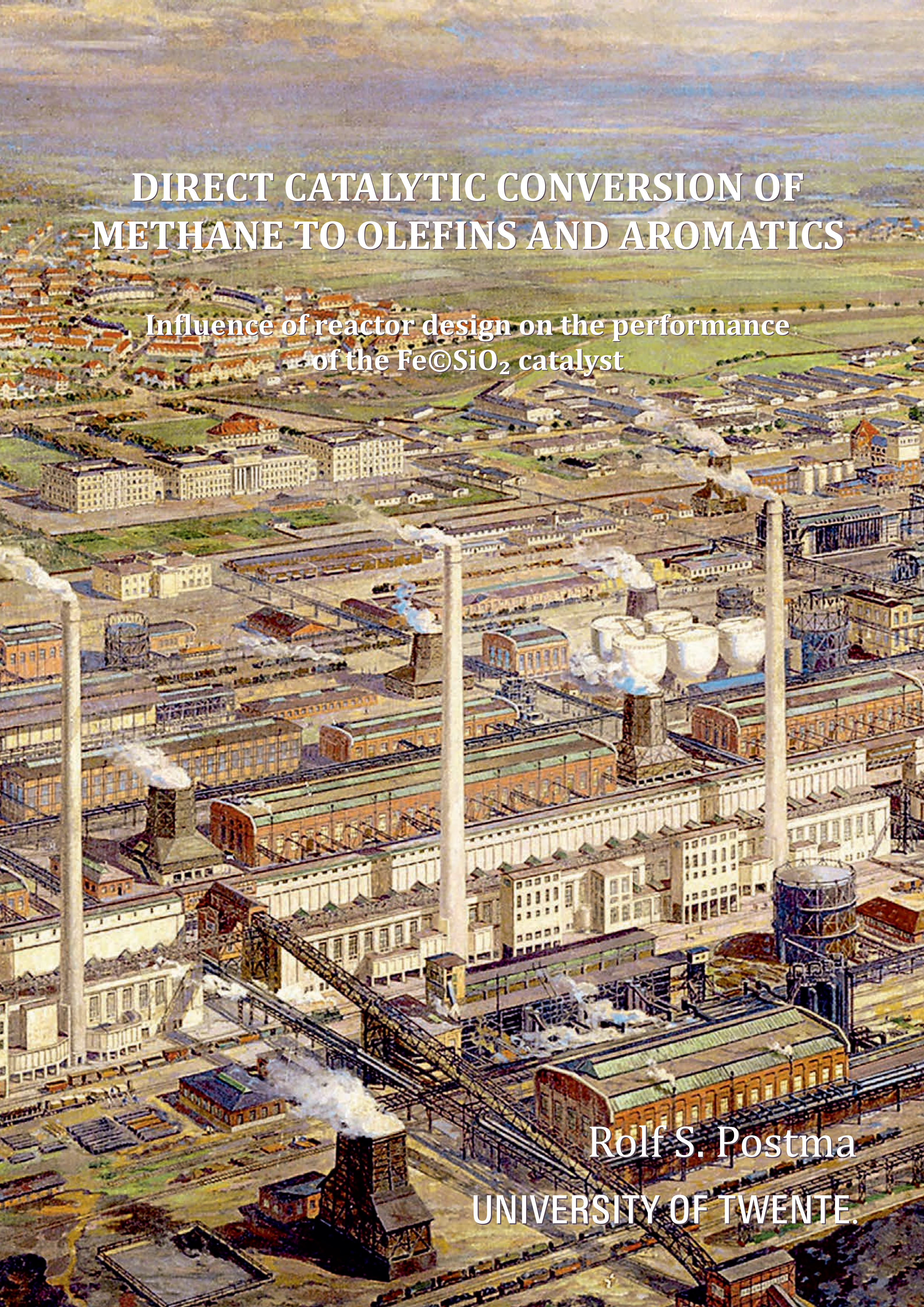

DIRECT CATALYTIC CONVERSION OF METHANE TO OLEFINS AND AROMATICS

Influence of reactor design on the performance of the Fe©SiO_2 catalyst

Rolf S. Postma

UNIVERSITY OF TWENTE.

DIRECT CATALYTIC CONVERSION OF METHANE TO OLEFINS AND AROMATICS

INFLUENCE OF REACTOR DESIGN ON THE PERFORMANCE OF THE Fe©SiO_2 CATALYST

Rolf Sybren Postma

DIRECT CATALYTIC CONVERSION OF METHANE TO OLEFINS AND AROMATICS

INFLUENCE OF REACTOR DESIGN ON THE PERFORMANCE OF THE Fe©SiO_2 CATALYST

PROEFSCHRIFT

ter verkrijging van
de graad van doctor aan de Universiteit Twente,
op gezag van de rector magnificus,
prof. dr. ir. A. Veldkamp,
volgens besluit van het College voor Promoties
in het openbaar te verdedigen
op vrijdag 3 december 2021 om 16.45 uur

door

Rolf Sybren Postma
geboren op 7 januari 1992
te Hoorn, Nederland

Dit proefschrift is goedgekeurd door:

Promotor
prof. dr. ir. L. Lefferts

Cover design:	C.C.M. van Leeuwen & B. Geerdink
Printed by:	Gildeprint
Lay-out:	R.S. Postma
ISBN:	978-90-365-5295-0
DOI:	10.3990/1.9789036552950

The cover image depicts the Leuna Werke Merseburg / Ammonia Plant Merseburg (painting Otto Bollhagen, 1924), permission for its use has been granted by BASF Corporate History (Ludwigshafen/Germany).

PROMOTIECOMMISSIE:

Voorzitter / secretaris:	prof.dr. J.L. Herek
Promotor:	prof.dr.ir. L. Lefferts
Leden:	prof.dr. F. Kapteijn prof.dr.ir. A. Nijmeijer prof.dr. S.R.A. Kersten dr.ing. A. Banerjee prof.dr.ir J.W. Thybaut dr.ir. T.A. Nijhuis dr.ir. S. van Bavel prof.dr.ir. E.J.M. Hensen

Contents

Chapter 1

Introduction

1.1 Motivation

Rapid industrialisation and the exponential increase in the world population has led to ever more rapid climate change, loss of biodiversity and other natural resource depletion [1]. IPCC predictions from 2018 show an increase of up to 4°C by the end of this century if no actions are taken to curb global greenhouse gas emissions [2]. Although immediate and drastic actions aimed to reduce CO_2 emissions can still limit the global temperature rise within 1.5°C by 2100, already to date an increase of 1.3°C is measured. It is predicted that if the global temperature increase will rise above 2°C it will lead to irreversible damage to the global eco-system. However, more and more solutions to diminish the effects of climate change are being implemented at a large scale: e.g. wind and solar [3], and the price of renewable energy is decreasing rapidly, becoming competitive with, or even cheaper than, fossil based energy [4].

Electrification of residential heating is being used to reduce the carbon dioxide emissions of households in the developed world [5]. Heat pumps use the refrigeration cycle, also employed by fridges and air-conditioning systems, to actively move heat from the environment into the house, these systems can have energy efficiencies of more than 500% [6]. The demand for both fuel oil as well as natural gas for heating will hence significantly decrease in the coming decades. Similar trends in electrification are expected to happen in the chemical industry [7, 8]. Per example, electric heating is also being investigated for large-scale processes, such as steam methane reforming [8], to alleviate the need for gas-burners to account for reactant heating and reaction endothermicity. Electrolysis has been a large-scale chemical process for decades, mainly being used for the synthesis of caustic soda and chlorine [9]. Recent years have seen a rapid increase of electrolysis for sustainable hydrogen production [10]. Large scale green hydrogen production using poly-electrolyte membrane (PEM) electrolysers can already compete with the price of methane steam reforming under the right conditions, although massive scale-up is still missing [11]. On top of this, significant research is being invested into electro-chemical synthesis. This research focuses on either traditional electrolytic synthesis [9], or via activation of molecules, using plasma [12] or an electric field [13] to drive up-hill reactions or to lower required reaction temperatures in the activation of stable molecules.

All these trends indicate that a decrease in the demand for natural gas as source for heating and power generation is eminent. Due to the still vast global availability of natural gas, it will be a readily available resource for chemical synthesis [3].

Predictions indicate that the annual production of crude oil will start decreasing around the middle of the 21st century [14, 15], due to the depletion of easily accessible oil as well as the increased cost of exploiting remote oil wells. The largest product fraction from refined oil is fuels [16], such as gasoline, diesel, jet-fuel and fuel-oil. The demand for transportation fuels will likely remain high at least for the coming decades, although new technologies, such as electric cars and trucks [17], as well as ammonia powered freight ships [18] will likely curb this demand.

Global warming is predominantly driven by the increase in total world population, which is predicted to surpass 10 billion in the 2050s [19]. This increase, combined with the increase in living standards in developing countries, such as China and India, will put a huge demand on not only food production, but also on commodity chemicals and their products. A significant fraction of commodity products is chemically synthesized using base-chemicals such as ethylene, propylene and aromatics, like alkyl-benzenes, as feedstock [20]. It is thus predicted that the demand for both olefins and aromatics will significantly increase over the coming century. Traditionally, these base-chemicals are obtained as a by-product from crude oil refining, accounting for up to 15% of the product yield [16]. This yield can, however, be substantially increased by cracking higher hydrocarbons. As discussed in the previous paragraph, crude oil will likely become more scarce, and hence expensive, hindering the future supply of olefins and aromatics needed for chemical synthesis.

1.2 Industrial application of natural gas for chemical synthesis

Natural gas is widely seen as a potent source for the synthesis of these base chemicals [21], due to the large proven reserves, low price [3] and predicted decrease in use as fuel as discussed above. Natural gas is already used on large scale for chemical synthesis, mainly as hydrogen precursor for the Haber-Bosch process to synthesize ammonia [22]. Synthesis of aliphatic hydrocarbons from methane is achieved on large industrial scale in so-called gas-to-liquid processes [23]. These processes start with steam-reforming of natural gas over a nickel catalyst to synthesis gas, a mix of hydrogen and carbon monoxide, followed by, either Fischer-Tropsch synthesis to obtain a paraffin-wax mixture [23], which in turn can be cracked, or by methanol synthesis, which can be followed methanol to olefins (MTO) [24] or methanol to gasoline (MTG) [25].

Fischer-Tropsch (FT) is a process developed in Germany during the 2nd world war to convert various carbonaceous feedstocks, such as coal and biomass into fuels and lubricants [23]. It was further developed in South-Africa in the 1990s due to bans on oil-imports as consequence of the internationally unpopular apartheid policy [26]. Currently, the biggest chemical plant based around the FT process is the Pearl plant operated by Shell in Qatar, converting $4.5 \cdot 10^7$ Nm^3 natural gas per day (Figure 1.1) [27].

Figure 1.1: A photo of the Shell Pearl plant in Qatar [27].

The methanol to olefins (MTO) process dehydrates methanol to light olefins, such as ethylene and propylene over a zeolite catalyst [24]. The process is already industrialized by companies such as DICP and UOP [28], with many other companies having process designs on the concept. The benefits of MTO over FT are a narrower product distribution, higher value products and no need for a cracking operation.

All these processes for converting natural gas into higher hydrocarbons have the substantial drawback of requiring many process steps at different conditions, making the processes both energy intensive and only viable at large installed capacities [29]. Direct conversion of methane into olefins and/or aromatics has the potential to be economically viable at much smaller capacities.

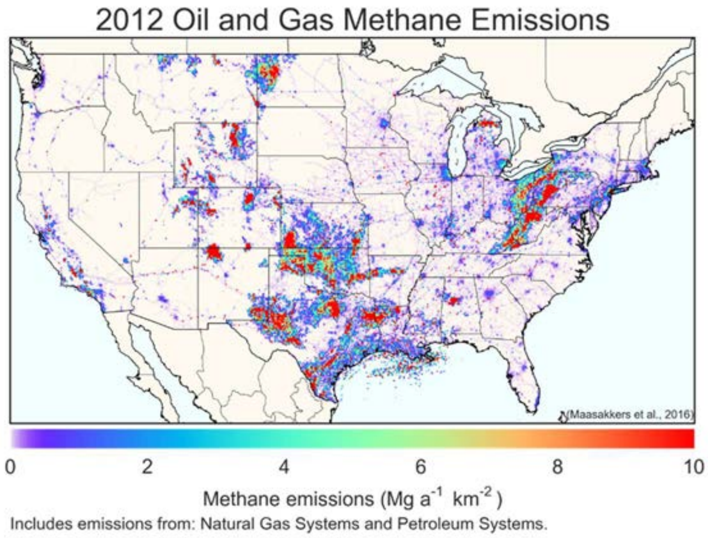

Figure 1.2: Methane venting in the united states in 2012 [30].

Especially the small plant size would be highly interesting for on-site upgrading of natural gas in smaller offshore gas-fields, for example around Australia, or more importantly for onsite-upgrading of the co-extracted natural gas at remote oilfields. Significant amounts of natural gas are currently flared or vented in the United States (Figure 1.2), Russia and Arabia, because transportation via either pipeline or in cryogenic tankers is deemed too expensive. Figure 1.3 shows an overlay between a normal an infrared-heatmap satellite photo of the world, clearly showing excessive flaring. Flaring of natural gas results in 295 Megaton CO_2 emitted per year according to a 2019 World Bank estimate [31], accounting for 0.8% of the total global CO_2 emissions [32]. This clearly shows the shocking level of natural gas flaring occurring across the planet.

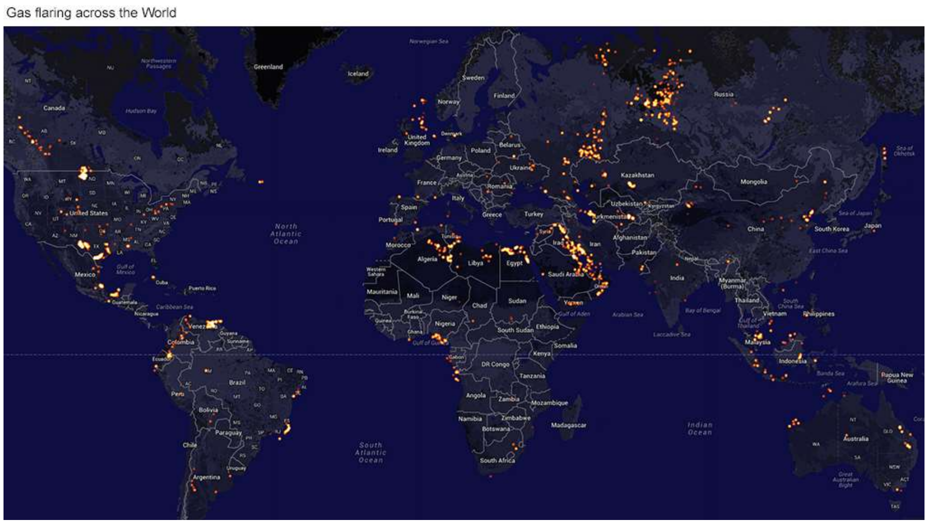

Figure 1.3: Heatmap showing natural gas-flares across the earth using an infrared satellite [33].

1.3 Biogas and CO_2 valorization

Fossil sources of hydrocarbons will most likely play a major role in the world energy mix for the decades to come [15], but for the long-term future more renewable sources are predicted to contribute majorly to bulk-chemical synthesis [34]. Biogas is a mix of mainly methane and carbon dioxide derived from the anaerobic digestion of biomass [35]. Low-value agricultural residues can be used as source for biogas, without competing with food-production or requiring the destruction of nature reserves, in contrast with other bio-fuels such as bio-ethanol [36, 37], or palm-oil derived fuels [38]. CO_2 can be converted into methane following the Sabatier reaction [39]. CO_2 methanation, following direct air capture, can be a negative emission [40] process for methane synthesis, provided that the hydrogen for the reaction is produced renewably. These sources of sustainably produced methane can be utilized in the synthesis of base-chemicals in the same fashion as fossil based natural gas.

1.4 Background information on natural gas and methane

Natural gas is a mixture of light hydrocarbons, mainly methane, traditionally defined as the gaseous by-product of oil extraction [41]. Sulphur compounds, as well as water and CO_2 are generally present as contaminants in natural gas and need to be removed before the gas can be used. The exact composition of natural gas depends heavily on the well it derives from. A typical composition of natural gas can be found in Table 1.1. Higher hydrocarbons can be removed from the natural gas depending on their concentration and their value as intermediate chemical, these recoveries are generally handled by cryogenic distillation [41].

Table 1.1: typical composition of natural gas [41].

Hydrocarbon compound	Vol%	Non-hydrocarbon compound	Vol%
Methane	75-99	**Nitrogen**	0-15
Ethane	1-15	**Carbon dioxide**	0-30
Propane	1-10	**Hydrogen sulfide**	0-30
n-Butane	0-2	**Helium**	0-5
Isobutane	0-1		
n-Pentane	0-1		
Isopentane	0-1		
Hexane	0-1		
Heptane and higher	0-0.1		

Methane (CH4) is the smallest and simplest hydrocarbon, its four equal C-H bonds and regular tetrahedral structure make is the most stable form of reduced carbon under atmospheric conditions [42, 43]. Direct conversion of methane to higher hydrocarbons is very difficult due to its high stability compared to any other hydrocarbon. Methane remains thermodynamically stable up to 400°C [44], after which it decomposes into carbon and hydrogen, full methane conversion occurs at temperatures in excess of 950°C as shown in Figure 1.4: the thermodynamic equilibrium between methane and coke + hydrogen as function of temperature [11].

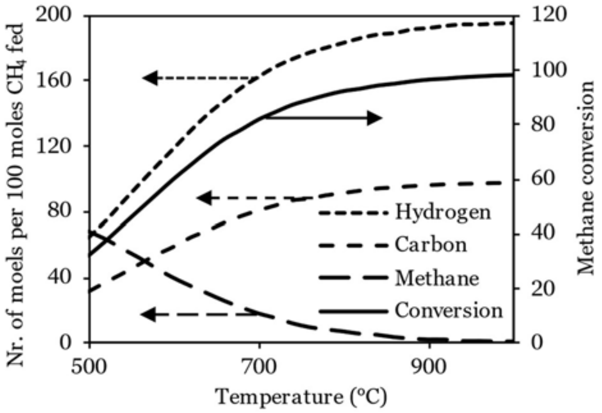

Figure 1.4: the thermodynamic equilibrium between methane and coke + hydrogen as function of temperature, at atmospheric pressure [42].

The main focus of this dissertation is on coupling methane to lower olefins and aromatics, although methane decomposition to hydrogen and carbon can be used as a method for generating clean hydrogen [42]. The thermodynamic equilibrium between methane and its main coupling products can be found in Figure 1.5. Significant methane conversion (>20%) to higher hydrocarbons is only possible at temperatures over 800°C. The increase in required temperature to form higher hydrocarbons compared to coke is due to the lower stability of these hydrocarbons, meaning that methane will stay the most stable form of carbon in this theoretical system for higher temperatures. Note that benzene and naphthalene are the thermodynamically most stable products between 600-1200°C, as apparent from Figure 1.5b, due to their delocalized pi structure. Acetylene become most stable above 1200°C due to entropic effects. Hydrogen will always be the volumetrically most significant product (Figure 1.5a), due to the stoichiometric of product formation as shown in Table 1.2.

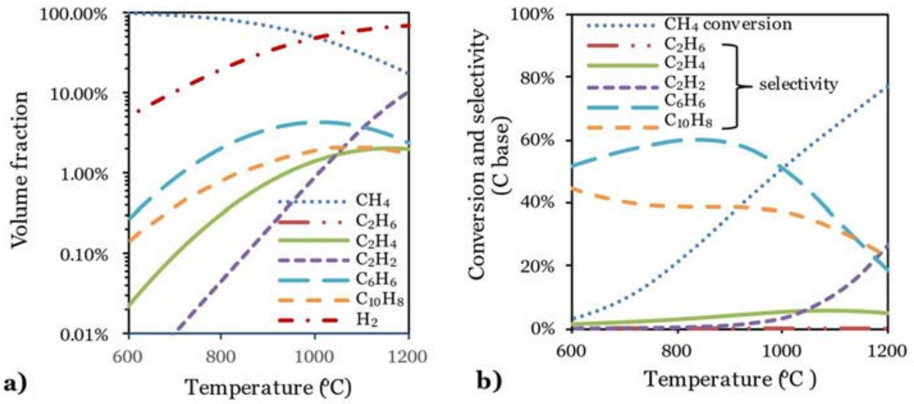

Figure 1.5: (a) Thermodynamic equilibrium concentration of methane decomposition, as function of temperature, at atmospheric pressure, excluding any solid formation (coke) only showing the main products (b) equilibrium methane conversion and carbon based product selectivity based on the thermodynamic data in a. Thermodynamic data is adapted from [43].

A direct route from methane to hydrocarbons is both scientifically as well as technically challenging due the thermodynamic stability of methane and coke compared to any desired hydrocarbon products, as well as the high endothermicity of the coupling reactions, shown in Table 1.2. This, however, has not prevented researchers from trying to find ways to overcome these difficulties. The results of this research will be summarized in the following section.

Table 1.2: Standard (1 atm, 25°C) enthalpy change of the three considered reactions, normalized per carbon atom [44].

Reaction	**STD enthalpy change (KJ/mol C)**
$2CH_4 \rightleftharpoons C_2H_4 + 2H_2$	101.1
$6CH_4 \rightleftharpoons C_6H_6 + 9H_2$	88.1
$10CH_4 \rightleftharpoons C_{10}H_8 + 16H_2$	89.2

1.5 Direct conversion of methane to higher hydrocarbons

Research into direct catalytic conversion of methane to higher hydrocarbons can be divided into three main categories, namely:

1. Methane dehydroaromatization [45]
2. Oxidative coupling of methane [46]
3. Catalytic non-oxidative coupling of methane [47]

Methane dehydroaromatization is a method for direct formation of aromatics, namely benzene from methane. It uses a highly active metal such as molybdenum in combination with a shape selective support such as a ZSM-5 to obtain a high aromatics selectivity.

Oxidative coupling of methane circumvents the thermodynamic limitation shown in Figure 1.5 by using an oxidant, oxygen or sulphur, to oxidize the formed hydrogen. This allows for significant methane conversion at lower temperatures (<750°C).

Catalytic non-oxidative coupling of methane uses a catalyst to activate methane at a higher temperature, without the steric effect used in methane dehydroaromatization. The product range is generally a mix of various olefins and aromatic species. Many of these systems operate via a free-radical gas phase reaction, but not exclusively.

1.5.1 Methane dehydroaromatization

In methane dehydroaromatization (MDA), first described by Wang et al. [48] in 1993, methane is activated and reacts to ethylene over a metal active site. Molybdenum is found to be one of the most active metals although other metal such as nickel, zinc, gallium and iron are also used. The formed ethylene will oligomerize over the Brønsted acid sites of the zeolite to form aromatic rings [45]. ZSM-5 is the most widely used and most effective zeolite in MDA due its pore size of 5.4–5.6Å [49], which is slightly bigger than the diameter of a benzene ring at 5Å [50]. The straight pores will thus steer the formation of poly aromatics towards linear acenes. These acenes are thermodynamically unstable and will dissociate to benzene and naphthalene. M CM-22 is also used as zeolite support, having a pore size of ~7.1Å [51], although methane conversion activity is comparable to ZSM-5, the benzene selectivity is generally significantly lower. Metal loading as well as the deposition and pre-treatment method have great influence on the activity of the MDA catalyst and is still not completely understood. It is generally accepted that a metal loading of ~6% Mo is ideal for high activity in methane conversion as well as high benzene selectivity [45]. The MDA reaction is generally carried out at temperatures between 700-800°C, benchmark figures for performance are around 16% single pass methane conversion and 70%

aromatics selectivity. MDA catalysts suffer from rapid deactivation due to coke formation, leading to complete loss of activity over a time span of a few hours, although most activity can be regained by oxidatively removing the formed coke. Operating at elevated pressures can significantly reduce coke formation due to the higher partial pressure of hydrogen, while simultaneously increasing the methane conversion rate.

1.5.2 Oxidative coupling of methane

Oxidative coupling of methane (OCM) reacts methane over a mixed metal oxide to olefins, first described by Keller et al. [52] in 1982. The oxidant, generally oxygen, is used to lower both the enthalpy and in turn the Gibbs free energy of the reaction to make it possible at lower temperatures, i.e. 750-900°C [46]. Ideally the oxidant will only oxidize the formed hydrogen, thus maximizing the olefin yield, although overoxidation of hydrocarbons to CO_x is the most pressing drawback in OCM. Mixed metal oxides used in OCM have encompassed a very wide range of transition and alkali metals. MgO is a commonly used as basis for the catalyst formulation [46]. The catalyst activates methane to form either surface CH_3 species or $CH_3\cdot$ radicals, which will combine to form ethane. The ethane will oxidatively dehydrogenate to form ethylene. The difficulty stems from tuning both catalyst as well as reaction condition in such a way to achieve high methane conversion while minimizing ethylene over oxidation. The best performance in a fixed bed operation was reported using a Fluorite-Structured Samarium–Yttrium–Bismuth Oxide catalyst [53], reporting 62% C_2 selectivity at 45% CH_4 conversion. Performance in OCM can be enhanced by using a membrane operation or by operating in a chemical-looping configuration [46].

1.5.3 Catalytic non-oxidative coupling of methane

Catalytic non-oxidative coupling of methane (CNOCM or NOCM) is a umbrella term for any non-oxidative method for coupling methane to higher hydrocarbons [47], that does not fit the definition of MDA. It can be argued that MDA is a part of NOCM, although they are treated as two separate categories in this dissertation. The CNOCM field is relatively new, it was sparked by the publication from Guo et al. [54] in 2014. They reported on an atomically dispersed Fe/SiO_2 catalyst capable of activating methane to methyl radicals at temperatures over 950°C. CH_4 conversion up to 48% at 1090°C was reported, with ethylene, benzene and naphthalene as only reported products, and crucially no coke formation was reported, as shown in Figure 1.6. The catalyst showed stable performance over a period of 60 h. The higher activity as well as the absence of any by-product formation was far beyond any performance reported on any other system for direct conversion of methane to higher hydrocarbons.

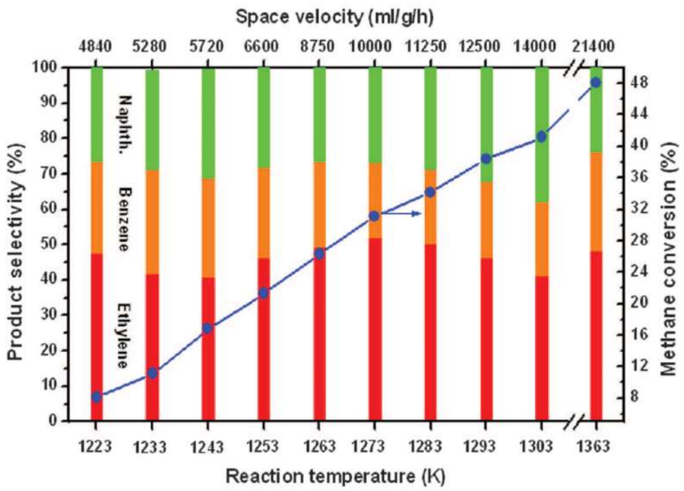

Figure 1.6: the performance reported for the Fe/SiO2 catalyst from Guo et al. [54], reprinted with permission from AAAS.

The Fe/SiO2 catalyst requires activation at lower temperatures to become active [55], during which the FeSiO2 site is carburized to FeC2Si. DFT calculations [54, 56] show that the atomically dispersed iron site will chemisorb a methane molecule, after which it is selectively dehydrogenated to a methyl radical which will desorb from the surface, the hydrogen atom will stay chemisorbed on the carbon atom, until two hydrogen atoms can desorb as a di-hydrogen molecule. The methyl radicals will undergo a free-radical coupling reaction in the gas phase to form the reported mixture of higher hydrocarbons, more details on this reaction will be given later in this chapter. Han et al. [57] undertook a thorough investigation into the characteristics of this Fe/SiO2 catalyst. They varied the crystal structure of the silica as well as the deposition method of iron. Their results showed that high methane conversion rates can already be achieved with bare silica, but the disperse nature of the iron is required for a high selectivity to methyl radical formation, as opposed to coke. Furthermore, the cristobalite phase of silica proved necessary to prevent excessive coke deposition on the catalyst surface. Similar observations were made by Sot et al. [58], who claim that the iron sites are required to suppress surface reactivity and in turn suppress carbon formation. Sakbodin et al. [59] demonstrated that methane conversion can be increased by in situ hydrogen removal, in essence shifting the reaction equilibrium to the product side (Table 1.2) Oh et al. [60] showed an increase in productivity when using a coated-wall reactor. They attributed this to improved heat transfer to the catalyst, which in turn can more easily overcome the significant endothermic energy barrier for methane dehydrogenation. It is to be noted that none of these works based on the catalyst described by Guo et al. [54] reproduced the high conversion and complete prevention of coke formation from the original publication. Details concerning the performance reported in these papers [54, 56-60] can be found in Table 1.3.

Various other catalysts have also been reported for the CNOCM reaction [61-68]. Gerceker et al. [65] reported that a bimetallic Pt-Sn catalyst can couple methane to ethylene at a rate comparable to that of Mo/ZSM-5. They furthermore showed that using an acidic support such as ZSM-5 can steer the selectivity from ethylene to aromatics. Nishikawa et al. [61] demonstrated a In/SiO_2 catalyst which couples methane to ethane at 850°C, the ethane converts in the gas phase to form a mixture of C_{2+} hydrocarbons. Okolie et al. [66] showed that a Ni/$CeZiO_4$ can convert methane at temperatures between 350-500°C to a range of hydrocarbons. The nickel particle size determines the formed products, with smaller particles mainly forming ethane, medium particles forming aromatics and larger particles leading to coke formation. The medium sized particles deactivate rapidly, decreasing methane conversion and leading to 100% ethane selectivity after 30h. Chen et al. [62] used a Pb/Albite and Fe/Albite to couple methane to a mixture of C_2 compounds, albite is naturally occurring zeolite. It was found that the Pb active site could prevent coke formation, whereas the Fe active site did show coking behaviour. This was attributed to the higher dispersion of Pb on the albite, which they could not achieve with Fe. A GaN catalyst was found to act as a MDA catalyst [67], converting methane to benzene. High rates of deactivation were shown, leading to complete deactivation after 8h on stream. Sheng et al. [68] showed that the Mo/ZSM-5 catalyst used in MDA produces exclusively ethylene when the Brønsted acid sites are neutralized by boron doping. Xiao et al. [63] showed that a Pt-Bi bimetallic catalyst can achieve both high methane conversion levels (5.5%) as well as low coking when the two metals are brought together in a Pt:Bi ratio of 0.8:1. A lower amount of Pt will results in excessive coking, whereas a higher amount of Pt will significantly reduce methane conversion. Atomically disperse platina on ceria was found to be highly active in methane conversion as well as coke resistant [64]. It achieves a C_2 combined selectivity of 75% at 15% CH_4 conversion, although measurements were performed in highly diluted systems (1% CH_4/N_2). The key performance figures of these papers have also been summarized in Table 1.3.

1.5.4 Alternative methods for methane activation

Alternative high-energy methods have also been proposed and investigated to overcome the thermodynamic stability of methane. The most widely researched alternative activation method involves non-thermal plasmas. A plasma is generated by applying a strong electric field over a volume of gas, which causes part of the gas to form ions and radicals [12]. These activated species can cause significant methane conversion at low, even ambient, temperatures [69, 70]. The main products of this reaction are acetylene [69] and polymer-like long chain hydrocarbons. The selectivity can however be steered to ethylene and short saturated hydrocarbons by using an in situ hydrogenation catalyst [71, 72]. Another, more novel method for methane conversion uses pulse-compression to significantly increase both pressure and temperature in the reactor to activate methane [73]. Rapid release of the pressure will also rapidly decrease the temperature, thus quenching the reaction and limiting carbon formation.

Table 1.3: Overview of the catalytic NOCM systems reported in literature

Reference	**topic**	**T range °C**	**SV range ml·g_{cat}^{-1}·h^{-1}**	**CH_4 conc.**	**Conversion range%CH_4**	**Coke select. C%**
Guo et al. [54]	Fe©SiO_2 catalyst	950-1090	4840-21400	90%CH_4/N_2	8.3-48.4%	0%
Sakbodin et al. [59]	membrane reactor	950-1050	3200	90%CH_4/Ar	2.1-23.7%	0%
Oh et al. [60]	coated wall reactor	1000	3200	90%CH_4/N_2	8-11.4%	10%
Han et al. [57]	support effect	1020	8250	90%CH_4/Ar	6.5%	2%
SABIC patent [74]	Effect of free volume	960-1030	4840-42800	90%CH_4/N_2	2.4-28.4%	5-70%
Kim et al. [56]	Microkinetic modelling	1020	300-10800	90%CH_4/Ar	1-42.3%	0-66.8%
Sot et al. [58]	Effect of Fe on catalysis	1000	120000	7.5%CH_4/Ar	3%	72%
Gerceker et al. [65]	PtSn	700	1260	100%CH_4	0.1%	0%
Nishikawa et al. [61]	In/SiO_2 liquid metal	750-900	6000	90%CH_4/Ar	0.2-4.6%	5-30%
Okolie et al. [66]	Ni/$CeZrO_4$	350-500	15000	5%CH_4/N_2	0.1-1.1%	0-20%
Chen et al. [62]	Pb/albite	600-900	1000-3000	90%CH_4/N_2	0.5-8%	0%
Dutta et al. [67]	GaN	650-710	600-3000	80%CH_4/N_2	1-7%	Undisclosed
Sheng et al. [68]	Mo/B-ZSM-5	650	1680	100%CH_4	0.8	0%
Xiao et al. [63]	1%Pt,0.8%Bi/ZSM5	650	825-18600	100%CH_4	5.50%	5%
Xie et al. [64]	Pt/CeO2	900-1000	6000	1%CH4/N_2	2-25%	0%

1.6 Methane pyrolysis

It is important to have a good understanding of the free radical gas-phase coupling mechanism of methane, due to the importance of gas-phase chemistry in the catalytic systems discussed above, especially in the case of the Fe/SiO_2 catalyst [54] studied in this thesis. High temperature gas phase conversion of methane has been a widely researched topic since the beginning of the 20th century [75, 76]. This process is generally referred to as methane pyrolysis, although (non-catalytic) non-oxidative coupling of methane (NOCM) is also used. Older literature on methane pyrolysis has been expertly summarized by the reviews of Khan [77] in 1970 and Arutyunov et al. [75] in 1991. In 1916 Slater [76] investigated the effect of different types of surfaces on methane dissociation rate at 910°C. It was found that silica and magnesia were inert, whereas most metals like iron and copper, as well as charcoal, graphite and carborundum (SiC) were highly active in dissociating methane. Van der Zwet [78] later added to this, by showing a linear relationship between methane conversion rate and the logarithm of the surface area in the reactor. He also showed that an increase in surface area leads to a significant increase in selectivity towards coke and tars. Lieberman et al. [79] reported on the effect of gas flowrate in isothermal methane pyrolysis, demonstrating very limited methane conversion at high flowrates, followed by a sharp increase in methane conversion upon lowering the gas flowrate, until full methane conversion was observed. They showed invariance in the production rate for ethylene, acetylene and benzene over the measured flowrate range, whereas C_{3-4} hydrocarbons are only observed in a narrow flow-rate range. In 1967 Palmer et al. [80] started the work on uncovering the gas-phase free radical mechanism involved in methane pyrolysis, continued in the 70s and 80s by Chen [81, 82], Roscoe [83] and Dean [84], mainly focussing on methane activation, formation of C_2 hydrocarbons and the subsequent coupling of C_2 hydrocarbons. In their works they discuss concepts such as the methane autocatalytic cycle, in which the products of methane coupling activate more methane in a positive feedback loop. In the 90s Anders Holmen [44, 85-87], Ola Olsvik [44, 85-88], Francis Billaud [43, 89-92] and Christophe Guéret [43, 89, 91, 92] continued this work, leading to many publication on methane pyrolysis, both experimental as well using computer simulations. These works will be discussed in more detail in the relevant chapters of this thesis, mainly **chapter 5**, but also **chapters 2-4**.

1.7 Scope and outline

This thesis deals with the effects of reactor design and process conditions on non-oxidative coupling of methane using the Fe/SiO_2 catalyst developed by Guo et al. [54]. It provided substantial insights into the complex free radical chemistry involved in the gas-phase coupling reaction in tandem with catalytic methane activation.

In **Chapter 2** the effect of the temperature profile surrounding the catalyst bed is investigated. Temperature and gas-phase residence time up-stream and down-stream of the catalyst were systematically varied, giving clear trends related to their influence on the performance of the system, both in terms of methane conversion as well as coke deposit formation.

Chapter 3 shows the influence of both ethane as well as ethylene addition on the performance of the system. Both C_2 hydrocarbons are potent free-radical initiators and can in turn activate methane, boosting the overall methane and hydrocarbon conversion rates.

The effect of hydrogen addition on deposit formation has been investigated in **Chapter 4**. Hydrogen is a product in all dehydrogenative coupling steps in the free-radical mechanism. Hydrogen can slow down these reactions, because these are equilibrium based. It is investigated to what extend hydrogen retards the reaction rate towards deposit formation, compared to retarding the reaction rate towards hydrocarbon product formation.

A detailed kinetic model is presented in **Chapter 5**, which gives fundamental insights into the qualitative observations presented in the previous 3 chapters. Optimization strategies are proposed with respect to initiating and propagating the free radical coupling reaction.

Chapter 6 gives a detailed process design for catalytic coupling of methane. It highlights the scientific as well as engineering challenges involved in a potential industrial process. In this way it highlights the opportunities for research, not only involving the coupling reaction, but also for the required separations as well as product upgrading.

Chapter 7 details alternative synthesis methods for both the original Fe©SiO_2 catalyst based on grafting of Fe-organic complexes, as well as the synthesis of a Ru/SiO_2 catalyst to evaluate the effect of a different active metal on the catalyst.

Chapter 8 summarizes the previous chapters. It also provides an outlook on the future of non-oxidative coupling of methane, proposing various avenues for continued research into this topic.

1.8 References

1. Ganivet, E., *Growth in human population and consumption both need to be addressed to reach an ecologically sustainable future*. Environment, Development and Sustainability, 2020. **22**: p. 4979-4998.

2. Collins, M. and R. Knutti, *Long-term Climate Change:Projections, Commitmentsand Irreversibility*. 2018, International Panel on Climate Change.

3. BP plc, *Statistical Review of World Energy*. 2020.

4. Broom, D., *5 charts show the rapid fall in costs of renewable energy*, in *Energypost*. 2020.

5. Karytsas, S. and H. Theodoropoulou, *Public awareness and willingness to adopt ground source heat pumps for domestic heating and cooling*. Renewable and Sustainable Energy Reviews, 2014. **34**: p. 49-57.

6. Valancius, R., R.M. Singh, A. Jurelionis, and J. Vaiciunas, *A Review of Heat Pump Systems and Applications in Cold Climates: Evidence from Lithuania*. Energies, 2019. **12**(22): p. 4331.

7. Yeh, S., N.P. Lutsey, and N.C. Parker, *Assessment of Technologies to Meet a Low Carbon Fuel Standard*. Environmental Science & Technology, 2009. **43**(18): p. 6907-6914.

8. Wismann, S.T., J.S. Engbæk, S.B. Vendelbo, F.B. Bendixen, W.L. Eriksen, K. Aasberg-Petersen, C. Frandsen, I. Chorkendorff, and P.M. Mortensen, *Electrified methane reforming: A compact approach to greener industrial hydrogen production*. Science, 2019. **364**(6442): p. 756-759.

9. Wendt, H., H. Vogt, G. Kreysa, D.M. Kolb, G.E. Engelmann, J.C. Ziegler, H. Goldacker, K. Jüttner, U. Galla, H. Schmieder, and E. Steckhan, *Electrochemistry*, in *Ullmann's Encyclopedia of Industrial Chemistry*. 2009.

10. IEA, *The Future of Hydrogen*, IEA, Editor. 2019, IEA: Paris.

11. Guerra, O.J., J. Eichman, J. Kurtz, and B.-M. Hodge, *Cost Competitiveness of Electrolytic Hydrogen*. Joule, 2019. **3**(10): p. 2425-2443.

12. Whitehead, J.C., *Plasma–catalysis: the known knowns, the known unknowns and the unknown unknowns*. Journal of Physics D: Applied Physics, 2016. **49**.

13. Che, F., J.T. Gray, S. Ha, N. Kruse, S.L. Scott, and J.-S. McEwen, *Elucidating the Roles of Electric Fields in Catalysis: A Perspective*. ACS Catalysis, 2018. **8**(6): p. 5153–5174.

14. Gargett, D., *Transport energy futures: long-term oil supply trends and projections*. 2009, Department of Infrastructure, Transport,Regional Development and Local Government: Canberra, Australia.

15. Caineng, Z., Z. Qun, Z. Guosheng, and X. Bo, *Energy revolution: From a fossil energy era to a new energy era*. Natural Gas Industry B, 2016. **3**: p. 1-11.

16. Alfke, G., W.W. Irion, and O.S. Neuwirth, *Oil Refining*, in *Ullmann's Encyclopedia of Industrial Chemistry*. 2007.

17. JeremyWebb, *The future of transport: Literature review and overview*. Economic Analysis and Policy, 2019. **61**: p. 1-6.

18. Gallucci, M., *Why the Shipping Industry Is Betting Big on Ammonia*, in *IEEE Spectrum*. 2021.

19. United Nations Department of Economic and Social Affairs, *World Population Prospects: The 2019 Revision*. 2019.

20. Schmidt, R., K. Griesbaum, A. Behr, D. Biedenkapp, H.W. Voges, D. Garbe, C. Paetz, G. Collin, D. Mayer, and H. Höke, *Hydrocarbons*, in *Ullmann's Encyclopedia of Industrial Chemistry*. 2014.

21. Taifan, W. and J. Baltrusaitis, *CH4 conversion to value added products: Potential, limitations and extensions of a single step heterogeneous catalysis*. Applied Catalysis B: Environmental, 2016. **198**: p. 525–547.

22. Appl, M., *Ammonia*, in *Ullmann's Encyclopedia of Industrial Chemistry*. 2011.

23. Klerk, A.d., *Fischer–Tropsch Process*, in *Kirk-Othmer Encyclopedia of Chemical Technology*. 2013. p. 1-20.

24. Tian, P., Y. Wei, M. Ye, and Z. Liu, *Methanol to Olefins (MTO): From Fundamentals to Commercialization*. ACS Catalysis, 2015. **5**(3): p. 1922-1938.

25. ExxonMobil Chemicals, *MTG Factsheet*. 2018.

26. Crawford, N.C., *Oil Sanctions Against Apartheid*, in *How Sanctions Work*, N.C. Crawford and A. Klotz, Editors. 1999, Palgrave Macmillan.

27. Royal Dutch Shell. *Pearl GTL - Overview*. [cited 2021; Available from: https://www.shell.com/about-us/major-projects/pearl-gtl/pearl-gtl-an-overview.html.

28. Huang, K., J.B. Miller, G.W. Huber, J.A. Dumesic, and C.T. Maravelias, *A General Framework for the Evaluation of Direct Nonoxidative Methane Conversion Strategies*. Joule, 2018. **2**: p. 349-365.

29. Mohajerani, S., A. Kumar, and A.O. Oni, *A techno-economic assessment of gas-to-liquid and coal-to-liquid plants through the development of scale factors*. Energy, 2018. **150**: p. 681-693.

30. Maasakkers, J.D., D.J. Jacob, M.P. Sulprizio, A.J. Turner, M. Weitz, T. Wirth, C. Hight, M. DeFigueiredo, M. Desai, R. Schmeltz, L. Hockstad, A.A. Bloom, K.W. Bowman, S. Jeong, and M.L. Fischer, *Gridded National Inventory of U.S. Methane Emissions*. Environmental Science & Technology, 2016. **50**(23): p. 13123-13133.

31. Bamji, Z., *Global Gas Flaring Tracker Report*. 2020, The World Bank.

32. Crippa, M., D. Guizzardi, M. Muntean, E. Schaaf, E. Solazzo, F. Monforti-Ferrario, J.G.J. Olivier, and E. Vignati, *Fossil CO2 emissions of all worldcountries*, in *JRC SCIENCE FOR POLICY REPORT*. 2020, European Commision.

33. Kroodsma, D.A. *Skytruth*. 2019 [cited 2021; Available from: https://skytruth.org.

34. Wilson, K. and A.F. Lee, *Catalyst design for biorefining*. Philosophical Transactions of the Royal Society A: Mathematical, Physical and Engineering Sciences, 2016. **374**(2061).

35. Nyns, E.J., M. Nikolausz, and J. Liebetrau, *Biogas*, in *Ullmann's Encyclopedia of Industrial Chemistry*. 2014.

36. Muscat, A., E.M.d. OldeI, J.M.d. Boer, and R. Ripoll-Bosch, *The battle for biomass: A systematic review of food-feed-fuel competition*. Global Food Security, 2020. **25**.

37. Ferrante, L. and P.M. Fearnside, *The Amazon: biofuels plan will drive deforestation*. Nature, 2020. **577**(170).

38. Taylor, M., *Analysis-Indonesia's palm oil-powered 'green diesel' fuels threat to forests*, in *Reuters*. 2021.

39. Sakpal, T. and L. Lefferts, *Structure-dependent activity of CeO2 supported Ru catalysts for CO2 methanation*. Journal of Catalysis, 2018. **367**: p. 171-180.

40. Meckling, J. and E. Biber, *A policy roadmap for negative emissions using direct air capture*. Nature Communications, 2021. **12**(1).

41. Hammer, G., T. Lübcke, R. Kettner, M.R. Pillarella, H. Recknagel, A. Commichau, H.J. Neumann, and B. Paczynska-Lahme, *Natural Gas*, in *Ullmann's Encyclopedia of Industrial Chemistry*. 2006.

42. Amin, A.M., E. Croiset, and W. Epling, *Review of methane catalytic cracking for hydrogen production*. International Journal of Hydrogen Energy, 2011. **36**(4): p. 2904-2935.

43. Guéret, C., M. Daroux, and F. Billaud, *Methane pyrolysis: thermodynamics*. Chemical Engineering Science, 1997. **52**(5): p. 815-827.

44. Holmen, A., O. Olsvikb, and O.A. Rokstad, *Pyrolysis of natural gas: chemistry and process concepts*. Fuel processing technology, 1995. **42**: p. 249-267.

45. Galadima, A. and O. Muraza, *Advances in Catalyst Design for the Conversion of Methane to Aromatics: A Critical Review*. Catalysis Surveys from Asia, 2019. **23**: p. 149-170.

46. Gao, Y., L.M. Neal, D. Ding, W. Wu, C. Baroi, A. Gaffney, and F. Li, *Recent Advances in Intensified Ethylene Production – A Review*. ACS Catalysis, 2019. **9**(9): p. 8592-5621.

47. Schwach, P., X. Pan, and X. Bao, *Direct Conversion of Methane to Value-Added Chemicals over Heterogeneous Catalysts: Challenges and Prospects*. Chemical Reviews, 2017. **117**: p. 8497-8520.

48. Wang, L., L. Tao, M. Xie, G. Xu, J. Huang, and Y. Xu, *Dehydrogenation and aromatization of methane under non-oxidizing conditions*. Catalysis Letters, 1993. **21**: p. 35-41.

49. Catlow, C.R.A., R.G. Bell, J.D. Gale, and D.W. Lewis, *Modelling of structure and reactivity in zeolites*, in *Studies in Surface Science and Catalysis*, L. Bonneviot and S. Kaliaguine, Editors. 1995, Elsevier: Québec, Canada.

50. Folkins, H.O., *Benzene*, in *Ullmann's Encyclopedia of Industrial Chemistry*. 2000, Wiley-VCH Verlag GmbH & Co. KGaA.

51. Narkhede, V.V. and H. Gies, *Crystal Structure of MCM-22(MWW)and Its Delaminated ZeoliteITQ-2 from High-Resolution Powder X-Ray Diffraction Data: AnAnalysis Using Rietveld Technique and Atomic Pair Distribution Function*. Chemistry of Materials 2009. **21**: p. 4339-4346.

52. Keller, G.E. and M.M. Bhasin, *Synthesis of ethylene via oxidative coupling of methane: I. Determination of active catalysts*. Journal of Catalysis, 1982. **73**(1): p. 9-19.

53. Zeng, Y., F.T. Akin, and Y.S. Lin, *Oxidative coupling of methane on fluorite-structuredsamarium–yttrium–bismuth oxide*. Applied Catalysis A: General 2001. **213**: p. 33-45.

54. Guo, X., G. Fang, G. Li, H. Ma, H. Fan, L. Yu, C. Ma, X. Wu, D. Deng, M. Wei, D. Tan, R. Si, S. Zhang, J. Li, L. Sun, Z. Tang, X. Pan, and X. Bao, *Direct, Nonoxidative Conversion of Methane to Ethylene, Aromatics, and Hydrogen*. Science, 2014. **344**(6184): p. 616-619.

55. Bao, X. *personal communication to:* L. Lefferts, 2016

56. Kim, S.K., H.W. Kim, S.J. Han, S.W. Lee, J. Shin, and Y.T. Kim, *Mechanistic and microkinetic study of non-oxidative methane coupling on a single-atom iron catalyst*. Communication Chemistry, 2020. **3**(58).

57. Han, S.J., S.W. Lee, H.W. Kim, S.K. Kim, and Y.T. Kim, *Nonoxidative Direct Conversion of Methane on Silica-Based Iron Catalysts: Effect of Catalytic Surface*. ACS Catalysis, 2019. **9**: p. 7984-7997.

58. Sot, P., M.A. Newton, D. Baabe, M.D. Walter, A.P.v. Bavel, A.D. Horton, C. Copére, and J.A.v. Bokhoven, *Non-oxidative Methane Coupling over Silica versus Silica-Supported Iron(II) Single Sites*. Chemistry—A European Journal, 2021. **26**: p. 8012-8016.

59. Sakbodin, M., Y. Wu, S.C. Oh, E.D. Wachsman, and D. Liu, *Hydrogen-Permeable Tubular Membrane Reactor: Promoting Conversion and Product Selectivity for Non-Oxidative Activation of Methane over an FeVSiO2 Catalyst*. Angewandte Chemie, 2016. **55**: p. 16149 –16152.

60. Oh, S.C., E. Schulman, J. Zhang, J. Fan, Y. Pan, J. Meng, and D. Liu, *Direct Non-Oxidative Methane Conversion in a Millisecond Catalytic Wall Reactor*. Angewandte Chemie, 2019. **58**: p. 7083-7086.

61. Nishikawa, Y., H. Ogihara, and I. Yamanaka, *Liquid-Metal Indium Catalysis for Direct Dehydrogenative Conversion of Methane to Higher Hydrocarbons*. ChemistrySelect, 2017. **2**: p. 4572-4576.

62. Chen, Y., X. Wang, X. Luo, X. Lin, and Y. Zhang, *Non-Oxidative Methane Conversion Using Lead- and Iron-Modified Albite Catalysts in Fixed-Bed Reactor*. Chinese Journal of Chemistry, 2018. **36**: p. 531-537.

63. Xiao, Y. and A. Varma, *Highly Selective Nonoxidative Coupling of Methane over Pt-Bi Bimetallic Catalysts*. ACS Catalysis, 2018. **8**: p. 2735-2740.

64. Xie, P., T. Pu, A. Nie, S. Hwang, S.C. Purdy, W. Yu, D. Su, J.T. Miller, and C. Wang, *Nanoceria-Supported Single-Atom Platinum Catalysts for Direct Methane Conversion*. ACS Catalysis, 2018. **8**: p. 4044-4048.

65. Gerceker, D., A.H. Motagamwala, K.R. Rivera-Dones, J.B. Miller, G.W. Huber, M. Mavrikakis, and J.A. Dumesic, *Methane Conversion to Ethylene and Aromatics on PtSn Catalysts*. ACS Catalysis, 2017. **7**: p. 2088-2100.

66. Okolie, C., Y. Lyu, L. Kovarik, E. Stavitski, and C. Sievers, *Coupling of Methane to Ethane, Ethylene, and Aromatics over Nickel on Ceria–Zirconia at Low Temperatures*. ChemCatChem, 2018. **10**: p. 2700-2708.

67. Dutta, K., P.G. Lu Lib, D.P. Gutierrez, and J. Kopyscinski, *Direct non-oxidative methane aromatization over gallium nitride catalyst in a continuous flow reactor*. Catalysis Communications, 2018. **106**: p. 16-19.

68. Sheng, H., E.P. Schreiner, W. Zheng, and R.F. Lobo, *Non-oxidative Coupling of Methane to Ethylene Using Mo2C/[B]ZSM-5*. ChemPhysChem, 2018. **19**: p. 504-511.

69. Scapinello, M., E. Delikonstantis, and G.D. Stefanidis, *The panorama of plasma-assisted non-oxidative methane reforming*. Chemical Engineering and Processing: Process Intensification, 2017. **117**: p. 120-140.

70. García-Moncada, N., G.v. Rooij, T. Cents, and L. Lefferts, *Catalyst-assisted DBD plasma for coupling of methane: Minimizing carbon-deposits by structured reactors*. Catalysis Today, 2021. **369**: p. 210-220.

71. Delikonstantis, E., M. Scapinello, and G.D. Stefanidis, *Low energy cost conversion of methane to ethylene in a hybrid plasma-catalytic reactor system*. Fuel Processing Technology, 2018. **176**: p. 33-42.

72. García-Moncada, N., T. Cents, G.v. Rooij, and L. Lefferts, *Minimizing carbon deposition in plasma-induced methane coupling with structured hydrogenation catalysts*. Journal of Energy Chemistry, 2021. **58**: p. 271-279.

73. Slotbooma, Y., S. Roosjen, A. Kronberg, M. Glushenkov, and S.R.A. Kersten, *Methane to ethylene by pulsed compression*. Chemical Engineering Journal, 2021. **414**.

74. Nagaki, D.A., Z. Zhao, M.N.Z. Myint, I. Lengyel, A. Mamedov, C.W. Gundlach, K. Sankaranarayanan, and D. Falcone, 2018, *Method for Producing Hydrocarbons by Non-Oxidative Coupling of Methane*, US 9 , 902 , 665 B2

75. Arutyunov, V.S. and V.I. Vedeneev, *Pyroylysis of methane in the temperature range 100-1700K* Russian Chemical Reviews, 1991. **60**(21): p. 1384-1396.

76. Slater, W.E., *The influence of different surfaces on the decomposition of methane*. Journal of the Chemical Society, Transactions, 1916. **109**: p. 160-164.

77. Khan, M.S. and B.L. Crynes, *Survey of Recent Methane Pyrolysis Literature*. Industrial & Engineering Chemistry, 1970. **62**(10): p. 54-59.

78. Zwet, G.P.v.d., P.A.J.M. Hendriks, and R.A.v. Santen, *Pyrolysis of methane and the role of surface area*. catalysis Today, 1989. **4**: p. 365-369.

79. Lieberman, M.L. and G.T. Noles, *Effect of Flow Rate on Gas Composition During the Isothermal Pyrolysis of Methane*. Carbon, 1973. **12**: p. 689-693.

80. Palmer, H.B., J. Lahaye, and K.C. Hou, *On the Kinetics and Mechanism of the Thermal Decomposition of Methane in a Flow System*. Journal of Physical Chemistry, 1968. **72**(1): p. 348-353.

81. Chen, C.J. and M.H. Back, *The Thermal Decomposition of Methane. I. Kinetics of the primary decomposition to* C_2H_6 *+*H_2*; Rate constant for the Homogeneous Unimolecular Dissociation of Methane and its Pressure Dependance*. Canadian Journal of Chemistry, 1975. **53**: p. 3580-3590.

82. Chen, C.J. and M.H. Back, *The thermal decomposition of methane. II. Secondary reactions, autocatalysis and carbon formations; non-arrhenius behaviour in the reaction of CH3 with ethane*. Canadian Journal of Chemistry, 1976. **54**(54): p. 3175-3184.

83. Roscoe, J.M. and M.J. Thompson, *Thermal decomposition of Methane: Autocatalysis*. International Journal of Chemical Kinetics, 1985. **17**: p. 967-990.

84. Dean, A.M., *Detailed Kinetic Modeling of Autocatlysis in Methane Pyrolysis*. Journal of Physical Chemistry, 1990. **94**: p. 1432-1439.

85. Rokstad, O.A., O. Olsvik, and A. Holmen, *Thermal Coupling of Methane*. Natural Gas Conversion, 1991: p. 533-539.

86. Olsvik, O., K. Heitnes, O.A. Rokstad, and A. Holmen, *Quenching of hot product gases from the pyrolysis of methane*. Studies in Surface Science and Catalysis, 1994. **81**: p. 573-575.

87. Olsvik, O., O.A. Rokstad, and A. Holmen, *Pyrolysis of Methane in the Presence of Hydrogen*. Chemical Engineering & Technology, 1995. **18**: p. 349-358.

88. Blekkan, E.A., R. Myrstad, O. Olsvik, and O.A. Rokstad, *Characterization of Tars and Coke formed during the Pyrolysis of Methane in a Tubular Reactor*. Carbon, 1992. **30**(4): p. 665-673.

89. Billaud, F. and C. Gueret, *Thermal decomposition of pure methane at 1263K. Experiments and mechanistic modelling*. Thermochimica Acta, 1992. **211**: p. 303-322.

90. Billaud, F.G. and F. Baronnet, *Thermal Coupling of Methane in a Tubular Flow Reactor: Parametric Study*. Industrial & Engineering Chemistry Research, 1993. **32**: p. 1549-1554.

91. Guéret, C. and F. Billaud, *Thermal coupling of methane: influence of hydrogen at 1330°C. Experimental and simulated results*. Journal of Analytical and Applied Pyrolysis, 1994. **29**: p. 183-205.

92. Guéret, C., F. Billaud, B. Fixari, and P.l. Perchec, *Thermal Coupling of Methane, Experimental investigations on Coke Deposits*. Carbon, 1994. **33**(2): p. 159-170.

Chapter 2

Influence of axial temperature profiles on Fe/SiO_2 catalysed non-oxidative coupling of methane

This chapter has been published as:

Influence of axial temperature profiles on Fe/SiO_2catalyzed non-oxidative coupling of methane ;R.S. Postma, L. Lefferts; ChemCatChem; 13, 4, 2021.

Abstract

The effect of the axial temperature profile upstream and downstream of catalyst bed on the performance of Non-Oxidative-Coupling-of-Methane (NOCM) over Fe©SiO_2 was determined. A three-zone oven was used with independent temperature control of the catalyst-zone as well as the zones upstream and downstream. It was found that catalytic initiation followed by residence time at 1000°C downstream the catalyst bed increases CH_4 conversion by a factor of 8, while decreasing carbonaceous deposit selectivity from 40 to 12 C%. Residence time at 1000°C upstream of the catalyst bed causes deposit formation on the catalyst without significantly influencing methane conversion. A shallow catalyst bed followed significant residence time at high temperature maximizes methane conversion and minimizes coking. This work shows that axial temperature profile and residence time upstream and downstream of the catalyst bed strongly influence the performance in catalytic NOCM.

2.1 Main text

Methane [1] is one of the most abundant hydrocarbons on the planet [2, 3] and is seen as a high potential intermediate in the transition towards renewable sources of chemicals [4]. Currently, methane is mainly used in domestic and industrial heating as well as electricity production [5]. The vast majority of industrial processes for converting natural gas into base chemicals and liquid fuels is based on reforming [5] followed by various syngas-based synthesis routes [6-10]. The multiple steps in these processes cause low energy efficiency and high investment costs [10, 11].

Thus, direct methane coupling has received a lot of attention both in industry as well as academia [4, 12-18]. The challenge is caused by the high stability of methane, its negligible electron affinity and low polarizability [19, 20], compared to the coupling products. Both Methane dehydroaromatization (MDA) [12, 13, 15, 17, 18] as well as oxidative coupling of methane (OCM) [14, 21-23] suffer from too low product yields to be industrially viable. Catalytic NOCM [3, 24-32] has recently gained much interest, achieving higher product yield and co-producing valuable hydrogen. The NOCM reaction requires operation temperatures above 900°C, to achieve significant conversion [19] usually resulting in significant coke formation.

In 2014 Guo et al. [3] reported coupling of methane to olefins and aromatics over an iron on silica catalyst (Fe©SiO_2) at temperatures in excess of 950°C, without coke formation. The maximum reported combined product yield was 48% at 1090°C. Other research groups also report low coking rates but have not yet been able to reproduce the performance reported by Guo *et al.* [24-26, 32, 33]. An overview of literature data on catalytic non-oxidative methane coupling is presented in S1. Despite the fact that many laboratories initiated work on the subject, the number of peer reviewed papers is rather limited, likely because it is not easy to prevent extensive coking. We will show in this study that the design of the lab reactor and the oven is essential for achieving this.

Methane is thermodynamically unstable at temperatures above 650°C [19, 34-37], which is confirmed by the blank experiments in several studies [3, 25, 26], showing significant methane conversion. DFT calculations [3, 32] suggest that the Fe©SiO_2 catalyst is involved exclusively in methane activation to methyl radicals and hydrogen, which are released to the gas phase. All further coupling reactions to olefins and aromatics are governed by gas phase free-radical propagation and termination reactions [3, 32]. Especially the recent patent [33] issued by SABIC supports this, showing that reactions in the gas phase downstream the catalyst bed influence conversion and product distribution significantly. It is remarkable that detailed information on reactor design, oven design, dimensions and temperature profile around the catalyst bed are generally not available [3, 24, 25, 27, 29, 31, 33]. This study demonstrates that axial temperature profiles, controlled with an oven designed for this purpose, influence not only conversion and product distribution, but also the formation of carbonaceous deposits significantly.

A custom-built oven was used to control the temperature profile in the reactor-zone, as well as the zones upstream and downstream of the catalyst bed (Figure 2.1). The temperature in each of the three zones is controlled independently up to 1100°C. Sharp temperature gradients were achieved by using close fitting thermal insulation between the zones. Residence time at high temperature upstream, inside and downstream of the catalyst bed were systematically changed by varying the amount of catalyst, the position of the catalyst bed inside the 6 cm reactor-zone as well as the temperatures of the pre-heater and the post-heater. Note that no catalyst bed diluent is used, due to the activity of bed diluent materials for methane activation at temperatures higher than 900°C [35].

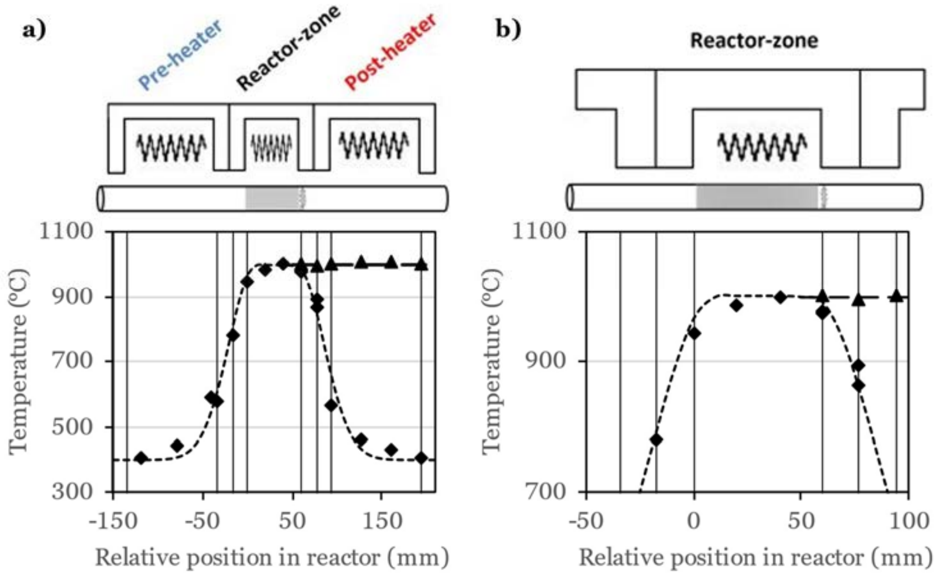

Figure 2.1: a) temperature profile inside the reactor including pre- and post-heater measured with an empty reactor tube b) zoom in on Figure 2.1a around the reactor-zone; gas-flow rates of 10 ml·min^{-1} N_2; Vertical bars represent the insulating layers between the 3 different zones. - - -◆- - - Pre- and post-heater at 400°C; reactor-zone at 1000°C; —▲- - Post-heater at 1000°C.

The terms “τ@upHT” and “τ@downHT” refer respectively to residence time in free-volume at 1000°C upstream of downstream of the catalyst bed. All residence times are calculated based on the volume of the relevant part of the reactor and the flowrate at STP. Details concerning the experimental setup and the equations applied to calculate conversion and selectivity to several products can be found in S4 and S5, respectively.

Figure 2.2 shows increasing methane conversion with increasing residence time at 1000°C downstream of the catalyst bed (τ@downHT), at constant conditions and contact time inside the catalyst bed. This effect is not observed when increasing residence time at 1000°C upstream of the catalyst bed (τ@upHT), as shown in Figure S 2.6. The conversion under the same conditions in absence of catalyst is low (Figure 2.2), in agreement with the hypothesis that the catalyst activates methane, forming methyl radicals [3, 32], followed by radical chain reactions. A similar autocatalytic phenomenon is also reported for non-catalytic non-oxidative coupling of methane [36, 38]. Apparently, residence time at high temperature downstream of the catalyst bed enables propagation of the radical chain reaction, increasing methane conversion substantially. Remarkably, this effect continues for at least 8 seconds residence time.

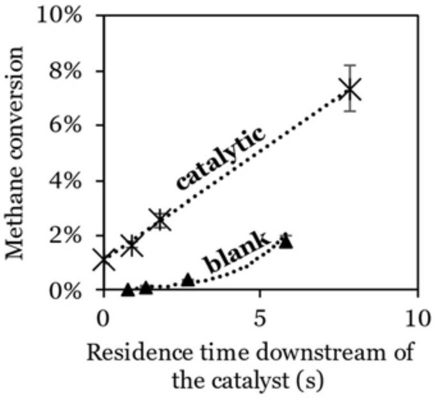

Figure 2.2: The effect of post-catalytic free- volume residence time at 1000°C, ✳ for methane activated by 0.26 g catalyst at 3.5 l·gcat^{-1}·h^{-1}, ▲gas-phase initiated system (no catalyst); 90% CH_4 in N_2; reactor-zone at 1000°C, pre-heater at 400°C; post-heater at 400°C for lower residence time in free volume and 1000°C for higher residence time in free volume.

Figure 2.3 shows the effect of τ@downHT on the yields of products. The yields of all products increase in the hot volume downstream the catalyst bed as conversion increases, except for the yield of ethane. Apparently, increasing consecutive conversion of ethane in the hot zone dominates over formation of ethane. Yield of carbon deposits, estimated assuming a closing C- mass balance, increases much less with increasing methane conversion than the other products (Figure 2.3). Figure S 2.7 presents the trends in selectivity with τ@downHT at constant conversion, confirming that the selectivity to carbon deposits decreases. In contrast, yields of acetylene, benzene and naphthalene all significantly increase and their production via free radical chain reactions apparently dominates over consecutive conversion reactions in the hot zone downstream the catalyst.

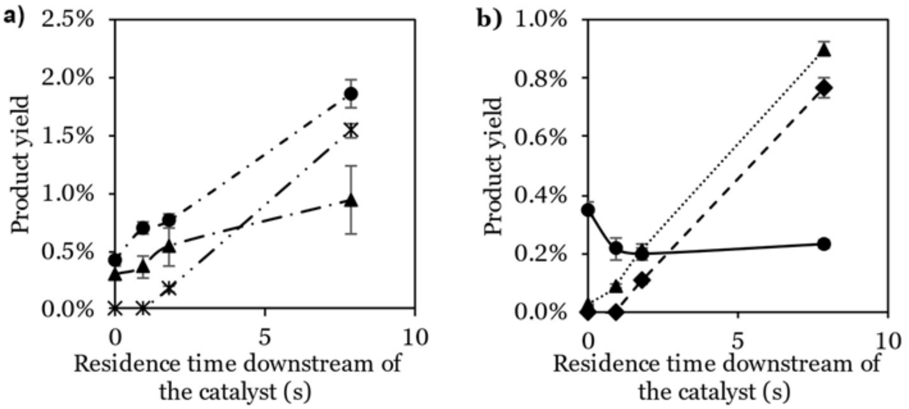

Figure 2.3: Influence of τ@downHT on the yield at $3.5\ l\cdot g_{cat}^{-1}\cdot h^{-1}$, matching the conversion shown in Figure 2; 0.26 g catalyst; 90% CH_4 in N_2; (a) major products and total carbon to products: —✱— Naphthalene; -·●·- Ethylene; —▲— Deposits; (b) minor products: —●— Ethane; - ◆ - Benzene; ·····▲·····; Acetylene; conditions according to Figure 2.2.

Table 2.1 compares the performance of Fe©SiO_2 in this work, both with and without extended residence time at 1000°C downstream of the catalyst bed, with the results reported in literature. It is remarkable that both activity as well as selectivity obtained when operating with high τ@downHT, are quite similar to results of Sakbodin et al. [24] and Oh et al. [25]. In contrast, fast quenching downstream the catalyst bed results in much lower conversion and more deposit formation.

Table 2.1**:** performance comparison between this work and others using the Fe(c)SiO_2 catalyst.

Paper	**Condition/ref**	**Temp °C**	**SV ml·g_{cat}^{-1}·h^{-1}**	**Conversion % CH_4**	**Olefins selectivity C%**	**Aromatics selectivity C%**	**Deposit selectivity C%**
This work	Fast quenching	1000	3650	0.9	61	0	39
This work	τ@downHT 8 sec	1000	3640	7.7	50	38	12
Guo et al.	[3]	1000	10000	31	21	79	0
Sakbodin et al.	[24]	1000	3200	8	37	63	0
Oh et al.	[25]	1000	3200	8	37	53	10
Han et al.	[26]	1020	8250	6.5	66	32	2
SABIC patent	[33]	1030	21400	7.5	44	50	6

Figure 2.4 shows that the apparent activation energy increases with increasing τ@downHT, based on experiments between 950 and 1100°C. We observe that apparent activation energy increases with increasing methane conversion in τ@downHT. Han *et al.* [26] reported an apparent activation energy of 334 kJ·mol^{-1}. Calculation of apparent activation energies based on the data of Guo *et al.* [3], Sakbodin *et al.* [24] and Oh et al. [25] resulted in 454 kJ·mol^{-1}, 333 kJ·mol^{-1} and 577 kJ·mol^{-1} respectively, as presented in Figure S 2.12. A coated wall reactor contains a large empty volume, explaining the high activation energy estimated based on the data of Oh. The high activation barrier estimated based on the results of Guo suggests a large contribution of reactions in the downstream zone, in agreement with the fact that conversion and activity were the highest reported so far. To lesser extent, the same is true for the results reported by Sakbodin et al. [24] and Han et al. [26].

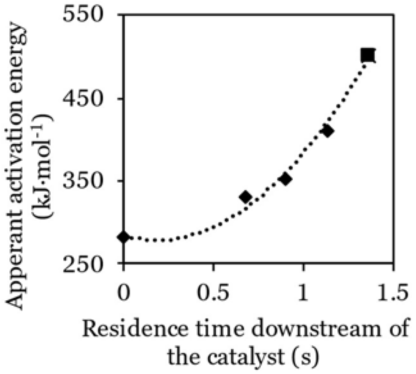

Figure 2.4: Apparent activation energy change when increasing the free-volume downstream of the catalyst, by decreasing the amount of catalyst; measured at constant flowrate: 33.3 ml·min^{-1}: 90% CH$_4$ in N$_2$ ◆; temperature of reactor-zone varied between 950-1100°C, pre-heater and post-heater at 400°C; note that the data point ■ at 1.35 s **no** catalyst; for details on catalyst placement refer to Supporting Information S.4.

Figure 2.5 presents the integral yields to products, deposits on the catalyst and deposits downstream during a 14 hours experiment under conditions as summarized in Table S 2.3. Figure 2.5 confirms that the product yield increases with increasing τ@downHT. Figure 2.5 also shows that formation of deposits on the catalyst is suppressed by rapid heating of the reactant gas before it reaches the catalyst, preventing soot formation in the gas phase that would be trapped by the catalyst bed.

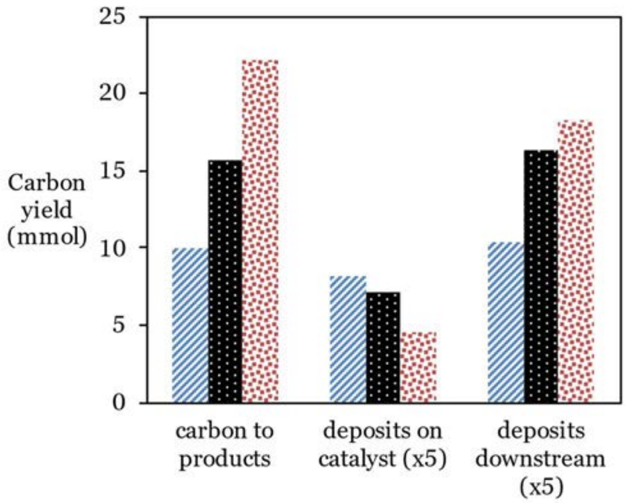

Figure 2.5: Effect of τ@upHT and τ@downHT on the integral product distribution over a full experiment during 14h at 1000°C with 90% CH_4 in N_2 during which flowrate and temperature was varied in time according a fixed program described in Supporting information S. 4; ▨ 0.5 ml τ@upHT; ■ 0.25 ml τ@upHT & 0.25 ml τ@downHT; ▒ 0.5 ml τ@downHT; deposits on the catalyst are measured using TGA and assumed to contain exclusively carbon. Deposit formation downstream of the catalyst estimated based on the C-mass balance; deposits on the catalyst and downstream of the catalyst have been multiplied by 5 for clarity; pre-heater and post-heater operated at 400°C.

In summary, methane conversion is dominated by propagation reactions in free volume at 1000°C downstream of the catalyst bed, after initiation of the free radical reaction by the catalyst, in agreement with the recent patent publication [33]. At the same time, formation of deposits is significantly reduced, whereas formation of olefins and aromatics in the hot zone dominate. Formation of deposits can be further suppressed by heating the reaction mixture rapidly, before contacting the catalyst. Residence time inside the catalyst bed should be minimized, since the catalyst is only required for initiation the free radical reaction and will cause significant deposit formation when in contact free radicals.

The design of the catalytic reactor and the oven determines to an important extent the performance in catalytic NOCM, with respect to both activity as well as minimizing formation of deposits. Unfortunately, these details are usually not reported. Especially the large effect on the formation of carbonaceous deposits is responsible for the fact that results depend strongly on experimental details.

2.2 Experimental section

The Fe©SiO_2 catalyst was prepared according procedures reported in literature [3] and the expected composition and structure were confirmed with XRF and XRD, respectively [3, 24, 26]. More detailed information on catalyst synthesis and characterization is presented in S2 and S3, illustrating our catalyst is very similar to Fe©SiO_2 catalysts synthesized in earlier studies.

2.3 Acknowledgements

We acknowledge support from the Dutch National Science Foundation (NWO) and the industrial partners: SABIC, Sasol and BASF. We thank ing. B. Geerdink, K.J. Altena, ing. T.L.M. Velthuizen and ir. T. Lubbers for their experimental and analytical support. We thank dr. T.A. Nijhuis and dr. D. Nagaki for inspiring discussions. Lastly, we thank dr. E. Postma for input in correcting the document.

Keywords: Fe©SiO2 · non-oxidative methane conversion · free radical reaction · coke formation

2.4 Supporting information

2.4.1 S.1 Overview of performance figures concerning catalytic NOCM

In 2014 Guo et al. [3] reported coupling of methane to olefins and aromatics over an iron on silica catalyst (Fe©SiO_2) at high temperature, between 950 and 1090°C, without suffering from coke formation. The catalyst was synthesized by fusing Fe_2SiO_4 into silica at 1700°C. The maximum reported conversion is 48.1% at 1090°C. The only hydrocarbons produced are ethylene, benzene and naphthalene, with an ethylene selectivity of ~50% between 950 and 1090°C. Other research groups have not yet been able to reproduce the performance reported by Guo *et al.* [24-26]. Sakbodin *et al.* [24] used the Fe©SiO_2 catalyst in a $SrCe_{0.7}Zr_{0.2}Eu_{0.1}O_{3-\delta}$ hydrogen permeable membrane reactor. It was shown that hydrogen removal from the reaction can increase the methane conversion, while still suppressing coke formation. CH_4 conversion was 8% at 1000°C in a fixed bed reactor, increasing to 13% under the same conditions using the membrane. Oh *et al.* [25] coated Fe©SiO_2 on the wall of a quartz reactor which increased methane conversion from 8 to 11.4%. Coking was reported at an average carbon selectivity of 10%. Han et al. [26] performed a thorough analysis of the effects of different silica polymorphs as well as iron deposition methods for Fe/SiO_2 catalysts. The Cristobalite phase of silica, formed above 1470°C [39]**,** was determined to be the most important factor in preventing coke formation. This high temperature silica polymorph raises the apparent activation energy for coke formation compared to the quartz phase, from 150 $kJ \cdot mol^{-1}$ for quartz to around 450 $kJ \cdot mol^{-1}$. Kim et al. [32] performed detailed DFT calculations on the active iron site in the Fe©SiO_2 catalyst. Their calculations show that methyl radical generation is in competition with direct acetylene production on the catalyst surface. Furthermore, the calculations show that gas-phase methyl radicals can abstract methyl species on the catalyst surface, thus enhancing the reaction rate.

Other catalysts are reported for the NOCM reaction with low coking rates, in most cases operated at lower conversion. Okolie *et al.* [28] reported CH_4 conversion up to 1.2% over a Ni/$Ce_{0.83}Zr_{0.17}O_2$ catalyst, operated at 300-500°C with a 5% CH_4/N_2 feed, into predominantly ethane, with traces of ethylene, benzene and toluene. Nishikawa *et al.* [31] screened a wide range of 10 wt% transition metals deposited on dense silica, In/SiO_2 showed by far the highest activity. Conversion was measured between 0.2 and 4.6%, forming mainly ethane and ethylene, with coke selectivity between 5 and 30% depending on the temperature. Chen *et al.* [27] reported a Pb/albite and Fe/albite catalysts achieving methane conversion up to 8% at 900°C. The only products reported are ethane and ethylene, with traces of acetylene. Xiao *et al.* [30] reported a bimetallic Pt-Bi catalyst, by tuning the ratio between Pt-Bi to 1%Pt,0.8%Bi/ZSM5 at 650°C a methane conversion of

5.5% was achieved with only 5% coke selectivity. Xie *et al.* [29] showed methane coupling over atomically dispersed Pt/CeO_2. Methane converts between 2% to 25% at temperatures between 900 and 1000°C, with high C_2 selectivity and no coking, using a highly diluted methane stream, i.e. 1% CH_4 in He. All data on catalytic non-oxidative methane coupling are summarized in Table S 2.1. The method used to determine or estimate the amount of coke is indicated: GC means that the amount of coke is estimated assuming a closed mass balance based on GC analysis of all compounds in the product mixture, W refers to determining the amount of coke more accurately by weighing the catalyst or reactor before and after reaction on a balance. TGA refers to Thermogravimetric analysis, TG-MS refers to a TGA analysis coupled with a mass spectrometer to analyse the evolving gasses.

Table S 2.1: Summary of papers on catalytic NOCM, showing the measured temperature range, used space velocities, feed-gas composition and the achieved methane conversion as well as coke selectivity.

Publication	**Topic**	**T range °C**	**SV range $ml \cdot g_{cat}^{-1} \cdot h^{-1}$**	**CH_4 conc**	**Conv range %CH_4**	**Coke selectivity C%**	**Coke determination method**
Guo et al. [3]	Fe©SiO_2 catalyst	950-1090	4840-21400	90%CH_4/N_2	8.3-48.4%	0%	GC
Sakbodin et al. [24]	Membrane reactor	950-1050	3200	90%CH_4/Ar	2.1-23.7%	0%	GC
Oh et al. [25]	Coated wall reactor	1000	3200	90%CH_4/N_2	8-11.4%	10%	W, TGA, TPO
Han et al. [26]	Support effect	1020	8250	90%CH_4/Ar	6.5%	2%	TGA
Nishikawa et al. [31]	In/SiO_2 liquid metal catalyst	750-900	6000	90%CH_4/Ar	0.2-4.6%	5-30%	GC
Chen et al. [27]	Pb/albite	600-900	1000-3000	90%CH_4/N_2	0.5-8%	0%	TGA
Xiao et al. [30]	1%Pt,0.8%Bi/ZSM5	650	825-18600	100%CH_4	5.50%	5%	GC
Xie et al. [29]	Pt/CeO2	900-1000	6000	1%CH_4/N_2	2-25%	0%	TG-MS
SABIC patent [33]	Effect of free volume	960-1030	4840-42800	90%CH_4/N_2	2.4-28.4%	5-70%	GC

2.4.2 S.2 Synthesis procedure of Fe©SiO₂ catalyst

Fe_2SiO_4 was synthesized according to the method reported by DeAngelis et al. [40] Toluene (375 ml, pro analysis, Emsure) is mixed with 175 ml methanol (pro analysis, Emsure) and added to a 1l three-neck round bottom flask. These necks are used to introduce 1.2 bar N_2, to introduce liquid via a drippling funnel (20 ml) and for a reflux condenser with a needle valve at the top, to release small amounts of gas. The solvent mixture is refluxed, under agitation, for 30 minutes at 250°C to remove any oxygen and left to cool down. 8.7 g of iron (II) chloride (99.5%, Alfa Aesar) is mixed with 9.3 g of sodium ethoxide (96%, Alfa Aesar) inside a glovebox and sealed in an airtight bottle. The bottle is placed in a gastight bag and sealed to the round bottom flask, after removing the dripping funnel. After addition of the powder the temperature is slowly increased to 150°C. 7.9 g TEOS (reagent grade, Aldrich) was slowly added using the dripping funnel. After 30 minutes 10 ml of 0.2 M NaOH (reagent grade, Emplura) was added. The solution is left to reflux overnight (16h). The formed gel was dried in a rotary evaporator under vacuum. Pressurization to atmospheric is done using N_2. The formed powder is heated at 5 $K{\cdot}min^{-1}$ to 800°C and held for 2h under N_2 atmosphere. The resulting Fe_2SiO_4 is analysed using XRD and XRF as described in S3, Figure S 2.1 and Table S 2.2.

The Fe_2SiO_4 was mixed with granulated quartz pro analysis (Merck). The mixture is milled in a Fritsch Pulverisette 5 planetary ball mill under N_2 atmosphere for 19h at 360 rpm operated with a Y-stabilized ZrO_2 milling jar with 0.5 mm milling balls. Typically, 30 g of pre-mixed Fe_2SiO_4 and quartz and 100 g milling balls are loaded in an 80 ml milling jar. The resulting powder is separated from the milling balls and about 1.5 g is added to a ZrO_2 crucible and placed inside a box-oven. The oven is first heated at 5°C·min^{-1} to 120°C, it is kept at 120°C for 1h to remove moisture. The oven is heated at 3°C·min^{-1} to 1600°C, the oven is heated further at 2°C·min^{-1} to 1700°C. The oven is kept at 1700°C for 6h. The oven is cooled down in the inverse order, from 1700°C to 1600°C at 2°C·min^{-1} and from 1600°C to room temperature at 3°C. The fused Fe/SiO_2 (Figure S 2.2) is removed from the crucible at room temperature. The fused slab is broken, milled and sieved into different size fractions. The fraction between 250-500 μm is used to measure the catalytic properties. The catalyst particles are leached for 2h in 0.5M HNO_3 (diluted from 65wt% reagent grade HNO_3, Emsure) under ultrasonic agitation at room temperature. Sieving is repeated after rinsing with Milli-Q water and drying at 105°C, removing a small fraction of fines.

2.4.3 S.3 Characterization of the synthesized catalyst and precursors

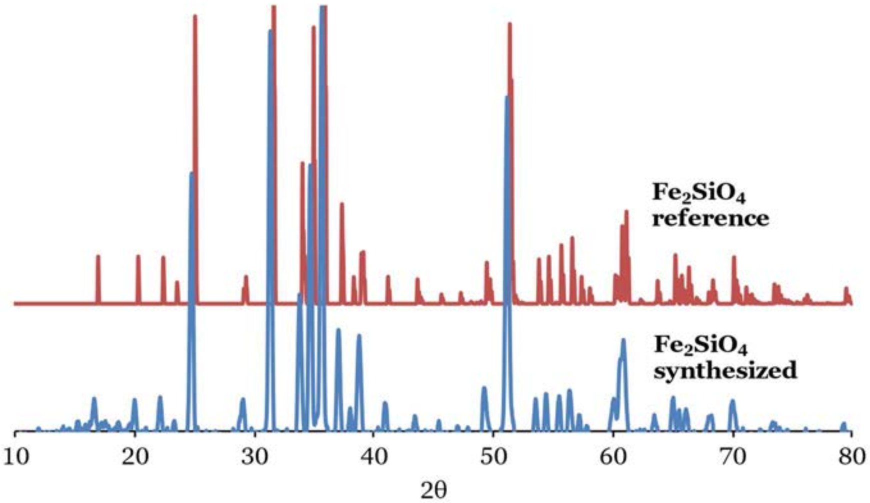

Figure S 2.1: XRD diffractogram of the synthesized fayalite (Fe_2SiO_4) catalyst precursor compared to literature [40, 41].

The Fe©SiO_2 catalyst as well as Fe_2SiO_4 are analysed using XRF (Bruker Tiger S8) to determine the chemical composition. XRD (Bruker D2 Powder) is used to determine the crystallographic structure of the catalyst as well as of potential impurities. The amount of carbon deposited on spent catalyst is determined with TGA (Mettler Toledo TGA/DSC 3+ Star System); typically, 30 mg of sample is loaded in the crucible, increasing the temperature with 5°C·min^{-1} until 1000°C in 50 vol% air in Ar (20 ml·min^{-1}).

Table S 2.2 shows that the composition of Fe_2SiO_4 is very similar to the theoretical composition. Also the similarity of XRD diffractogram (Figure S 2.3) of in-house synthesized cristobalite with literature [41] confirms successful preparation of cristobalite. The catalyst contains 45.4 weight percent of silicon and 0.5 W% Fe, as expected. Furthermore, traces of both zirconia and yttria were found, similar as reported by Han *et al.* [26] following the same synthesis procedures. Both zirconia and yttria are trace elements introduced during the ball-milling step, through unavoidable attrition of the milling balls. No further contaminations were detected. Figure S 2.3 shows the XRD diffractogram of Fe©SiO_2 and. All peaks of Fe©SiO_2 catalyst are shifted slightly to lower 2θ values as compared to the cristobalite reference as well as literature data [41]. The Fe©SiO_2 diffractograms shows minor peaks at 20°, 26.9°, 30.1° and 36.3°, attributed to zircon ($ZrSiO_4$) [41] and pyroxferroite ($FeSiO_3$) [41]. The shift in the spectrum might be caused by the presence of traces of e.g. Fe, Zr or Y ions in the cristobalite crystal structure. Peaks attributed to both zircon ($ZrSiO_4$) [41] and pyroxferroite ($FeSiO_3$) [41] were detected, although at very low intensities (not shown). Han et al. [26] reported presence of the same phases, in a study showing that catalysts containing cristobalite phase of quartz cause less coking than other quartz polymorphs. Han et al. [26] also reported presence of zirconia-containing phases in Fe©SiO_2, attributing peaks for ZrSiO4 at 2θ values of 27.0° and 30.2° in agreement with our results, although the 30.2° peak could also be attributed to $FeSiO_3$ [41].

Figure S 2.2: Fe©SiO_2 after 6h fusion at 1700°C.

Table S 2.2: Elemental composition of the catalyst and precursors as determined by XRF.

Element	Fe©SiO_2 Wt%	Fe_2SiO_4 Wt%	Fe_2SiO_4 theoretical Wt%
Si	45.4	13.2	13.9
Fe	0.5	55.1	54.8
Zr	2.1	0	0
Y	0.2	0	0
O (rest)	51.8	31.7	31.4

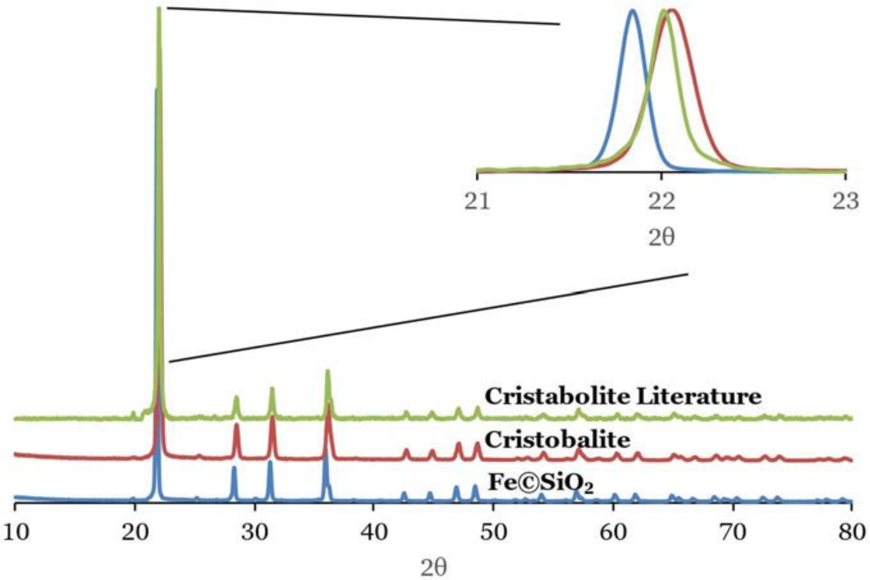

Figure S 2.3: XRD diffractogram of fresh Fe©SiO2 compared with diffractograms of Cristobalite and Cristobalite literature reference [41]. The zoom in of the major diffraction peak shows a subtle shift in the peak position.

2.4.4 S.4 Reactor setup and catalytic testing

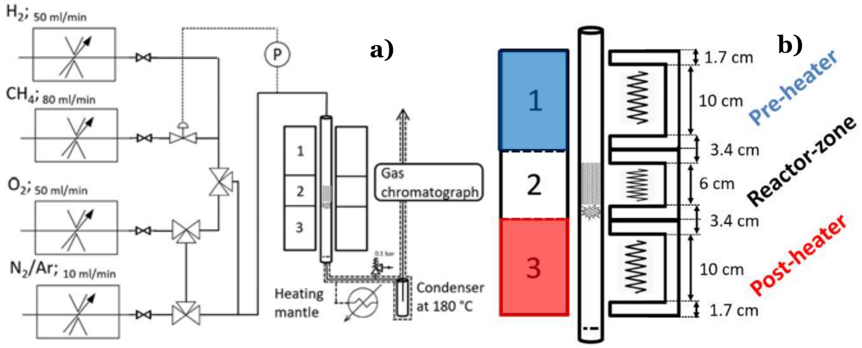

Figure S 2.4: a) Flow scheme of the reaction system; b) detailed overview of the reactor-system, each zone is separated by two insulating layers (each 1.7 cm thick), which have a hole in the middle, allowing the reactor to pass through. The left side shows the labels as used in the manuscript, the right side shows the inside cut-away, including dimensions.

Figure S 2.4a presents a scheme of the equipment to measure the catalytic performance. Four mass-flow-controllers supply gasses to the reactor. The gas feed generally consists of 90% CH_4 and 10% N_2, which is used as an internal standard, at atmospheric pressure. A pressure indicator measures the pressure before the reactor and shuts off the methane flow in case carbon formation would block the reactor. The oven is segmented in three thermally insulated zones, which will be described in detail below. The tubing between the reactor and the GC is traced at 200°C to minimize condensation of products. A condenser at 150°C is placed between the reactor and the GC to prevent accumulation of higher aromatics (C_{10+}) in the GC. GC-MS analysis of the condensate, presented in section 2.4.8, show a mixture of polyaromatic species with at least three aromatic rings. A pressure relief valve after the reactor, opening at 0.07 bar overpressure, limits the pressure build-up over the GC at high flowrates.

Figure S 2.4b shows details of the oven and reactor operated in down-flow; the zones denoted 1 and 3 are the pre-heater and post-heater, respectively. The reactor system is designed inhouse and produced by Elicra electrowarmte b.v.. Zone 2 is termed the reactor-zone. The temperatures in each zone can be controlled independently. The heated zone in the pre-heater and post-heater are both 10 cm in length the heated zone of the reactor zone is 6 cm in length. Each section has an insulation layer of 1.7 cm in length at both the entrance and exit, thermally isolating the three zones. The pre-heater and post-heater are operated at 400°C, unless otherwise noted. The temperature of the reactor-zone is varied between 950 and 1100°C. The inner diameter of the oven is 12 mm, whereas the reactor is a high purity quartz tube with 4 mm inner diameter, 6 mm outer diameter and a length of 350 mm. The space between the reactor-tube and the oven is plugged with quartz wool in the top of the pre-heater and bottom of the post-heater to prevent any updraft. The temperature profiles in the reactor are measured using a quartz capillary with an outer diameter of 1.2 mm and inner diameter of 0.9 mm containing 7 k-type thermocouples each with a diameter of 0.25 mm. The position of thermocouples in the capillary.

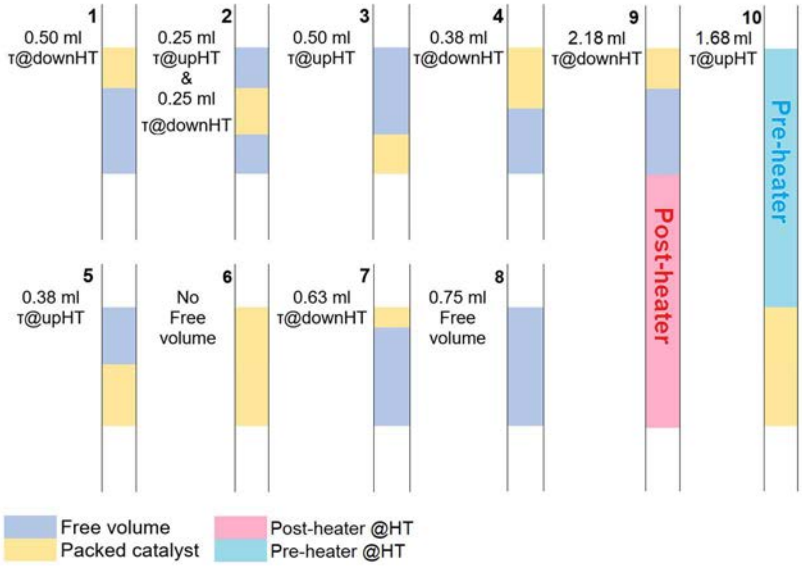

Figure S 2.5: Seven ways to position the catalyst inside the 6 cm zone of oven segment 2. Situations 1,2 and 3 contain 260 mg catalyst resulting in a bed-height of 2 cm, whereas situation 4 and 5 contain a catalyst bed 3 cm height (420 mg), situation 6 a catalyst bed height of 6 cm (820 mg), leaving no free volume at reaction temperature. 7 contains a 1 cm high bed (160 mg), whereas situation 8 is an empty reactor; case 9 demonstrates case 1, including the post-heater at higher temperature; case 10 demonstrates case 6, including the pre-heater at high temperature.

Figure S 2.5 shows how the amount of catalyst as well as the position of the catalyst-bed was varied inside the 6 cm reactor-zone (Figure S 2.4b). The positioning of the free volume with respect to the catalyst bed is used as denotation: τ@downHT signifies volume, and thus residence time, at the catalyst temperature downstream of the catalyst bed; in the same fashion τ@upHT refers to residence time above the catalyst bed. The volume downstream or upstream is varied by changing the amount of catalyst in the reactor-zone, as is evident in the different cases presented in Figure S 2.5. The total volume of the reactor zone is 0.75 ml, both pre-heater as well as post-heater have a volume of 1.68 ml each. Residence time is calculated at STP, using the flowrates controlled by the mass flow controllers. Residence time in the catalyst bed is calculated assuming a packing density of 0.4, i.e. a free volume fraction of 0.6. For example, if case 1 (Figure S 2.5) is used including the post-heater, giving case 9, at a flowrate of 16.6 ml·min^{-1}, the catalyst residence time will be: $0.25\ ml_{cat} * 0.6/(16.6\ ml \cdot min^{-1}/60) =\ 0.54\ s$; the free-volume residence time will be $(0.5 + 1.68)\ ml_{free\ volume}/(16.6\ ml \cdot min^{-1}/60) = 7.9\ s$.

The catalyst is placed at the desired position in the quartz reactor according to Figure S 2.5, held in position by a small quartz wool plug. The reactor is flushed for 10 minutes with 10 ml·min^{-1} N_2. The catalyst is heated with 20°C·min^{-1} to 900°C under 10 ml·min^{-1} N_2. The catalyst is then exposed to 90 vol% CH_4 in N_2 at 1000 ml·g_{cat}^{-1}·h^{-1} during two hours to activate, following the procedure of Bao pers. commun. [42]. After activation, the reactor is flushed for 10 minutes at 900°C with N_2 10 ml·min^{-1}. The temperature is increased to the desired reaction temperature, with a heating rate 20°C·min^{-1} and the experiment is started by feeding 90 vol% CH_4 balanced with N_2. The residence time in the reactor zone is varied during experiments at 1000°C by varying the flow rate between 55.55 ml·min^{-1} and 3.33 ml·min^{-1}. Temperature is varied between 950 and 1100°C in experiments with a flow rate of 33.3 ml·min^{-1} (90% CH_4 in N_2).

Table S 2.3: The sequence of flowrates and temperatures of the reactor-zone used in the integral experiments presented in Figure 2.5 of the main text.

Condition (flow &temp)	**Time (h)**
Activation	2:00
55.55 ml·min^{-1} 1000°C	1:20
33.33 ml·min^{-1} 1000°C	1:20
16.66 ml·min^{-1} 1000°C	1:20
7.77 ml·min^{-1} 1000°C	1:20
3.33 ml·min^{-1} 1000°C	1:20
33.33 ml·min^{-1} 950°C	1:20
33.33 ml·min^{-1} 1000°C	1:20
33.33 ml·min^{-1} 1050°C	1:20
33.33 ml·min^{-1} 1100°C	1:20
Total	14h

Product mixtures are analysed using a three-channel Varian CP3800 online gas chromatography (GC). The GC contains a permanent gas channel for N_2 and CH_4 analysis with a TCD, using He as carrier gas, a dedicated hydrogen channel, with nitrogen as carrier gas and TCD detection, and an FID channel with a GS Gaspro capillary column for analysis of hydrocarbons. The valve box of the GC is heated at 190°C. Samples are taken and analysed every 27 minutes. Each data point is the average of at least 3 measurements in steady state conditions.

2.4.5 S.5 Reaction performance calculations

Methane conversion is calculated in two different ways, one method used at low conversion (<2%) based on formed products including hydrogen, and a second method more accurate for conversions above 2% using nitrogen as an internal standard. At these higher conversions the two calculation methods show perfect overlap.

Methane conversion is thus calculated according:

$$\xi_{CH_4} = 1 - \frac{P_{CH_4out} \cdot P_{N_2in}}{P_{CH_4in} \cdot P_{N_2out}} \; in\ case\ of\ conversion\ > 2\% \qquad \text{Eq. 1}$$

$$\xi_{CH_4} = 1 - \frac{P_{CH_4out}}{\Sigma C_{out}} \; in\ case\ of\ conversion\ < 2\% \qquad \text{Eq. 2}$$

Methane conversion is corrected for any change in the molar flow rate based on change in the nitrogen tracer concentration according Eq. 1 [3, 43]. This method is inaccurate at low conversion and therefore conversions below 2% are calculated based the measured concentrations of all hydrocarbons according Eq. 2 [31]. The concentration of carbon in the product stream is calculated according Eq. 3, including not only unconverted methane and the moles of carbon in products detected with GC, but also including an estimation of the amount of carbon in deposits. This amount is estimated based on the amount of H_2 produced, exceeding the amount that would be expected based on the formation of products detected with GC. Note that it is assumed that the deposits do not contain any hydrogen.

$$\Sigma C_{out} = P_{CH_4out} + \Sigma\left(x \cdot P_{C_xH_y}\right) + \frac{(P_{H_2} - \frac{\Sigma\left(4 \cdot x - y \cdot P_{C_xH_y}\right)}{2})}{2} \; for\ x \geq 2 \qquad \text{Eq. 3}$$

Selectivity is always calculated on molar carbon base, corrected for any change in the molar flow rates based on the concentration of the N_2 tracer, Eq. 4 [3, 43].

$$\mathrm{S}_{C_xH_y} = \frac{x \cdot P_{C_xH_y}}{\xi_{CH_4}} \cdot \frac{P_{N_2in}}{P_{N_2out} \cdot P_{CH_4in}} \qquad \text{Eq. 4}$$

Selectivity to deposits is defined as the residual term left from the summation of all product selectivity.

$$S_C = \Sigma \mathrm{S}_{C_xH_y} \qquad \text{Eq. 5}$$

Integral calculations of conversion, selectivity and coke deposition are made in order to compare with data on the amount of deposits on the catalyst as measured with TGA. Equation 6 calculates the total amount of carbon converted in the full experiment:

$$C_{converted\ CH_4} = \int_{t=0}^{t=14h} \phi_{CH_4 in} \cdot \xi_{CH_4} \cdot \frac{1}{V_m} \qquad \text{Eq. 6}$$

The total amount of carbon that is converted to deposits during an integral experiment is calculated in:

$$C_{total\ in\ products} = \int_{t=0}^{t=14h} \phi_{CH_4 in} \cdot \xi_{CH_4} \cdot S_c \cdot \frac{1}{V_m} \qquad \text{Eq. 7}$$

The amount of deposits formed during a full experiment can also be calculated based on the weight loss during oxidation of the spent catalyst in TG, according Eq. 8, assuming that the deposits contain exclusively C:

$$C_{deposits\ on\ catalyst} = \Delta W_{TGA} \cdot \frac{Q_{cat}}{M_C} \qquad \text{Eq. 8}$$

Symbol list

ξ_{CH_4}: $conversion\ of\ methane\ (-)$
P_X: $partial\ pressure\ of\ compound\ X\ (bar)$
ΣC_{out}: $total\ theoretical\ carbon\ partial\ pressure\ in\ the\ outflow\ (bar)$
$S_{C_xH_y}$: $selectivity\ towards\ C_xH_y\ hydrocarbon\ (-)$
S_c: $total\ carbon\ to\ products\ selectivity\ (-)$
ϕ_x: $flow\ of\ x\ (ml \cdot s^{-1})$
V_m: $molar\ volume\ at\ SPT\ (ml \cdot mol^{-1})$
M_C: $molar\ mass\ of\ carbon\ (g \cdot mol^{-1})$
ΔW_{TGA}: $the\ percentage\ of\ mass\ lost\ in\ the\ TGA\ analysis\ (-)$
Q_{cat}: $amount\ of\ catalyst\ loaded\ in\ the\ reactor\ (-)$
$C_{converted\ CH_4}$: $total\ amount\ of\ carbon\ from\ converted\ CH_4\ accoring\ to\ GC\ measurement\ (mol)$
$C_{total\ in\ products}$: $total\ amount\ of\ carbon\ in\ products\ according\ to\ the\ GC\ measurement\ (mol)$
$C_{deposits\ on\ catalyst}$: $total\ carbon\ molar\ yield\ of\ deposits\ on\ the\ catalyst\ (mol)$

2.4.6 S. 6 Additional Results and Discussion

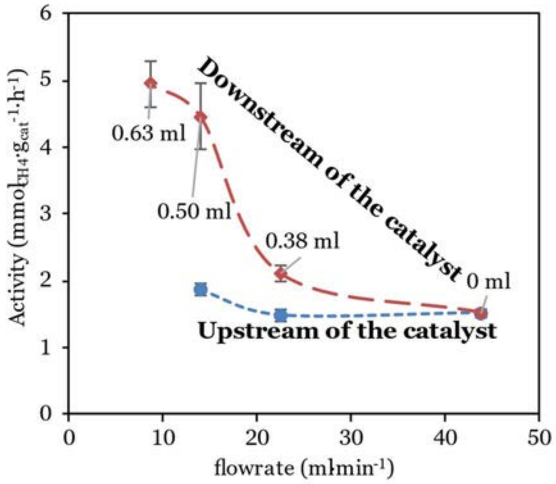

Figure S 2.6: Catalyst activity as function of the free-volume upstream or downstream of the catalyst bed; space velocity: 3.2 $l\cdot gcat^{-1}\cdot h^{-1}$; T reactor-zone: 1000°C; T pre-heater and post-heater 400°C.

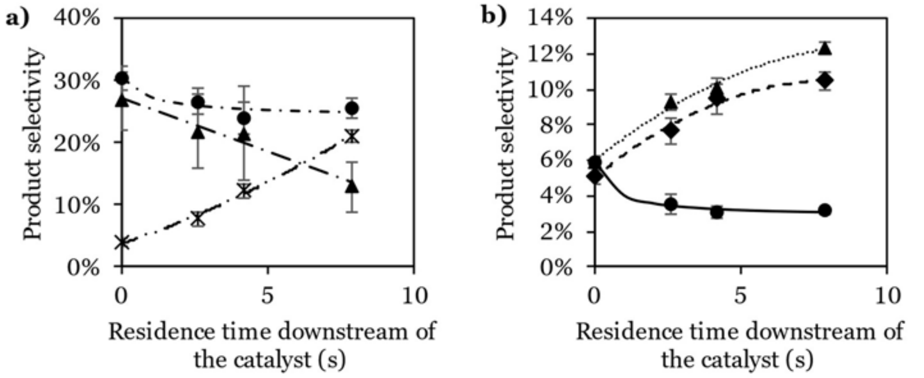

Figure S 2.7: carbon to product selectivity when varying the residence time at 1000°C downstream of the catalyst bed; interpolated at 7.3% constant methane conversion; 0.26 g catalyst; (a) major products: —✱— Naphthalene; -·●·- Ethylene; —▲— Carbon deposits; (b) minor products: —●— Ethane; - -◆- - Benzene; ·····▲·····; Acetylene.

Figure 2.2 and Figure 2.3 originate from the data in Figure S 2.9. The fact that ethane is the dominant product at low conversion (Figure S 2.9a and Figure S 2.10) suggest that ethane is the primary product, i.e. by recombination of two methyl radicals. Ethylene is the secondary product, achieving maximal selectivity at typically 1% conversion as shown in Figure S 2.9b. Selectivity to ethylene remains significant at higher methane conversions, typically around 20-30% on carbon basis, similar to results of Guo *et al.* and Sakbodin *et al.* [24]. This is in agreement with the fact that ethylene is relatively stable at temperatures around 1000°C [3, 19, 24-26, 32]. Benzene and naphthalene are ternary products, as can be seen in Figure S 2.9c and d. It is generally accepted that carbonaceous deposits form via acetylene dehydrogenation as well as further oligomerization [44, 45]. Other minor products detected are acetylene, propylene, butene and butadiene, toluene, styrene and xylenes (Figure S 2.11). This sequence of product formation has not yet been reported for methane pyrolysis over Fe©SiO2, but is very similar to reaction scheme of non-catalytic methane pyrolysis [36-38, 46-48].

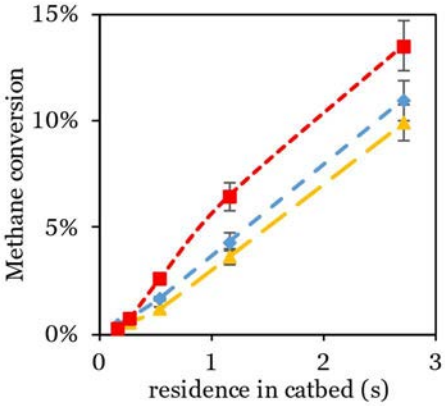

Figure S 2.8: Effect of residence time in the catalyst bed on methane conversion for different residence times up and downstream of the catalyst bed; 0.26 g catalyst, reactor-zone at 1000°C, pre-heater and post-heater at 400°C; —▲— 0.5 ml τ@upHT ; – ◆ – 0.25 ml τ@upHT & 0.25 ml τ@downHT; --■-- 0.5 ml τ@downHT; included as background information to Figure S 2.9.

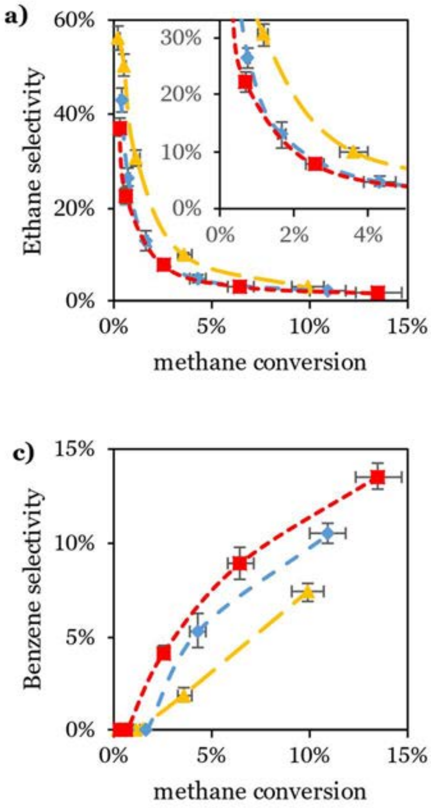

Figure S 2.9: Selectivity to ethane (a), ethylene (b), benzene (c) and naphthalene (d) as function of methane conversion varied by changing residence time as reported in

Figure S 2.8 for differing residence time up and downstream of the catalyst bed; 0.26 g catalyst, reactor-zone at 1000°C, pre-heater and post-heater at 400°C; —▲— 0.5 ml τ@upHT ; – ◆ – 0.25 ml τ@upHT & & 0.25 ml τ@downHT; --■-- 0.5 ml @downHT.

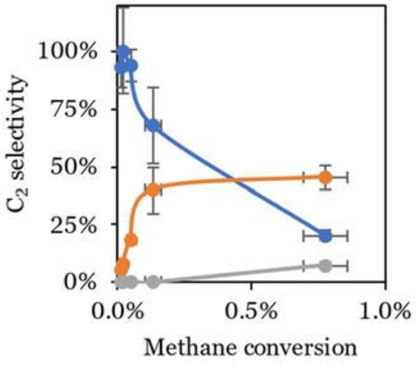

Figure S 2.10: C_2 selectivity at low conversion; measured using a blank quartz tube at higher space velocities, reaction zone at 1000° C; pre- and post-heater at 400°C; —●— Ethane; —●— Ethylene; —●— Acetylene.

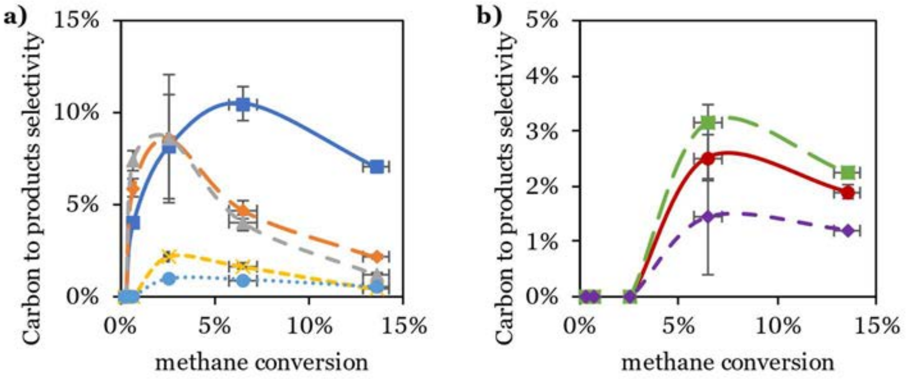

Figure S 2.11: Selectivity to (a) minor aliphatics and (b) minor aromatics; as function of methane conversion varied by changing residence time as reported in Figure S 2.8 for 0.5 ml τ@downHT; 0.26 g catalyst, reactor-zone at 1000°C, pre-heater and post-heater at 400°C; for (a) —■— acetylene; —◆— propylene; – ▲ – butene; --×-- butadiene; ···●··· cyclopentadiene; for (b) —●— toluene; —■— xylenes; – ◆ – styrene.

2.4.7 S.7 Calculations of apparent activation energy

Apparent activation energy was calculated based on Arrhenius plots for temperatures between 950 and 1100°C, using exclusively data under differential conditions (conversion <15%), presented in Figure S 2.12. Data for the apparent activation energies of Guo et al. [3], Sakbodin et al. [24] and Oh et al. [25] were obtained from the respective supporting information sections. Note that for Sakbodin and Oh the limit of <15% conversion is maintained. For Guo this proved impossible. It was chosen to take all data points up to 1303K (41.5% conversion) to match the temperature range with Sakbodin and Oh. Note that excluding higher temperature and conversion point will lead to a higher apparent activation energy.

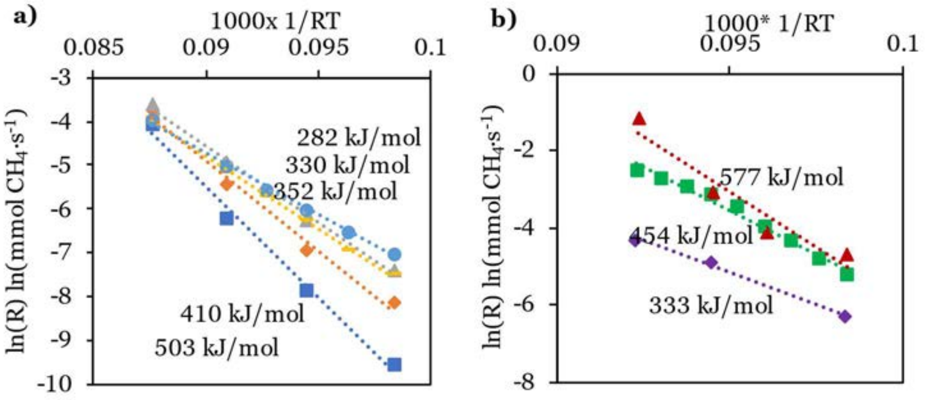

Figure S 2.12: Activation energy calculations for a) different amounts of catalyst placed at the top of the reactor zone according to Figure S5, ■case 8; ◆case 7; ▲case 1; −case 4; ● case 6; b) those calculated based on literature data from ■Guo et al. [1] ; ◆Sakbodin et al. [2a] ; ▲Oh et al. [2b].

2.4.8 S.8 Analysis of the condensate recovered from the reaction system

Figure 2.5 introduced the distinction between coke-on-catalyst and deposits-downstream of the catalyst bed, the former measured by TGA and the latter estimated based on the C-balance. The deposits on the catalyst resembled a soot-like coke, which proved impossible to dissolve in acetone. The deposits formed on the reactor-wall downstream of the catalyst in the zone, where the temperature was higher than 900°C, was silver in colour and flaked easily on agitation. This silver coloured deposit is presumed to be graphite based on physical appearance and the high temperature zone it was found. The cooler parts of the reactor, as well as the traced line leading up to the GC and the condenser (see S.4 Reactor setup and catalytic testing for setup details) contained a tar-like deposit ranging from light orange to black in colour. This deposit was recovered with acetone by repeated flushing and ultrasonic agitation. The samples were sent to the Laboratory for Chemical Technology at Ghent University for GCxGC FID analysis by Hang Dao Thi. Results showed a wide array of poly aromatic species with carbon numbers between 6 (benzene) and 28. The most abundant (i.e. higher than 3%) species are summarized in Table S 2.4. All species have a highly aromatic nature, with few branches and no non-aromatic ring structures as shown in the molecular structures in Table S 2.5. These results match with high selectivity to benzene and naphthalene compared to other aromatic species. The 4 specifically identified species in Table S 2.4, i.e. pyrene, indeno[1,2,3-cd]pyrene, dibenzo[def,mno]chrysene and coronene all have a compact structure that minimizes hydrogenated carbon atoms.

Table S 2.4: the most abundant (>3%) species in the condense recovered from the reactor, tubing and condenser. Melting and boiling points obtained from [49]. Estimated values for melting and boiling point calculated using the Joback method [50].

Compound	**abundance in condense**	**nr C atoms**	**nr of benzene rings**	**MP (°C)**	**BP(°C)**
Pyrene	3.4%	16	4	145	404
C_{20} naphthenotetraaromatics	10.6%	20	4	248 (est)	490 (est)
C_{21} naphthenotetraaromatics	4.0%	21	4	272 (est)	518 (est)
Indeno[1,2,3-cd]pyrene	3.9%	22	5	164	536
Dibenzo[def,mno]chrysene	10.5%	22	6	258	555
C_{22} hexaaromatics	5.7%	22	6	317 (est)	556 (est)
C_{24} naphthenohexaaromatics	3.5%	24	6	365 (est)	612 (est)
Coronene	3.5%	24	6	437	525
C_{26} naphthenoheptaaromatics	5.8%	26	7	439 (est)	674 (est)
C_{28} naphthenooctaaromatics	15.8%	28	8	497 (est)	735 (est)
C_{28} nonaaromatics	7.6%	28	9	508 (est)	740 (est)

The deposition of these poly-aromatic compounds at places where the temperature is low enough to extinguish the free radical reaction (T<600°C) shows that they must have formed in the reaction-zone and condensed further downstream. This shows that gas-phase formation of coke, via growth of poly-aromatic species via addition of smaller olefins is a likely route for the formation of carbonaceous deposits as proposed by Guéret et al. [51]. Deposit formation tends to occur via two mechanisms [51], radicals will adsorb on the surface of the reactor, creating nucleation points for the formation of graphite and carbon-carbon coupling will lead to poly-aromatic structures that will condense to form a more soot or tar like deposit, in line with results found in this thesis.

Table S 2.5: Molecular structures of the most abundant poly-aromatic compounds found in the condense of the NOCM reaction.

Species name	Molecular structure
Phenanthrene	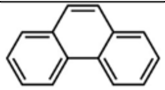
Anthracene	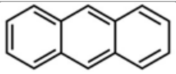
Pyrene	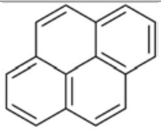
Fluoranthene	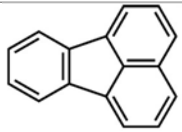
Benzanthracene	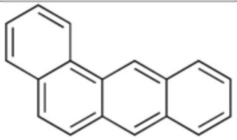
Indeno[1,2,3-cd]pyrene	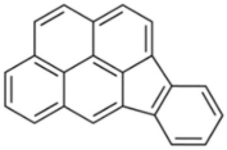
Dibenzo[def,mno]chrysene	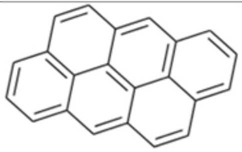
Coronene	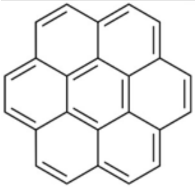

2.5 References

1. Foss, M.M., *Interstate Natural Gas-Quality Specifications & Interchangeability* 2004, Center for Energy Economics.

2. BP plc, *BP Statistical Review of World Energy 2019*. 2019.

3. Guo, X., G. Fang, G. Li, H. Ma, H. Fan, L. Yu, C. Ma, X. Wu, D. Deng, M. Wei, D. Tan, R. Si, S. Zhang, J. Li, L. Sun, Z. Tang, X. Pan, and X. Bao, *Direct, Nonoxidative Conversion of Methane to Ethylene, Aromatics, and Hydrogen*. Science, 2014. **344**(6184): p. 616-619.

4. Schwach, P., X. Pan, and X. Bao, *Direct Conversion of Methane to Value-Added Chemicals over Heterogeneous Catalysts: Challenges and Prospects*. Chemical Reviews, 2017. **117**: p. 8497-8520.

5. U.S. Energy Information Administration, *Electric Power Monthly*, in *Monthly Electric Power Industry Report*. 2020.

6. Klerk, A.d., *Fischer–Tropsch Process*, in *Kirk-Othmer Encyclopedia of Chemical Technology*. 2013. p. 1-20.

7. Wittcoff, H.A., B.G. Reuben, and J.S. Plotkin, *Chemicals from Methane*. 2012, John Wiley & Sons, Inc.

8. Wang, B., S. Albarracín-Suazo, Y. Pagán-Torres, and E. Nikolla, *Advances in methane conversion processes*. Catalysis Today, 2017. **285**: p. 147-158.

9. Huang, K., J.B. Miller, G.W. Huber, J.A. Dumesic, and C.T. Maravelias, *A General Framework for the Evaluation of Direct Nonoxidative Methane Conversion Strategies*. Joule, 2018. **2**: p. 349-365.

10. Amghizar, I., L.A. Vandewalle, K.M.V. Geem, and G.B. Marin, *New Trends in Olefin Production*. Engineering, 2017. **3**: p. 171-178.

11. Mohajerani, S., A. Kumar, and A.O. Oni, *A techno-economic assessment of gas-to-liquid and coal-to-liquid plants through the development of scale factors*. Energy, 2018. **150**: p. 681-693.

12. Galadima, A. and O. Muraza, *Advances in Catalyst Design for the Conversion of Methane to Aromatics: A Critical Review*. Catalysis Surveys from Asia, 2019. **23**: p. 149-170.

13. Sun, K., D.M. Ginosar, T. He, Y. Zhang, M. Fan, and R. Chen, *Progress in Nonoxidative Dehydroaromatization of Methane in the Last 6 Years*. Industrial & Engineering Chemistry Research, 2018. **57**: p. 178-1789.

14. Taifan, W. and J. Baltrusaitis, *CH4 conversion to value added products: Potential, limitations and extensions of a single step heterogeneous catalysis*. Applied Catalysis B: Environmental, 2016. **198**: p. 525–547.

15. Olivos-Suarez, A.I., A.g. Szécsényi, E.J.M. Hensen, J. Ruiz-Martinez, E.A. Pidko, and J. Gascon, *Strategies for the Direct Catalytic Valorization of Methane Using Heterogeneous Catalysis: Challenges and Opportunities*. ACS Catalysis, 2016. **6**: p. 2965-2981.

16. Mesters, C., *A Selection of Recent Advances in C1 Chemistry*. Annual Review of Chemical and Biomolecular Engineering, 2016. **7**: p. 223-238.

17. Kondratenko, E.V., T. Peppel, D. Seeburg, V.A. Kondratenko, N. Kalevaru, A. Martin, and S. Wohlrab, *Methane conversion into different hydrocarbons or oxygenates: current status and future perspectives in catalyst development and reactor operation*. Catalysis Science & Technology, 2017. **7**: p. 366-381.

18. Karakaya, C. and R.J. Kee, *Progress in the direct catalytic conversion of methane to fuels and chemicals*. Progress in Energy and Combustion Science, 2016. **55**: p. 60-97.

19. Guéret, C., M. Daroux, and F. Billaud, *Methane pyrolysis: thermodynamics*. Chemical Engineering Science, 1997. **52**(5): p. 815-827.

20. Carey, F.A. and R.J. Sundberg, *Structural Effects on Stability and Reactivity*, in *Advanced Organic Chemistry Part A: Structure and Mechanisms*. 2007, Springer.

21. Kee, R.J., C. Karakaya, and H. Zhu, *Process intensification in the catalytic conversion of natural gas to fuels and chemicals*. Proceeding of the Combustion Institute, 2017. **36**: p. 51-76.

22. Farrell, B.L., V.O. Igenegbai, and S. Linic, *A Viewpoint on Direct Methane Conversion to Ethane and Ethylene Using Oxidative Coupling on Solid Catalysts*. ACS Catalysis, 2016. **6**: p. 4340-4346.

23. Gao, Y., L.M. Neal, D. Ding, W. Wu, C. Baroi, A. Gaffney, and F. Li, *Recent Advances in Intensified Ethylene Production – A Review*. ACS Catalysis, 2019. **9**(9): p. 8592-5621.

24. Sakbodin, M., Y. Wu, S.C. Oh, E.D. Wachsman, and D. Liu, *Hydrogen-Permeable Tubular Membrane Reactor: Promoting Conversion and Product Selectivity for Non-Oxidative Activation of Methane over an FeVSiO2 Catalyst*. Angewandte Chemie, 2016. **55**: p. 16149 –16152.

25. Oh, S.C., E. Schulman, J. Zhang, J. Fan, Y. Pan, J. Meng, and D. Liu, *Direct Non-Oxidative Methane Conversion in a Millisecond Catalytic Wall Reactor*. Angewandte Chemie, 2019. **58**: p. 7083-7086.

26. Han, S.J., S.W. Lee, H.W. Kim, S.K. Kim, and Y.T. Kim, *Nonoxidative Direct Conversion of Methane on Silica-Based Iron Catalysts: Effect of Catalytic Surface*. ACS Catalysis, 2019. **9**: p. 7984-7997.

27. Chen, Y., X. Wang, X. Luo, X. Lin, and Y. Zhang, *Non-Oxidative Methane Conversion Using Lead- and Iron-Modified Albite Catalysts in Fixed-Bed Reactor*. Chinese Journal of Chemistry, 2018. **36**: p. 531-537.

28. Okolie, C., Y. Lyu, L. Kovarik, E. Stavitski, and C. Sievers, *Coupling of Methane to Ethane, Ethylene, and Aromatics over Nickel on Ceria–Zirconia at Low Temperatures*. ChemCatChem, 2018. **10**: p. 2700-2708.

29. Xie, P., T. Pu, A. Nie, S. Hwang, S.C. Purdy, W. Yu, D. Su, J.T. Miller, and C. Wang, *Nanoceria-Supported Single-Atom Platinum Catalysts for Direct Methane Conversion*. ACS Catalysis, 2018. **8**: p. 4044-4048.

30. Xiao, Y. and A. Varma, *Highly Selective Nonoxidative Coupling of Methane over Pt-Bi Bimetallic Catalysts*. ACS Catalysis, 2018. **8**: p. 2735-2740.

31. Nishikawa, Y., H. Ogihara, and I. Yamanaka, *Liquid-Metal Indium Catalysis for Direct Dehydrogenative Conversion of Methane to Higher Hydrocarbons*. ChemistrySelect, 2017. **2**: p. 4572-4576.

32. Kim, S.K., H.W. Kim, S.J. Han, S.W. Lee, J. Shin, and Y.T. Kim, *Mechanistic and microkinetic study of non-oxidative methane coupling on a single-atom iron catalyst*. Communication Chemistry, 2020. **3**(58).

33. Nagaki, D.A., Z. Zhao, M.N.Z. Myint, I. Lengyel, A. Mamedov, C.W. Gundlach, K. Sankaranarayanan, and D. Falcone, 2018, *Method for Producing Hydrocarbons by Non-Oxidative Coupling of Methane*, US 9 , 902 , 665 B2

34. Zwet, G.P.v.d., P.A.J.M. Hendriks, and R.A.v. Santen, *Pyrolysis of methane and the role of surface area*. catalysis Today, 1989. **4**: p. 365-369.

35. Slater, W.E., *The influence of different surfaces on the decomposition of methane*. Journal of the Chemical Society, Transactions, 1916. **109**: p. 160-164.

36. Dean, A.M., *Detailed Kinetic Modeling of Autocatlysis in Methane Pyrolysis*. Journal of Physical Chemistry, 1990. **94**: p. 1432-1439.

37. Chen, C.J. and M.H. Back, *The Thermal Decomposition of Methane. I. Kinetics of the primary decomposition to* C_2H_6 *+*H_2*; Rate constant for the Homogeneous Unimolecular Dissociation of Methane and its Pressure Dependance*. Canadian Journal of Chemistry, 1975. **53**: p. 3580-3590.

38. Roscoe, J.M. and M.J. Thompson, *Thermal decomposition of Methane: Autocatalysis*. International Journal of Chemical Kinetics, 1985. **17**: p. 967-990.

39. Mishchik, K., *Ultrafast laser-induced modification of optical glasses : a spectroscopy insight into the microscopic mechanisms*, in *Optics, photonics and hyperfrequencies*. 2012, Université Jean Monnet – Saint-Étienne. p. 172.

40. DeAngelis, M.T., A.J. Rondinone, M.D. Pawel, T.C. Labotka, and L.M. Anovitz, *Sol-gel synthesis of nanocrystalline fayalite (Fe2SiO4)*. American Mineralogist, 2012. **97**: p. 653–656.

41. Lafuente, B., R.T. Downs, H. Yang, and N. Stone, *The power of databases: the RRUFF project*, in *Highlights in Mineralogical Crystallography*, T. Armbruster and R.M. Danisi, Editors. 2015, W. De Gruyter: Berlin. p. 1-30.

42. Bao, X. *personal communication to:* L. Lefferts, 2016

43. Liu, S., L. Wang, R. Ohnishi, and M. Ichikawa, *Bifunctional Catalysis of Mo/HZSM-5 in the Dehydroaromatizationof Methane to Benzene and Naphthalene XAFS/TG/DTA/MASS/FTIR Characterization and Supporting Effects*. Journal of Catalysis, 1999. **181**: p. 175-188.

44. Khan, M.S. and B.L. Crynes, *Survey of Recent Methane Pyrolysis Literature*. Industrial & Engineering Chemistry, 1970. **62**(10): p. 54-59.

45. Holmen, A., O.A. Rokstad, and A. Solbakken, *High-Temperature Pyrolysis of Hydrocarbons. 1. Methane to Acetylene*. Industrial & Engineering Chemistry Process Design and Development, 1975. **15**(3): p. 439-444.

46. Palmer, H.B., J. Lahaye, and K.C. Hou, *On the Kinetics and Mechanism of the Thermal Decomposition of Methane in a Flow System*. Journal of Physical Chemistry, 1968. **72**(1): p. 348-353.

47. Chen, C.J. and M.H. Back, *The thermal decomposition of methane. II. Secondary reactions, autocatalysis and carbon formations; non-arrhenius behaviour in the reaction of CH3 with ethane*. Canadian Journal of Chemistry, 1976. **54**(54): p. 3175-3184.

48. Billaud, F. and C. Gueret, *Thermal decomposition of pure methane at 1263K. Experiments and mechanistic modelling*. Thermochimica Acta, 1992. **211**: p. 303-322.

49. Haynes, W.M., *CRC Handbook of Chemistry and Physics*. 2014: CRC press.

50. Joback, K.G. and R.C. Reid, *Estimation of Pure-Component Properties from Group-Contributions*. Chemical Engineering Communications, 1987. **57**: p. 233-243

51. Guéret, C., F. Billaud, B. Fixari, and P.l. Perchec, *Thermal Coupling of Methane, Experimental investigations on Coke Deposits*. Carbon, 1994. **33**(2): p. 159-170.

Chapter 3

Effect of ethane and ethylene on catalytic non oxidative coupling of methane

---

This chapter has been published as:

Effect of ethane and ethylene on catalytic non oxidative coupling of methane; R.S. Postma, L. Lefferts; Reaction Chemistry & Engineering; Advance Article 2021.

Abstract

The effect of addition of ethane and ethylene (C_2) on methane coupling at 1000°C was investigated. A Fe/SiO_2 catalyst was used to determine the contributions of catalytic as well as C_2 initiated methane activation. The catalyst load as well as the residence times at 1000°C downstream the catalyst bed were varied. C_2 addition significantly increases methane conversion rates, similarly for both ethane and ethylene, although ethylene is more effective when operating with long residence times in the post-catalytic volume. Methane activation via C_2 addition proceeds dominantly in gas-phase whereas catalytic C_2 activation is negligible. The catalyst has no effect on methane conversion when the feed contains more than 2 vol% C_2. Product selectivity distribution as well as total hydrocarbon yield at 10% conversion is not influenced by C_2 addition, but is influenced by the amount of catalyst as well as residence time in the post-catalytic volume at high temperature. It is proposed that C_2 impurities in natural gas change from a nuisance to an advantage by enhancing methane conversion and simplifying purification of the natural gas feed. A process is proposed in which ethylene is recycled back into the reactor to initiate methane coupling, leading to a process converting methane to aromatics.

3.1 Introduction

Natural gas, consisting typically of 90 vol% CH_4 and 5 vol% C_2 hydrocarbons [1], is considered as a highly interesting resource for the production of olefins and aromatics [2-4]. Traditionally, these products are by-products of crude oil refining [5, 6]. It is, however, predicted that raw oil extraction will reach peak production in the coming decades [7], and hence the increase of global olefins and aromatics demand needs to be met via another process. Natural gas is already used on large industrial scale for the synthesis of base chemicals and fuels [8-10]. These processes convert natural gas to specific hydrocarbons with high carbon efficiencies to olefins and aromatics over crude oil refining [11, 12].

Current industrial methods for converting natural gas into base chemicals are multistep processes starting from methane steam-reforming to obtain syngas [13]. The syngas can be converted into paraffins in the Fischer-Tropsch (FT) process [8] or used for methanol synthesis, followed by methanol to gasoline (MTG)[14] or methanol to olefins (MTO) [12]. The large number of process steps at different temperatures and pressures makes the processes energy intensive and only viable at large installed capacities [15].

Direct conversion of methane to higher hydrocarbons is hence receiving a growing interest over the last decades, as a more efficient alternative to the indirect routes mentioned before. Three main research directions can be distinguished, i.e. methane dehydro-aromatization (MDA) [16], oxidative coupling of methane (OCM) [17] and non-oxidative coupling of methane (NOCM) at high temperature [18]. Both MDA as well as OCM suffer from low single pass conversion as well as low product yields [16, 17]. Guo et al. [19] reported in 2014 that a Fe/SiO_2 catalyst is able to couple methane non-oxidatively to olefins and aromatics at high conversion levels and without coke formation. Measurements were carried out at temperatures in excess of 950°C. Follow-up research showed that methane conversion can be increased by in-situ hydrogen removal [20], by using a catalytic wall reactor [21] and by increasing the residence time in the reactor at high temperature downstream the catalyst bed (post-catalytic volume) Discussed in **chapter 2** as well as a SABIC patent [22]. However, all these studies reported coke formation and lower catalytic activity [19-24] compared to the original work of Guo et al. [19]. It is generally accepted that the catalyst initiates methane conversion, through formation of methyl radical, followed by free radical chain reactions and coupling reactions in gas phase, determining the product distribution [19, 24], as also discussed in **chapter 2**. The publications concerning the Fe/SiO_2 catalyst have focused on a pure methane feed, even though natural gas contains a significant fraction of C_2 hydrocarbons [1].

Ethane and ethylene readily form radicals that participate in the autocatalytic cycle of methane pyrolysis at reaction temperature, i.e. above 950°C [25-28]. Addition of ethane can significantly reduce the induction period during non-catalytic methane pyrolysis as reported in early work by Germain et al. [29]. Methane conversion rates can thus be significantly increased by introduction of small amounts of C_2 hydrocarbons, up to 3%, into the reactant mixture as reported in early work by Schneider [28] and Rokstad et al [30]. Ogihara et al. [31] reported recently that methane is activated by ethane addition even at relatively low temperatures 700-800°C in absence of any catalyst. Guo et al. [19] reported a significant increase in methane conversion upon addition of 1-5% C_2H_6 at 900°C using the Fe/SiO_2 catalyst, although ethane addition caused coke formation, which crucially was not observed in their experiments using pure methane. SABIC [22] patented a concept where post-catalytic ethane injection would quench the free radical coupling reaction, stabilizing the formed olefin products. The effect of addition of C_2 hydrocarbons in presence or absence of the Fe©SiO_2 catalyst on methane conversion and especially product distribution has not been reported, to the best of our knowledge.

This chapter reports for the first time on the interaction between catalytic methane activation and activation via the addition of free-radical initiators, i.e. ethane and ethylene, to determine their contributions to methane conversion, product selectivity distribution and deposit formation.

3.2 Experimental

3.2.1 Catalyst synthesis

The Fe/SiO_2 catalyst is synthesized according to the method described in [19] and details concerning the catalyst synthesis as well as characterization can be found in **chapter 2**. In short, inhouse synthesized Fe_2SiO_4 is mixed with quartz and ball-milled in N_2 atmosphere overnight using a zirconia milling jar. The resulting powder is fused for 6h at 1700°C in air. The resulting slab is crushed and sieved, the fraction between 250-500 µm is used in the experiments. The sieved catalyst particles are leached for 2h in 0.5 M HNO_3, rinsed and dried to obtain the final catalyst.

3.2.2 Reactor setup

A modular three-zone oven is used for catalytic testing. Each zone is thermally insulated from the others and from the environment, allowing for steep temperature gradients, as presented in Figure 2.1. The pre-heater is always operated at 400°C and the reactor-zone, containing the catalyst, at 1000°C. The post-heater is either operated at 400°C, cooling down the gas-stream directly after the reactor-zone, or at 1000°C to create an extended residence time at higher temperature, increasing the conversion as reported in **chapter 2**. Both temperature profiles, for operating the poster-heater at 400°C or 1000°C have been included in Figure 2.1. Gas flowrates are controlled using digital mass flow controllers. Product gasses are analysed using a three-channel Varian CP-3800 in-line gas chromatograph, the tubing between the reactor and the GC is heated to 200°C to minimize hydrocarbon condensation. Further details concerning the reactor setup are presented in **chapter 2**.

3.2.3 Experimental procedure

The experimental procedure is adapted from **chapter 2**. The catalyst is placed at the desired position in the quartz reactor according to Figure 3.1, held in position by a small quartz wool plug. The reactor is flushed for 10 minutes with 10 $ml{\cdot}min^{-1}$ N_2. The catalyst is heated with 20°C$\cdot min^{-1}$ to 900°C under 10 $ml{\cdot}min^{-1}$ N_2. The catalyst is then activated in 90 vol% CH_4 in N_2 at 1000 $ml{\cdot}g_{cat}^{-1}{\cdot}h^{-1}$ during two hours, following the procedure of Bao pers. commun. [32]. After activation, the reactor is flushed for 10 minutes at 900°C with N_2 10 $ml{\cdot}min^{-1}$. The temperature is increased to the desired reaction temperature, with a heating rate of 20°C$\cdot min^{-1}$ and the experiment is started by feeding 90 vol% CH_4 balanced with N_2. Ethane or ethylene are added while reducing the amount of nitrogen in the feed, keeping the methane concentration as well as the total flowrate constant. Catalyst[19], gas-phase[26] and reactor-wall[33] all contribute to methane conversion so that space velocity is not useful as a descriptor; therefore the total gas flowrate was kept constant at 16.6 $ml{\cdot}min^{-1}$ to allow for a fair comparison. The product gas is analysed using an online three channel gas chromatograph (Varian CP-3800), measuring CH_4 and N_2 on the first channel, H_2 on the second channel and all hydrocarbon products on a third FID channel. At the end of an experiment, the reactor is flushed for 10 minutes with N_2 at 10 $ml{\cdot}min^{-1}$ after which the reactor ovens are turned off and left to cool, maintaining the N_2 flow while cooling. The catalyst is removed from the reactor and analysed for coke deposition using TGA (Mettler Toledo TGA/DSC 3+ Star System). Details on the temperature-programmed-oxidation measurement in the TGA can be found in **chapter 2**. The online GC samples every 27 minutes and all data points presented are based on at least 3 measurements in steady state conditions.

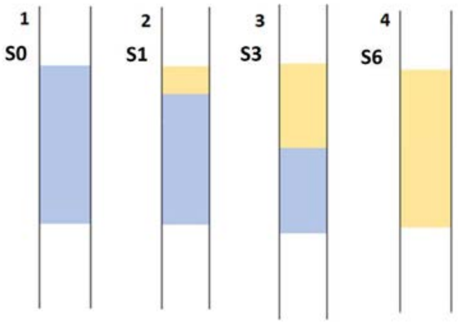

Figure 3.1: 3 ways to position the catalyst inside the 6 cm zone of oven segment 2. Case 1 (S0) contains no catalyst, Case 2 (S1) contains a 1 cm high bed (160 mg), Case 3 (S3) contains a catalyst bed 3 cm height (420 mg), situation 4 (S6) a catalyst bed height of 6 cm (820 mg), leaving no free volume at reaction temperature.

Methane conversion is calculated according:

$$\xi_{CH_4} = 1 - \frac{P_{CH_4out} \cdot P_{N_2in}}{P_{CH_4in} \cdot P_{N_2out}} \qquad \text{Eq.1}$$

ξ_{CH_4}: $conversion\ of\ methane\ (-)$
P_X: $partial\ pressure\ of\ compound\ X\ (bar)$

Methane conversion is corrected for any change in the molar flow rate based on change in the nitrogen tracer concentration according Eq.1 [19, 34]. In the same way, the conversion of the C_2 reactant is calculated, according Eq.2. Note that C_2 conversion as calculated is determined by both C_2 fed to the reactor and formation of the same C_2 species in the reactor, therefore this value can also become negative when formation dominates over conversion.

$$\xi_{C_2} = 1 - \frac{P_{C_2out} \cdot P_{N_2in}}{P_{C_2in} \cdot P_{N_2out}} \qquad \text{Eq.2}$$

ξ_{C_2}: $overall\ conversion\ of\ the\ added\ C_2\ hydrocarbon\ (-)$

Product selectivity is calculated on carbon base, corrected for any change in the molar flow rates based on the concentration of the N_2 tracer, Eq.3 [19, 34]. The selectivity calculation takes into account conversion of both methane and C_2, adjusting for stoichiometry.

$$S_{C_xH_y} = \frac{x \cdot P_{C_xH_y} \cdot P_{N_2in}}{P_{N_2out} \cdot \left(P_{CH_4in} + 2 \cdot P_{C_2in}\right) - P_{N_2in} \cdot \left(P_{CH_4out}\right)} \qquad \text{Eq.3}$$

$S_{C_xH_y}: selectivity\ towards\ C_xH_y\ hydrocarbon\ (-)$

The measured hydrogen signal was used to validate the calculated conversion and selectivity distribution and closes to within 5%.

Experiments were performed over a maximum period of 8h, a stability test over 16h showed a deactivation of 10% methane conversion in a test using pure methane at 1.8% conversion.

3.3 Results

3.3.1 Effects on methane and C_2 conversion

Figure 3.2 shows the effect of adding small amounts of ethane and ethylene to the reactant mixture, varying the amount of catalyst and post-catalytic volume. Addition of ethane and ethylene significantly increases CH_4 conversion. Interestingly, there is no discernible difference between the methane conversion when adding ethane (Figure 3a and b) or ethylene (Figure 3.2c). The effect of C_2 addition on methane conversion is decreases with increasing catalyst amount, to the extent that catalyst has no effect when at least ~2% ethane is added (Figure 3.2b. Figure 3.2d shows a linear correlation, including the origin, between the free-volume in the reactor-zone and the linear acceleration in methane conversion rate by addition of C_2 molecules, as calculated based on Figure 3.2a and c.

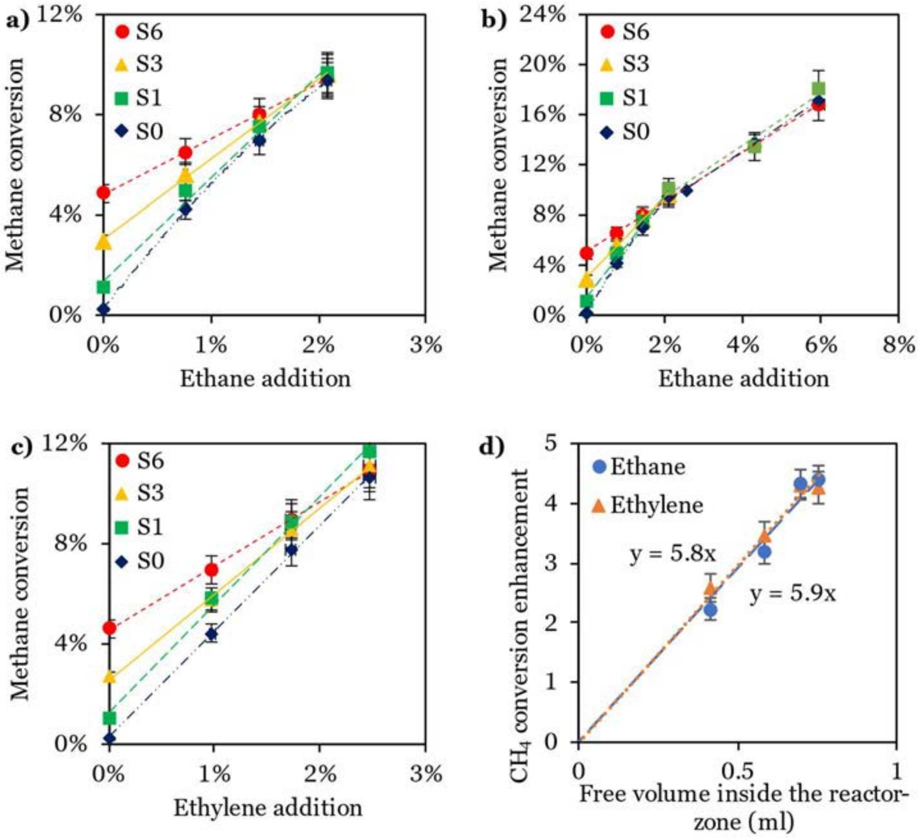

Figure 3.2: effect of C_2 addition on methane conversion, varying the amount of catalyst inside the reactor-zone: (a) ethane addition for lower concentration and b) higher ethane concentration; (c) ethylene addition; (d) slope of increase in methane conversion as function of C_2 addition shown figures (a) and (c), plotted function of free volume inside the reactor; taking into account the free volume surrounding the catalyst particles as well as the free volume downstream of the catalyst bed at packing density of 0.45; 90% CH_4 N_2 balance; 16.6 ml·min^{-1} total flowrate. Reactor-zone at 1000°C, pre-heater and post-heater at 400°C.

Figure 3.3 shows the overall ethane and ethylene conversion in all experiments. Ethane is close to completely converted in all cases although conversion is somewhat lower when employing a large catalyst bed. Ethylene conversion on the other hand is always lower than 50%. Interestingly, ethylene production dominates over conversion when using the post-heater and when using a large catalyst bed (S6), i.e. conditions resulting in high methane conversion. Note that the C_2 conversions presented in Figure 3.3 are the result of C_2 conversion and C_2 production in the reactor.

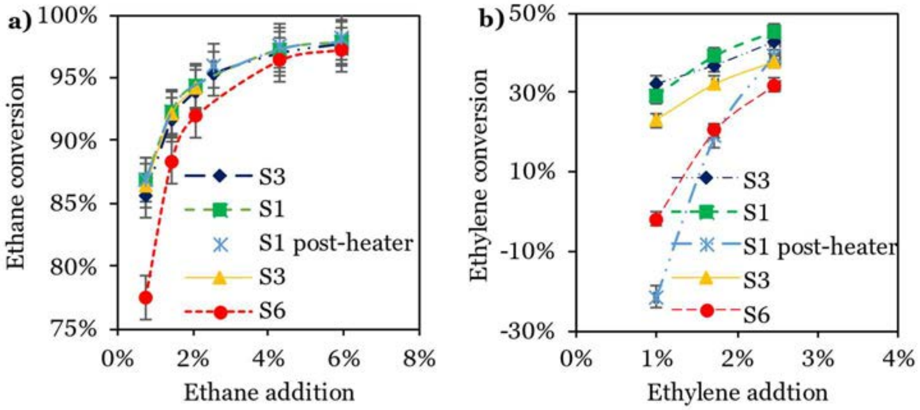

Figure 3.3: C_2 conversion as function of C_2 addition, (a) ethane, (b) ethylene; 90% CH_4 N_2 balance; 16.6 ml·min^{-1} total flowrate. Reactor-zone at 1000°C, pre-heater and post-heater at 400°C, except for S1 post-heater having $T_{postheater}$ at 1000°C.

The post catalytic residence time at high temperature can also be increased by using the post-heater as shown in Figure 2.1. Figure 3.4 shows a significant increase in methane conversion, keeping the level of ethane addition constant, when operating the post-heater at the same temperature as the reactor, i.e. 1000°C. Figure 3.4 also shows that ethylene addition results in the highest methane conversion when compared with ethane addition at the same concentration. Note that the difference in post-catalytic volume between the S1 case with or without post-heater is a factor of 3.7, significantly larger than the increase in conversion observed in Figure 5, showing a diminishing return of C_2 addition at longer residence time.

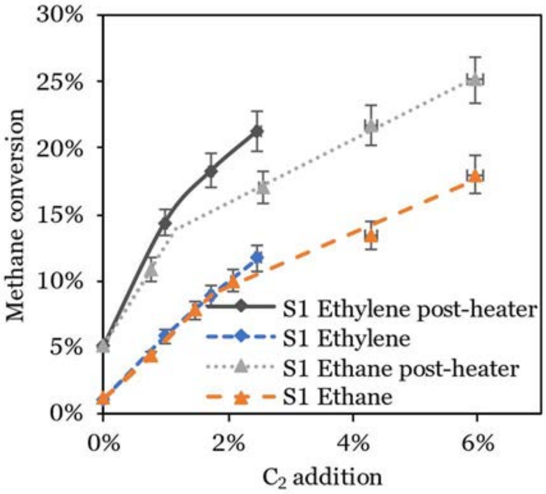

Figure 3.4: Effect of the post-heater on methane conversion with ethane or ethylene added, compared the effect of ethane addition without the post-heater (identical to S1 case Figure 3.2a). 90% CH_4, N_2 balance; 16.6 ml·min^{-1} total flowrate. Reactor-zone and post-heater at 1000°C (except for S1 ethane case), pre-heater at 400°C.

Figure 3.5 shows the selectivity towards the 3 major product groups: C_2 hydrocarbons, C_{3-5} hydrocarbons and aromatics, keeping the conversion constant at 10%. This conversion level was achieved by either addition of ethane, addition of ethylene, or by changing the flow rate and consequently space-velocity without any addition of C_2. The selectivity data at 10% conversion of hydrocarbon in the feed stream, assuming full conversion of the added C_2 species, are obtained by interpolation as presented in the supporting information, Figure S 3.1 and Figure S 3.2. It is assumed that the added C_2 compounds are completely converted whereas any ethane and ethylene detected in the product is assigned to formation in the reactor. In Figure 3.5, data are interpolated to 10% conversion of hydrocarbons in the feed stream including full conversion of the added C_2 compounds. Figure S 3.5 in SI presents the same type of analysis at 10% methane conversion, disregarding the conversion of C_2 compounds, resulting in very similar trends. Figure 3.5 shows that, within the error margin, the selectivity to the various product groups is constant, independent of the method to enhance CH_4 conversion to 10%, i.e. C_2 addition or decreasing space velocity. The formation of aromatic products is somewhat suppressed when ethylene is added, as well as when a full-catalyst bed is used (S6). The product distribution of all hydrocarbon products is given in Figure S 3.4.

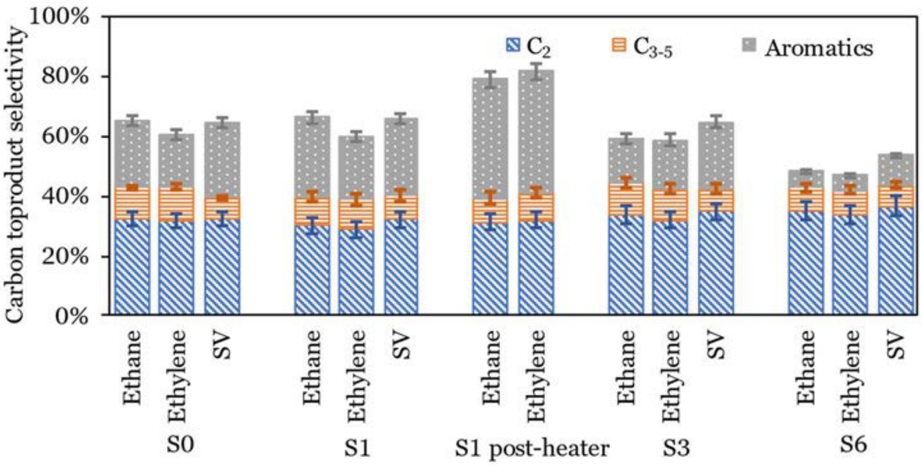

Figure 3.5: Product selectivity distribution for different methods of increasing methane conversion, by ethane addition or ethylene addition to the reactant mixture or by decreasing space velocity. The results have been linearly interpolated at 10% total hydrocarbon conversion as explained in the experimental section. Similarly, selectivity is also calculated based on total hydrocarbon conversion. reactor-zone at 1000°C; Pre-heater and post-heater are both at 400°C, except for the S1-post-heater in that case $T_{post\text{-}heater}$=1000°C. The total flowrate for the cases with ethane or ethylene addition is 16.6 ml·min^{-1} 90% CH_4, N_2 as balance. The graphs used for the interpolation can be found in Figure S 3.1 and Figure S 3.2.

Figure 3.6 shows the product yield to the three main product groups as function of conversion obtained with the small catalysts bed (S1) with and without the post-heater at high temperature, as a result of adding ethane (Figure 3.6a) and ethylene (Figure 3.6b). C_2 yield and $C_{3\text{-}5}$ yield are independent of the use of the post-heater, in contrast the aromatics yield which increased when using the post-heater.

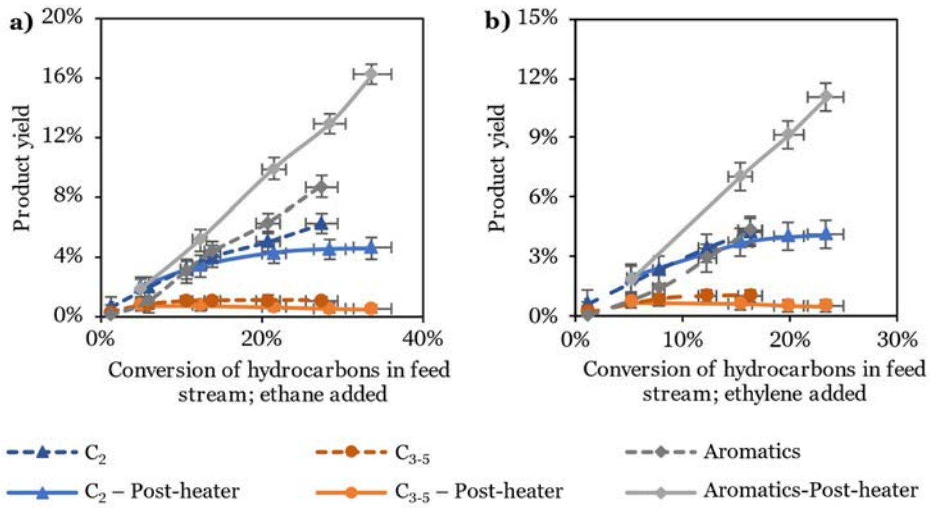

Figure 3.6: Effect on product yield when using the post-heater in the S1 case, (a) ethane, (b) ethylene; 90% CH_4 N_2 balance; 16.6 ml·min^{-1} total flowrate. Reactor-zone at 1000°C, pre-heater and post-heater at 400°C, except for S1 post-heater having $T_{\text{post-heater}}$ at 1000°C.

3.4 Discussion

3.4.1 Addition of ethane

Methane conversion is significantly increased on ethane addition, apparent from Figure 3.2a and b. The explanation for this significant enhancement in methane conversion is found in the studies of Roscoe and Thompson[26] as well as Dean[27] and schematically presented in Figure 3.7. Formation of higher hydrocarbons from ethane, via ethyl radicals, releases hydrogen radicals which react with methane according to $CH_4 + H\cdot \rightarrow CH_3\cdot + H_2$, which is the dominant reaction for activation of methane. The methyl radicals react to ethane, which maintains the cycle in Figure 3.7, known as methane auto-catalysis [26, 27]. In the presence of catalyst, methyl radicals form on the Fe active sites while the hydrogen atoms stay on the active site, to combine to form di-hydrogen, according to DFT calculations [19, 24].

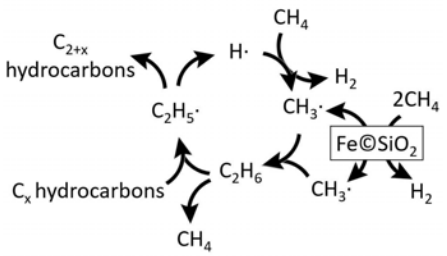

Figure 3.7: proposed reaction paths for methane activation and product formation, based on [26, 27].

A similar enhancement in methane conversion is also observed in non-catalytic operation in literature [28-30]. Germain et al. [29] and Rokstad et al.[30] observed a decreasing effectiveness of ethane addition on methane conversion when the ethane concentration is above 2% in absence of catalyst, very similar to the observation with catalyst in Figure 3.2b, which Germain attributed to scavenging of free radical by formed aromatic species.

The catalyst has no effect on methane conversion at ethane concentrations above 2%. This shows that ethyl radicals and consequently H radicals mainly form in gas phase whereas catalytic ethane activation is negligible. This is further supported by the linear correlation between the enhancement of methane conversion due to ethane addition and the free volume available in the reactor, as shown in Figure 3.2d, as well as by the observation that a large amount of catalyst reduces the ethane conversion, as shown in Figure 3.3a. Methane conversion is not influenced by the presence of catalyst when at least 2% ethane is added, as shown in Figure 3b. Apparently, enhancement of methane conversion on the catalyst is compensated by a decrease is methane conversion by decreasing the free volume when catalyst is introduced.

Figure 3.4 shows that the increase in methane conversion due to an extended post-catalytic residence time, discussed in **chapter 2,** is also observed when adding ethane, although the effect is relatively mild when compared with the 5-fold enhancement in absence of ethane. The activity for methane conversion without C_2 addition in the post-catalytic free-volume, as discussed in **chapter 2**, is attributed largely to C_2 hydrocarbon formation via catalytic methane activation.

The selectivity distribution over the main product groups at 10% conversion of hydrocarbons in the feed in Figure 3.5 is obtained by interpolation, based on the data in Figure S 3.1 and Figure S 3.2 in the supporting information. The selectivity to ethane is included by assuming that the ethane in the feed is completely converted, as observed in Figure 3.3a especially when the concentration of ethane added is high. The relatively small amount of ethane in the product stream is therefore counted as a product. Figure S 3.4 shows the selectivity for all hydrocarbon compounds detected. Product selectivity at 10% conversion level is independent from the method applied to achieve 10% conversion, i.e. catalytic or by ethane addition (Figure 3.5). Figure 3.5 shows that the total hydrocarbon selectivity decreases with increasing the amount of catalyst (S3, S6) in presence of ethane, probably because of the increased formation of coke-on-catalyst with increasing catalyst amount as observed in Figure S 3.7. The observed influence of the amount of catalyst on coke formation on the catalyst is well in line with findings in **chapter 2**. The highest total hydrocarbon selectivity is achieved using the post-heater, in which the 10% conversion level is achieved via a significantly increased residence time at 1000°C, rather than via addition of C_2.

The invariance of the product selectivity of C_2 addition is also reported by Ogihara et al. [31] for non-catalytic pyrolysis of mixtures of ethane-methane between 700 and 800°C. The results in the supporting information of Guo et al. [19] confirm that product selectivity is unaffected by C_2H_6 addition, in good agreement with our results. Aromatic products dominate when the conversion is high by adding more C_2 as shown in Figure 3.6, which also shows that product yield is mainly determined by the conversion level. The main C_2 specie measured at high conversion levels is ethylene whereas benzene and naphthalene are the dominant aromatic species (Figure S 3.3), in agreement with the observations by Guo et al. [19] at high conversion.

3.4.2 Addition of ethylene

Ethylene has a very similar effect on methane conversion as ethane, shown in Figure 3.2c and even better exemplified in Figure 3.4 as the effects of ethane and ethylene are the same within experimental error. This is in agreement with Roscoe and Thompson [26] as well as Dean [27], reporting that ethylene participates in methane activation in the same way as ethane. Ethylene causes a slightly higher methane conversion compared to ethane when operating with a long post-catalytic residence time as presented in Figure 5. This is speculatively attributed to the higher thermal stability of ethylene compared to ethane [35], releasing radicals in a more dosed manner, continuing in the post-heater at relatively long residence times. In contrast, ethane is likely to decompose more readily, forming radicals only in the first part of the reactor and increasing the probability of unproductive termination by coupling of two hydrogen radicals to form H_2. It must also be noted that likely a significant fraction of ethane dehydrogenates to ethylene, giving an alternative explanation for the similarity in effectiveness between ethylene and ethane addition.

C_2 compounds can consecutively dehydrogenate, from ethane via ethylene to acetylene to finally coke [36, 37]. $C_2H_5\cdot$ radical formed from ethane can release a hydrogen radical to form ethylene, in addition to the pathways presented in Figure 3.7. Furthermore, ethylene can decompose to $C_2H_3\cdot$ via hydrogen abstraction by a methyl radical, followed by a similar cycle as described for ethane in Figure 3.7. These consecutive dehydrogenation reactions consume one methyl radical and form one hydrogen radical and thus have no net impact on the free radical propagation [26, 27].

Note that ethane and ethylene need to react to form higher hydrocarbons in order to propagate the cycle in Figure 3.7, limiting the maximum C_2 yield when CH_4 activation via gas phase autocatalysis is dominant. The auto-catalytic activation of methane will be discussed in more detail in **chapter 5**.

Based on the similarity of the effect of ethane and ethylene on the conversion of methane and the fact that ethane converts almost completely, we assume that also all added ethylene is converted. In other words, the limited ethylene conversion in Figure 4b is attributed to production of ethylene as a result of methane conversion and the product distribution presented in Figure 3.5 is calculated based on the same assumption. Figure 3.5 as well as Figure S 3.4 show that ethylene addition has no significant effect on the product distribution at 10% conversion, similar to ethane addition. Increasing the methane conversion by ethylene addition results in slightly lower selectivity to aromatics (Figure 3.5), which is attributed to enhanced consecutive formation of deposits-downstream.

3.4.3 Industrial relevance

Addition of C_2 significantly increases the methane conversion rate in the reactor (Figure 3.2) while maintaining product selectivity (Figure 3.5), thus increasing productivity per unit reactor volume. C_{2+} hydrocarbons are often present in natural gas with typical concentrations similar to the concentrations used in this study, for example Gulf-coast natural gas contains up to 4.9 vol% C_2 hydrocarbons [1] (details in Table S 3.1). Our study implies that removal of ethane from natural gas is not required, simplifying the purification of natural gas. The catalyst becomes obsolete at C_2 concentrations above 2 vol% as shown in Figure 3.2. Thus, the reaction can be operated at high productivity without requiring a catalyst, simplifying the reactor design and operation. Deposit build-up on the catalyst can be prevented and catalyst purchasing, handling, disposal and plant-stops for catalyst replacement are all not required. Rapid control of reactor capacity would be possible by tuning the concentration of the C_2 initiator in the reactor feed.

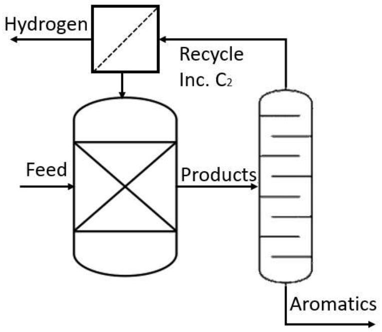

Figure 3.8: Basic schematic concept process for natural gas to aromatics based on NOCM including C_2 recycle.

Overall ethylene conversion is typically low or even negative, meaning net-production at high methane conversion levels as shown in Figure 4b. Ethylene can be recycled back into the reactor, to generate a process with a net-zero consumption of ethylene, as presented in the schematic process diagram in Figure 3.8. In this scheme, the aromatic products are separated from the olefins, which are recycled back to the reactor, after separation of hydrogen. Figure S 3.3 in the supporting information shows that the yields of ethane as well as C_{3-5} hydrocarbons becomes negligible at high methane conversion levels. The activity increase in the reactor can be achieved both by recycled ethylene as well as ethane in the feed. Figure 3.3b shows that overall ethylene conversion is positive at higher added ethylene concentrations and negative, i.e. net-production, at lower ethylene concentrations, demonstrating an internal feedback-loop that will prevent both ethylene accumulation as well as depletion in the process. This results in a process converting methane to aromatics, also alleviating the energy intensive cryogenic recovery of ethylene. The highest single pass methane conversion achieved in this paper, 25%, with 16% aromatics yield is already higher than benchmark performance of MDA, around 15% conversion and 11% aromatics yield [16]. On the other hand, it must be noted that the main product is naphthalene compared to more valuable benzene produced in the MDA reaction and additional conversion might be required. Also, this scheme is obviously not producing any ethylene as originally targeted with methane pyrolysis.

3.5 Conclusions

The effect of C_2 addition on non-oxidative methane coupling at high temperature was investigated. Addition of ethane and ethylene (C_2) up to 6 vol-% in methane significantly increases methane conversion during both catatlytic as wel as non-catatytic NOCM. The activation of methane through C_2 addition is a dominated by homogenous gas-phase reaction and catalytic ethane or ethylene conversion is negligable. Product selectivity at constant conversion is unaffected by C_2 addition and is influenced by catalyst amount and residence time in the hot zone of the reator, both within and downstream of the catalyst bed, in line with our previuous work. The catalyst has no effect on methane conversion at C_2 concentrations above 2%, showing that an optimal reaction design involves either no catalyst at all or a minimal amount of catalyst. The catalyst is needed to initiate methane coupling via radical chain reactions only when less then 2 vol-% of ethene or ethylene are present in the feed. C_2 addition during NOCM significantly increases productivity and allows simplification of purification of the reactor-feed. A process design is envisioned in which the produced ethylene is recycled back into the reactor to iniate the methane conversion, resulting in a process converting methane to aromatics.

3.6 Acknowledgements

We acknowledge support from the Dutch National Science Foundation (NWO) and the industrial partners: SABIC, Sasol and BASF. We thank ing. B. Geerdink, K.J. Altena, ing. T.L.M. Velthuizen and ir. T. Lubbers for their experimental and analytical support.

3.7 Supporting Information

3.7.1 Product distribution as function of conversion level and product yield distribution when using the post-heater

Figure S 3.1 and Figure S 3.2 show the measured selectivity data as function of hydrocarbon conversion used for the interpolation of Figure 3.5 in the main text.

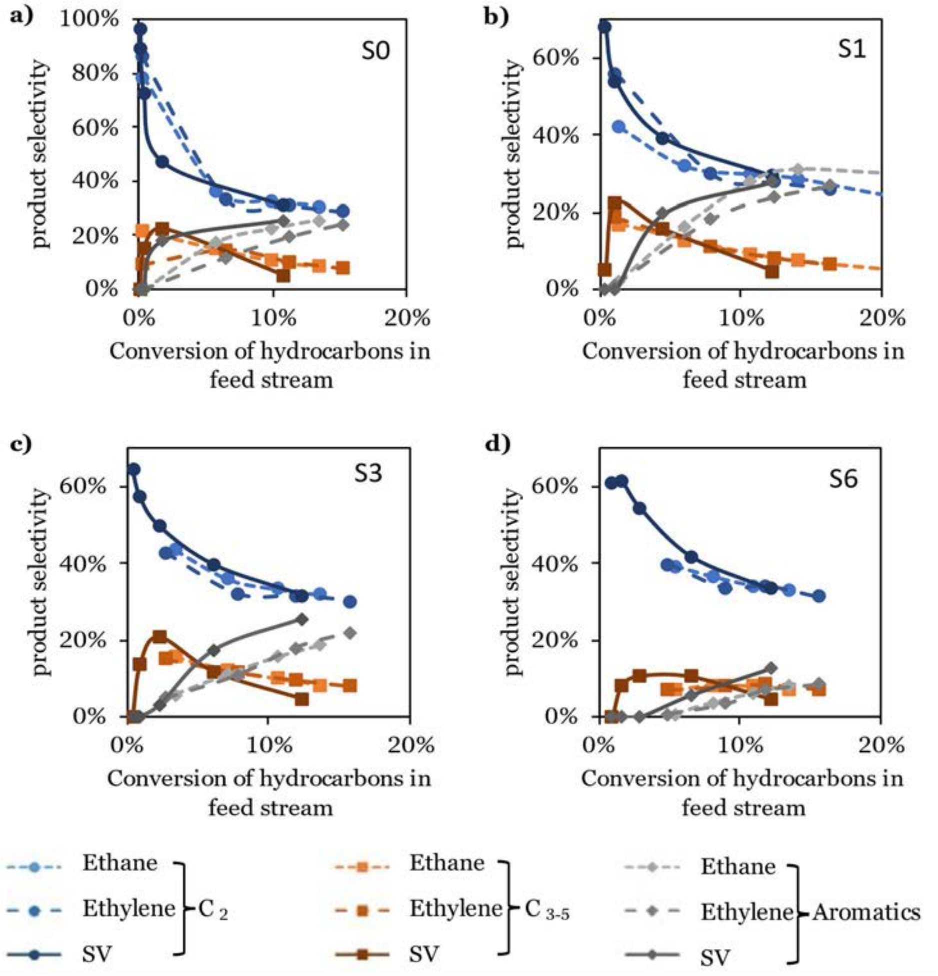

Figure S 3.1: Selectivity distribution over major product groups as function of hydrocarbon conversion level, used to interpolate the data shown in Figure 3.5 and Figure S 3.4, (a) a blank reactor, S0, (b) S1, (c) S3, (d) S6, 90% CH_4 N_2 balance; 16.6 ml·min^{-1} total flowrate. Reactor-zone at 1000°C, pre-heater and post-heater at 400°C.

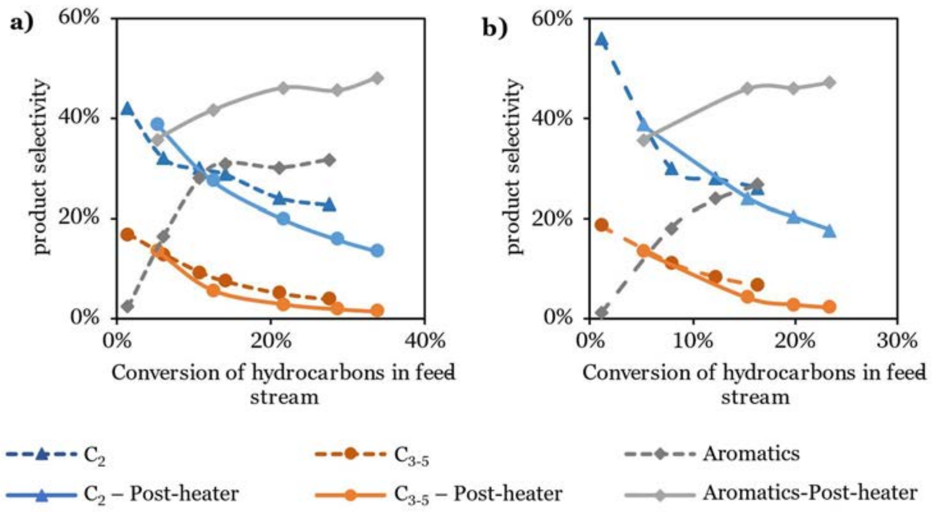

Figure S 3.2: Selectivity distribution over major product groups as function of hydrocarbon conversion level for employing the post-heater compared to the S1 case without post-heater (shown in Figure S 3.1), for (a) ethane and (b) ethylene addition used to interpolate the data shown in Figure 3.5 and Figure S 3.4, 90% CH_4 N_2 balance; 16.6 ml·min^{-1} total flowrate. Reactor-zone at 1000°C, pre-heater and post-heater at 1000°C.

Figure S 3.3 shows the product yield distribution over all measured hydrocarbons when increasing the post-catalytic residence time by employing the post-heater. The same data presented in product groups is shown in Figure 3.6 in the main text.

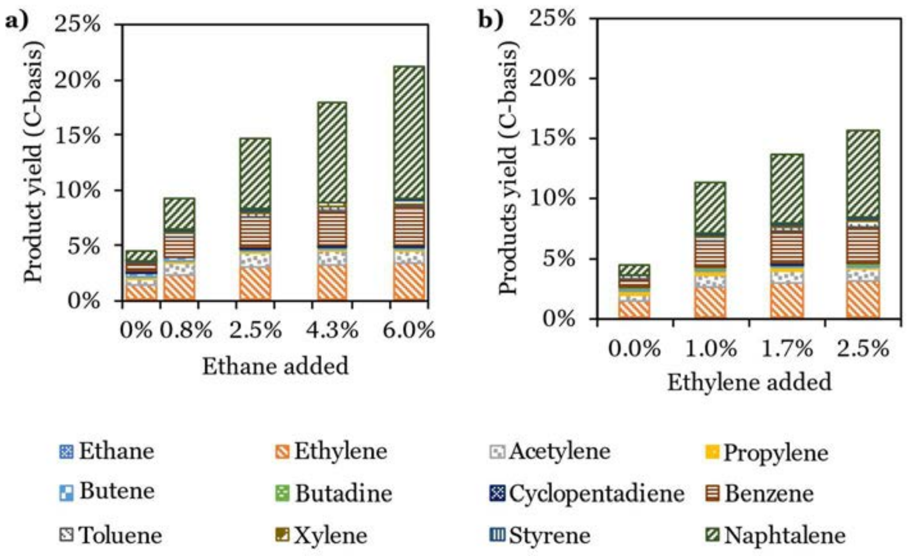

Figure S 3.3: Product yield distribution as function of the volume of C_2 added to the reactant mixture for the S1 case including post-heater (a) ethane and (b) ethylene addition, 90% CH_4 N_2 balance; 16.6 ml·min^{-1} total flowrate. Reactor-zone at 1000°C, pre-heater and post-heater at 1000°C.

3.7.2 S.2 Product distribution per individual hydrocarbon at 10% total HC conversion

Figure S 3.4 is a copy of Figure 3.5 in the main text, split out over all measured hydrocarbon products, rather than the grouped presentation in Figure 3.5. Figure S 3.5 and Figure S 3.6 show the same information as Figure 3.5 but calculated in a different fashion. Figure S 3.5 is interpolated at 10% methane conversion rather than the 10% conversion of fed-hydrocarbons in Figure 3.5. Figure S 3.6 is calculated assuming partial conversion of the added C_2 compound, at 10% added hydrocarbon conversion.

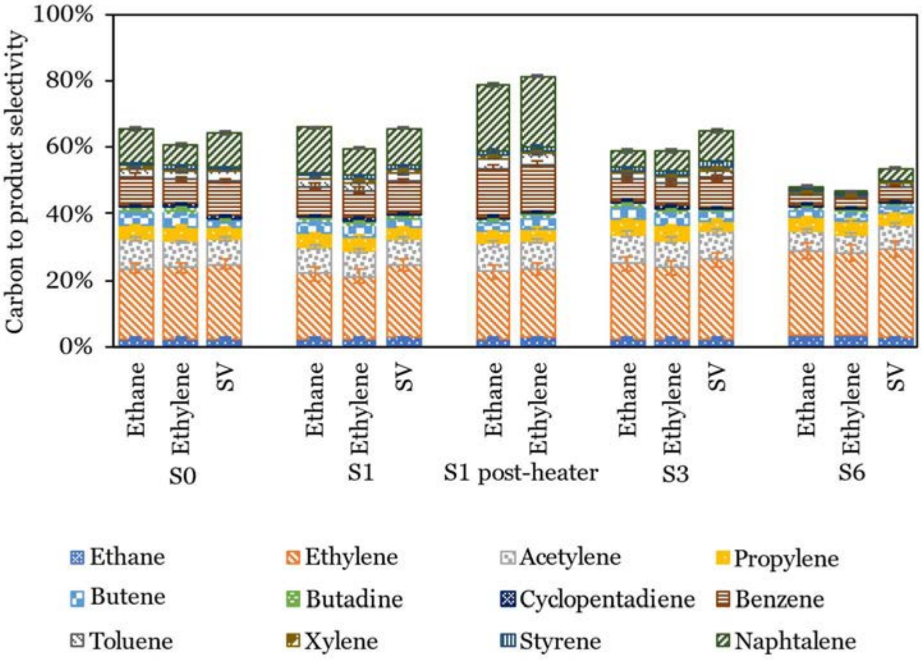

Figure S 3.4: Product selectivity distribution for different methods of increasing methane conversion, by ethane addition or ethylene addition to the reactant mixture or by decreasing space velocity. The results have been linearly interpolated at 10% total hydrocarbon conversion as explained in the experimental section, Similarly selectivity is also calculated based on total hydrocarbon conversion. reactor-zone at 1000°C; Pre-heater and post-heater are both at 400°C, except for the S1 post-heater in that case $T_{postheater}$=1000°C. The total flowrate for the cases with ethane or ethylene addition is 16.6 ml·min^{-1} 90% CH_4, N_2 as balance. The graphs used for the interpolation can be found in Figure S 3.1 and Figure S 3.2.

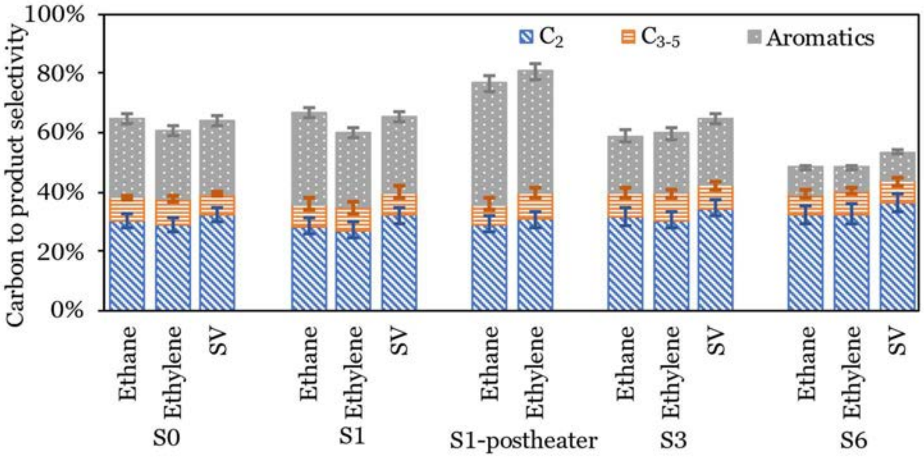

Figure S 3.5: Product selectivity distribution for different methods of increasing methane conversion, by ethane addition or ethylene addition to the reactant mixture or by decreasing space velocity. The results have been linearly interpolated at 10% **CH_4 conversion**, selectivity is calculated based on total hydrocarbon conversion. reactor-zone at 1000°C; Pre-heater and post-heater are both at 400°C, except for the S1 post-heater in that case $T_{postheater}$=1000°C. The total flowrate for the cases with ethane or ethylene addition is 16.6 ml·min^{-1} 90% CH_4, N_2 as balance.

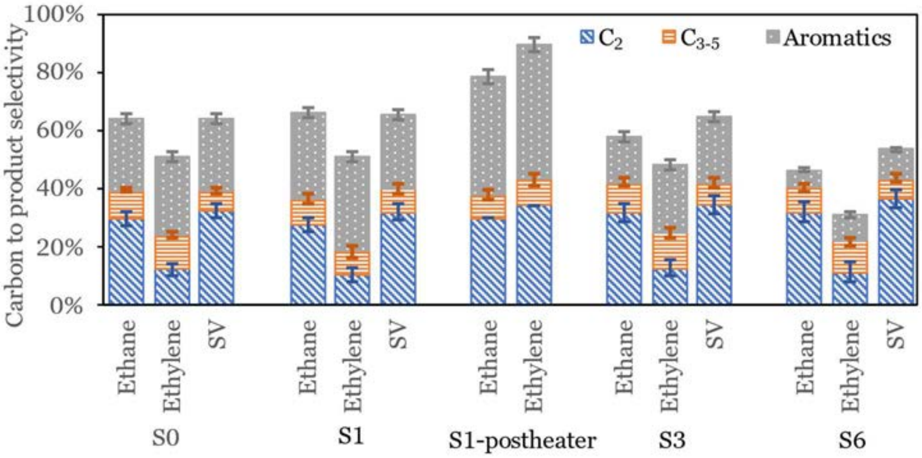

Figure S 3.6: Product selectivity distribution for different methods of increasing methane conversion, by ethane addition or ethylene addition to the reactant mixture or by decreasing space velocity. The results have been linearly interpolated at 10% hydrocarbon conversion, based on the partial conversion of methane (Figure 3.2) and the partial conversion of the added C_2 molecule (Figure 3.3), selectivity is calculated based on hydrocarbon conversion discussed before. Note that this means that there is **no** ethane selectivity in case ethane is added and **no** ethylene selectivity when ethylene is added; the exception to this is the S1-post-heater case with ethane, since as Figure 3.3b shows, it has a **negative** ethylene conversion and thus a selectivity can be calculated. reactor-zone at 1000°C; Pre-heater and post-heater are both at 400°C, except for the S1 post-heater in that case $T_{postheater}$=1000°C. The total flowrate for the cases with ethane or ethylene addition is 16.6 ml·min^{-1} 90% CH_4, N_2 as balance.

3.7.3 S.3 Deposit formation and mass balance analysis

Figure S 3.7 shows the integral product yields of both coke-on-catalyst and deposits-downstream during a full experiment in which the concentration of added C_2 addition was varied between 0 and 2%. Coke-on-catalyst is measured with TGA and the formation of deposits-downstream of the catalyst is calculated based on the mass-balance. The experiment consists of the standard activation procedure as described in the experimental section and by Bao pers. commun. [32], followed by 2h of reaction using 90% CH_4 in N_2 without any addition of C_2. After that, the catalyst is exposed to three different C_2 concentrations (0.8-1.5-2.1 for C_2H_6 and 1.0-1.7-2.5 for C_2H_4) during 4 hours in total, keeping the total flowrate at 16.6 $ml \cdot min^{-1}$ and the methane concentration at 90%. Consequently, the catalyst is exposed to methane during 8h in total. There is no difference in coke-formation on the catalyst when adding either ethane or ethylene, shown in Figure S 3.7a. Coke-on-catalyst formation increases more relative to the increase in catalyst mass added, showing the higher coking rates further downstream in the catalyst, as discussed in **chapter 2**. Overall, ethane addition results in a lower deposits-downstream yield, as shown in Figure S 3.7b.

Coke-on-catalyst as well as deposits-downstream are calculated according to the following equations: The total carbon-to-products selectivity is the summation of the selectivity to all GC-measured products.

$$S_C = \Sigma S_{C_xH_y} \qquad \text{Eq. 1}$$

S_c: $total\ carbon\ to\ products\ selectivity\ (-)$

Integral values of conversion, selectivity and coke deposition are calculated in order to compare with data on the amount of deposits on the catalyst after a full experiment as measured with TGA. Eq. 2 is used to calculate the total amount of carbon converted in the full experiment:

$$C_{converted\ CH_4} = \int_{t=0}^{t=14h} \phi_{CH_4 in} \cdot \xi_{CH_4} \cdot \frac{1}{V_m} \qquad \text{Eq. 2}$$

ϕ_x: $flow\ of\ x\ (ml \cdot s^{-1})$
V_m: $molar\ volume\ at\ SPT\ (ml \cdot mol^{-1})$

The total amount of carbon that is converted to deposits during an integral experiment is calculated based on the difference in mass-balance closure as presented in Eq. 3:

$$C_{deposits-downstream} = \int_{t=0}^{t=8h} \phi_{CH_4 in} \cdot \xi_{CH_4} \cdot (1 - S_c) \cdot \frac{1}{V_m} \qquad \text{Eq. 3}$$

Deposits can form either on the catalyst, named ‘coke-on-catalyst’ or down-stream of the catalyst-bed on the reactor-wall or in the tubing to the GC, named ‘deposits-downstream’.

The amount of coke formed on the catalyst during a full experiment is also be calculated based on the weight loss during oxidation of the spent catalyst in TGA, according to Eq. 4, assuming coke-on-catalyst contains exclusively C:

$$C_{coke-on-catalyst} = \Delta W_{TGA} \cdot \frac{Q_{cat}}{M_C} \qquad \text{Eq. 4}$$

$M_C: molar\ mass\ of\ carbon\ (g \cdot mol^{-1})$
$\Delta W_{TGA}: the\ percentage\ of\ mass\ decrease\ in\ the\ TGA\ analysis\ (-)$
$Q_{cat}: amount\ of\ catalyst\ in\ the\ reactor\ (g)$

Deposits-downstream include a wide array of poly aromatic hydrocarbons of C_{10+} in carbon number, as well as coke deposited on the reactor-wall downstream of the catalyst, as presented in **chapter 2**.

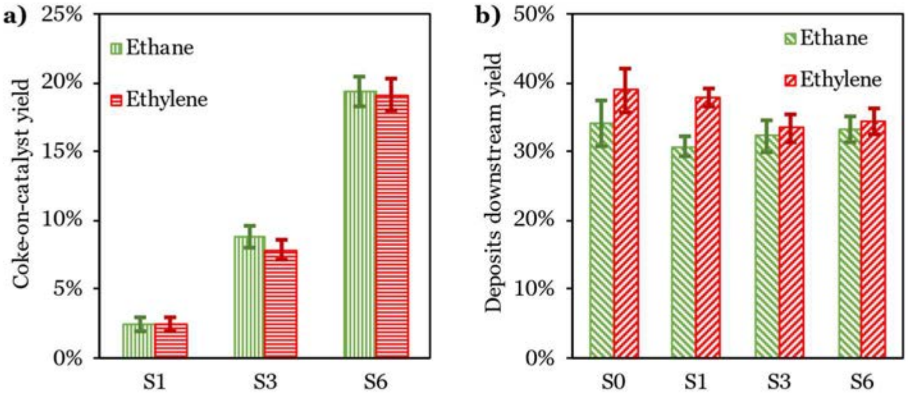

Figure S 3.7: (a) the yield of coke-on-catalyst during a complete experiment as described in the text and (b) the yield of deposits formed downstream of the catalyst assuming a closing mass balance. Reactor temperature 1000°C; pre-heater and post-heater operated at 400°C; 90% CH_4 in N_2. Complete experiment during 8h, varying ethane or ethylene concentration between 0 and 2.5%.

3.7.4 S.4 The average composition of natural gas in the US Gulf-Coast

Table S 3.1: The composition of US gulf-coast natural gas according to [1].

Component	**Mole fraction (%)**	**Trace components**	**Amount**
N_2	1.25	S-components	5.5 mg·m^{-3}
CH_4	91.01	H_2O	<65 mg·m^{-3}
C_2	4.88	O_2	0.01 mole%
C_3	1.69	CO_2	0.01 mole%
C_4	0.66		
C_5	0.27		
C_6	0.13		
C_7 *and above*	0.11		

3.8 References

1. Uniongas. *Chemical Composition of Natural Gas*. 2017; Available from: https://www.uniongas.com/about-us/about-natural-gas/chemical-composition-of-natural-gas.

2. Mesters, C., *A Selection of Recent Advances in C1 Chemistry*. Annual Review of Chemical and Biomolecular Engineering, 2016. **7**: p. 223-238.

3. Karakaya, C. and R.J. Kee, *Progress in the direct catalytic conversion of methane to fuels and chemicals*. Progress in Energy and Combustion Science, 2016. **55**: p. 60-97.

4. Taifan, W. and J. Baltrusaitis, *CH4 conversion to value added products: Potential, limitations and extensions of a single step heterogeneous catalysis*. Applied Catalysis B: Environmental, 2016. **198**: p. 525–547.

5. Zimmermann, H. and R. Walzl, *Ethylene*, in *Ullmann's Encyclopedia of Industrial Chemistry*. 2009, Wiley-VCH Verlag GmbH & Co. KGaA.

6. Folkins, H.O., *Benzene*, in *Ullmann's Encyclopedia of Industrial Chemistry*. 2000, Wiley-VCH Verlag GmbH & Co. KGaA.

7. Caineng, Z., Z. Qun, Z. Guosheng, and X. Bo, *Energy revolution: From a fossil energy era to a new energy era*. Natural Gas Industry B, 2016. **3**: p. 1-11.

8. Klerk, A.d., *Fischer–Tropsch Process*, in *Kirk-Othmer Encyclopedia of Chemical Technology*. 2013. p. 1-20.

9. Wittcoff, H.A., B.G. Reuben, and J.S. Plotkin, *Chemicals from Methane*. 2012, John Wiley & Sons, Inc.

10. Appl, M., *Ammonia*, in *Ullmann's Encyclopedia of Industrial Chemistry*. 2011.

11. Lunsford, J.H., *Catalytic conversion of methane to more useful chemicals and fuels: a challenge for the 21st century*. Catalysis Today, 2000. **63**(2-4): p. 165-174.

12. Tian, P., Y. Wei, M. Ye, and Z. Liu, *Methanol to Olefins (MTO): From Fundamentals to Commercialization*. ACS Catalysis, 2015. **5**(3): p. 1922-1938.

13. Abdulrasheed, A., A.A. Jalil, Y. Gambo, M. Ibrahim, H.U. Hambali, and M.Y.S. Hamid, *A review on catalyst development for dry reforming of methane to syngas: Recent advances*. Renewable and Sustainable Energy Reviews, 2019. **108**: p. 175-193.

14. Kianfar, E., S. Hajimirzaee, S. mousavian, and A.S. Mehr, *Zeolite-based catalysts for methanol to gasoline process: A review*. Microchemical Journal, 2020. **156**.

15. Mohajerani, S., A. Kumar, and A.O. Oni, *A techno-economic assessment of gas-to-liquid and coal-to-liquid plants through the development of scale factors*. Energy, 2018. **150**: p. 681-693.

16. Galadima, A. and O. Muraza, *Advances in Catalyst Design for the Conversion of Methane to Aromatics: A Critical Review*. Catalysis Surveys from Asia, 2019. **23**: p. 149-170.

17. Amghizar, I., L.A. Vandewalle, K.M.V. Geem, and G.B. Marin, *New Trends in Olefin Production*. Engineering, 2017. **3**: p. 171-178.

18. Schwach, P., X. Pan, and X. Bao, *Direct Conversion of Methane to Value-Added Chemicals over Heterogeneous Catalysts: Challenges and Prospects*. Chemical Reviews, 2017. **117**: p. 8497-8520.

19. Guo, X., G. Fang, G. Li, H. Ma, H. Fan, L. Yu, C. Ma, X. Wu, D. Deng, M. Wei, D. Tan, R. Si, S. Zhang, J. Li, L. Sun, Z. Tang, X. Pan, and X. Bao, *Direct, Nonoxidative Conversion of Methane to Ethylene, Aromatics, and Hydrogen*. Science, 2014. **344**(6184): p. 616-619.

20. Sakbodin, M., Y. Wu, S.C. Oh, E.D. Wachsman, and D. Liu, *Hydrogen-Permeable Tubular Membrane Reactor: Promoting Conversion and Product Selectivity for Non-Oxidative Activation of Methane over an FeVSiO2 Catalyst*. Angewandte Chemie, 2016. **55**: p. 16149 –16152.

21. Oh, S.C., E. Schulman, J. Zhang, J. Fan, Y. Pan, J. Meng, and D. Liu, *Direct Non-Oxidative Methane Conversion in a Millisecond Catalytic Wall Reactor*. Angewandte Chemie, 2019. **58**: p. 7083-7086.

22. Nagaki, D.A., Z. Zhao, M.N.Z. Myint, I. Lengyel, A. Mamedov, C.W. Gundlach, K. Sankaranarayanan, and D. Falcone, 2018, *Method for Producing Hydrocarbons by Non-Oxidative Coupling of Methane*, US 9 , 902 , 665 B2

23. Han, S.J., S.W. Lee, H.W. Kim, S.K. Kim, and Y.T. Kim, *Nonoxidative Direct Conversion of Methane on Silica-Based Iron Catalysts: Effect of Catalytic Surface*. ACS Catalysis, 2019. **9**: p. 7984-7997.

24. Kim, S.K., H.W. Kim, S.J. Han, S.W. Lee, J. Shin, and Y.T. Kim, *Mechanistic and microkinetic study of non-oxidative methane coupling on a single-atom iron catalyst*. Communication Chemistry, 2020. **3**(58).

25. Chen, C.J. and M.H. Back, *The thermal decomposition of methane. II. Secondary reactions, autocatalysis and carbon formations; non-arrhenius behaviour in the reaction of CH3 with ethane*. Canadian Journal of Chemistry, 1976. **54**(54): p. 3175-3184.

26. Roscoe, J.M. and M.J. Thompson, *Thermal decomposition of Methane: Autocatalysis*. International Journal of Chemical Kinetics, 1985. **17**: p. 967-990.

27. Dean, A.M., *Detailed Kinetic Modeling of Autocatlysis in Methane Pyrolysis*. Journal of Physical Chemistry, 1990. **94**: p. 1432-1439.

28. Schneider, I.A., *Über die Rolle des Äthans bei der thermishen Methanzersetzung*. Zeitschrift für Physikalische Chemie, 1963. **223**(1): p. 234-248.

29. Germain, J. and C. Vaniscotte, *Craquage du Methane dans un Reacteur Tubulaire. 3. Effet Iniateur de l'Ethane*. bulletin de la Société Chimique de France, 1958.

30. Rokstad, O.A., O. Olsvik, and A. Holmen, *Thermal Coupling of Methane*. Natural Gas Conversion, 1991: p. 533-539.

31. Ogihara, H., H. Tajima, and H. Kurokawa, *Pyrolysis of mixtures of methane and ethane: activation of methane with the aid of radicals generated from ethane*. Reaction Chemistry & Engineering, 2020. **5**: p. 145-153.

32. Bao, X. *personal communication to:* L. Lefferts, 2016

33. Slater, W.E., *The influence of different surfaces on the decomposition of methane*. Journal of the Chemical Society, Transactions, 1916. **109**: p. 160-164.

34. Liu, S., L. Wang, R. Ohnishi, and M. Ichikawa, *Bifunctional Catalysis of Mo/HZSM-5 in the Dehydroaromatizationof Methane to Benzene and Naphthalene XAFS/TG/DTA/MASS/FTIR Characterization and Supporting Effects*. Journal of Catalysis, 1999. **181**: p. 175-188.

35. Guéret, C., M. Daroux, and F. Billaud, *Methane pyrolysis: thermodynamics*. Chemical Engineering Science, 1997. **52**(5): p. 815-827.

36. Khan, M.S. and B.L. Crynes, *Survey of Recent Methane Pyrolysis Literature*. Industrial & Engineering Chemistry, 1970. **62**(10): p. 54-59.

37. Holmen, A., O.A. Rokstad, and A. Solbakken, *High-Temperature Pyrolysis of Hydrocarbons. 1. Methane to Acetylene*. Industrial & Engineering Chemistry Process Design and Development, 1975. **15**(3): p. 439-444.

Chapter 4

The effect of hydrogen addition on product distribution and coke formation in catalytic coupling of methane

This chapter will be submitted as:

The effect of hydrogen addition on product distribution and coke formation in catalytic coupling of methane; R.S. Postma, L. Lefferts

Abstract

The effect of hydrogen addition on catalytic non-oxidative coupling of methane was investigated. Experiments were performed at varying ratios between catalyst to post-catalytic volume, to discern the effect of hydrogen on the catalytic reaction as well as the gas-phase reaction. Hydrogen contributes solely in reducing gas-phase reaction rates. This leads to halving the methane conversion at 10% H_2 addition, with little influence of the ratio between catalyst and post-catalytic residence time. C_2 hydrocarbon yield is unchanged by hydrogen addition up to 10 vol%, whereas aromatic selectivity is significantly reduced. The reduction in product yield can be mainly attributed to a decrease in methane conversion. Coke formation of the catalyst is reduced by an order of magnitude, when dosing up to 10% H_2. These results allow to speculate on a process in which produced hydrogen is recycled back into the reactor, to maximize the carbon selectivity to C_2 hydrocarbons, while minimizing both aromatics and, most crucially, coke formation.

4.1 Introduction

Methane is receiving a growing interest as chemical feedstock for the production of liquid fuels and base chemical [1-3], such as olefins and aromatics. The traditional role of methane rich natural gas for heating and electricity production is expected to be taken over by renewable sources such as solar or wind [4-7], making natural gas available for synthesis of chemicals. Most processes for methane valorisation to higher hydrocarbons rely on steam reforming of methane to synthesis gas, followed by various processes to produce paraffins, olefins or aromatics [8, 9].

Direct catalytic non-oxidative coupling of methane has seen a steep increase in interest over the last decade [3, 10, 11]. The traditional methods for direct methane coupling, namely oxidative coupling of methane (OCM) [12] and methane dehydroaromatization (MDA) [13] suffer from low single pass conversions and low selectivity caused by formation of CO_2 and coke, respectively. In 2014 Guo et al. [14] reported coupling of methane over a Fe©SiO_2 catalyst to a mix of olefins and aromatics at temperatures above 950°C. They reported single pass hydrocarbon yields as high as 48% at 1080°C, without coke formation and long-term stability up to 60h. The absence of coke formation has since only been reproduced by Sakbodin et al. [15], who tested the same catalyst in a hydrogen permeable membrane reactor. Other sources report coke formation during methane coupling using the Fe©SiO_2 catalyst [16-19]. Han et al. [17] reported that the cristobalite phase of the SiO_2 as well as the atomically disperse nature of the iron sites is crucial for minimizing coke formation. **Chapter 2** as well as a SABIC patent [19] showed that coking can be minimized by using the catalyst for only initiation by forming free-radicals, while most of the CH_4 conversion occurs in the post-catalytic volume. Furthermore, **chapter 2** showed that rapid heating upstream of the catalyst bed, preventing gas phase methane activation, also minimizes coking.

Research on non-catalytic direct coupling of methane, generally called methane pyrolysis, surged in the 80s and 90s [20-25]. Most of these studies focussed on unravelling the free-radical gas phase mechanism in direct methane coupling. Hydrogen is sometimes used as co-reactant to slow down the free radical reactions and to prevent excessive deposit formation [24, 26-29]. Guéret et al. [28] showed that hydrogen addition at ratios of H_2:CH_4 between 0.5 and 2 causes as significant decrease in methane conversion as well as a decrease in both ethylene and acetylene dehydrogenation rates and also a decrease in the cyclization to form benzene at 1330°C. They attribute all these effects to scavenging of $CH_3\cdot$ radicals. Olsvik et al. [29] investigated the effect of H_2 addition at temperatures between 1200-1500°C, showing that hydrogen addition prevents excessive carbon formation. Arutyunov reviewed a large set of data on methane pyrolysis, spanning from 1862 up to

1990 [30], including the work of Germain et al. [31], who demonstrated that dilution of methane by hydrogen significantly decreases the methane conversion rate whereas dilution with nitrogen had no significant effect. In contrast, Kunugi et al. [32] showed that addition of relatively small concentration of hydrogen, less than 20%, increases the methane conversion rate at temperatures above 1300°C. Kim et al. [33] trained a neural network with a large set of experimental data on methane pyrolysis, to determine the optimum reaction conditions, namely pressure, temperature, flow-rate, H_2 co-feeding, reactor length and reactor diameter. Hydrogen was found to be a main determining factor in methane conversion as well as C_2 selectivity, the optimum hydrogen concentration was calculated at 3.6 vol%, at a reaction temperature of 1200°C.

There is little data on the effect of hydrogen addition on the catalytic coupling of methane. Sakbodin et al. [15] showed the effect of H_2 addition up to 16.7% during catalytic methane pyrolysis using Fe©SiO_2 as catalyst. Methane conversion is roughly halved by the addition of 9.1% H_2 hydrogen, while the selectivity to C_2 products increased significantly and selectivity to aromatics decreased. Interestingly, C_2 yield remains relatively unchanged, whereas the aromatic yield drops significantly. Note that Sakbodin did not report on any coke formation.

This study reports on the effect of hydrogen addition on catalytic non-oxidative coupling of methane, including the formation of coke on the Fe©SiO_2 catalyst as well as formation of deposit downstream of the catalyst bed. Furthermore, the effect of hydrogen addition on the product slate will be shown varying the residence times at high temperature downstream of the catalyst bed, revealing the contribution of gas phase radical reactions after initiation on the catalyst.

4.2 Experimental

4.2.1 Catalyst synthesis

The catalyst is synthesized according to the method described in [14], while details concerning catalyst synthesis as well as characterisation can be found in **chapter 2**. In short, in-house synthesized Fe_2SiO_4 is mixed with quartz and ball-milled in N_2 atmosphere overnight using a zirconia milling jar. The resulting powder is fused for 6h at 1700°C in air. The resulting slab is crushed and sieved, the fraction between 250-500 µm is used in the experiments. The sieved catalyst particles are leached for 2h in 0.5 M HNO_3, rinsed and dried to obtain the final catalyst. The catalyst is analysed with both XRD and XRF, showing the expected cristobalite crystal structure and 0.5 wt% Fe loading. For more details concerning the catalyst characterisation, please refer to **chapter 2**.

4.2.2 Reactor setup

A modular three-zone oven, introduced in **chapter 2,** is used for catalytic testing. Each zone is thermally insulated from the others and from the environment, allowing for steep temperature gradients, as presented in Figure 2.1. The pre-heater is always operated at 400°C and the reactor-zone at 1000°C, the post-heater is either operated at 400°C or 1000°C, as shown by the two separate lines in Figure 2.1. Gas flows are controlled using digital mass flow controllers. Product gasses are analysed using a 3 channel Varian CP-3800 in-line gas chromatograph, the tubing between the reactor and the GC is heated to 200°C to prevent hydrocarbon condensation. Further details concerning the reactor setup can be found in **chapter 2**.

4.2.3 Experimental procedure

The experimental procedure is similar to that presented in **chapter 2**. The catalyst is placed at the desired position in the quartz reactor according to Figure 4.1, held in position by a small quartz wool plug. Three different catalyst positions are considered, in case 1 the complete reactor-zone (Figure 4.1) is filled with catalyst, minimizing free-volume at T>950°C. In both case 2 and 3 only the top 2 cm of the 6 cm reactor-zone is filled with catalyst, in case 2 only the reactor-zone is at 1000°C, resulting in 0.5 ml free volume at reaction-temperature, in case 3 the post-heater (Figure 4.1) is also heated to 1000°C, resulting in 2.2 ml free volume at reaction temperature downstream of the catalyst. The reactor is flushed for 10 minutes with 10 $ml \cdot min^{-1}$ N_2. The catalyst is heated with $20°C \cdot min^{-1}$ to 900°C under 10 $ml \cdot min^{-1}$ N_2. The catalyst is then exposed to 90 vol% CH_4 in N_2 at 1000 $ml \cdot g_{cat}^{-1} \cdot h^{-1}$ during two hours for activation, following the procedure of Bao pers. commun. [34]. After activation, the reactor is flushed for 10 minutes at 900°C with

N_2 10 ml·min^{-1}. The temperature is increased to 1000°C, with a heating rate 20°C·min^{-1} and the experiment is started by feeding 90 vol% CH_4 balanced with N_2. Hydrogen is added while reducing the amount of nitrogen in the feed, to keep the methane concentration as well as the total flowrate constant. The total space velocity was kept constant at 2440 ml·h^{-1}g$_{cat}$$^{-1}$ unless otherwise noted. At the end of an experiment the reactor is flushed for 10 minutes with N_2 at 10 ml·min^{-1}, after which the reactor ovens are turned off and left to cool, maintaining the N_2 flow while cooling. The catalyst is removed from the reactor at the end of an experiment and analysed for coke deposition using TGA (Mettler Toledo TGA/DSC 3+ Star System), heating the sample at 10°C·min^{-1} to 1000°C in 1:1 air/Ar, for more details refer to **chapter 2**. The online GC samples every 27 minutes and all data points are based on at least 3 measurements in steady state conditions.

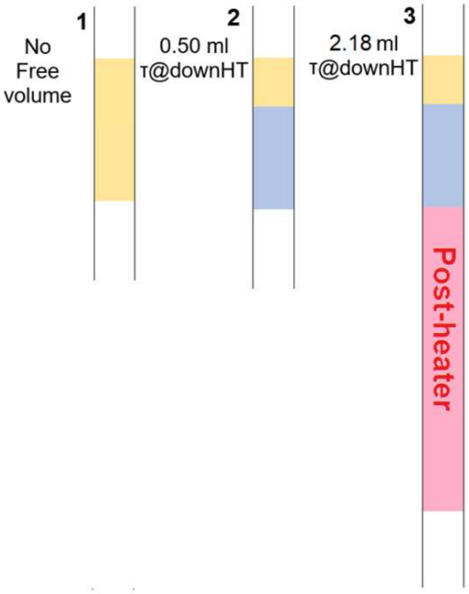

Figure 4.1 3 Positioning of the catalyst inside the 6 cm zone of oven segment 2. Case 1 operated with a catalyst bed height of 6 cm (820 mg), leaving no free volume at reaction temperature; case 2 contains a 2 cm high bed (260 mg) at the top of the 6 cm reactor-zone; case 3 is similar to situation 2, but with the post-heater at the same temperature as the reactor-zone.

Methane conversion is calculated according:

$$\xi_{CH_4} = 1 - \frac{P_{CH_4out} \cdot P_{N_2in}}{P_{CH_4in} \cdot P_{N_2out}} \qquad \text{Eq. 1}$$

$\xi_{CH_4}: conversion\ of\ methane\ (-)$
$P_X: partial\ pressure\ of\ compound\ X\ (bar)$

Methane conversion is corrected for any change in the molar flow rate based on change in the nitrogen tracer concentration according Eq. 1 [14, 35].

Selectivity is calculated on molar carbon base, corrected for any change in the molar flow rates based on the concentration of the N_2 tracer, Eq. 2 [14, 35], adjusting for stoichiometry.

$$\mathrm{S}_{C_xH_y} = \frac{x \cdot P_{C_xH_y} \cdot P_{N_2in}}{P_{N_2out} \cdot P_{CH4in} - P_{N_2in} \cdot P_{CH_4out}} \qquad \text{Eq. 2}$$

$\mathrm{S}_{C_xH_y}: selectivity\ towards\ C_xH_y\ hydrocarbon\ (-), x\ refering\ to\ the\ carbon\ number$

The total carbon-to-products-selectivity is the summation of selectivity to all products, as shown in Eq. 3.

$$S_C = \Sigma \mathrm{S}_{C_xH_y} \qquad \text{Eq. 3}$$

$S_c: total\ carbon\ to\ products\ selectivity\ (-)$

Integral calculations of conversion, selectivity and coke deposition are made in order to compare with data on the amount of deposits on the catalyst as measured with TGA. Eq. 4 calculates the total amount of carbon converted in the full experiment:

$$C_{converted\ CH_4} = \int_{t=0}^{t=14h} \phi_{CH_4in} \cdot \xi_{CH_4} \cdot \frac{1}{V_m} \qquad \text{Eq. 4}$$

$\phi_x: flow\ of\ x\ (ml \cdot \mathrm{s}^{-1})$
$V_m: molar\ volume\ at\ SPT\ (ml \cdot mol^{-1})$

The total amount of carbon that is converted to deposits during an integral experiment is calculated based on the difference in mass-balance closure as presented in Eq. 5:

$$C_{total\ in\ products} = \int_{t=0}^{t=14h} \phi_{CH_4in} \cdot \xi_{CH_4} \cdot (1 - S_c) \cdot \frac{1}{V_m} \qquad \text{Eq. 5}$$

Deposits can form either on the catalyst, named 'coke-on-catalyst' or down-stream of the catalyst-bed on the reactor-wall or in the tracing leading up to the GC, named 'deposits-downstream'. The amount of coke formed on the catalyst during a full experiment is calculated based on the weight loss during oxidation of the spent catalyst in TGA, according Eq. 6, assuming that the deposits contain exclusively C:

$$C_{deposits\ on\ catalyst} = \Delta W_{TGA} \cdot \frac{Q_{cat}}{M_C} \qquad \text{Eq. 6}$$

$M_C: molar\ mass\ of\ carbon\ (g \cdot mol^{-1})$
$\Delta W_{TGA}: the\ percentage\ of\ mass\ lost\ in\ the\ TGA\ analysis\ (-)$
$Q_{cat}: amount\ of\ catalyst\ loaded\ in\ the\ reactor\ (g)$

The remaining gap in the mass balance is attributed to formation of 'deposit' in the system downstream of the catalyst bed. Deposits include a wide array of poly aromatic hydrocarbons of C_{10+} in carbon number, as well as coke deposited on the reactor-wall downstream of the catalyst, as presented in **chapter 2**.

4.3 Results

Figure 4.2 shows the effect of dosing up to 10% hydrogen into the reactant mixture for the 3 different cases of operating the reactor, as shown in Figure 4.1. Note that Figure 4.2a and b show the same way of loading the reactor, but at different space velocity. Figure 4.2a presents results obtained with the same space velocity as used for (c) and (d), i.e. the flowrate for (b) and (c) was decreased with a factor 3. The result reported in Figure 4.2b was obtained with the same lower flowrate. For a detailed breakup of the product selectivity please refer to Figure S 4.1. As a general trend the total carbon-to-products-selectivity increases significantly when dosing small amounts of hydrogen, while at the same time methane conversion significantly decreases. The selectivity of C_2 hydrocarbons increases most significantly on H_2 addition. The carbon to product selectivity increases most in case a full catalyst bed was used, i.e. case 1 Figure 4.2a and b. A full catalyst bed causes a low aromatics selectivity, but the selectivity to aromatics increases significantly on increasing the post-catalytic volume, i.e. case 2 and 3 Figure 4.2c and d, in accordance with **chapter 2**. The addition of hydrogen causes a significant decrease in aromatic selectivity in the cases with significant post-catalytic volume as shown in Figure 4.2c and d.

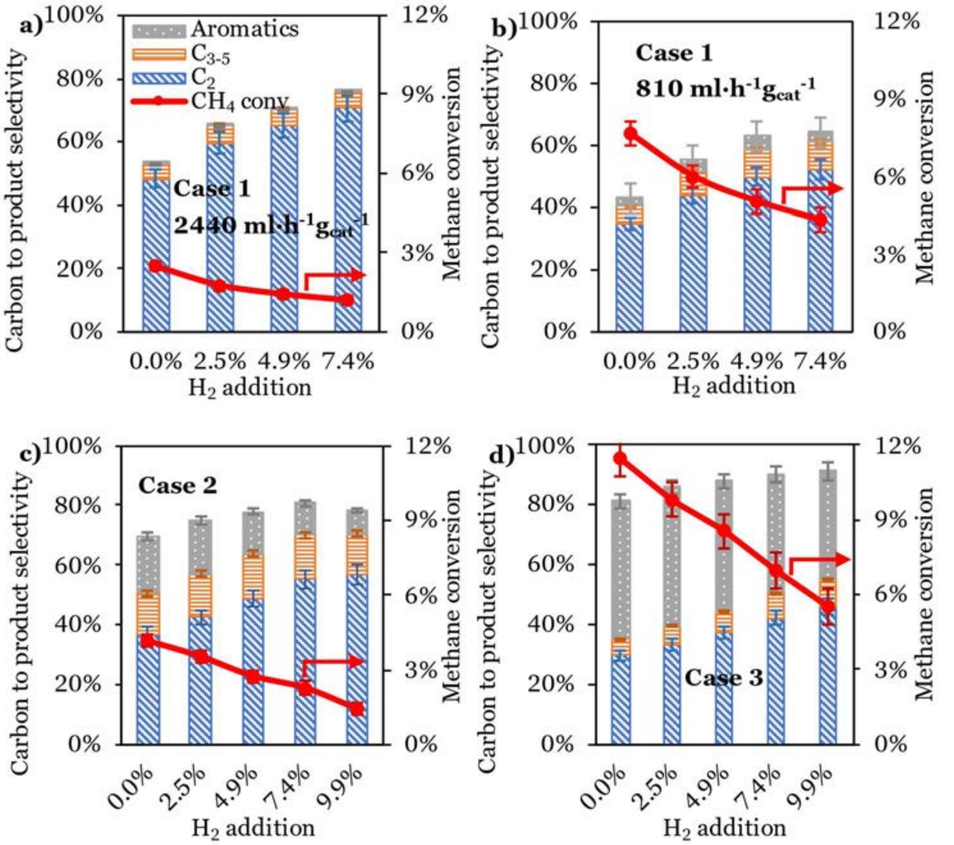

Figure 4.2: Effect of hydrogen addition on methane conversion and carbon to product selectivity, 90% CH_4, N_2 balance; reactor-zone at 1000°C and pre-heater at 400°C; (a) case 1, large catalyst bed, post-heater at 400°C, space velocity: 2440 ml·h^{-1}g$_{cat}$$^{-1}$, flowrate of 33.3 ml·min^{-1}; (b)) case 1, large catalyst bed, post-heater at 400°C, space velocity: 810 ml·h^{-1}g$_{cat}$$^{-1}$, flowrate of 11.1 ml·min^{-1}; (c) case 2, small catalyst bed, post-heater at 400°C, space velocity: 2440 ml·h^{-1}g$_{cat}$$^{-1}$, flowrate of 11.1 ml·min^{-1}; (d) case 3, small catalyst bed, post-heater at 1000°C, space velocity: 2440 ml·h^{-1}g$_{cat}$$^{-1}$, flowrate of 11.1 ml·min^{-1}.

Figure 4.3 shows the product yield distribution including the formation of deposits and coke on the catalyst for experiments with a small catalyst bed. Figure 4.3a presents results obtained with a small catalyst bed without post-heater (case 2 in Figure 4.1), corresponding to the results in Figure 4.2c. Figure 4.3b presents case 3 from Figure 4.1, corresponding to Figure 4.2d. Measurements of 6h were conducted for every hydrogen concentration of Figure 4.3a, in order to determine the quantity of coke-on-catalyst formed during 6 hours at that hydrogen concentration via TGA. It is assumed that the quantity of coke is also valid for Figure 4.3b, since both measurements are identical with respect to the catalyst bed, the only difference being the use of the post-heater. This assumption is further supported by the observation of very similar coke quantities after two experiments in which hydrogen concentration was varied, as reported in Figure 4.2. This assumption is further supported by the observation that the amount of coke on catalyst formed is very similar, as determined with TGA, during the experiment in Figure 4.2c and Figure 4.2d, respectively without and with post-heater, resulting in in 8.58 and 8.35 mg coke on catalyst respectively. The formation of deposits-downstream in Figure 4.3 is estimated based on the mass-balance. Hydrogen addition causes a decrease in yield of all products. The decrease is more significant for products with a higher carbon number, being most significant for coke formation on the catalyst. The decrease in C_2 hydrocarbon yield is very small over the range from 0-10% H_2 addition.

Reductive coke removal was attempted in a separate experiment, by first coking the catalyst at severe conditions followed by subjecting it to a pure hydrogen flow. Coke removal at reaction conditions (i.e. 1000°C, 1 atmosphere) proved impossible, due to kinetic constrains in absence of a hydrogenation catalyst [2].

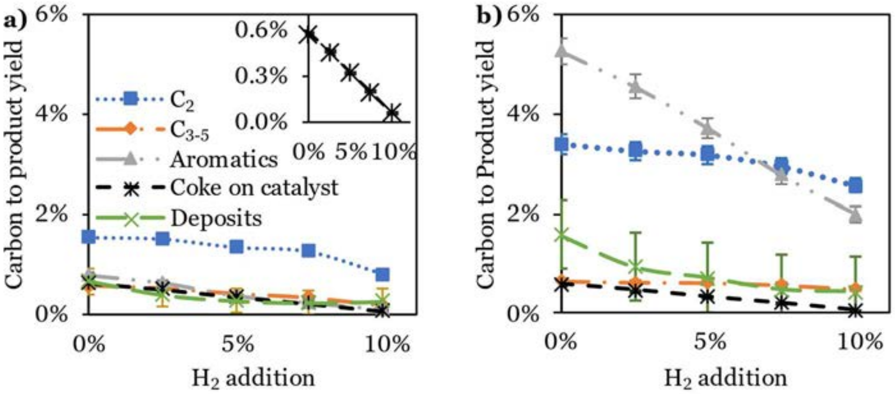

Figure 4.3: Effect of hydrogen addition on C-yield distribution over hydrocarbon products, coke-on-catalyst (TGA basis) and deposits-downstream of the catalyst (based on the mass balance); reactor-zone at 1000°C, pre-heater at 400°C, space velocity: 2440 ml·h^{-1}g$_{cat}$$^{-1}$; (a) case 2 with small catalyst bed and post-heater at 400°C; (b) case 3 with small catalyst bed with post-heater at 1000°C.

4.4 Discussion

Methane conversion is significantly reduced when hydrogen is added to the reactant mixture. Figure 4.4 shows that the relative decrease in methane conversion is slightly larger in the case of a full catalyst bed, i.e. case 1 and smaller in case of an extended free-volume residence time, i.e. case 3. On the other hand, the differences between the three cases is not very large, suggesting that the effect of hydrogen is mainly a gas phase phenomenon. Similar observations were made by Germain and Vaniscotte [30, 31] as well as Guéret and Billaud [28] in absence of catalyst, attributing the reduction in methane conversion to scavenging of the formed CH_3· radicals by hydrogen. The larger effect of hydrogen on case 1, i.e. a full catalyst bed, is likely due to the fast scavenging of the methyl radicals desorbing from the catalyst surface. The observed 50% decrease of methane conversion by adding typically 7.5% to 10% hydrogen, depending on the case (Figure 4.4), is in line with observations by Sakbodin et al. [15].

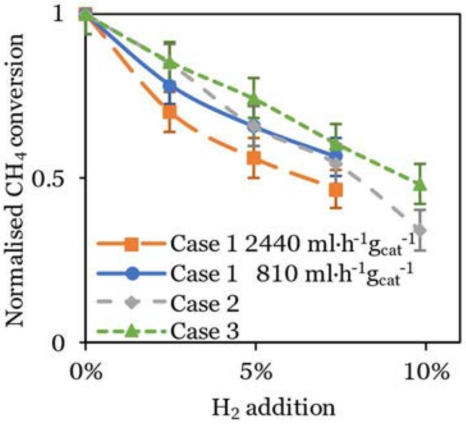

Figure 4.4: The normalized reduction in methane conversion as function of H_2 addition presented in Figure 4.2.

The selectivity distribution shifts strongly towards C_2 hydrocarbons when dosing hydrogen. As conversion decreases, this results in constant C_2 yields as shown in Figure 4.3, in agreement with Sakbodin et al. [15]. The selectivity towards C_{3-5} hydrocarbons remains unchanged on hydrogen addition, while selectivity to aromatics decreases. Figure 4.5 compares the selectivity distribution as function of methane conversion, when adding hydrogen in this work, with the effect of conversion when changing methane conversion via the space-velocity, as presented in **chapter 2**. The change in selectivity when adding hydrogen is within experimental error identical to the change in selectivity when changing conversion via the space velocity. This signifies that the change in product distribution on hydrogen addition is mainly a consequence of the lower methane conversion level. This is different from the results of Guéret and Billaud [28], reporting that the scavenging of the formed $CH_3\cdot$ radicals reduces all reaction rates involving these radicals, which would results in stabilization of C_2H_4 and slowing down the coupling reaction of C_2H_2 to C_4 and C_6 hydrocarbons. The difference is probably due to the higher temperature and H_2 partial pressure used in their work, 1300°C and 33-66 vol% H_2 respectively.

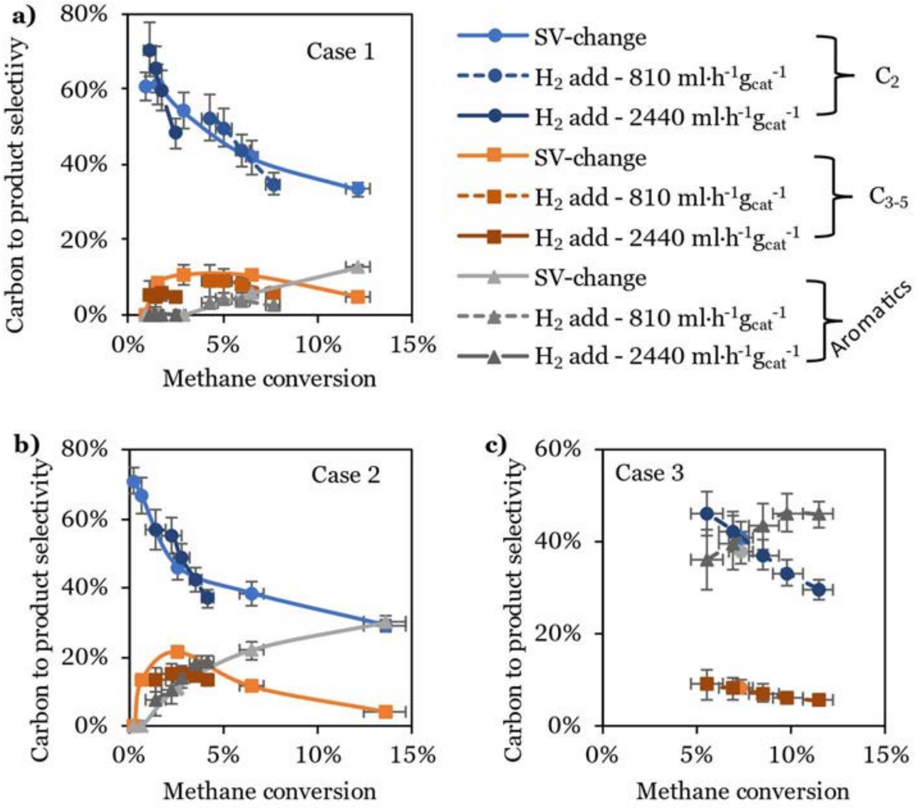

Figure 4.5: Selectivity distribution over major product groups as function of methane conversion, varying methane conversion via either hydrogen addition or space velocity increase. All data on the effect space velocity change without hydrogen addition have been adopted from **chapter 2**. Reactor-zone at 1000°C, pre-heater at 400°C; (a) case 1 with large catalyst bed at both space velocities (2440 ml·h^{-1}g$_{cat}^{-1}$ and 810 ml·h^{-1}g$_{cat}^{-1}$), post-heater at 400°C with hydrogen addition between 0-7.4 vol% and space velocity variation between 4060-240 ml·h^{-1}g$_{cat}^{-1}$ without hydrogen addition; (b) case 2, small catalyst bed, post-heater at 400°C, space velocity 2440 ml·h^{-1}g$_{cat}^{-1}$ with hydrogen addition between

0-9.9 vol% and space velocity between 13200 – 800 ml·h^{-1}g$_{cat}^{-1}$ without hydrogen addition; (c) case 3, small catalyst bed, post-heater at 1000°C, space velocity of 2440 ml·h^{-1}g$_{cat}^{-1}$ with hydrogen addition between 0-9.9 vol% and without hydrogen addition at a fixed space velocity of 4000 ml·h^{-1}g$_{cat}^{-1}$.

Hydrogen addition significantly reduces formation of coke on the catalyst, up to an order a magnitude at 10% hydrogen addition, as shown in Figure 4.3. Coke formation on the catalyst requires deep dehydrogenation of precursors, e.g. acetylene and aromatics [36], which is suppressed by increasing the hydrogen pressure. Deposit formation downstream of the catalyst, estimated based on the mass balance (Figure 4.3), decreases in a similar fashion. The coke formed on the catalyst cannot not be removed with hydrogen at reaction temperatures. Thus, the decrease in amount of coke on catalyst is caused by suppression of formation. Unfortunately, no data are available on coke-on-catalyst formation at a fixed space velocity and temperature, as these data were measured for **chapter 2**, where these conditions were varied during the experiments.

Hydrogen addition can be a potent tool to control coke formation while maintaining C_2 yield in non-oxidative coupling of methane. Hydrogen is a product of the NOCM reaction and can thus be recycled back into the reactor, which would also simplify hydrogen purification. Hydrogen recycling can thus be highly valuable for designing a non-oxidative route for direct ethylene synthesis from methane, maximizing carbon utilization.

4.5 Conclusions

The effect of hydrogen addition on coke formation and product distribution in direct catalytic coupling of methane to higher hydrocarbons was investigated. Variation in post-catalytic residence time was used to discern the effect on both catalytic as well as gas-phase reactions. It was found that hydrogen addition up 10% in the reactor feed, when operating the reactor at 1000°C, decreases methane conversion by a factor 2. This decrease in methane conversion is dominated by reactions in gas phase, caused by methyl radical scavenging by the added hydrogen. The total hydrocarbon selectivity increases significantly, although this phenomenon can be largely attributed to the decrease in methane conversion level. The addition of hydrogen also decreases the selectivity to deposits downstream of the catalyst by a factor of two while formation of coke on the catalyst decreases one order of magnitude. The yield of light olefins remained unaffected by addition of hydrogen, opening a pathway to a process running at high olefins yields while minimizing formation of coke on the catalyst, deposits downstream of the catalyst as well as higher aromatic products.

4.6 Acknowledgements

We acknowledge support from the Dutch National Science Foundation (NWO) and the industrial partners: SABIC, Sasol and BASF. We thank ing. B. Geerdink, K.J. Altena, ing. T.L.M. Velthuizen and ir. T. Lubbers for their experimental and analytical support.

Keywords: Fe©SiO2 · non-oxidative methane conversion · coke mediation · free radical reaction

4.7 Supporting Information

4.7.1 Detailed product distribution

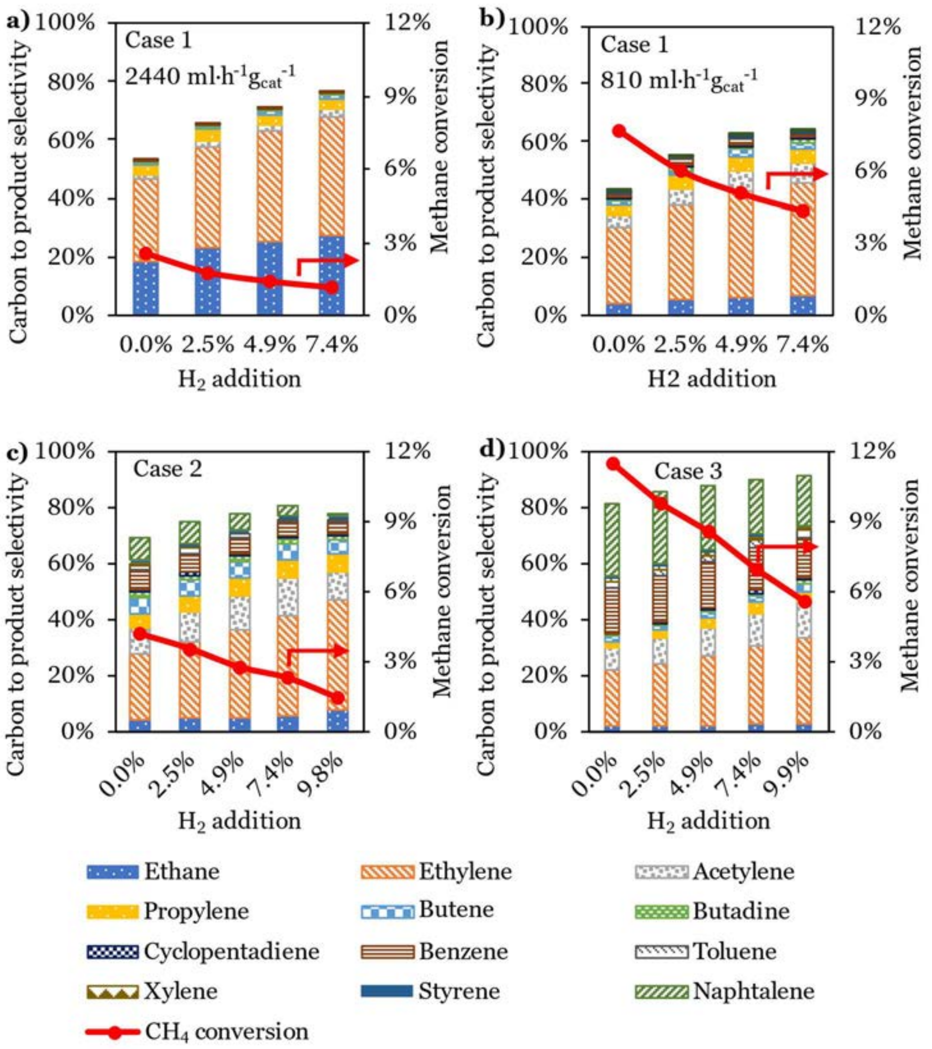

Figure S 4.1: (a) carbon to product selectivity and methane conversion when dosing small amounts of hydrogen into the reactant mixture; reactor-zone at 1000°C, pre-heater at 400°C; post-heater at 400°C for (a), (b) and (c), and 1000°C for (d); (a) and (b) present case 1, (c) presents case 2 and (d) presents case 3, Space velocity: 2440 ml·h^{-1}g$_{cat}$$^{-1}$ for (a), (c) and (d); Space velocity: 810 ml·h^{-1}g$_{cat}$$^{-1}$ for (b).

4.8 References

1. Mesters, C., *A Selection of Recent Advances in C1 Chemistry*. Annual Review of Chemical and Biomolecular Engineering, 2016. **7**: p. 223-238.

2. Karakaya, C. and R.J. Kee, *Progress in the direct catalytic conversion of methane to fuels and chemicals*. Progress in Energy and Combustion Science, 2016. **55**: p. 60-97.

3. Taifan, W. and J. Baltrusaitis, *CH4 conversion to value added products: Potential, limitations and extensions of a single step heterogeneous catalysis*. Applied Catalysis B: Environmental, 2016. **198**: p. 525–547.

4. Abbasi, H., C. Benson, T. Briselden, P. Angelini, and D. Brooks, *Roadmap for Process Heating Technology*. 2001, Industrial Heating Equipment Association.

5. Orella, M.J., Y. Román-Leshkov, and F.R. Brushett, *Emerging opportunities for electrochemical processing to enable sustainable chemical manufacturing*. Current Opinion in Chemical Engineering, 2018. **20**: p. 159-167.

6. Yeh, S., N.P. Lutsey, and N.C. Parker, *Assessment of Technologies to Meet a Low Carbon Fuel Standard*. Environmental Science & Technology, 2009. **43**(18): p. 6907-6914.

7. Wismann, S.T., J.S. Engbæk, S.B. Vendelbo, F.B. Bendixen, W.L. Eriksen, K. Aasberg-Petersen, C. Frandsen, I. Chorkendorff, and P.M. Mortensen, *Electrified methane reforming: A compact approach to greener industrial hydrogen production*. Science, 2019. **364**(6442): p. 756-759.

8. Klerk, A.d., *Fischer–Tropsch Process*, in *Kirk-Othmer Encyclopedia of Chemical Technology*. 2013. p. 1-20.

9. Wittcoff, H.A., B.G. Reuben, and J.S. Plotkin, *Chemicals from Methane*. 2012, John Wiley & Sons, Inc.

10. Sun, K., D.M. Ginosar, T. He, Y. Zhang, M. Fan, and R. Chen, *Progress in Nonoxidative Dehydroaromatization of Methane in the Last 6 Years*. Industrial & Engineering Chemistry Research, 2018. **57**: p. 178-1789.

11. Schwach, P., X. Pan, and X. Bao, *Direct Conversion of Methane to Value-Added Chemicals over Heterogeneous Catalysts: Challenges and Prospects*. Chemical Reviews, 2017. **117**: p. 8497-8520.

12. Gao, Y., L.M. Neal, D. Ding, W. Wu, C. Baroi, A. Gaffney, and F. Li, *Recent Advances in Intensified Ethylene Production – A Review*. ACS Catalysis, 2019. **9**(9): p. 8592-5621.

13. Galadima, A. and O. Muraza, *Advances in Catalyst Design for the Conversion of Methane to Aromatics: A Critical Review*. Catalysis Surveys from Asia, 2019. **23**: p. 149-170.

14. Guo, X., G. Fang, G. Li, H. Ma, H. Fan, L. Yu, C. Ma, X. Wu, D. Deng, M. Wei, D. Tan, R. Si, S. Zhang, J. Li, L. Sun, Z. Tang, X. Pan, and X. Bao, *Direct, Nonoxidative Conversion of Methane to Ethylene, Aromatics, and Hydrogen*. Science, 2014. **344**(6184): p. 616-619.

15. Sakbodin, M., Y. Wu, S.C. Oh, E.D. Wachsman, and D. Liu, *Hydrogen-Permeable Tubular Membrane Reactor: Promoting Conversion and Product Selectivity for Non-Oxidative Activation of Methane over an FeVSiO2 Catalyst*. Angewandte Chemie, 2016. **55**: p. 16149 –16152.

16. Oh, S.C., E. Schulman, J. Zhang, J. Fan, Y. Pan, J. Meng, and D. Liu, *Direct Non-Oxidative Methane Conversion in a Millisecond Catalytic Wall Reactor*. Angewandte Chemie, 2019. **58**: p. 7083-7086.

17. Han, S.J., S.W. Lee, H.W. Kim, S.K. Kim, and Y.T. Kim, *Nonoxidative Direct Conversion of Methane on Silica-Based Iron Catalysts: Effect of Catalytic Surface*. ACS Catalysis, 2019. **9**: p. 7984-7997.

18. Kim, S.K., H.W. Kim, S.J. Han, S.W. Lee, J. Shin, and Y.T. Kim, *Mechanistic and microkinetic study of non-oxidative methane coupling on a single-atom iron catalyst*. Communication Chemistry, 2020. **3**(58).

19. Nagaki, D.A., Z. Zhao, M.N.Z. Myint, I. Lengyel, A. Mamedov, C.W. Gundlach, K. Sankaranarayanan, and D. Falcone, 2018, *Method for Producing Hydrocarbons by Non-Oxidative Coupling of Methane*, US 9 , 902 , 665 B2

20. Chen, C.J. and M.H. Back, *The Thermal Decomposition of Methane. I. Kinetics of the primary decomposition to C_2H_6 +H_2; Rate constant for the Homogeneous Unimolecular Dissociation of Methane and its Pressure Dependance*. Canadian Journal of Chemistry, 1975. **53**: p. 3580-3590.

21. Chen, C.J. and M.H. Back, *The thermal decomposition of methane. II. Secondary reactions, autocatalysis and carbon formations; non-arrhenius behaviour in the reaction of CH3 with ethane*. Canadian Journal of Chemistry, 1976. **54**(54): p. 3175-3184.

22. Roscoe, J.M. and M.J. Thompson, *Thermal decomposition of Methane: Autocatalysis*. International Journal of Chemical Kinetics, 1985. **17**: p. 967-990.

23. Dean, A.M., *Detailed Kinetic Modeling of Autocatlysis in Methane Pyrolysis*. Journal of Physical Chemistry, 1990. **94**: p. 1432-1439.

24. Rokstad, O.A., O. Olsvik, and A. Holmen, *Thermal Coupling of Methane*. Natural Gas Conversion, 1991: p. 533-539.

25. Billaud, F. and C. Gueret, *Thermal decomposition of pure methane at 1263K. Experiments and mechanistic modelling*. Thermochimica Acta, 1992. **211**: p. 303-322.

26. Blekkan, E.A., R. Myrstad, O. Olsvik, and O.A. Rokstad, *Characterization of Tars and Coke formed during the Pyrolysis of Methane in a Tubular Reactor*. Carbon, 1992. **30**(4): p. 665-673.

27. Billaud, F.G. and F. Baronnet, *Thermal Coupling of Methane in a Tubular Flow Reactor: Parametric Study*. Industrial & Engineering Chemistry Research, 1993. **32**: p. 1549-1554.

28. Guéret, C. and F. Billaud, *Thermal coupling of methane: influence of hydrogen at 1330°C. Experimental and simulated results*. Journal of Analytical and Applied Pyrolysis, 1994. **29**: p. 183-205.

29. Olsvik, O., O.A. Rokstad, and A. Holmen, *Pyrolysis of Methane in the Presence of Hydrogen*. Chemical Engineering & Technology, 1995. **18**: p. 349-358.

30. Arutyunov, V.S. and V.I. Vedeneev, *Pyroylysis of methane in the temperature range 100-1700K* Russian Chemical Reviews, 1991. **60**(21): p. 1384-1396.

31. Germain, J. and C. Vaniscotte, *Craquage du Methane dans un Reacteur Tubulaire. 2. Effects de Dilution*. Bulletin de la Société Chimique de France, 1958. **3**: p. 319.

32. Kunugi, T., T. Tamura, and T. Naito, *New acetylene process uses hydrogen dilution*. Chemical Engineering Progress, 1961. **57**(43).

33. Kim, H.W., S.W. Lee, G.S. Na, S.J. Han, S.K. Kim, J.H. Shin, H. Chang, and Y.T. Kim, *Reaction condition optimization for non-oxidative conversion of methane using artificial intelligence*. Reaction Chemistry & Engineering, 2021. **6**: p. 235-243.

34. Bao, X. *personal communication to:* L. Lefferts, 2016

35. Liu, S., L. Wang, R. Ohnishi, and M. Ichikawa, *Bifunctional Catalysis of Mo/HZSM-5 in the Dehydroaromatizationof Methane to Benzene and Naphthalene XAFS/TG/DTA/MASS/FTIR Characterization and Supporting Effects*. Journal of Catalysis, 1999. **181**: p. 175-188.

36. Guéret, C., F. Billaud, B. Fixari, and P.l. Perchec, *Thermal Coupling of Methane, Experimental investigations on Coke Deposits*. Carbon, 1994. **33**(2): p. 159-170.

Chapter 5

Modelling of the catalytic initiation of methane coupling under non-oxidative conditions

---

This chapter has been submitted and under revision as:

Modelling of the catalytic initiation of methane coupling under non-oxidative conditions; R.S. Postma, P.S.F. Mendes, L. Pirro, A. Banerjee, J.W. Thybaut, L. Lefferts; Chemical Engineering Journal; 2021

Abstract

The experimentally observed interplay between catalytic activation of methane on Fe©SiO_2 and gas-phase free radical methane coupling at non-oxidative conditions is analysed by mechanistic modelling as well as by experimentation. For the modelling, an off-the shelf gas-phase model, AramcoMech 3.0, was used unaltered to keep the number of adjustable parameters as low as possible. It was complemented by surface reactions specifically accounting for methane activation to methyl radicals. The model was validated against an independent set of experimental data and exhibited good accordance. The results provided strong evidence that the Fe©SiO_2 catalyst is only involved in methane activation and not in its coupling. The model accurately captured the significant contribution of gas-phase methane conversion observed in the post-catalytic zone, indicative of gas-phase autocatalytic methane coupling. The low-activity induction period in gas-phase methane pyrolysis can effectively be overcome by adequate catalytic activation. Simulations demonstrated that the optimum catalytic conversion roughly amounts to 4% at 1000°C and 1 atm. An equivalent effect can be reached by adding 2% of ethane or ethylene to the feed. Detailed reaction-path analyses were employed to corroborate these phenomena. Gas-phase reactions were found to be very rapid at 1000°C, hence determining the product selectivity, without impact from either catalyst or C_2 hydrocarbon addition.

5.1 Introduction

Natural gas, consisting for 75-99% of methane depending on its origin [1], is considered a strategically useful source for C_{2+} hydrocarbon production [2]. The large quantity of proven natural gas reserves [3] combined with the expected decrease in crude oil production [4] leads to the prediction that natural gas will supersede crude oil as the main source of olefins and aromatics in the 21st century [5]. Industrial processes are already operated at large scale for the synthesis of fuels and base chemicals, e.g., by the Fischer-Tropsch [6] and methanol-to-olefins [7] reactions. These processes all involve multiple conversion steps, starting with methane steam reforming for synthesis gas (CO and H_2) production [8] and are only viable at large installed capacities [9]. Direct methane coupling to higher hydrocarbons has therefore been a highly researched topic in the chemical community for over a century [10, 11].

Early research focused on non-catalytic conversion of methane at high temperatures [10, 12], i.e. ‘methane pyrolysis’. The main drawbacks of methane pyrolysis are these high operation temperatures (950-1700°C) and/or long residence times (6-15s @ 1000°C) required to achieve significant methane conversion [10, 13]. These challenges stem from the high thermal stability of methane [14] as well as the pronounced endothermicity of the dehydrogenative coupling reactions [15]. Another important issue in methane pyrolysis is the significant carbon deposition at high methane conversion [16-18]. Starting in the 1970s, a tremendous effort was made to understand the highly complex free radical reactions involved in methane pyrolysis. Chen et al. [19, 20] reported on the reactions responsible for the formation of the primary product, ethane, and secondary product, ethylene. Their model showed great compliance with experimental data at low methane conversion. Roscoe and Thompson continued this investigation [21] and were the first to propose a mechanism explaining the autocatalysis phenomenon, in which the methane conversion rate increases sharply after a so-called induction period. These authors attributed this phenomenon to the coupling reaction involving ethylene, acetylene and hydrocarbons with more than two C-atoms. This model was further developed by Dean [22], who showed the importance of the reversibility of the reactions proposed by Roscoe and Thompson [21]. This work was continued in the 90s by the research group of Holmen [15, 23-25] as well by Billaud and Guéret [14, 26-29]. The culmination of this work has been summarized in a model by Matheu et al. [30], which gave extra attention to the contributions of propyne, allene and fulvene in the autocatalytic cycle. Oxidative coupling of methane (OCM) [31, 32] as well as methane dehydroaromatization (MDA) [33, 34] offer alternative ways to overcome the challenges encountered in methane pyrolysis. Although the product yield and single pass conversion in these processes are still too low for industrial relevance.

In 2014, Guo et al. [35] reported a Fe/SiO_2 catalyst capable of coupling methane non-oxidatively to ethylene and aromatics at temperatures above 950°C. This catalyst is referred to as Fe©SiO_2 to denote the lattice confined single atom nature of the iron. Most crucially, these authors reported the absence of coke formation, even at high methane conversion (48%), and catalyst stability during up to 60h. These performance figures proved difficult to reproduce [36-40], nevertheless these latter publications contributed to better understanding of the catalytic system. The sole function of the Fe©SiO_2 catalyst in the overall reaction mechanism is the formation of $CH_3\cdot$ radicals, while all other reactions, including the coupling reaction, occur in the gas-phase [35]. Another DFT study by Kim et al. [39] confirms this assessment, although these authors propose that direct acetylene formation on the catalyst is theoretically also possible. Liu et al. [41] propose that C-C coupling to directly form ethylene can occur on the Fe©SiO_2 catalyst. The work by Toraman et al. [42], for the first time, combined a detailed surface mechanism with an extensive propene pyrolysis gas-phase model from Wang et al. [43] to elucidate the interplay between heterogeneously catalysed and gas-phase reactions. These authors propose that the Fe©SiO_2 catalyst predominantly forms ethylene, with catalytic $CH_3\cdot$ radical generation playing only a minor role. Thus far no experimental evidence has been provided to prove either the catalytic $CH_3\cdot$ or C_2H_4 formation hypothesis.

The significance of gas-phase reactions was experimentally validated in **chapters 2-4** as well as in a patent filed by SABIC [44]. It was shown that the catalyst is exclusively required for initiation of the coupling reaction, after which post-catalytic residence time is the predominant factor in propagating the coupling reaction, leading to significant methane conversion in gas-phase. A long residence time inside the catalyst bed and residence time at reaction temperature upstream of the catalyst bed were both detrimental to the total hydrocarbon selectivity, enhancing formation of deposits, without significantly increasing methane conversion. The addition of ethane and ethylene can significantly increase the methane conversion rate [45, 46] as discussed in **chapter 3**.

The present work provides a quantitative assessment of the interplay between the initiation of the reaction on the Fe©SiO_2 catalyst and the subsequent gas-phase coupling reactions, focusing for the first time on catalytic $CH_3\cdot$ radical generation via an in-house developed microkinetic model in combination with an existing gas-phase microkinetic model. Emphasis is put on the impact of the catalytic reactions on the rate of gas-phase reactions, involving a detailed quantification of catalytic initiation and gas-phase propagation of the NOCM reaction. Reaction-path analysis is used to explain the experimental product distribution. The model is used to maximize reactor productivity by optimizing the catalyst-free volume and catalyst contact time. Lastly, the effect of addition of ethane and ethylene on the methane coupling reaction is elucidated.

5.2 Methodology

5.2.1 Catalyst synthesis

The Fe©SiO_2 catalyst is synthesized according to the method described by Guo et al. [35]. The Fe_2SiO_4 precursor was synthesized according to the method described by DeAngelis et al. [47], which is then mixed with high purity quartz and milled overnight in a planetary ball mill. The resulting powder is fused for 6h in air at 1700°C. The resulting slab is crushed and sieved to the desired particle size and leached for 2h in 0.5M HNO_3. Any further details as well as catalyst characterization has been reported in **chapter 2**. Two particle size fractions are used, namely 100-250 μm and 250-500 μm. The data obtained with the 100-250 μm fraction is used for fitting of the model, see below, because it meets all criteria for intrinsic kinetics measurements following the method described by Berger [48], i.e. mass and heat transport are not limiting and ideal plug-flow behaviour is obtained. The 250-500 μm fraction is used for validation and further analysis of the gas-phase-catalyst interaction, because this is the fraction used in **chapters 2-4**. Note that 250-500 μm fraction is predicted to have a slight radial temperature profile smaller than 3 K.

5.2.2 Kinetic measurements

Catalytic tests are carried out in a quartz tube, ID 4mm, which is placed in a 3-zone oven with thermal insulation between each zone, described in detail in **chapter 2**. The catalyst is inserted into the desired position in the quartz reactor, as displayed in Figure 5.1a. The catalyst is held in place by small quartz wool plugs. The catalyst is first exposed to 90 vol% CH_4 in N_2 at 1000 $ml \cdot g_{cat}^{-1} \cdot h^{-1}$ for two hours for activation purposes, following the procedure of Bao pers. commun. [49], to carburize the active site forming a FeC_2Si site [35]. After activation, the temperature is increased to the desired reaction temperature, in the range between 950°C and 1100°C. A blank measurement following the same procedure as catalytic measurements was performed to ensure that the reactor is exposed to the same pre-treatment prior to measuring. Blank measurements are performed in an empty reactor tube, on similar note, the free volume presented in Figure 5.1a refers to gaseous volume. No bed-diluent is used due to the activity of any surface area at reaction conditions [16, 38]. Product mixtures are analysed using a three-channel Varian CP3800 online gas chromatograph (GC). Any further details concerning the setup, experimental procedures and calculation methods can be found in **chapter 2**. The temperature profile considered in the model is based on the measured temperature profile in the lab-setup (Figure S 5.1).

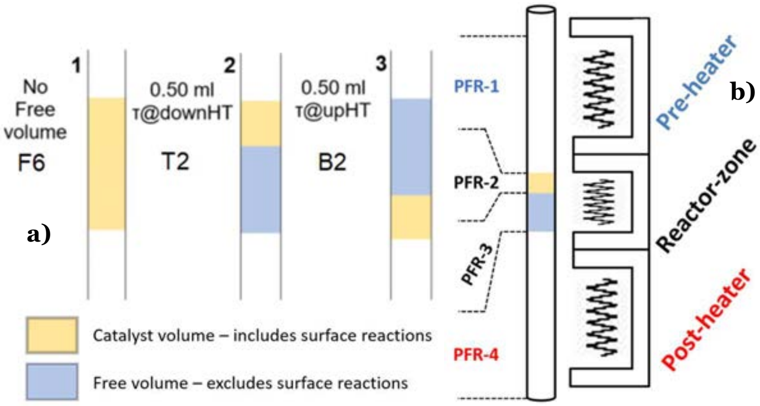

Figure 5.1: (a) Three different catalyst loadings considered for the model: (1) a reactor-zone completely filled with catalyst (820 mg), from now on called 'F6' fully filled for 6 cm; (2) a medium catalyst bed (260 mg) at the top of the reactor-zone, named 'T2' top-filled 2 cm; (3) a medium catalyst bed (260 mg) at the bottom of the reactor zone, named 'B2' bottom-filled 2 cm. (b) the differentiation the reactor modelled by the four PFRs.

5.2.3 Model development

A top-down approach [50] has been chosen for the model development due to the system's complexity. Firstly, the physical description of the reactor is generated, due to the significant impact of the temperature profile on the reaction as shown in **chapter 2**. Afterwards the gas-phase model is selected based on its compliance with the blank experiment and lastly the catalytic surface reactions are included.

5.2.3.1 Reactor model

ChemKin-Pro 2020 R2 was used to perform the calculations. The constructed reactor model comprises four consecutive zones, simulated as plug-flow-reactors (PFR), see Figure 5.1b. The first and last zones model the pre-heater and post-heater respectively and exclusively consider gas-phase reactions. Zones 2 and 3 simulate the reactor-zone, by splitting it into a part with catalyst where surface reactions contribute, and a part without catalyst considering exclusively gas-phase reactions. The different catalyst positions shown in Figure 5.1a can be accurately described in this way. The temperature profile presented in (Figure S 5.1) was used as the temperature profile in the four zones, with a discretization point every 1 cm, in order to account for reactions occurring during heating and quenching of the gas stream.

5.2.3.2 Gas-phase model

Five gas-phase models, available in literature, i.e. Matheu et al. [30], Aramcomech 3.0 [51], Nuigmech 1.1 [52], Gudiyella et al. [53] and Chu et al. [54] were evaluated based on their compliance with the blank experiments (see supporting information S.2). AramcoMech 3.0 [51] was chosen due to its accurate description of methane autocatalysis, the accurate prediction of the product range as well as the trends in methane conversion and product selectivity.

The two major shortcomings of the AramcoMech 3.0 model in reproducing the experimental observations are situated in the ethylene selectivity, which is significantly overpredicted, and in the selectivity towards the 2-ring aromatics, naphthalene and indene. The overprediction of the ethylene is characteristic of the AramcoMech 3.0 model. Concerning the 2-ring aromatics, the model seems to replace the naphthalene ($C_{10}H_8$) selectivity with indene (C_9H_8), which is actually not detected at all. To address this discrepancy, it is assumed that indene predicted by the model represents naphthalene observed in the measurements, including a correction for the difference in number of carbon atoms in the molecules. The parity diagrams presented in SI Figure S.5 show that the gas-phase kinetic model predicts the selectivity to the major products well.

5.2.3.3 Surface reaction model

The catalytic surface reactions are based on the work of Guo et al. [35] and are schematically presented in Figure 5.2. In the first reaction step (I^a), dissociative adsorption of methane forms a surface CH_3 species bonded to the iron site and hydrogen species bonded to one of the carbon atoms. In the second step (II^a), the CH_3 species desorbs yielding a gas-phase $CH_3\cdot$ radical, liberating the iron active site for another methane molecule to adsorb in a repetition of step one. After the 2nd $CH_3\cdot$ radical has desorbed in step II^b, the two hydrogen species combine and desorb as dihydrogen in step III. Table 5.1 shows the activation energies of these elementary surface reactions involved in methane activation as adopted from Guo et al. [35]. It is assumed that the dissociative adsorptions of methane to CH_3 species on the catalyst surface are kinetically relevant, because they have the highest activation barrier and are the only endothermic reactions in the cycle [35].

The pre-exponential factors of the rate constants are fitted manually by running simulations considering the whole reactor, including the gas-phase model and temperature profile, as discussed above, to match the experimental data measured with the 100-250 μm particle size fraction at 1000°C. An average catalytic surface area per reactor length is used to account for the quantity of catalyst. The catalyst particles are assumed to be dense and perfectly spherical with an diameter of 175 µm and a packing density of 0.6, resulting in a surface area of 129 mm^2 per mm reactor length.

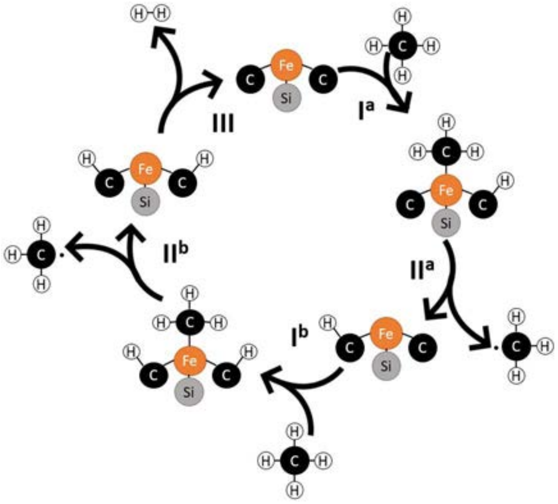

Figure 5.2: Schematic overview of the conversion of methane to $CH_3\cdot$ radicals and hydrogen over the Fe©SiC_2 active site, adapted from [35].

Table 5.1: Catalytic reactions considered in the activation of methane over the Fe(c)SiO_2 catalyst [35, 55].

	Catalytic reactions	**E_a (kJ/mol) [35]**	**Fitted k0**	**Kinetic relevance**
I^a	$CH_4(g) + FeC_2\ast \rightarrow CH_3Fe\ast HC\ast C\ast$	**280**	**$6.77\cdot10^{17}$**	Relevant
II^a	$CH_3Fe\ast HC\ast C\ast \rightarrow CH_3\cdot(g) + Fe\ast HC\ast C\ast$	**224**	**$1.55\cdot10^{13}$**	Not relevant
I^b	$CH_4(g) + Fe\ast HC\ast C\ast \rightarrow CH_3Fe\ast HC\ast HC\ast$	**298**	**$3.36\cdot10^{18}$**	Relevant
II^b	$CH_3Fe\ast HC\ast HC\ast \rightarrow CH_3\cdot(g) + Fe\ast HC\ast HC\ast$	**211**	**$4.50\cdot10^{12}$**	Not relevant
III	$Fe\ast HC\ast HC\ast \rightarrow H_2(g) + FeC_2\ast$	**155**	**$5.30\cdot10^{10}$**	Not relevant

5.3 Results and Discussion

5.3.1 Model validation

The pre-exponential factors of the rate constants of the catalytic surface reactions resulting from the fit are shown in Table 5.1. Figure 5.3 shows the parity plots comparing the developed model against the experimental data used for fitting. It is clear from Figure 5.3a and c that the model accurately predicts the methane conversion when varying either the residence time at constant temperature, or the temperature at constant residence time.

The slight deviation at higher conversion can be attributed to the absence of coke formation in the model, which in reality will partly block active sites, thus limiting conversion. The product selectivity presented in Figure 5.3b and d also shows reasonable agreement, although the selectivity to renowned coke precursor molecules such as acetylene, benzene and naphthalene are overpredicted due to the absence of coking in the model. Ethylene selectivity is also overpredicted as consequence of the AramcoMech 3.0 model, as discussed before.

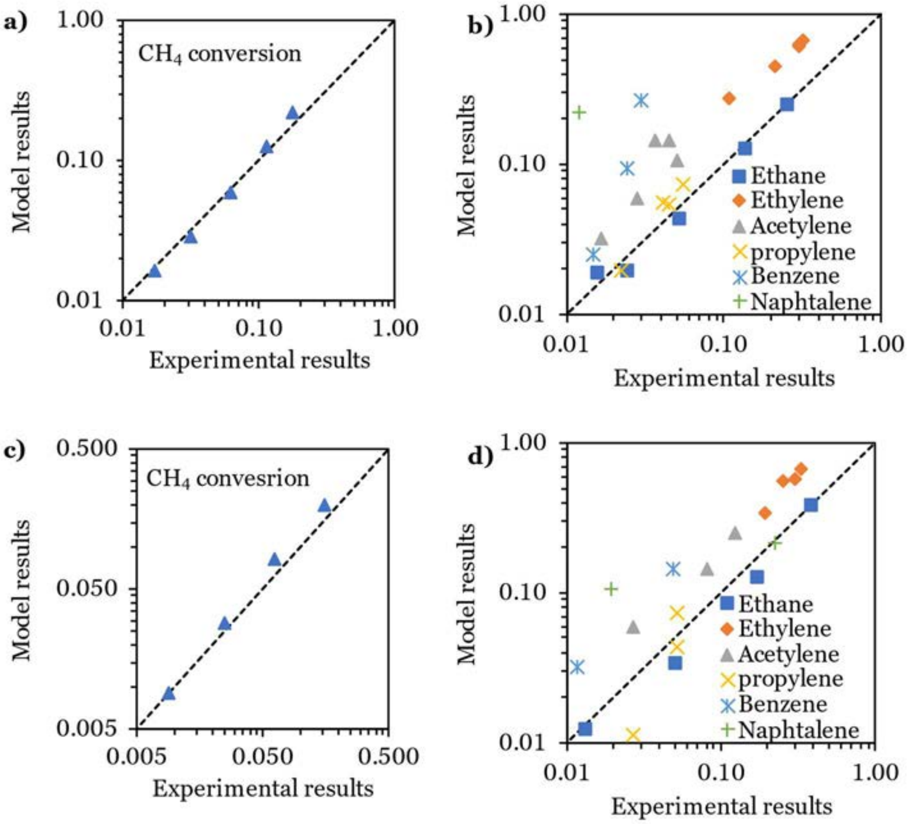

Figure 5.3: Parity plots comparing the results of the model with the experimental results measured with the reactor completely filled with with 840 mg Fe©SiO_2 100-250 µm (Figure 5.1a); pre-heater and post-heater at 400°C; (a) Methane conversion and (b) product selectivity to major hydrocarbons when changing the SV between 240-4000 ml·g_{cat}^{-1}·h^{-1} with the reactor-zone at 1000°C; (c) Methane conversion and (d) product selectivity to major hydrocarbons when changing the temperature of the reactor zone between 950-1100°C, at constant SV of 2400 ml· g_{cat}^{-1}·h^{-1}.

Chapters 2-4 used a larger Fe©SiO$_2$ particle size fraction: 250-500 µm. Validation of the model was also performed against the data from this set. The active surface area per length of the catalyst bed was reduced in the model from 129 mm^2·mm^{-1} to 60 mm^2·mm^{-1}, accounting for the difference in average particle size in the two data sets. The results of the validation are shown in Figure 5.4. It is evident that the effect of varying space velocity and temperature (Figure 5.4a) is also accurately described for the larger particle size fraction. The product selectivity is predicted even better for the larger particle fraction, due to the lower coke selectivity observed with the higher particle size fraction.

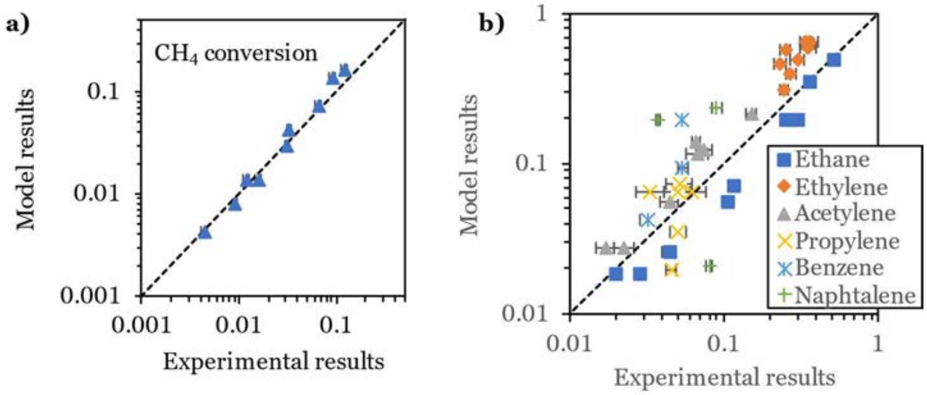

Figure 5.4: Parity plots comparing the results of the model with the experimental results measured with the complete reactor zone (Figure 5.1b) filled with 840 mg Fe©SiO$_2$ 250-500 µm; pre-heater and post-heater at 400°C (Figure 5.1a), shown in **chapter 2** (a) Methane conversion and (b) product selectivity to major hydrocarbons when changing the SV between 240-4000 ml·g$_{cat}^{-1}$·h^{-1}with the reactor-zone at 1000°C and when changing the temperature of the reactor zone between 950-1100°C, at constant SV of 2400 ml·g$_{cat}^{-1}$·h^{-1}.

5.3.2 Catalytic initiation of the reaction

Gas-phase reactions contribute significantly to both product formation as well as methane conversion [42]. Simulations are performed evaluating the effect of free volume at 1000°C upstream and downstream of the catalyst bed, to decouple the gas-phase reactions from the catalytic reactions. The effect of free volume upstream or downstream of the catalyst (Figure 5.1) is accurately predicted by the model, as shown in Figure 5.5a. Product selectivity is also predicted reasonably well as shown in Figure 5.5c and d. Figure 5.5b shows the modelled effect of total gas-flowrate on methane conversion with free volume upstream or downstream of the catalyst bed, using the full reactor model. The inverse of the flowrate on the x-axis is proportional to both residence time inside the catalyst bed as well as the residence time in the gas-phase upstream or downstream of the catalyst. At high flowrate, i.e. short residence times in both free volume and catalyst bed, there is no difference between extended gas-phase residence time upstream (B2) or downstream (T2) of the catalyst bed. At lower flowrates, however, the conversion with extended gas-phase residence time downstream of the catalyst bed (T2) becomes significantly higher compared to extended gas-phase residence time upstream (B2), at the same flowrate and total (gas-phase + catalyst) residence times, as shown in Figure 5.5b. These results are in agreement with experimental results in **chapter 2**. The significant increase in gas-phase activity in the post-catalytic volume is most likely caused by catalytic initiation of the free-radical coupling reaction.

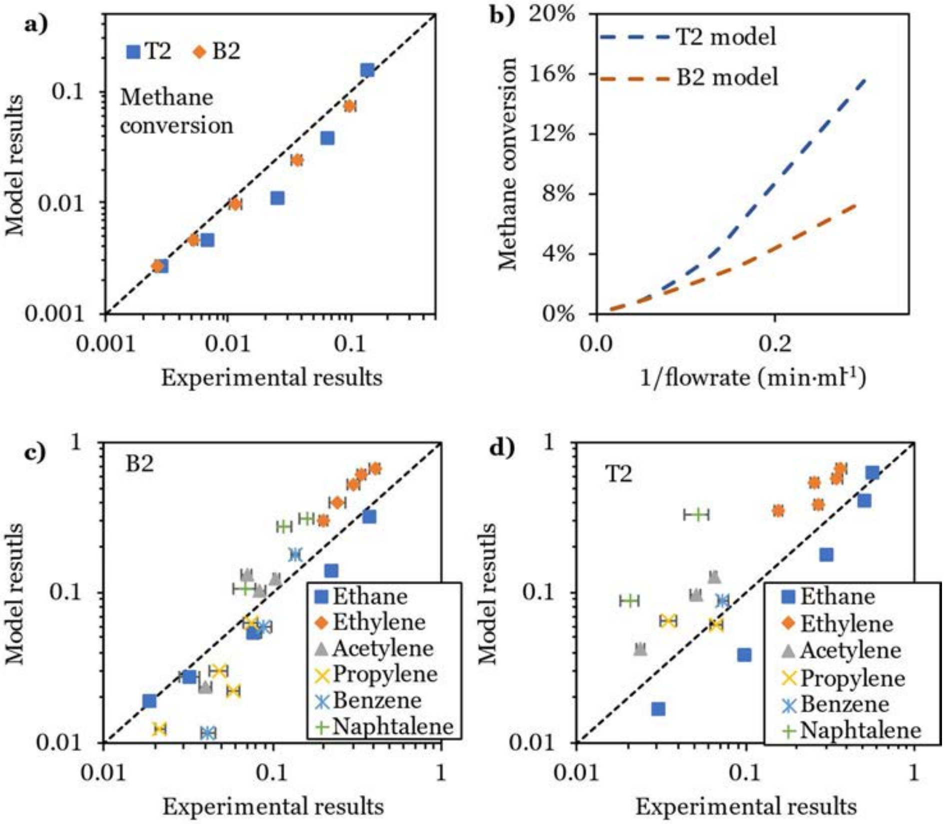

Figure 5.5: (a) parity plot of model results compared to experimental results from **chapter 2** concerning the effect of extended gas-phase residence time at 1000°C upstream (B2) and downstream (T2) of the catalyst and (b) Modelled methane conversion for the T2 and B2 case as function of inverse total gas-flowrate; (c) &(d): parity plot comparing the selectivity of model to experimental selectivity from **chapter 2** concerning the effect of extended gas-phase residence time at 1000°C for the (a) B2 and (b) T2 cases; Reactor-zone at

1000°C, pre-heater and post-heater at 400°C; Fe©SiO_2 250-500 µm; 260 mg catalyst and 0.50 ml free volume either upstream (B2) or downstream (T2) of the catalyst.

5.3.3 Contribution of methane conversion in the gas-phase

To simplify the analysis and better understand the catalyst role, an idealized system, i.e. assuming an uniform reactor temperature of 1000°C and no conversion in the volume upstream of the catalyst, was studied. Figure 5.6a shows the effect of residence time (analogous to 1/flowrate in Figure 5.6b) on methane conversion, equivalent to an axial profile, for the T2 system in which the catalyst contributes via catalytic initiation. Figure 5.6b shows the same in absence of catalyst, i.e. with gas-phase reactions only. The T2 system (Figure 5.6a) shows significantly more conversion in the free-volume section downstream than the empty reactor (Figure 5.6b) at the same residence time; note the different scales of the time axis in Figures 6a and 6b.

In order to assess the impact of the catalyst in the gas-phase reactions, the conversion at the end of the catalyst bed (about 4%, indicated with the dotted line) is matched with the same conversion in the blank experiment (in practice, by combining graphs in Figure 5.6a and b in Figure 5.6c, with the x-axis of Figure 5.6a shifted to the right). The same method is used for all graphs in Figure 5.6c and d as well as Figure 5.7. Figure 5.6c and d and Figure 5.7 thus show the conversion and concentration profiles as function of residence time for the T2 case as well as the empty reactor.

The simulation of the empty reactor shown in Figure 5.6b shows two regimes: methane conversion rate at short residence time is small and increases with increasing residence time and conversion, typical for autocatalysis. Figure 5.6c shows that the catalyst effectively shortens the induction phase, while not influencing the conversion profile in the post-catalytic free-volume. This was further verified by varying the catalyst residence time (see Figure 6d). Note that this would also be the case if the conversion in the catalyst bed would be increased by using a catalyst more active in methyl radical formation. Figure 6d also indicates that the influence of the catalyst on conversion is the largest when aiming at roughly 4% conversion. This is analysed in more detail mathematically in supporting information S.5. Lower conversion in the catalyst bed would lead to a significantly larger reactor because more volume downstream of the catalyst would be required, whereas the marginal gain in reactor volume becomes very small with higher conversion in the catalyst bed. However, the main disadvantage of a larger catalyst bed is increased formation of carbonaceous deposits as shown in **chapter 2**.

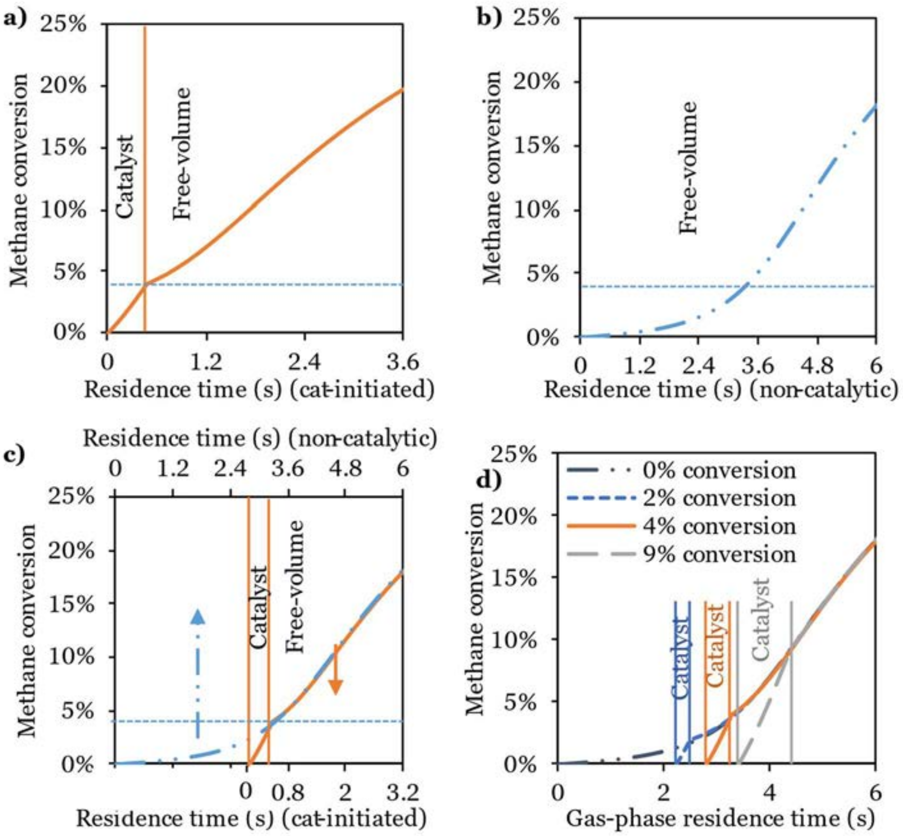

Figure 5.6: (a) An idealized simulation of the 'T2' case, uniform 1000°C and no residence time upstream of the catalyst, achieving 4% CH_4 conversion in the catalyst bed (b) Idealized empty reactor simulation, uniform 1000°C (c) A comparison between the simulation shown in (a) and (b), showing a catalyst initiated system and a pure gas-phase system at a constant temperature of 1000°C (d) shows the effect of the amount of catalyst, achieving 0% (blank), 2% (0.32 s catalyst residence time), 4% (optimal, 0.48 s catalyst residence time) or 9% (0.63 s catalyst residence time) CH_4 conversion in the catalyst bed, on the conversion curve in the post-catalytic volume. Note that the residence time on the x-axis refers only the free-volume curve the residence times for the 3 catalytic cases starts at zero at each respective left catalyst boundary; the vertical lines denote the residence in the catalyst bed. The horizontal blue dotted line denotes 4% conversion.

5.3.4 Mechanistic evaluation of acceleration in methane conversion rate

Figure 5.7 shows the concentration profiles of important intermediate species and products as function of residence time, similar to Figure 5.6 for methane conversion. C_1, C_2 and H· species are the main contributors to the chemistry involved in gas-phase methane activation [21, 22]. The concentration profiles as function of residence time in the empty reactor as shown in Figure 5.7 are obviously based on the reaction mechanism and microkinetic model for gas-phase methane auto-catalysis according to the AramcoMech 3.0 model [51]. A schematic overview of this reaction cycle can be found in Figure 5.8. The following section details this mechanism with respect to the concentration profiles for the empty reactor in Figure 5.7.

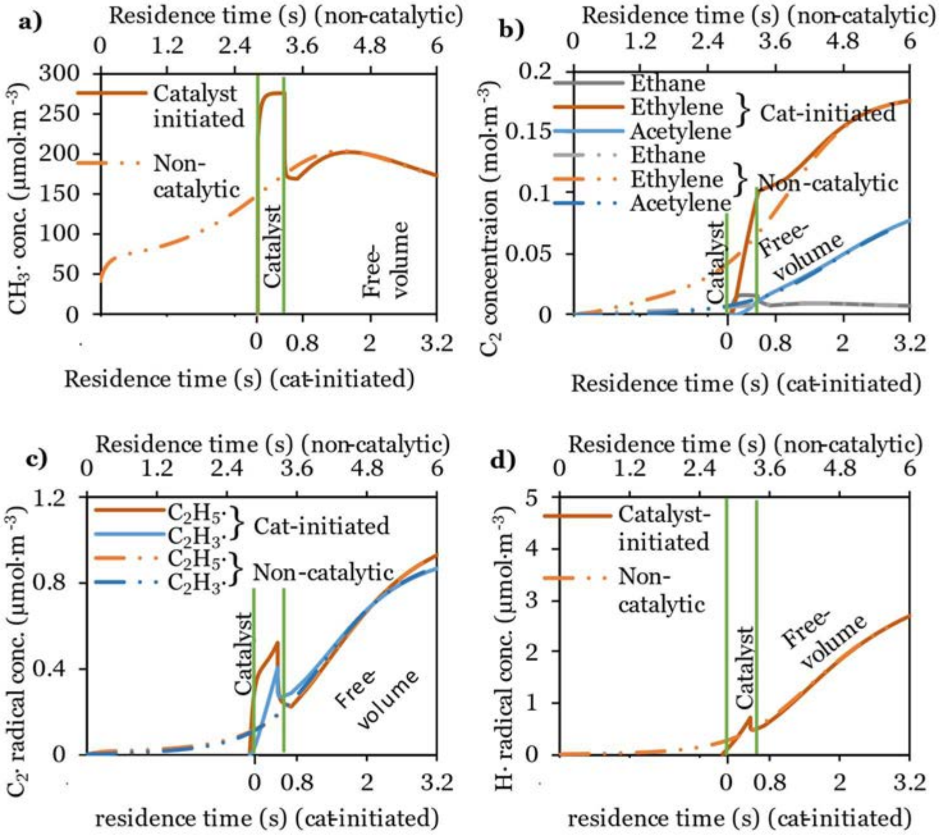

Figure 5.7: concentration profiles of (a) CH_3· radicals (b) C_2 hydrocarbon (c) C_2H_5· and C_2H_3· radicals (d) H· radical; concerning the catalyst-initiated system and a pure gas-phase system at a constant temperature of 1000°C as in Figure 5.6.

Firstly, the profiles in Figure 5.7 will be discussed in the light of gas-phase chemistry based on earlier publications [19-22] (see reaction 1 to reaction 10 below), followed by a discussion on the interplay between catalytic and gas-phase reactions. In the induction phase, i.e. at low methane conversion, and in absence of catalysts slow heterogeneous activation of methane (reaction 1) on the reactor-wall or impurities dominates. The heterogeneous nature is included in the model in reaction 1 by the (m) active site species, because spontaneous gas-phase methane dissociation is highly improbable. This is not essential though for our discussion, the low rate of reaction 1 is much more important. Initially each H· radical formed via reaction 1 will activate another methane molecule via reaction 2, causing equal rates of reactions 1 and 2 during the induction phase. H· radical concentration stays low even though CH_3· radical concentration increases significantly, as seen in Figure 5.7a and d, due to the rapid consumption of H· radicals in reaction 2. The CH_3· radicals combine to form ethane (reaction 3); subsequently, ethane reacts with another CH_3· radical, forming an C_2H_5· radical and CH_4 (react. 4). This reaction is fast, demonstrated by the low concentration of ethane in Figure 5.7b, while both C_2H_5· radical and ethylene concentration keep increasing (Figure 5.7b and c). C_2H_5· radicals are very reactive and readily dissociate to ethylene and a H· radical (Eq. 5), explaining the rapid and immediate increase in ethylene seen in simulations in Figure 5.7b in absence of catalyst. Similar to ethane, ethylene can dehydrogenate further towards acetylene following reactions 6 and 7 with C_2H_3· as reactive intermediary radical. Note that the consecutive dehydrogenation of C_2 hydrocarbons, shown in Eq. 4-7, has no effect on methane conversion, since for every produced H· radical (reactions 5 and 7) another methane molecule is generated from a CH_3· radical (reactions 4 and 6). Ethylene is significantly less reactive than ethane and CH_3· and C_2H_5· radicals as is apparent from Figure 5.7b, showing significant higher concentrations of ethylene and acetylene compared to ethane.

Note that, even though H· radicals do not selectively react with methane, reaction with methane is dominant because of the high methane concentration compared with all other molecules and radicals. For the autocatalysis to take effect, a net formation of H· radicals needs to occur [21, 22], to activate methane via reaction 2. All reactions generating these surplus H· radicals require C-C coupling to higher hydrocarbons. Reaction 1 is an exception, but this reaction is slow and constant in gas phase in absence of catalyst. Acetylene exclusively reacts to higher hydrocarbons according to the model, whereas in reality it is also subject to dehydrogenation resulting in coke formation as shown in **chapter 2**. The formed C_{3+} hydrocarbons are very reactive under reaction conditions and spontaneously dehydrogenate, yielding even more hydrogen radicals, an example of which is shown in reaction 10.

$CH_4 + (m) \rightarrow CH_3\cdot\ + H\cdot\ + (m)$ Reaction 1

$CH_4 + H\cdot \rightleftharpoons CH_3\cdot\ + H_2$ Reaction 2

$2CH_3\cdot \rightleftharpoons C_2H_6$ Reaction 3

$C_2H_6 + CH_3\cdot \rightleftharpoons C_2H_5\cdot + CH_4$ Reaction 4

$C_2H_5\cdot \rightarrow C_2H_4 + H\cdot$ Reaction 5

$C_2H_4 + CH_3\cdot \rightleftharpoons C_2H_3\cdot + CH_4$ Reaction 6

$C_2H_3\cdot \rightarrow C_2H_2 + H\cdot$ Reaction 7

$C_2H_4 + CH_3\cdot \rightleftharpoons C_3H_6 + H\cdot$ Reaction 8

$C_2H_4 + C_2H_{5-3}\cdot \rightleftharpoons C_4H_{8-6} + H\cdot$ Reaction 9

$C_3H_6 \rightleftharpoons C_3H_5\cdot + H\cdot$ Reaction 10

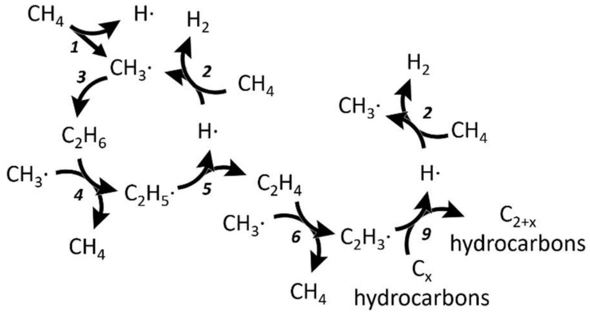

Figure 5.8: The proposed autocatalytic cycle for accelerated methane activation in the gas phase, reactions numbered following the reaction scheme presented above.

The catalytic reaction generating methyl-radicals, discussed at length in section 5.3.3 and shown in Figure 5.2 and Table 5.1, is equivalent to the combination of reactions 1 and 2 of the gas-phase mechanism discussed above. The catalytic formation of methyl radicals appears much faster than the slow heterogenous activation of methane in absence of catalyst, in line with the observation that presence of the catalyst causes significantly increased concentration of $CH_3\cdot$ radicals (Figure 5.7a). Also, the concentrations of all C_2 species increase significantly in presence of catalyst (Figure 5.7b and c), caused by rapid coupling of the generated methyl radicals to ethane in gas phase (reaction 3). The high ethylene concentration achieved inside the catalyst bed is due to the quick consecutive reactions 4 and 5. H· radical concentration remains low in the catalyst bed (Figure 5.7d), due to both the requirement for C_2 hydrocarbons to undergo C-C coupling as well as the high reactivity of H· radicals with methane as discussed for the gas-phase system. As a reminder, chemisorbed hydrogen stays on the active site until it can desorb as a di-hydrogen molecule (Figure 5.2, [35]).

The concentration of all species presented in Figure 5.7a-d for the catalyst initiated system converge to the same concentration as observed in simulations of the empty reactor (i.e. pure gas phase). This effect is very rapid for all radical species (Figure 5.7a, c and d) due to their high reactivity, whereas the effect is slower for ethylene (Figure 5.7b).

5.3.5 Effect of C_2 addition

Ethane and ethylene addition is also known to shorten the induction phase during non-oxidative methane coupling [45] and **chapter 3**. Experimentally, the increase in methane conversion rate was maximal at 2% ethane or ethylene addition in a non-catalytic system [46] and **chapter 3**. Parity plots comparing the model predictions and experimental data for an empty reactor, including the reactor temperature profile as discussed in the experimental section, have been included in Figure S 5.7a. The model accurately predicts the trends on C_2 addition (Figure S 5.7b), although the model underpredicts the effect on methane conversion.

Simulations of an idealized system, i.e. empty reactor completely isothermal at 1000°C, have been performed to investigate the influence of C_2 species in the auto-catalytic cycle discussed before. Figure 5.9a shows the effect of residence time on methane conversion when adding 2 vol% ethane, ethylene and acetylene [12]. The significant effect of C_2 addition is evident when compared with the simulation for pure methane. In order to understand compare the effect of C_2 addition to that of catalyst initiation, in Figure 5.9b the conversion curve according the simulation for pure methane is translated down by 4% conversion and to the left by 3.3 s residence time, analogous to Figure 5.6c, i.e. redefining the origin of the simulation with respect to pure-methane in Figure 5.9a. The conversion axes are thus different for the pure-methane and C_2 addition curves in Figure 5.9b. There is a remarkable overlap of the translated conversion curve for pure-methane with the conversion curve in presence of ethane as well as ethylene. This implies that C_2 addition can effectively overcome the induction period and directly cause a reaction rate equal to pure methane in the auto-catalytic regime. Note as a qualitative observation that converting methane at 4% corresponds stoichiometrically to the addition of 2% C_2 hydrocarbons.

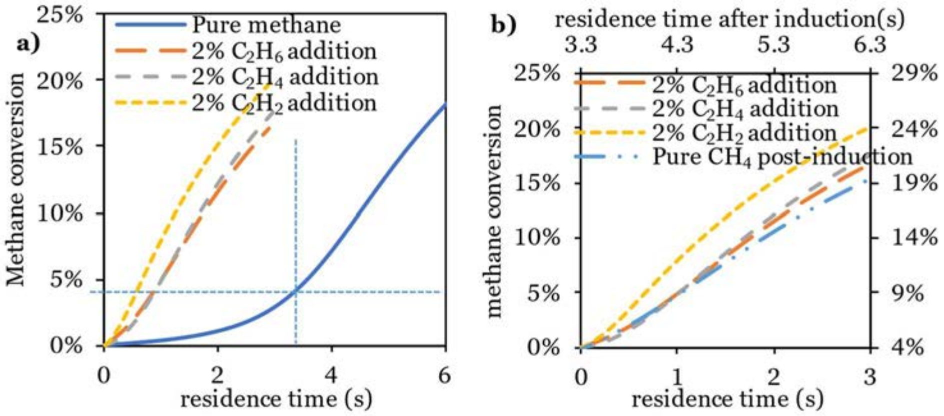

Figure 5.9: (a) Modelled methane conversion when dosing 2% C_2 into the reactant mixture in a gas-phase system compared to the pure methane simulation (b) The same modelled methane conversion when dosing 2% C_2 as shown in Figure 5.9a, but with the conversion curve for pure methane translated by 3.3 s residence time to the left and 4% conversion downwards, to make the 4% conversion point at the origin, the 2nd x and y-axis refer to the pure-methane after induction curve. All simulations done for an empty reactor system at a constant 1000°C.

When ethane is added, the excess of ethane molecules reverses reaction 3, i.e. ethane dissociates into $CH_3\cdot$ radicals instead of recombining, shown by the immediate high $CH_3\cdot$ concentration (in Figure S 5.8a). The $CH_3\cdot$ radicals attack ethane via reaction 4, which following reaction 5, results in the instant formation of a surplus of $H\cdot$ radicals that can activate methane (Figure S 5.8d). In contrast, ethylene and acetylene do not spontaneously decompose and, initially, methane conversion via reaction 1 is required to activate ethylene and acetylene. Methyl radicals formed in reaction 1 convert ethylene to either $C_2H_3\cdot$ radicals via reaction 6, or follow the reactions shown in Eq. 6-9, causing the acceleration in methane conversion by forming $H\cdot$ radicals as discussed in section 5.3.4. About 0.5 s residence time is required for both ethylene and acetylene to increase the $H\cdot$ radical concentration to level beyond the corresponding $H\cdot$ radical concentration for pure methane in the auto-catalysis regime (Figure S 5.8d). In short, a pathway to significantly increase the concentration of $H\cdot$ radicals via reactions with ethylene and acetylene is responsible for the acceleration. Notwithstanding, overall the concentration profiles of radicals and C_2 hydrocarbons (in Figure S 5.8) show similar trends to pure methane, except for slightly higher C_2 hydrocarbon and radical concentration. The more significant effect predicted by the model for acetylene addition (Figure 5.9) can be mechanistically explained by the conversion of acetylene to higher hydrocarbons, thus releasing hydrogen radicals and accelerating methane conversion. However, in reality, a significant fraction of acetylene reacts to coke [12], which is not included in the model.

The product distributions as well as the radical concentration profiles in case of either C_2 addition or in the presence of catalyst, forming $CH_3\cdot$ radicals, are identical. This makes it impossible to distinguish between catalytic $CH_3\cdot$ radicals generation as proposed by Guo et al. [35], versus direct ethylene formation as proposed by Toraman et al. [42].

5.4 Conclusions

The interplay between catalytic and gas-phase reactions in non-oxidative coupling of methane was investigated. Via kinetic modelling, the considered surface reactions for a Fe©SiO_2 catalyst, involving exclusively conversion of methane to CH_3· radicals, can accurately predict the activity and selectivity in catalytic NOCM, when used in combination with a comprehensive gas-phase reaction mechanism from literature, i.e. the AramcoMech 3.0 model. The activation barriers proposed in literature accurately describe the experimental data in the temperature range between 950-1100°C. The model predicts the significant contribution of the post-catalyst volume to methane conversion.

The catalyst enhances the formation of methyl radicals, thereby speeding up the formation of C_2 hydrocarbons via gas-phase reactions. The presence of C_2 hydrocarbons enables fast formation of H· radicals, which is the key radical responsible for autocatalytic conversion of methane. The induction period observed in the gas phase can be prevented not only by using a catalyst, but also by adding C_2 hydrocarbons in the feed, without any catalyst. The catalyst has no significant impact on the chemistry downstream of the catalyst bed. All concentrations of intermediate species and products become similar to the concentrations obtained in absence of catalyst. The gas-phase reactions involving C_{2+} hydrocarbons are fast at 1000°C determining the product distribution, while catalyst or C_2 addition exclusively enhance the initiation of the NOCM reaction, allowing for optimal reactor design. These conclusions show the potential of methane and ethane co-pyrolysis for conversion of natural gas to olefins and aromatics.

5.5 Acknowledgements

We acknowledge support from the Dutch National Science Foundation (NWO) and the industrial partners: SABIC, Sasol and BASF. We thank ing. B. Geerdink, K.J. Altena, ing. T.L.M. Velthuizen and ir. T. Lubbers for their experimental and analytical support. We furthermore would like to thank Prof. dr. ir. K.M. van Geem and Y. Cheng for their input during discussions, Prof. dr. W.H. Green and dr. D.M. Matheu for providing the Chemkin models and last but not least Dr. ir. J.B,W. Kok and the Thermal Engineering group at the University of Twente for providing acces to the Chemkin software.

Keywords: Fe©SiO2 · non-oxidative methane conversion · ethane pyrolysis · microkinetic modelling

5.6 Supporting Information

5.6.1 S.1 Reactor temperature profile

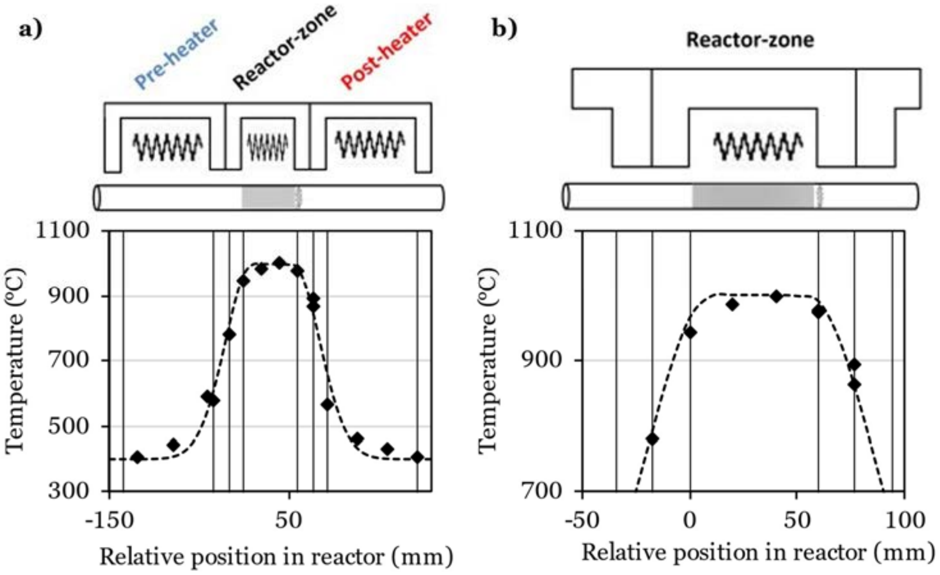

Figure S 5.1: Temperature profile inside the reactor measured with an empty reactor tube b) zoom in on Figure S 5.1a; gas-flow rate of 10 ml·min^{-1} N_2; Vertical bars represent the insulating layers between the 3 different zones. --◆-- Pre- and post-heater at 400 °C; reactor-zone at 1000 °C; The points are the measured values, the line represents the fit used in the model. The data are identical to Figure 2.1 in **chapter 2.**

5.6.2 S.2 Evaluation of different gas-phase models

The choice of gas-phase model is highly important for the accurate evaluation of the catalyst-free volume interaction. Five separate gas-phase models available in open literature were evaluated:

- AramcoMech3.0 [51]
- NuigMech1.1 [52]
- The gas-phase model compiled by Matheu et al. [30] based on the work by Dean [22]
- The gas-phase model used by Gudiyella et al. [53] for modelling methane flame pyrolysis to acetylene
- The gas-phase model used by Chu et al. [54] for modelling methane flame pyrolysis to aromatics

No model was found to be a perfect fit to the blank experiments. The results of each model evaluated under isothermal conditions (i.e. 1000°C) are presented in Figure S 5.2 for methane conversion and Figure S 5.3 for selectivity to major products. One of the main requirements for the model was an accurate portrayal of the methane autocatalytic cycle involving C_2 hydrocarbons at methane conversion between 2-10%, as described in the main text. This eliminated the NuigMech1.1 [52] model and the model published by Matheu et al. [30], as these showed a linear trend in methane conversion with respect to residence time, as can be seen in Figure S 5.2. Both AramcoMech3.0 [51] as well as the model published by Gudiyella et al. [53] and Chu et al. [54] are valid options. The choice for AramcoMech3.0 was made because it is the culmination of many different modelling works involving a large variety of hydrocarbon pyrolysis reactions.

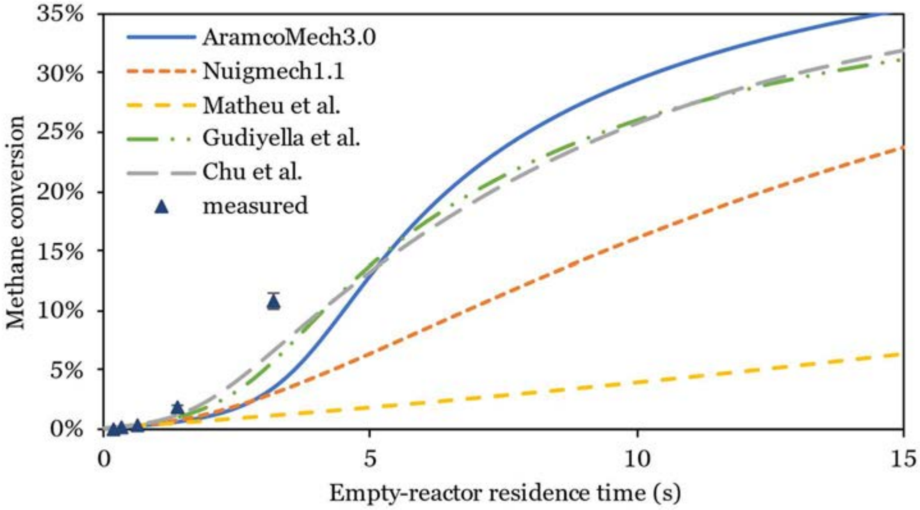

Figure S 5.2: Methane conversion comparison of various gas-phase models in a non-catalytic isothermal reactor as function of residence time.

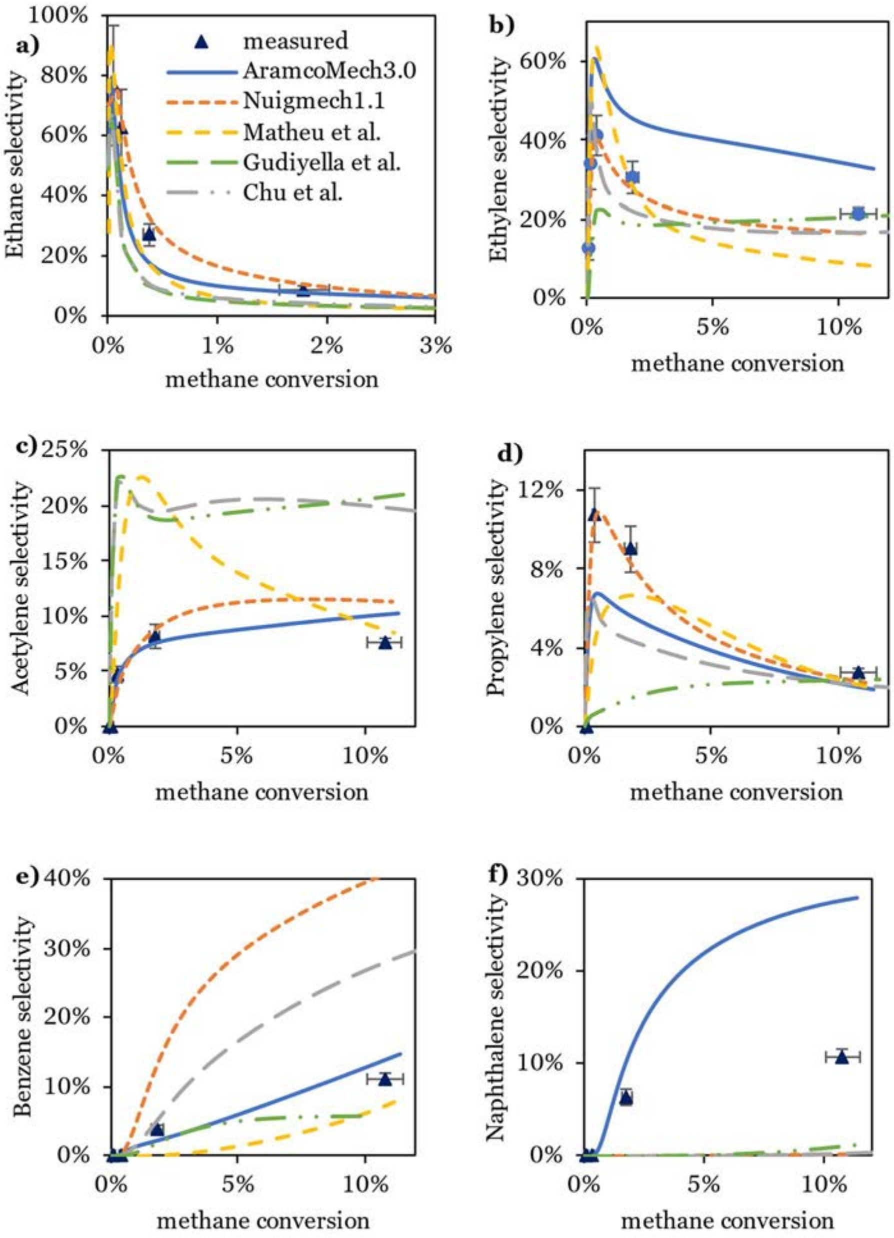

Figure S 5.3: Selectivity comparison between the various gas-phase models with the measured data points included.

5.6.3 S.3 Evaluation of AramcoMech 3.0 compared to experimental data

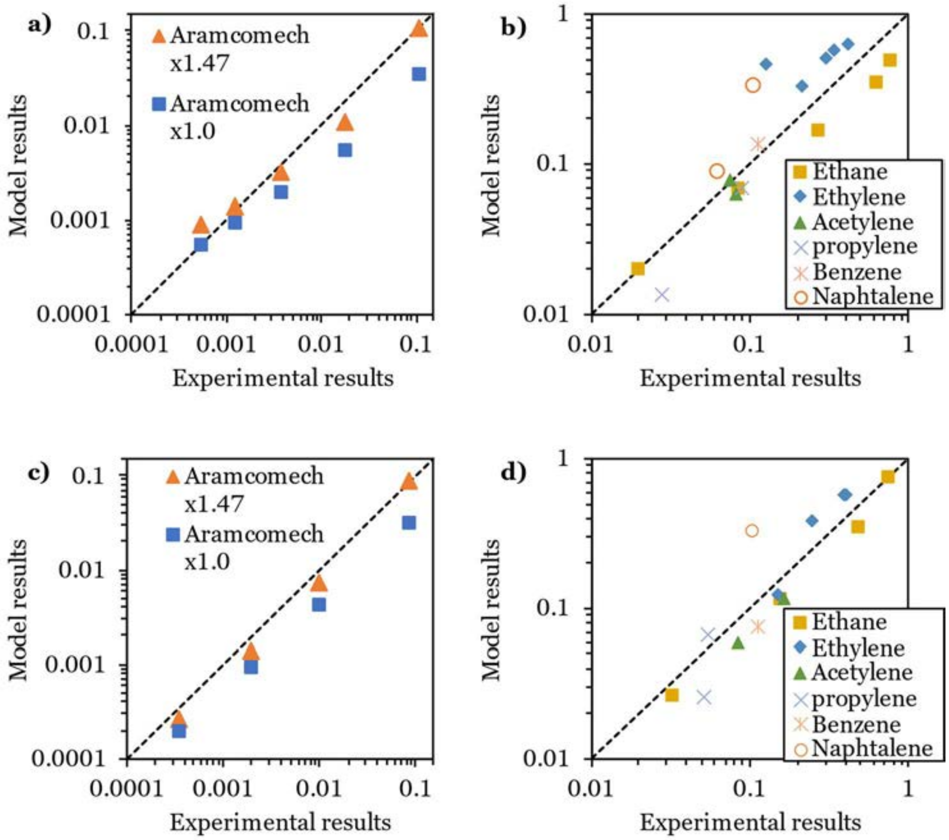

Figure S 5.4: Parity plots comparing the results of the AramcoMech 3.0 model against the experimental results in a blank reactor, (a) Methane conversion, (b) selectivity towards major hydrocarbon products; measured using a quartz tube containing no catalyst at flowrates between 3.3-55.5 ml·min^{-1}, reaction zone at 1000° C; pre- and post-heater at 400°C; (c) Methane conversion and (d) product selectivity to major hydrocarbons when changing the temperature of the reactor zone between 950-1100°C, at constant flowrate of 33.3 ml·min^{-1}.

5.6.4 S.4 Additional data concerning model development

5.6.4.1 Methane conversion in a blank system

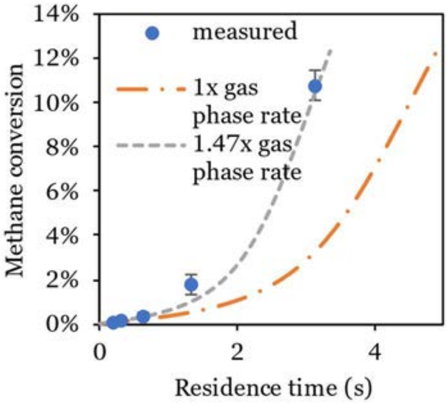

Figure S 5.5: The modelled methane conversion using either 1x or 1.47x the gas-phase reaction rate compared to experimental data measured in a blank-reactor.

The methane conversion as function of residence time for a blank experiment is slightly underpredicted by the AramcoMech 3.0 model as shown in Figure S 5.5. This could be corrected by multiplying the gas-phase reaction rates with a factor of 1.47 in ChemKin, resulting in a good fit of conversion as function of residence time as shown in Figure S 5.5. This difference is probably due to underestimation of homolytic methane activation in the gas-phase model, considering that practical methane activation is enhanced by non-idealities, such as activity of the reactor wall and trace contaminations in the gas mixture. Note however that the gas-phase reaction rate factor has however been kept at 1.0 to prevent the overestimation of other, faster, gas-phase reactions. Thus the homolytic methane activation reaction is slightly underestimate, resulting in an overall overestimation of the induction period.

5.6.4.2 Fitting of the pre-exponential factors and the resulting surface coverage

The pre-exponential factors of the non-rate-limiting steps are adjusted to the lowest value that still prevented significant concentration of these species on the active sites (i.e. <0.1% occupation) as can be seen in Table S 5.1, the value of 0.1% is arbitrarily chosen.

Table S 5.1: Average surface coverage on the Fe active side predicted by the surface reaction model.

Catalyst intermediate species	Average surface coverage @1000°C conv < 10%
Fe (empty site)	**47.4%**
Fe-H-CH_3	**0.1%**
Fe-H	**52.4%**
Fe-H-H-CH_3	**0.1%**
Fe-H-H	**0.0%**

5.6.5 Analysis of the methane conversion profile in a modelled blank reactor

Figure 5.6 reports methane conversion in a blank system, as well as the conversion rate and change in conversion rate (i.e. acceleration in methane conversion). The acceleration in methane conversion rate is a good measure for the gas-phase reaction activity. Both conversion-rate and conversion-acceleration have been plotted alongside the normal conversion curve in Figure S 5.6 The maximum effectiveness of the gas-phase activation is reached when the acceleration in rate is maximum. Note that the methane conversion rate will keep on increasing until the acceleration becomes negative. Non-catalytic methane pyrolysis can be divided in three regimes: firstly an induction period, where methane conversion is slow and mainly determined by low levels of activation via impurities in the gas-feed or in the reactor material used. The gas-phase AramcoMech3.0 model accounts for this activity by including a heterogenous reaction for methane activation. Note that the rate of methane activation in the induction period is dependent on the system used, i.e. purity of the methane feed and internal surface area in the reactor. A clear acceleration is observed once sufficient methane conversion is achieved, due to the activation of methane by the formed products as discussed in the main text, this regime is known as the autocatalytic regime [21, 22]. The third regime concerns the reduction in methane conversion rate when approaching thermodynamic equilibrium [14]. The maximum acceleration in gas-phase methane conversion-rate is achieved at 3.3 s residence time, and

4% methane conversion, as shown by the lines added to the Figure 5.6. This shows that for the AramcoMech3.0 model the maximum effectiveness of the autocatalytic cycle is achieve at 4% methane conversion at 1000°C.

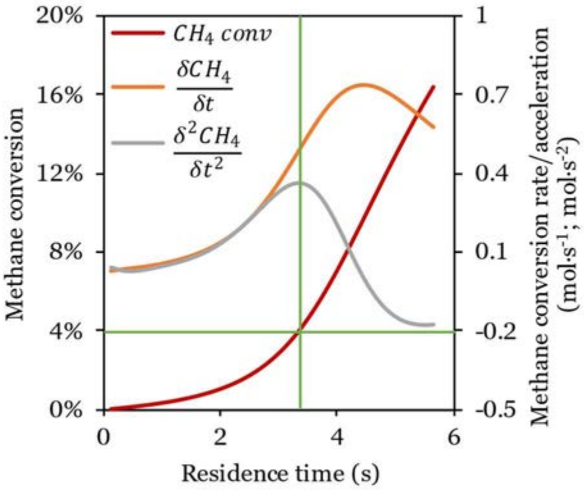

Figure S 5.6: Analysis of the methane conversion rate and conversion acceleration in a purely gas-phase initiated system, based on the AramcoMech 3.0 gas-phase model.

5.6.6 S.6 Data concerning C_2 addition with respect to concentration profiles, C_2 conversion and product selectivity

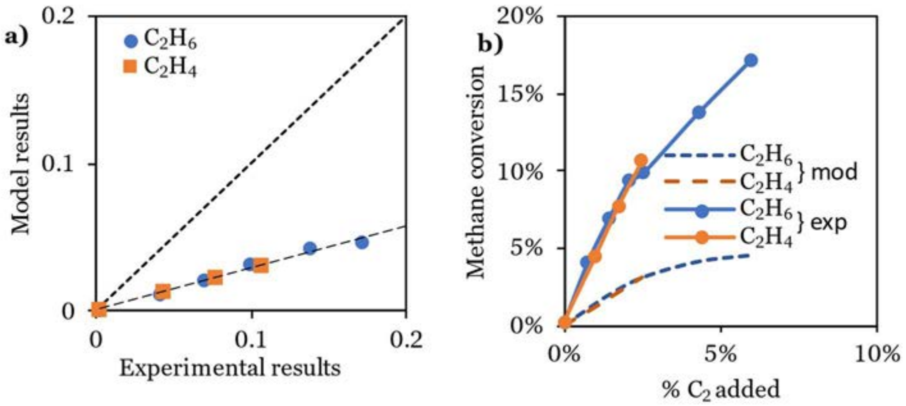

Figure S 5.7: (a) Parity plot of modelled methane conversion in an empty reactor, considering the full temperature profile compared to experimental methane conversion from **chapter 3** concerning the effect of C_2 addition on non-catalytic methane pyrolysis at 1000°C; (b) modelled methane conversion as function of C_2 addition and measured methane conversion as function of C_2 addition, adopted from **chapter 3**, for an empty reactor, considering the full temperature profile.

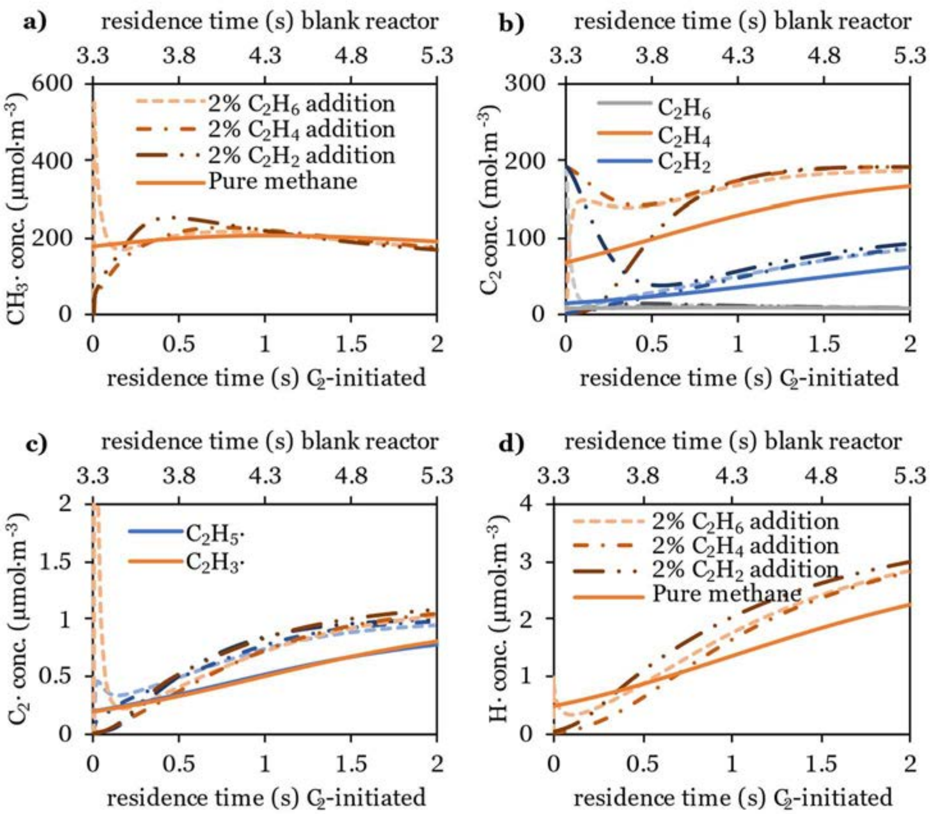

Figure S 5.8: Concentration profiles of (a) $CH_3\cdot$ radicals (b) C_2 hydrocarbons (c) $C_2H_5\cdot$ and $C_2H_3\cdot$ radicals (d) H· radical; concerning initiation by 2% C_2 addition compared to pure methane at a constant temperature of 1000°C as shown in Figure 5.9 in the main text; analogous to Figure 5.7 in the main text for a catalyst initiated system; note the legend style in terms of grey-scale and line-style from figures a and d should also be used the legends in b and d.

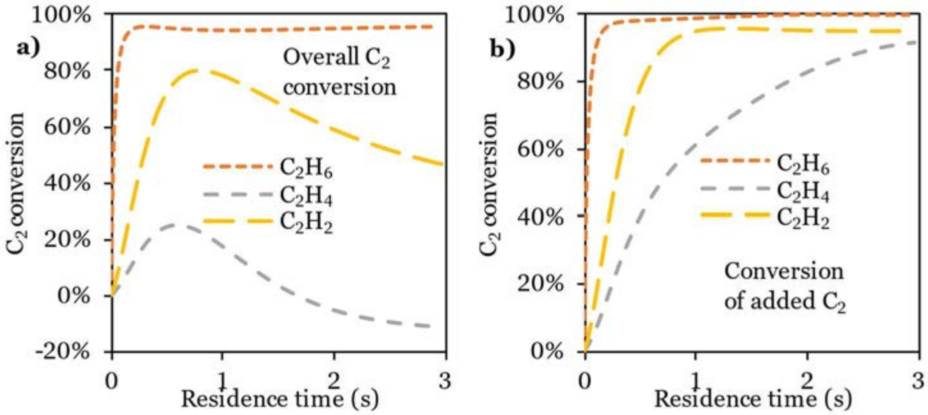

Figure S 5.9: Overall conversion of the added C_2 hydrocarbon according to the AramcoMech 3.0 gas-phase model.

Figure S 5.9a shows the modelled conversion of the added C_2 compounds as function of residence time. Note that these values are a combination of conversion towards other compounds as well as formation from the CH_4 feedstock. Figure S 5.9b shows the conversion of the added C_2 species corrected for the production from CH_4, to get an accurate picture of the true consumption. These values are obtained by subtracting the concentration of the added C_2 compound in a simulation with pure methane at the corresponding methane conversion level. From Figure S 5.9a it is clear that nearly all ethane is converted instantly, which is logical when looking at the reaction 3. Acetylene converts significantly slower than ethane, but still significantly quicker than ethylene.

5.7 References

1. Hammer, G., T. Lübcke, R. Kettner, M.R. Pillarella, H. Recknagel, A. Commichau, H.J. Neumann, and B. Paczynska-Lahme, *Natural Gas*, in *Ullmann's Encyclopedia of Industrial Chemistry*. 2006.

2. Schwach, P., X. Pan, and X. Bao, *Direct Conversion of Methane to Value-Added Chemicals over Heterogeneous Catalysts: Challenges and Prospects*. Chemical Reviews, 2017. **117**: p. 8497-8520.

3. BP plc, *BP Statistical Review of World Energy 2019*. 2019.

4. Caineng, Z., Z. Qun, Z. Guosheng, and X. Bo, *Energy revolution: From a fossil energy era to a new energy era*. Natural Gas Industry B, 2016. **3**: p. 1-11.

5. Taifan, W. and J. Baltrusaitis, *CH4 conversion to value added products: Potential, limitations and extensions of a single step heterogeneous catalysis*. Applied Catalysis B: Environmental, 2016. **198**: p. 525–547.

6. Klerk, A.d., *Fischer–Tropsch Process*, in *Kirk-Othmer Encyclopedia of Chemical Technology*. 2013. p. 1-20.

7. Tian, P., Y. Wei, M. Ye, and Z. Liu, *Methanol to Olefins (MTO): From Fundamentals to Commercialization*. ACS Catalysis, 2015. **5**(3): p. 1922-1938.

8. Abdulrasheed, A., A.A. Jalil, Y. Gambo, M. Ibrahim, H.U. Hambali, and M.Y.S. Hamid, *A review on catalyst development for dry reforming of methane to syngas: Recent advances*. Renewable and Sustainable Energy Reviews, 2019. **108**: p. 175-193.

9. Mohajerani, S., A. Kumar, and A.O. Oni, *A techno-economic assessment of gas-to-liquid and coal-to-liquid plants through the development of scale factors*. Energy, 2018. **150**: p. 681-693.

10. Arutyunov, V.S. and V.I. Vedeneev, *Pyroylysis of methane in the temperature range 100-1700K* Russian Chemical Reviews, 1991. **60**(21): p. 1384-1396.

11. Slater, W.E., *The influence of different surfaces on the decomposition of methane*. Journal of the Chemical Society, Transactions, 1916. **109**: p. 160-164.

12. Khan, M.S. and B.L. Crynes, *Survey of Recent Methane Pyrolysis Literature*. Industrial & Engineering Chemistry, 1970. **62**(10): p. 54-59.

13. Choudhary, T.V., E. Aksoylu, and D.W. Goodman, *Nonoxidative Activation of Methane*. Catalysis Reviews, 2003. **45**(1): p. 151-203.

14. Guéret, C., M. Daroux, and F. Billaud, *Methane pyrolysis: thermodynamics*. Chemical Engineering Science, 1997. **52**(5): p. 815-827.

15. Holmen, A., O. Olsvikb, and O.A. Rokstad, *Pyrolysis of natural gas: chemistry and process concepts*. Fuel processing technology, 1995. **42**: p. 249-267.

16. Zwet, G.P.v.d., P.A.J.M. Hendriks, and R.A.v. Santen, *Pyrolysis of methane and the role of surface area*. catalysis Today, 1989. **4**: p. 365-369.

17. Blekkan, E.A., R. Myrstad, O. Olsvik, and O.A. Rokstad, *Characterization of Tars and Coke formed during the Pyrolysis of Methane in a Tubular Reactor*. Carbon, 1992. **30**(4): p. 665-673.

18. Palmer, H.B., J. Lahaye, and K.C. Hou, *On the Kinetics and Mechanism of the Thermal Decomposition of Methane in a Flow System*. Journal of Physical Chemistry, 1968. **72**(1): p. 348-353.

19. Chen, C.J. and M.H. Back, *The Thermal Decomposition of Methane. I. Kinetics of the primary decomposition to C_2H_6 +H_2; Rate constant for the Homogeneous Unimolecular Dissociation of Methane and its Pressure Dependance*. Canadian Journal of Chemistry, 1975. **53**: p. 3580-3590.

20. Chen, C.J. and M.H. Back, *The thermal decomposition of methane. II. Secondary reactions, autocatalysis and carbon formations; non-arrhenius behaviour in the reaction of CH3 with ethane*. Canadian Journal of Chemistry, 1976. **54**(54): p. 3175-3184.

21. Roscoe, J.M. and M.J. Thompson, *Thermal decomposition of Methane: Autocatalysis*. International Journal of Chemical Kinetics, 1985. **17**: p. 967-990.

22. Dean, A.M., *Detailed Kinetic Modeling of Autocatlysis in Methane Pyrolysis*. Journal of Physical Chemistry, 1990. **94**: p. 1432-1439.

23. Rokstad, O.A., O. Olsvik, and A. Holmen, *Thermal Coupling of Methane*. Natural Gas Conversion, 1991: p. 533-539.

24. Olsvik, O., O.A. Rokstad, and A. Holmen, *Pyrolysis of Methane in the Presence of Hydrogen*. Chemical Engineering & Technology, 1995. **18**: p. 349-358.

25. Olsvik, O. and F. Billaud, *Modelling of the decomposition of methane at 1273 K in a plug flow reactor at low conversion*. Journal of Analytical and Applied Pyrolysis, 1993. **25**: p. 395-405.

26. Billaud, F. and C. Gueret, *Thermal decomposition of pure methane at 1263K. Experiments and mechanistic modelling*. Thermochimica Acta, 1992. **211**: p. 303-322.

27. Billaud, F.G. and F. Baronnet, *Thermal Coupling of Methane in a Tubular Flow Reactor: Parametric Study*. Industrial & Engineering Chemistry Research, 1993. **32**: p. 1549-1554.

28. Guéret, C. and F. Billaud, *Thermal coupling of methane: influence of hydrogen at 1330°C. Experimental and simulated results*. Journal of Analytical and Applied Pyrolysis, 1994. **29**: p. 183-205.

29. Guéret, C., F. Billaud, B. Fixari, and P.l. Perchec, *Thermal Coupling of Methane, Experimental investigations on Coke Deposits*. Carbon, 1994. **33**(2): p. 159-170.

30. Matheu, D.M., A.M. Dean, J.M. Grenda, and W.H. Green, *Mechanism Generation with Integrated Pressure Dependence: A New Model for Methane Pyrolysis*. The Journal of Physical Chemistry A, 2003. **107**(41): p. 8552–8565.

31. Keller, G.E. and M.M. Bhasin, *Synthesis of ethylene via oxidative coupling of methane: I. Determination of active catalysts*. Journal of Catalysis, 1982. **73**(1): p. 9-19.

32. Gao, Y., L.M. Neal, D. Ding, W. Wu, C. Baroi, A. Gaffney, and F. Li, *Recent Advances in Intensified Ethylene Production – A Review*. ACS Catalysis, 2019. **9**(9): p. 8592-5621.

33. Galadima, A. and O. Muraza, *Advances in Catalyst Design for the Conversion of Methane to Aromatics: A Critical Review*. Catalysis Surveys from Asia, 2019. **23**: p. 149-170.

34. Wang, L., L. Tao, M. Xie, G. Xu, J. Huang, and Y. Xu, *Dehydrogenation and aromatization of methane under non-oxidizing conditions*. Catalysis Letters, 1993. **21**: p. 35-41.

35. Guo, X., G. Fang, G. Li, H. Ma, H. Fan, L. Yu, C. Ma, X. Wu, D. Deng, M. Wei, D. Tan, R. Si, S. Zhang, J. Li, L. Sun, Z. Tang, X. Pan, and X. Bao, *Direct, Nonoxidative Conversion of Methane to Ethylene, Aromatics, and Hydrogen*. Science, 2014. **344**(6184): p. 616-619.

36. Sakbodin, M., Y. Wu, S.C. Oh, E.D. Wachsman, and D. Liu, *Hydrogen-Permeable Tubular Membrane Reactor: Promoting Conversion and Product Selectivity for Non-Oxidative Activation of Methane over an FeVSiO2 Catalyst*. Angewandte Chemie, 2016. **55**: p. 16149 –16152.

37. Oh, S.C., E. Schulman, J. Zhang, J. Fan, Y. Pan, J. Meng, and D. Liu, *Direct Non-Oxidative Methane Conversion in a Millisecond Catalytic Wall Reactor*. Angewandte Chemie, 2019. **58**: p. 7083-7086.

38. Han, S.J., S.W. Lee, H.W. Kim, S.K. Kim, and Y.T. Kim, *Nonoxidative Direct Conversion of Methane on Silica-Based Iron Catalysts: Effect of Catalytic Surface*. ACS Catalysis, 2019. **9**: p. 7984-7997.

39. Kim, S.K., H.W. Kim, S.J. Han, S.W. Lee, J. Shin, and Y.T. Kim, *Mechanistic and microkinetic study of non-oxidative methane coupling on a single-atom iron catalyst*. Communication Chemistry, 2020. **3**(58).

40. Sot, P., M.A. Newton, D. Baabe, M.D. Walter, A.P.v. Bavel, A.D. Horton, C. Copére, and J.A.v. Bokhoven, *Non-oxidative Methane Coupling over Silica versus Silica-Supported Iron(II) Single Sites*. Chemistry—A European Journal, 2021. **26**: p. 8012-8016.

41. Liu, Y., J.-C. Liu, T.-H. Li, Z.-H. Duan, T.-Y. Zhang, M. Yan, W.-L. Li, H. Xiao, Y.-G. Wang, C.-R. Chang, and J. Li, *Unravelling the Enigma of Nonoxidative Conversion of Methane on Iron Single-Atom Catalysts*. Angewandte Chemie, 2020. **59**(42): p. 18586-18590.

42. Toraman, H.E., K. Alexopoulos, S.C. Oh, S. Cheng, D. Liu, and D.G. Vlachos, *Ethylene production by direct conversion of methane over isolated single active centers*. Chemical Engineering Journal, 2021.

43. Wang, K., S.M. Villano, and A.M. Dean, *Fundamentally-based kinetic model for propene pyrolysis*. Combustion and Flame, 2015. **162**(12): p. 4456-4470.

44. Nagaki, D.A., Z. Zhao, M.N.Z. Myint, I. Lengyel, A. Mamedov, C.W. Gundlach, K. Sankaranarayanan, and D. Falcone, 2018, *Method for Producing Hydrocarbons by Non-Oxidative Coupling of Methane*, US 9 , 902 , 665 B2

45. Germain, J.E. and C. Vaniscotte, *Craquage du Methane dans un Reacteur Tubulaire. 3. Effet Iniateur de l'Ethane*. Bulletin de la Société Chimique de France,, 1958.

46. Schneider, I.A., *Über die Rolle des Äthans bei der thermischen Methanzersetzung*. Zeitschrift für Physikalische Chemie, 1963. **2230**(1): p. 234-248.

47. DeAngelis, M.T., A.J. Rondinone, M.D. Pawel, T.C. Labotka, and L.M. Anovitz, *Sol-gel synthesis of nanocrystalline fayalite (Fe2SiO4)*. American Mineralogist, 2012. **97**: p. 653–656.

48. Rob. J. Berger, E.H. Stitt, G.B. Marin, F. Kapteijn, and J.A. Moulijn, *Eurokin. Chemical Reaction Kinetics in Practice*. CATTECH, 2001. **5**: p. 36-60.

49. Bao, X. *personal communication to:* L. Lefferts, 2016

50. Reyniers, M.-F. and G.B. Marin, *Experimental and Theoretical Methods in Kinetic Studies of Heterogeneously Catalyzed Reactions*. The Annual Review of Chemical and Biomolecular Engineering, 2014. **5**(5): p. 63-94.

51. Yang, L., ZhouChong-Wen, K.P. Somers, Z. Kuiwen, and H. J.Curran, *The oxidation of 2-butene: A high pressure ignition delay, kinetic modeling study and reactivity comparison with isobutene and 1-butene*. Proceedings of the Combustion Institute, 2017. **36**(1): p. 403-411.

52. Martinez, S., M. Baigmohammadi, V. Patel, S. Panigrahy, A.B. Sahu, S.S. Nagaraja, A. Ramalingam, A.A.E.-S. Mohamed, K.P. Somers, K.A. Heufer, A. Pekalski, and H.J. Curran, *An experimental and kinetic modeling study of the ignition delay characteristics of binary blends of ethane/propane and ethylene/propane in multiple shock tubes and rapid compression machines over a wide range of temperature, pressure, equivalence ratio, and dilution*. Combustion and Flame, 2021. **228**: p. 401-414.

53. Gudiyella, S., Z.J. Buras, T.-C. Chu, I. Lengyel, S. Pannala, and W.H. Green, *Modeling Study of High Temperature Pyrolysis of Natural Gas*. Industrial & Engineering Chemistry Research, 2018. **57**: p. 7404-7420.

54. Chu, T.-C., Z.J. Buras, P. Oßwald, M. Liu, M.J. Goldmana, and W.H. Green, *Modeling of aromatics formation in fuel-rich methane oxy-combustion with an automatically generated pressure-dependent mechanism*. Physical Chemistry Chemical Physics, 2019. **21**(2): p. 813-832.

55. Kim, S.K., H.W. Kim, S.J. Han, S.W. Lee, J. Shin, and Y.T. Kim, *Mechanistic and microkinetic study ofnon-oxidative methane coupling on asingle-atom iron catalyst*. Communication Chemistry, 2020. **3**(58): p. 1-8.

Chapter 6

A techno-economic evaluation of industrial implementation of catalytic direct non-oxidative methane coupling

---

This chapter has been submitted and under revision as:

A techno-economic evaluation of industrial implementation of catalytic direct non-oxidative methane coupling; Rolf S. Postma; Dylan J. Keijsper; Bart F. Morsink; Erwin H. Siegers; Erkan M.E.E. Mercimek; Lance K. Nieukoop; Henk van den Berg; Aloijsius G.J.van der Ham; Leon Lefferts; Industrial and Engineering Chemistry Research; 2021

Abstract

This paper presents a process design for catalytic non-oxidative natural gas conversion to olefins and aromatics in a single step at high temperature. The process is designed based on existing industrial technologies and the best reactor performance reported in literature. It will highlight the opportunities and challenges involved in industrial non-oxidative coupling of methane (NOCM). Direct coupling of methane can be profitable due to the low price and high availability of natural gas, as well as the high price and large market for light olefins and aromatics. Previous works on process designs for catalytic NOCM was limited to economic aspects, whereas this paper emphases scientific and engineering challenges. Challenges in the process stem from the low pressure and high temperature required, along with the high endothermicity of the reaction. Furthermore, low partial pressures of hydrocarbon products, even at high single pass methane conversion, lead to complex separation trains. The process design and modelling result in an optimal reactor pressure of about 5 bar, when operating at 1000 °C, minimizing reactor size and compressor duty as well as maintaining a sufficiently high single-pass natural gas conversion. A very large heat exchanger is required to heat the reactor feed with the product stream, as both gas streams are sizeable and have a low pressure. Recovery of ethylene is economically unattractive, due to the low ethylene concentration in the product stream, leading to a methane to aromatics process, where the ethylene is recycled to the reactor inlet. This makes benzene the most valuable produced hydrocarbon with an efficiency of 0.31 $kg_{benzene}\cdot kg_{methane}^{-1}$. Hydrogen is a major by-product of the reaction, potentially increasing the profitability of the process if properly purified, pressurized and transported. Lastly, naphthalene is the dominant product, at 0.52 $kg_{naphthalene}\cdot kg_{methane}^{-1}$, with unfortunately low economic value and small market size. The total overall carbon efficiency of the designed process is 86%. Part of the produced naphthalene could be burned for heat generation, resulting in large CO_2 emissions and decreasing the carbon efficiency to 54%, or could be converted (for instance by hydrocracking) to more valuable BTX products in an additional downstream process. The process is calculated to be profitable, resulting in 107 $ profit per ton CH_4.

6.1 Introduction

Natural gas is seen as a high potential intermediate source of base chemicals, such as ethylene and benzene [1-5], replacing crude oil in the change towards renewable sources of energy and chemicals. Currently, the production of bulk chemicals, such as ethylene and benzene is based on petroleum feedstock [6, 7]. The worldwide known natural gas reserve is around $2 \cdot 10^{15}$ m^3 [6, 7]. The global usage is expected to grow from $4.1 \cdot 10^{12}$ $m^3 \cdot y^{-1}$ in 2020 [8] to $5.75 \cdot 10^{12}$ $m^3 \cdot y^{-1}$ in 2040, an average growth of 3.0% a year [9]. This can be attributed to the increased production of natural gas with a high methane content as seen in the exploitation of shale gas and tight oil [10]. A result of this increased production is a significant drop in the price of natural gas when comparing to crude oil. Both residential and commercial heating, as well as the production of power are a major part of the total natural gas consumption. The use of natural gas and other fossil fuels to generate energy is not sustainable due to the high greenhouse gas emissions and the resulting impact on the climate. Furthermore, renewable energy sources such as wind and solar are expected to take over the energy and heating requirements both for residential as well as industrial applications [11-16]. Due to the decreasing natural gas price and slow phase out of natural gas as energy carrier, it remains economically interesting to evaluate the possibilities to use natural gas as a feedstock for chemical synthesis.

6.1.1 Industrial state of the art

There are already several industrial processes for converting methane into hydrocarbons, most of them based on multiple conversion steps, starting with syngas production [17-19]. Syngas is produced by steam reforming of natural gas over nickel catalysts [20]. Common synthesis routes starting from syngas include Fischer-Tropsch (FT) synthesis to paraffinic waxes, methanol synthesis and ammonia synthesis [17-19, 21-24]. A FT based process generally uses Fe or Co-based catalysts to convert syngas into linear aliphatic hydrocarbons. Catalyst as well as process conditions dictate the chain growth and thus the product distribution. Generally, FT synthesis is followed by cracking the products to lower alkanes and olefins [25] , yielding at overall carbon efficiency between 60-65% [26]. Methanol can be converted into gasoline using the methanol-to-gasoline (MTG) process, in which methanol is first dehydrated over an acid catalyst to dimethyl ether, which is subsequently converted into a gasoline blend [27]. The full route from natural gas to higher hydrocarbons using either the FT or MTG reactions is called the 'gas-to-liquid' (GTL) process. To date, the largest industrial plant using FT technology is the Shell Pearl GTL plant converting $4.5 \cdot 10^7$ $m^3 \cdot day^{-1}$ natural gas to hydrocarbons [28]. Along the same line, methanol-to-olefins (MTO) shows great promise as source of olefins from methane [22, 23]. MTO starts with steam reforming methane to syngas, followed by methanol synthesis.

The methanol is converted to light olefins, such as ethylene and propylene. The advantages of MTO over GTL are the production of more valuable products and a more narrow product distribution [17, 23]. MTO has already been commercialized on smaller scale by DICP and UOP [29, 30], while other companies already developed process designs [30, 31]. The disadvantages of any indirect route for methane coupling to higher hydrocarbons are the inevitable production of oxygen containing by-products (water and CO_2) as well as the required separation and purification between each consecutive synthesis step [32]. All current industrial methane conversion processes require large installed capacities to become economically viable [33], making them unattractive for smaller remote gas fields. Pipelines and cryogenic transport for centralized methane conversion are generally too costly to be viable [3, 34, 35]. For this reason, many small gas fields for instance at the coast of Australia remain unexploited [36]. Also, many relatively small and remote (shale-) oil fields in the USA resort to flaring or venting to get rid of their co-produced natural gas, leading to unnecessary greenhouse emissions [37]. Direct coupling of methane to higher hydrocarbons is likely economically more attractive for operation at small capacity [3] compared to alternatives, due to the reduced number of process steps and limited variation in process conditions. This would make direct methane coupling interesting as an on-site process for smaller oil and gas fields, especially if the product is liquid under standard conditions. The different methods for coupling methane to different higher hydrocarbons, both industrially applied as well as academically investigated, are summarized in Figure 6.1.

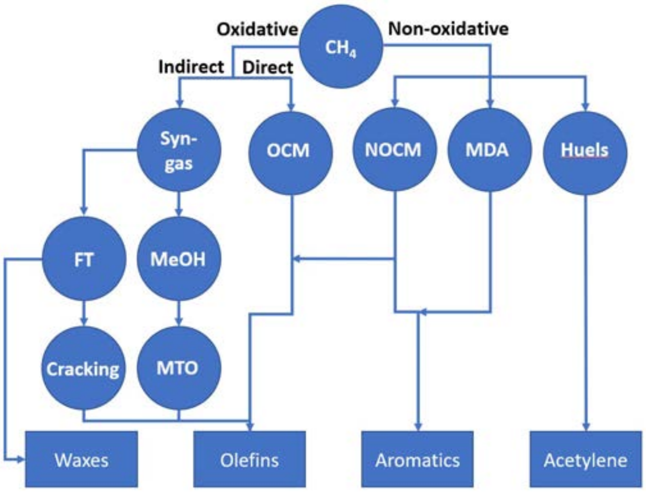

Figure 6.1: Different conversion strategies for methane into higher hydrocarbons, explanation of abbreviations can be found at the end of this chapter.

Direct coupling of methane has seen a steady increase in research over the last years for these reasons. This research is focused on three potential strategies:

1. methane dehydroaromatization (MDA) [4, 19, 38-40]
2. oxidative coupling of methane (OCM) [19, 41]
3. non-oxidative coupling of methane (NOCM) [32, 42-50]

6.1.2 Methane dehydroaromatization

MDA is a process in which methane is directly converted to lower aromatics, such as benzene and naphthalene [4]. Generally, the catalysts used consist of a transition metal (e.g. Mo) supported on a zeolite (e.g. ZSM-5). Confinement in the pores of the zeolite is responsible for the selectivity towards aromatics rather than coke. Galadima et al. [4] reviewed results obtained with several metal-modified zeolites in the MDA reaction. The general drawbacks of the MDA reaction are low product yields, low single pass methane conversion and high coking rates. The highest single pass aromatic yield of 11% is obtained at 700°C and atmospheric pressure with a 6 wt% Mo/H-ZSM-5 catalyst, as reported by Zhao et al. [4, 51]. The single pass methane conversion is low due to the unfavourable equilibrium at reaction temperature of around 700°C [4]. Figure 6.2 shows that at 700°C the maximum theoretical methane conversion is 11% when coking is not taken into account. In general, MDA suffers from high coking rates, requiring catalyst regeneration within a time span of minutes [4].

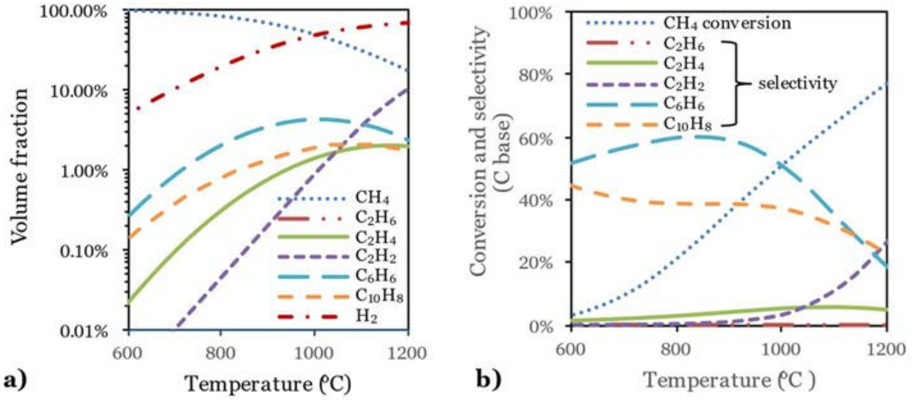

Figure 6.2: (a) Thermodynamic equilibrium concentration of methane decomposition, excluding any solid formation (coke) only showing the main products (b) equilibrium methane conversion and carbon based product selectivity based on the thermodynamic data in (a); Thermodynamic data is adapted from [52]; The same image is also shown in the introduction to this thesis, Figure 1.5.

6.1.3 Oxidative coupling of methane

Oxidative coupling of methane (OCM) circumvents the thermodynamic restrains shown in Figure 6.2, by dosing small amounts of oxidant (oxygen or sulphur) in the reactant mixture. The thermodynamic equilibrium shifts to higher methane conversion via oxidation of the hydrogen product. The main product group of OCM is light olefins, with CO_2 and water as significant by-products. OCM was first reported in 1982 [53], sparking a worldwide research surge [54, 55]. Hundreds of catalytic materials have since been synthesized and tested, mostly in the 1990s but also in recent years [5]. Ideally, the oxidant is only used to decrease the methane activation barrier, after which the formed methyl radicals react to C_2 hydrocarbons [56]. Unfortunately, the presence of O_2 leads to significant oxidation of the formed hydrocarbons, limiting the single-pass hydrocarbon yield to below 30%, at 60% C_{2+} selectivity [3, 5]. Thus, the carbon utilization efficiency of OCM remains relatively low [57, 58]. Process modelling showed that OCM can only be economically viable if single pass conversions and C_2 selectivity are at least 30% and 90% respectively [59, 60]. Therefore, even the Bi-Y-SM catalyst reporting the highest C_2 yield thus far [61] at 28% conversion and 53% selectivity does not approach the industrial requirements.

6.1.4 Non-oxidative coupling of methane

Catalytic non-oxidative coupling of methane (NOCM) is generally used as an overarching term for non-oxidative routes to methane coupling. We have opted to exclude MDA from this category, because MDA requires an addition steric effect to steer selectivity, which warrants its own section. NOCM generally operates at even higher temperature, above 900°C, in order to achieve industrially relevant methane conversion (i.e.>10% conversion) [52], as illustrated in Figure 6.2b. Hydrogen is co-produced as a valuable by-product, while formation of coke can pose practical limitations such as catalyst deactivation, process disorder as well as carbon yield loss. In 2014 Guo et al. [32] reported a Fe/SiO_2 catalyst, capable of converting CH_4 non-oxidatively to ethylene, benzene and naphthalene. Crucially, it was claimed that this catalyst does not cause coke formation, even at high conversion level, i.e. 48% at 1080°C. A constant molar ethylene selectivity of ~50% was reported for temperatures between 950 and 1080°C. Atomically dispersed Fe(II) sites on silica are postulated to selectively dehydrogenate CH_4 to methyl ($CH_3\cdot$) radicals, initiating free radical coupling reactions in the gas phase. This has been supported with DFT calculations by Kim et al. [50]. Guo et al. [32] named this specific catalyst Fe©SiO_2, which notation will also be adopted in this paper. Sakbodin et al. [42] demonstrated that methane conversion over the Fe©SiO_2 catalyst can be significantly boosted by introducing a hydrogen permeable membrane in the reactor to remove hydrogen in-situ. Oh et al. [43] demonstrated that a coated wall reactor using Fe©SiO_2 also causes an increase in methane conversion. Han et al. [44] reported that SiO_2 in the cristobalite crystal phase is required to minimize coke formation, requiring the high fusion temperature during catalyst preparation (1700°C). Furthermore, atomically dispersion of Fe prevents coke formation on the active site of the catalyst. Results from **chapter 2** and a SABIC patent [62] showed experimentally that the catalyst is only required for methane activation after which propagation occurs in the post-catalytic volume. Other types of catalysts have also been reported for the NOCM reaction [45-49], but these show low conversion, high coking rates, or are only tested at low CH_4 partial pressures.

Table 6.1: General overview of performance figures obtained from various publication concerning the three types of catalytic reactions to convert methane to higher hydrocarbons.

CH_4 conv. method	**MDA**	**OCM**	**NOCM**
C_2 single pass yield	1% [63]	30 C% [3, 5]	9.3 C% [32]
Aromatic single pass yield	11% [4]	N/A	39.1 C% [32]
Coke selectivity	28% [4] 32% (1 bar), 12% (10 bar) [63]	N/A	0% [32, 42], 12% [43]
Economic viability requirements	Conversion > 25% HC selectivity > 30% [64]	Conversion > 30% C_2 selectivity > 90%[59, 60]	Conversion> 32% HC selectivity > 80% [22]
By-products	H_2 & coke	H_2O & CO_2	H_2 & coke
Carbon efficiency over the process	31% [64]	60% [3, 5]* *Experimental	100% [22] 82.7% [65]

6.1.5 Process designs concerning direct coupling of methane

The reported high conversion and high resistance to coking of Fe©SiO_2 is interesting for possible industrial application. However, the severe reaction conditions as well as the broad product distribution presents various challenges in terms of process design. Many process design studies concerning single step conversion of methane focussed on MDA and OCM reactions [60, 64, 66-71]. In contrast, there are currently only two papers on process design addressing high temperature catalytic NOCM [22, 65]. The general conclusions from these process designs studies have been summarized in Table 6.1. The product yields and coke selectivity in Table 6.1 are the best experimental results reported in literature. The economic viability requirement shows the minimum single-pass methane conversion and hydrocarbon selectivity required.

Huang et al. [22] performed a study to screen how certain conditions affect the net present value (NPV) of a NOCM process. A detailed process design including economic evaluation is presented, the process design is evaluated starting from a base case, in which process and economic variables are systematically varied, to evaluate the sensitivity for the NPV. The base case evaluated assumes the following conditions and productivity $T_{conversion}$: 800°C, CH_4 single-pass conversion: 25%, coke selectivity: 0% and ethylene selectivity: 20 C%, the benzene and naphthalene selectivity are both 30 C% with the remaining 20 C% divided over minor olefins and aliphatics (i.e. ethane, propane, propylene, butane and butene). This base case is actually not realistic when looking at Figure 6.2, which shows that the maximum methane conversion based on thermodynamics, without allowing coking, is 20% at 800°C. They concluded that the single-pass conversion of methane and coke selectivity are the main parameters affecting profitability. The single-pass conversion of methane should be above 25% and coke selectivity should not exceed 20%. Furthermore, they concluded that profitability can be increased by increasing olefin yield over aromatic yield, as expected. Do et al. [65] performed a techno-economic feasibility study of a direct methane coupling process, similar to Huang et al. [22]. After the conversion step, all products are systematically removed, starting with the aromatics and ending with cryogenic recovery of the produced ethylene. The reactor is operated at 1200°C and atmospheric pressure and it is stated that a product distribution is assumed, without further detail. They conclude that the most important factors determining profitability are the cost of natural gas and electricity as well as the sales price of ethylene. Unfortunately, the importance of minimum conversion and selectivity was not discussed.

Table 6.2: Standard (1 atm, 25°C) enthalpy and Gibbs free energy change of the three considered reactions, normalized per carbon atom [72].

Reaction	**STD enthalpy change ($KJ \cdot mol_C^{-1}$) [72]**	**STD Gibbs energy change ($KJ \cdot mol_C^{-1}$) [73]**
$2CH_4 \rightleftharpoons C_2H_4 + 2H_2$	101.1	-16.6
$6CH_4 \rightleftharpoons C_6H_6 + 9H_2$	88.1	-29.9
$10CH_4 \rightleftharpoons C_{10}H_8 + 16H_2$	89.2	-37.9

Several points have not been addressed so far when evaluating industrial application of NOCM in addition to the selection of the reaction conditions:

1. Separation scheme of the products, by-products and unconverted reactant.
2. Heat supply to the reactor, considering the endothermicity of the reaction (Table 6.2), as well as the intensive heat transfer required between feed and product streams
3. Strategy for operating the reactor, considering coking
4. Regeneration of the catalyst/reactor in case of coking

This paper presents a detailed design of a plant using the Fe©SiO_2 catalyst to convert natural gas using the NOCM reaction. The main aim is to evaluate possible solutions for the four challenges above, using proven industrial technologies. The insights obtained will give directions for both further research on the catalyst, as well as on other technologies required. Note that many of the aspects discussed in this paper are general to any NOCM reaction and not specific to the Fe©SiO_2 catalyst.

6.2 Process design

The scope of the design is a process with a capacity of 200 ktpa benzene with a purity of 99.8 wt.% based on the Fe©SiO_2 catalyst to convert natural gas using the NOCM reaction. Catalyst performance data, concerning both activity and selectivity have been taken from the original work on the Fe©SiO_2 catalyst by Guo et al. [32] and shown in Table 6.4. It must however be noted that other papers [42-44, 50, 62] reporting on this catalyst as well as **chapters 2-4** of this thesis showed a broader product range of minor products, including ethane, acetylene, C_{3-5} olefins and alkyl benzenes. The selectivity to these products becomes negligible at higher methane conversion (**chapter 3)** and are therefore not included to reduce complexity. In this study a standard composition for dry natural gas in the USA is used, presented in Table 6.3 [74, 75]. It is assumed that all hydrocarbons are alkanes.

Table 6.3: Composition of natural gas found in the US Gulf Coast area [74, 75].

Component	**Mole fraction (%)**	**Trace components**	**Amount**
N_2	1.25	S-components	5.5 mg·m^{-3}
CH_4	91.01	H_2O	<65 mg·m^{-3}
C_2	4.88	O_2	0.01 mole%
C_3	1.69	CO_2	0.01 mole%
C_4	0.66		
C_5	0.27		
C_6	0.13		
C_7 and above	0.11		

6.2.1 Methodology

The applied design methodology is based on the method described by James M. Douglas and is derived from the book "Conceptual Design of Chemical Processes" [76]. Separation method selection is based on the selection schemes published by Barnicki and Fair [77, 78].

Various alternatives were identified and the least attractive were rejected based on heuristics, as recommended by Douglas [76]. Several iterations were made, ending up with the final operation block diagram as presented in Figure 6.3. The final flow sheet was evaluated using Aspen Plus [79]. Note that exclusively the heat-exchanger over the reactor has been included in Figure 6.3, due to its importance both for the process design (further explained in section 6.2.8) and process economics (explained in section 6.2.9).

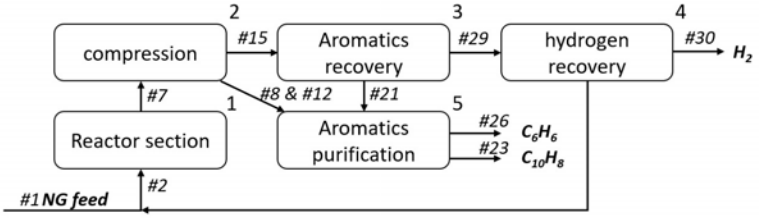

Figure 6.3: Functional block diagram of the designed process for direct coupling of methane using the Fe©SiO2 catalyst, for more details see Figure 6.5 and Table 6.5.

6.2.2 Gas pre-treatment

Natural gas contains many impurities as shown in Table 6.3. It is likely that these impurities will poison or foul process steps and need to be removed. All sulphurous compounds are removed using a caustic scrubber, which also removes any CO_2. It is chosen to leave all hydrocarbons in the feed stream, to maximize carbon utilization and to prevent high separation costs for removing the C_{2+} hydrocarbons at these concentrations. It is assumed that the natural gas has already been cleaned before entering the process.

6.2.3 Physical and chemical considerations for the reaction

All research concerning the NOCM reaction reported thus far, was performed at atmospheric or sub atmospheric pressures [32, 42-49]. This is highly undesirable from a design perspective, because low pressures require larger volumes for the installed reactor and the additional unit operations such as heat exchangers. Furthermore, low pressures are highly disadvantageous for gas-gas heat exchange. On top off that, higher pressures are required to facilitate the separation of the products. This clearly shows the requirement for the reactor to operate at elevated pressures. Kosinov et al. [63] reported that increasing pressure from 1 to 15 bar reduces coke selectivity from 33% to 11% and also increased catalyst productivity from 33 to 160 mmol$CH_4 \cdot g_{cat}^{-1}$ in the MDA reaction.

$$xCH_4 \rightleftharpoons C_xH_y + \left(2x - \frac{y}{2}\right) H_2 \qquad \textbf{\textit{equation 1}}$$

The NOCM reaction results in a considerable increase in volume, due to the significant co-production of hydrogen (***equation 1***). Le Chatelier's principle dictates that at higher pressure the equilibrium of ***equation 1*** will favour the reactant side and thus methane conversion will be limited. The equilibrium methane conversion as function of total pressure was modelled, using Aspen Plus [79], allowing ethylene, benzene, naphthalene and hydrogen as products (Figure 6.4). The reported minimum single-pass conversion for a feasible methane coupling process is between 25-30% depending on the process [22, 59, 60]. The influence of pressure on the maximum achievable conversion in the reactor was estimated by correcting the conversion achieved by Guo et al. [32] at 1 atm and 1000°C along the equilibrium line shown in Figure 6.4 and corrected for the decreasing coke formation as function of pressure reported by Kosinov [63]. It was found that 5 bar is the optimal pressure for the reactor operated at 1000°C, resulting in 28% single-pass methane conversion, details can be found in S.1.

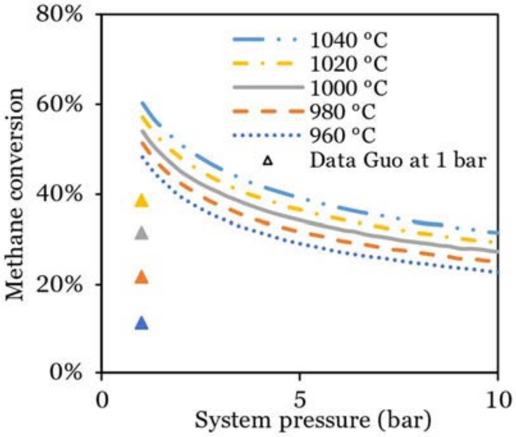

Figure 6.4: Methane conversion at thermodynamic equilibrium as function of reactor pressure at temperatures ranging from 960 to 1040°C; calculated using Aspen plus [79], using a Gibbs reactor allowing for the formation of ethylene, benzene, naphthalene and hydrogen; The colour coded triangles represent the maximum reported experimental conversion at the stated temperatures [32] (all at 1 bar).

The selectivity data presented by Guo et al. [32] at 1000°C and 1 atm pressure will be used, because this is the only paper that reports data measured at industrially relevant conversion levels. The selectivity values have been corrected for the increase in pressure, as described in detail in S.2. The selectivity values are presented in Table 6.4. Note that the reported selectivity distribution is already close to thermodynamic equilibrium when compared to Figure 6.2b, the main difference is a higher ethylene selectivity.

Table 6.4: The assumed carbon selectivity of methane towards the three carbon-containing products based on [32].

Hydrocarbon product	Carbon selectivity
Ethylene (C_2H_4)	21 C%
Benzene (C_6H_6)	26 C%
Naphthalene ($C_{10}H_8$)	53 C%

The reactor feed contains not only methane, but also small amounts of C_{2+} hydrocarbons (percentage level), as shown in Table 6.5. These hydrocarbons are significantly less stable under reaction conditions compared to CH_4. Guo et al. [32] showed that addition of small amounts of ethane to the reaction mixture will both cause a significant increase in reaction rate, but also co-produce coke. Ethane and ethylene are potent free radical initiators [80-83] and **chapter 3**, significantly enhancing methane conversion. It can be safely assumed, based on experimental data from **chapter 3**, that increasing the space velocity can largely prevent the coke formation due to C_{2+} hydrocarbons, while keeping the same conversion as a consequence of the increasing reaction rate. However, it is unlikely that coke formation can be completely prevented by tuning the space velocity. Unfortunately, there is no information on the effect of addition of small amounts of C_{3+} hydrocarbon on the performance of the NOCM reaction. Therefore, it is assumed for design purposes that coking from $C_{2\text{-}4}$ hydrocarbons can be prevented, but that all C_{5+} hydrocarbons will react swiftly to coke. In reality, all C_{2+} hydrocarbons will cause formation of some deposits. Note that a variance in the coke selectivity will not significantly impact the carbon balance of the process, as long as fuel combustion is required to overcome the endothermicity of the reaction. More details concerning the impact of the assumed coking rate will be given in section 6.2.5.

6.2.4 Process overview

A detailed overview of the process can be seen in Figure 6.5. Cleaned makeup-gas enters in stream #1 and is mixed with the recycle stream #36. It passes a heat-exchanger (Hex-102) and a furnace (HU-101) before entering the reactor (R-101). An FCC-type reactor has been chosen for continuous coke removal from the catalyst, more details concerning the reactor are given in section 6.2.5. The product gas from the reactor is first quenched to 600°C in an oil-quench (CU-101), to stabilize the product mixture after the reactor and prevent further coupling and coke formation. The stream after the quench (#5) is further cooled with the feed stream (#2) in a heat exchanger (HEX-102). In R-101 the NOCM reactions proceed at 5 bar and 1000°C as discussed in the previous section. In Section 2 the product gas is compressed first from 5 to 35 bar, with interstage coolers CU-103 and CU-104 and condensate separators (S-101 and S-102) to remove any aromatic condensates. After compression, the remaining aromatic species are removed (in section 3) in an absorption column using sulfolane (S-103). After regeneration of the sulfolane (S-105) the aromatic streams from the condensate separators (stream 8 and 12) as well as the absorption section (stream 21) are mixed and upgraded in section 5 by distillation (S-107) to get the products benzene (#24) and naphthalene (#23). Part of the naphthalene stream (#23b) can be split off to use in both heater HU-101 and the reactor (R-101) to accommodate part of the heating duty, with the remainder of the naphthalene following stream #23a. The benzene stream is cooled and treated in a phase separator (S-108) to reach the final purity of 99.8%. The aromatic-free product stream (#29) of the absorber S-103 continues to the membrane section (section 4) for hydrogen separation (S-104). The remaining hydrocarbon stream (#32), consisting mainly of methane and low concentrations of ethylene, is mixed with stream #28 from the benzene purification section and recycled to the reactor inlet and mixed with the fresh-feed stream. The recycle contains a purge (#35) of 2% to prevent the build-up of inert impurities in the system. The stream size and composition concerning these sections are presented in Table 6.5. The choices made in the sequence and techniques used for product separation and purification are detailed in the section below.

Table 6.5: The conditions and molar flows of the main streams represented in Figure 6.5. The content and conditions of all other flows are presented in Table S 6.1 in S.4; note that most streams omitted from this table have got the same composition as ones presented

Stream	**1**	**2**	**7**	**8**	**12**	**15**	**21**	**22**	**23**	**26**	**28**	**29**	**30**	**31**	**34**	**35**
T (°C)	20	21	90	90	90	90	210	152	250	20	105	94	94	94	21	21
P (bar)	5	5	5	5	12	35	2	2	2	2	5	35	1	35	5	5
n (Mmol·hr^{-1})	4.7	20	24	0.22	0.05	23	0.42	0.68	0.28	0.28	0.13	23	7.1	16	16	0.32
CH_4 (mol%)	91.0	83.0	55.6	0.39	0.98	56.2	24.2	14.8	0	0.45	78.3	56.8	4.1	80.6	80.5	80.5
C_2H_6 (mol%)	4.9	1.1	0	0	0	0	0	0	0	0	0.04	0	0	0	0	0
C_2H_4 (mol%)	0	2.2	2.0	0.05	0.13	2.0	3.0	1.9	0	0.29	9.3	2.0	0.08	2.9	2.9	2.9
C_6H_6 (mol%)	0	0.09	1.3	4.7	11.4	1.3	64.8	41.6	0	99.2	5.0	0.05	0	0.08	0.12	0.12
$C_{10}H_8$ (mol%)	0	0.01	1.2	94.6	87.4	0.11	5.6	40.3	99.8	0.01	0	0.01	0	0.01	0.01	0.01
H_2 (mol%)	0	4.1	32.4	0.01	0.03	32.8	0.7	0.45	0	0	2.4	33.4	95.5	5.4	5.4	5.4
N_2 (mol%)	1.3	8.8	7.5	0.02	0.06	7.6	1.6	0.95	0	0.01	5.0	7.7	0.34	11.0	11.0	11.0
Other (mol%)	2.9	0.68	0	0.25	0.02	0	0	0	0.19	0.01	0.01	0	0	0	0.01	0.01

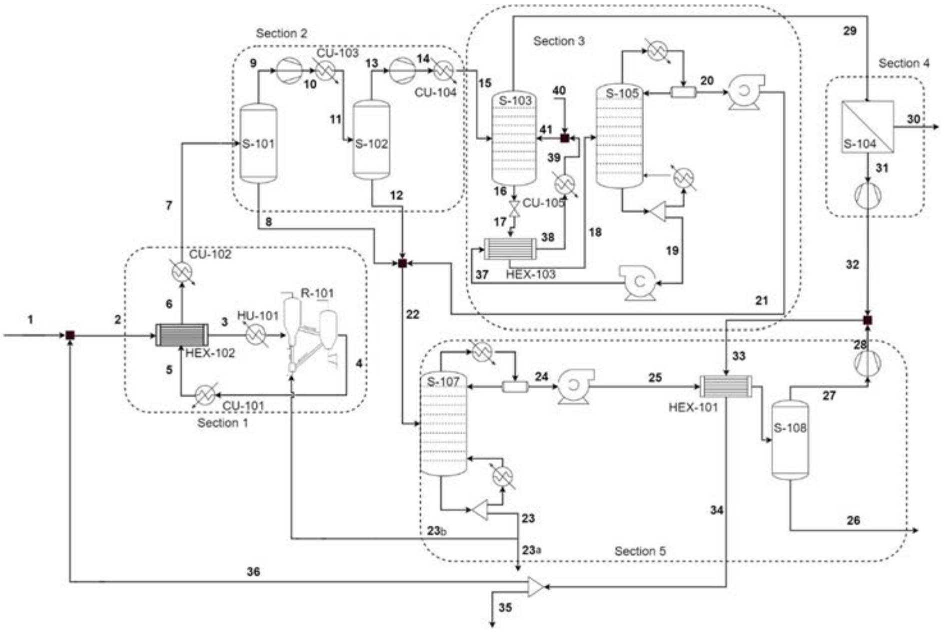

Figure 6.5: Process flow diagram, divided in five operational sections, based on function. Section 1 is the conversion section, concerning the reactor and heating and cooling. Section 2 concerns the compression of the product stream, with intermediate flash-tanks to remove any condensing aromatics. Second 3 removes the remaining aromatics from the product stream. Section 4 consists of membranes to separate most of the hydrogen. Section 5 concerns the aromatic purification.

6.2.5 Reactor design

The reactor performance (i.e. conversion and selectivity) has been estimated and fixed in this process design, because of the uncertainties in performance of non-oxidative coupling of methane reaction with respect to the effects of operating conditions on methane conversion, selectivity distribution and coking rates, as discussed in section 6.2.3. Reactor design consideration will still be discussed below, due to the high importance of reactor design on process performance.

Preheating in the heat-exchanger in section 1, Figure 6.5, is limited to 600°C in order to prevent coke formation in the feed before reaching the catalyst bed. Heating from 600 to 1000°C must be realised as quickly as possible in the reactor, just upstream of the catalyst bed as shown in **chapter 2**. The required heat input for preheating the feed from 600 to

1000°C is calculated at 165 MW (2.0 $\mathrm{MJ \cdot kg_{methane}^{-1}}$). The reaction itself is highly endothermic, as shown in Table 6.2. The required heat amounts to 142 MW (1.7 $\mathrm{MJ \cdot kg_{methane}^{-1}}$), calculated with Aspen Plus [79], resulting in a total heat input for the reactor of 307 MW (3.7 $\mathrm{MJ \cdot kg_{methane}^{-1}}$) (Table 6.6). This sizable heat input can be accommodated in various ways, firstly 61 MW can be accommodated by burning the purge gas (mainly methane, stream #35) and another 10 MW can be obtained by burning the formed coke during catalyst regeneration. The remaining 236 MW can be generated by either i) burning the naphthalene, from stream #23, ii) burning the hydrogen, from #30, produced in the process, iii) by burning part of the methane process feed, iv) by electric heating. Burning hydrogen or electric heating, at 4 $\mathrm{\$ct \cdot kWh^{-1}}$ [84] are both deemed too expensive in the current market, although both options will significantly reduce the CO_2 emissions of the process. Natural gas is the cheapest option for supplying the required heat [85, 86]. However, for this process design it was chosen to use the naphthalene as heat source for the remaining 236 MW, due to the large quantity of naphthalene produced as well as the limited market size [87]. Using the lower heating value of 38.9 $\mathrm{MJ \cdot kg^{-1}}$ [86] it can be calculated that 6.0 $\mathrm{kg \cdot s^{-1}}$ naphthalene is required, out of the 10 $\mathrm{kg \cdot s^{-1}}$ from stream #23 (Figure 6.5 & Table 6.5). Providing the required heat to the reactor will be very challenging, due to the high required heating rate to prevent coking (**chapter 2)**. The feed can be heated from 600°C to 1000°C with a multi-tubular gas-fired heater (unit HU-101 in Figure 6.5),, comparable to a cracking furnace. It is imperative to make the thermal driving force as large as possible, as well as supplying an inert lining on the inside of the tubes, to prevent heterogeneous activation of methane and especially higher hydrocarbons. The method to add heat for the endothermicity of the reaction depends on the choice of reactor. In a fluidized bed reactor, such as a FCC-type reactor, the heat can be supplied by preheating the catalyst. The catalyst is synthesized at 1700°C [32] and is therefore expected to be stable up to ~1600°C. As discussed above, 10 MW of heat can produced by burning of the coke on the catalyst during regeneration. The rest (142-10=132 MW) is supplied by burning the naphthalene. Assuming the catalyst is cooled from 1600°C to 1000°C during the reaction, this would result in a catalyst recirculation rate of 310 $\mathrm{kg \cdot s^{-1}}$ (resulting in a catalyst to gas mass flow ratio of 3:1). This catalyst recirculation rate can be lowered, or even a fixed-bed operation can be used, if the heat is supplied through multi-tubular gas-fired heaters, similar to pre-heating of the gas.

Coking will likely occur in the reactor, independent of the catalyst or reactor design, as discussed above. This coke has to be removed from the reactor to prevent deactivation, fouling or blocking. Two types of industrial reactors will be able to handle these conditions, namely a FCC-type of reactor [88], with an independent conversion and regeneration section, or a Catofin reactor [89], where conversion and regeneration are handled in a simulated moving bed arrangement. The FCC reactor is optimal for high coking rates, leading to deactivation in a timespan from seconds to minutes, whereas a Catofin reactor is most useful when regeneration is required between tens of minutes to hours. The FCC reactor was chosen for this process design, as coking rates are probably significant, leading to the formation of a monolayer of coke on the catalyst in 36 to 80 seconds. This assumption is based on the time required for the C_5 components to form a monolayer of graphitic carbon on the surface of the catalyst [89]. Furthermore, **chapter 2** and a SABIC patent [62] both showed that limiting the contact time in the catalyst-bed, in favour of longer residence time in the gas-phase in the reactor at high temperature, increases productivity while decreasing deposit formation. It must be noted that the work by Guo et al. [32], used as performance data for the FCC reactor in this process design, was measured on lab scale in a fixed bed reactor. As discussed in the process overview, an oil-quench will be used to quickly bring down the temperature and stabilize the product mixture after the reactor, as discussed by Nagaki et al. [62].

Table 6.6: The parameters chosen or calculated for the reactor; the selectivity distribution is shown in Table 6.4.

Reactor parameter	**Chosen or calculated value**
Temperature	1000°C
Pressure	5 bar
Single pass methane conversion	28%
Single pass C_2+ conversion	100%
Required heat input: pre-heating feed	165 MW
Required heat input: reaction endothermicity	142 MW
Total required heat input to reactor	307 MW

6.2.6 Separation parameters

It is best practice to evaluate first separation of the largest product fraction, as described by Douglas et al. [76] and Barnicki and Fair [77, 78]. In this case, the main product from the NOCM reaction is hydrogen, accounting for up to 32 vol% of the reactor outlet stream, as can be seen in Table 6.5. All hydrogen separation technologies considered tend to foul in the presence of aromatic compounds [90-92] and naphthalene will condense at the used temperature and pressure ranges. Thus, deep aromatic removal is required as first separation step. Deep aromatic removal is most easily achieved with an absorption process using sulfolane as solvent, commonly used in industry for aromatic separation [7]. It was also considered to use the produced naphthalene, or high-boiling oil as solvent, but this did not yield the required separation efficiency. Other options considered and evaluated were a simple flash or a distillation column. Both, either did not yield the required separation, or were too costly due to the required temperatures.

The sulfolane is recovered by means of distillation. The resulting aromatic streams are combined and distilled to obtain a pure benzene (99.2 vol%) and pure naphthalene stream (99.8%).

Polymeric membranes are the most suitable option for hydrogen separation [90-93], based on their maturity in industry as well as the process conditions. This results in a hydrogen stream with 95.5 vol% purity, which can be further increased by use of PSA, although this is out of the scope of this study. Other evaluated options include different types of membranes, i.e. palladium, silica or carbon based membrane [86, 94-98] and pressure swing adsorption (PSA) [99]. The concentration of hydrogen in stream #29 is lower than required for PSA separation[99], although this technique can be used to further purify the permeate stream (#30) and thus increase the value of the produced hydrogen. Palladium membranes are too expensive[94], silica membranes tend to suffer from rapid degradation and have not yet seen industrial use[98] and carbon-based membranes have thus far not been used for separating hydrogen from hydrocarbon mixtures.

The remaining stream after hydrogen separation contains mainly methane with percentage amounts of ethylene, around 3 vol% at this stage, see Table 6.5, stream #31. Cryogenic distillation is the only ethylene recovery method applied at large-scale [100]. The separation costs per ton of ethylene is estimated at 1900 $\$\cdot\text{ton}^{-1}$(see supporting information S.3), significantly more than the 2020 ethylene retail price of 1,000 $\$\cdot\text{ton}^{-1}$[101]. A more energy efficient method to separate ethylene from methane is needed, or the ethylene concentration should be at least doubled, in order to make the recovery viable. For this reason, all ethylene is recycled back into the reactor, converting it further to benzene and other aromatics. This results in the loss of 104 $\text{kton}\cdot\text{y}^{-1}$ ethylene, for a total gross value of 104 $\text{mln}\$\cdot\text{y}^{-1}$ in ethylene, although it must be noted that the ethylene is converted into benzene, naphthalene and hydrogen in the recycle, thus minimizing the value lost.

6.2.7 Carbon efficiency

The total carbon efficiency of the process amounts to 86%, based on the mass balance in Table 6.5. This value becomes 54%, when discounting for the naphthalene burned for supplying the heat to the reactor. These values are in the ballpark of the current Fischer-Tropsch style processes, which operate at carbon efficiencies between 60-65% [26]. Unfortunately, the process yield of benzene is only 32% based on carbon, the rest of the carbon ends up in naphthalene. Therefore, naphthalene upgrading to added value products is necessary. Currently, naphthalene is used as precursor to phthalic anhydride, as well as various azo-dyes and pesticides [102]. Naphthalene can be selectively hydrocracked to mono-aromatic hydrocarbons, using a blend of hydrogen and methane as cracking agents, at 400°C and 40 bar [103]. Full naphthalene conversion was achieved after 1 h in an autoclave, using Zn/HY as catalyst. The main products are toluene and propane.

Hydrogen is also a major product of the NOCM process, which should be considered as a valuable product in the emerging hydrogen economy [104].

6.2.8 Heat integration and pinch study

The total heating duty required in the process is 187 MW and the total cooling duty amounts to 247 MW (9.8 $\mathrm{MJ \cdot kg_{methane}^{-1}}$ and 13.0 $\mathrm{MJ \cdot kg_{methane}^{-1}}$ fed to the process respectively). This includes the heating of the reactor feed to 600 C. However, it excludes the preheating of the reactor feed from 600-1000°C, the endothermic heat input for the reactor, as well as the cooling duty required in the initial quenching of the product mixture from 1000-600°C after the conversion reactor. These heat duties are left out since they cannot be used in heat-integration due to the high required heating and cooling rates to prevent coke-formation (**chapter 2)**, as explained in the reactor design section. The heat in the oil used to quench the reactant mixture is exchanged to generate high pressure steam.

The heat integration evaluation for this process is based on a pinch-study using 10°C as temperature difference at the pinch. The resulting composite curves can be found in Figure 6.6a. The pinch temperature is at 600°C which means all streams evaluated are below the pinch and only cooling utility is needed. Based on the composite curve a network of heat-exchangers and coolers is developed, presented in Figure 6.6b and also incorporated in the PFD (Figure 6.5). The first heat-exchanger (HEX-101) is used to cool the benzene stream from distillation column S-107 before it is flashed to remove any remaining lighter hydrocarbons (S-108), the cooling is done with the expanded gasses of the recycle. The second heat exchanger (HEX-102) is used to heat the reactor feed and cool the product stream, note that this heat exchanger needs to exchange 149 MW of heat (1.4 $\mathrm{MJ \cdot Kg_{stream}^{-1}}$), which considering the heat exchange between two gas streams results in 68000 m^2 of heat-exchange area required, due to the low ΔT of 10°C at the pinch. The third heat exchanger (HEX-103) is used to heat the feed of the sulfolane recovery distillation column (S-105) while cooling the returning lean sulfolane from the reboiler of the distillation column. After which only a cooling duty of about 45 MW is left, which will be handled by cooing water since it is below 140°C.

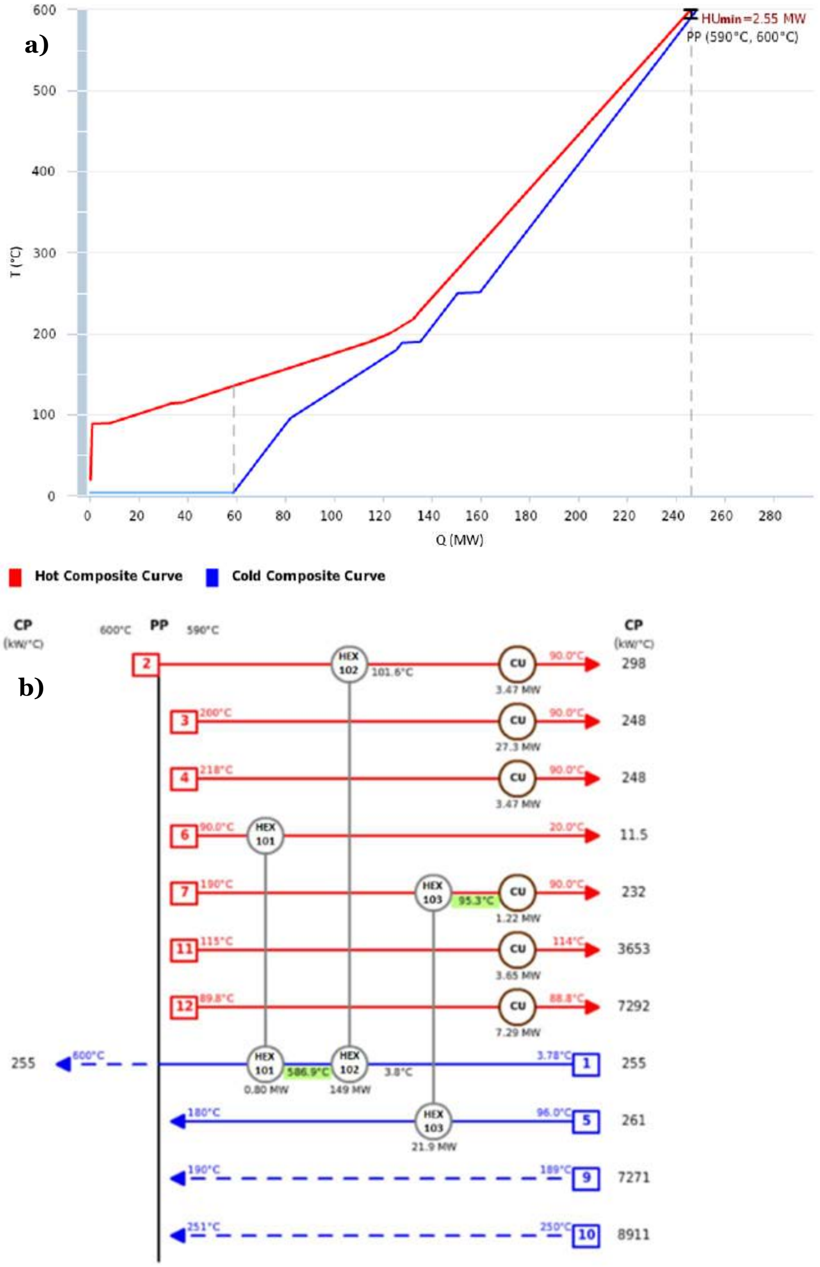

Figure 6.6: (a) Composite curve following the pinch study; (b) heat exchanger network developed based on the pinch study.

Considering the very large required surface area for heat exchange and similarly large investment costs associated with HEX-102, it needs to be re-evaluated. An increase in minimum temperature difference over the heat exchanger will significantly reduce the required surface area for heat exchange, at the cost of requiring additional heating and cooling duty. If both the costs of HEX-102 and the additional costs of extra required cooling and heating are taken into account, calculated over the depreciation period of 10 years, assuming 15% interest per year over the investment, one obtains Figure 6.7. It is clear that the costs for HEX-102 will be minimal at a minimum temperature difference of 40°C, which is a reasonable value for gas-gas heat exchangers. The size of the heat-exchanger can be reduced to 20000 m^2 heat exchange area at this temperature difference, but does require both 8 MW additional heating and cooling. Although 20000 m^2 is still a very large heat exchanger, it is technically feasible. Note that the additional costs for heating and cooling equipment is not taken into account for this calculation. These optimization calculations are not included in the final economic evaluation, due to the low impact.

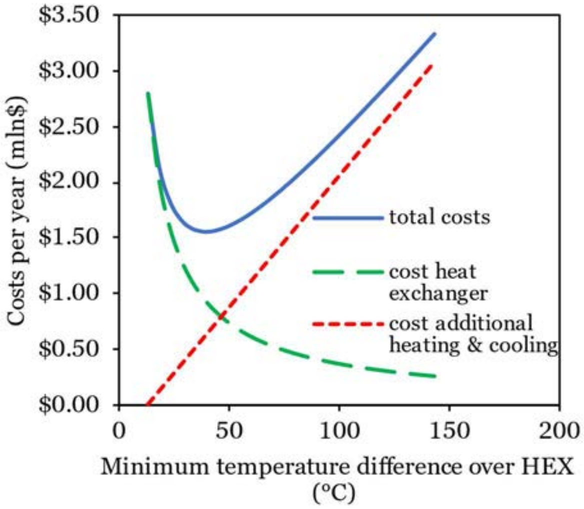

Figure 6.7: Optimization of costs for the main heat exchanger (HEX-102), considering a depreciation period of 10 years.

6.2.9 Economic evaluation

The plant economics are calculated in US$ in the year 2018, for a benzene production capacity of 200 ktpa. Equipment was sized using basic design principles. The capital expenditure (CAPEX) for the equipment was estimated using a combination of cost estimation tools [105-107]. Equipment costs are estimated using the tools from Matche [105] and Equipment Costs correlations published in Plant Design and Economics for Chemical Engineers [106]. The scaling factors for inside and offside battery limits (ISBL and OSBL) described by Sinnot et al. [107] are used to adjust for installation costs, piping and other auxiliaries, generally resulting in a Lang factor of 6 (Table 6.7). The CAPEX cost was corrected for inflation to 2018 using the Chemical Engineering Plant Cost Index (CEPCI). Note that the used costs for the reactor as well as the membrane section already include the installation costs, thus their Lang factor was kept at 1. Table 6.7 shows the capital expenditure split over the different types of installed units, note that 'columns' includes both the distillation equipment as well as the flash drums. Using the ISBL and OSBL factors the total capital expenditure is also shown in Table 6.7. Note that the inaccuracy of CAPEX costs can be up to 30%, especially considering the uncertainty surrounding the optimal reactor design.

Table 6.7: Purchased Cost of the main process equipment, the applied Lang factor and the corresponding total capital investment (TCI).

Equipment	**Purchased Cost (mln $)**	**Lang Factor**	**TCI (mln $)**
HEX	32.3	6	194
Pump	0.02	6	0.1
Compressors	25.4	6	152
Columns	1.2	6	7.3
Reactor	120.7	1	121
Mixers	0.2	6	1.1
Membranes	6.1	1	6.1
Total (ISBL)			481
Total (ISBL+OSBL)	(OSBL = 40% of ISBL)		700

Table 6.8 presents the costs of raw material, products revenue and utility costs. The amounts are based on the mass and energy balance from Table 6.5. Note that Table 8 shows the results for two situations: 1) 60% of the naphthalene is used for heating the reactor and the rest is sold, 2) naphthalene is completely sold (results given between brackets), while natural gas will be used for heating the reactor feed (corresponding value between brackets). These options will both result in significant CO_2 emissions, making the process not environmentally friendly. Technologies like carbon capture and storage (CCS) can be used to mitigate this effect but will result in a significant increase in cost. Other heating options considered include hydrogen as fuel, or electric heating, but these are both expensive and will yield a large naphthalene product stream without sizable market. This can only be solved by another process that converts naphthalene (for instance by hydrocracking) in marketable products. It is assumed that catalyst losses are negligible, due to the long-term stability [32]. The hydrogen price is relatively low as a result of the low purity achieved by the membrane. The designed process does not produce any organic waste streams requiring treatment, as all waste-streams containing hydrocarbons are combusted for heat generation. Spent catalyst will be returned to the manufacturer.

Table 6.8: Overview of total Raw material costs, product revenues and utility costs for two situations. Without brackets shows the value in case naphthalene is partly combusted for reactor heating. Between bracket shows the value in case naphthalene is fully sold and extra natural gas is combusted for heating the reactor. The estimates for the costs and replenishment rate of the catalyst are based on the FCC process [108].

Raw material costs

Components	**Price ($\$\cdot\text{ton}^{-1}$)**	**Amount ($\text{kton}\cdot\text{year}^{-1}$)**	**Total cost ($\text{mln}\$\cdot\text{year}^{-1}$)**
Natural gas	125 [85]	739 (897)	92 (112)
Sulfolane	3000 [109]	0.6	2
Catalyst	3000 (own estimation)	1	3
Total ($\text{mln}\$\cdot\text{year}^{-1}$)	97 (117)		

Products revenue

Components	**Price ($\$\cdot\text{ton}^{-1}$)**	**Amount ($\text{kton}\cdot\text{year}^{-1}$)**	**Revenue ($\text{mln}\$\cdot\text{year}^{-1}$)**
Benzene	860 [110]	194	167
Naphthalene	450 [111]	123 (314)	55 (142)
Hydrogen	800 [112]	119.5	95.6
Steam (from CU-101)	12.1 [107]	2890	35
Total ($\text{mln}\$\cdot\text{year}^{-1}$)	353 (440)		

Utility costs

Components	**Price**	**Amount (year^{-1})**	**Total costs ($\text{mln}\$\cdot\text{year}^{-1}$)**
Electricity	$40\$\cdot\text{MWh}^{-1}$ [107]	399 GWh	16
Cooling water	$13\cdot10^{-3}\$\cdot\text{m}^{-3}$ [107]	$52.4\cdot10^{6}$ m^{3}	0.7
Steam	$12.1\ \$\cdot\text{ton}^{-1}$ [107]	126 kton	1.5
Total ($\text{mln}\$\cdot\text{year}^{-1}$)	18.1		

Table 6.9 presents the auxiliary costs of the process, namely the costs for wages, technical assistance and overhead. We have chosen to also include the depreciation of the capital expenditure in this table, assuming total depreciation of the plant over 10 years.

Table 6.10 calculates the total profitability of the process, taking into account the information from Table 6.7, Table 6.8 and Table 6.9. Furthermore, the sales, R&D, administration and management costs are included as well as profit tax.

Table 6.9: Auxiliary operational costs, including wages, services, property tax, insurance and depreciation of the CAPEX as presented in Table 6.7.

Fixed costs	**Remarks**	**OPEX cost (mln$·year^{-1})**
Operating labour including supervision	5 shifts of 10 operators each	5.0
Overhead		2.5
Maintenance		30.0
Property tax and insurance	1% of TCI	7.0
depreciation	10% of TCI	70.0
Total		114.0

Table 6.10: General expenses, taxes and total profitability of the process, taking into account the figures shown in Table 6.8 and Table 6.9.

General expenses (GE)	***% of revenue***	***Total (mln$)***
Sales	3.0%	10.5
R&D	5.3%	18.5
Administration	2.0%	7.0
Management	4.0%	14.0
Totaal		50.0
OPEX + depreciation + GE		279.0
Profit before tax		74
Tax	20% of profit	15
Total Profit		59

The total profitability for the base-case process is calculated to be 59 mln$·y^{-1} after taxes. It is clear that a process around methane coupling can potentially be very profitable. Even though this process design is as much as possible based on proven industrial techniques and processes, it is still based on various significant assumptions in terms of conversion, product selectivity and costs. Figure 6.8 presents a sensitivity analysis from the base case presented in Table 7 and 8 The sensitivity analysis presented in Figure 6.8a shows that the product prices (especially the price of benzene) mainly determines the profitability of the process. This shows that the profitability can grow considerably if the marketability of naphthalene increases. Figure 6.8b shows that the natural gas price also has a significant impact on the profitability. Figure 6.8c also shows that the CAPEX determines the profitability only to a limited extend, which is positive considering the high CAPEX estimate for the reactor and main heat-exchanger (HEX-102) and its uncertainty. The range of 50% is appropriate for natural gas, which price fluctuated by an average of 30% on annual basis between 2000 and 2020 in the USA market, decreasing by 50% over this total period [113]. The market price of benzene fluctuates significantly less at an average of 13% per year, although 2020 saw a drop of 51% in benzene price[114]. These values were not available for naphthalene and hydrogen, although it can be safely assumed that the hydrogen price will closely follow the natural gas price.

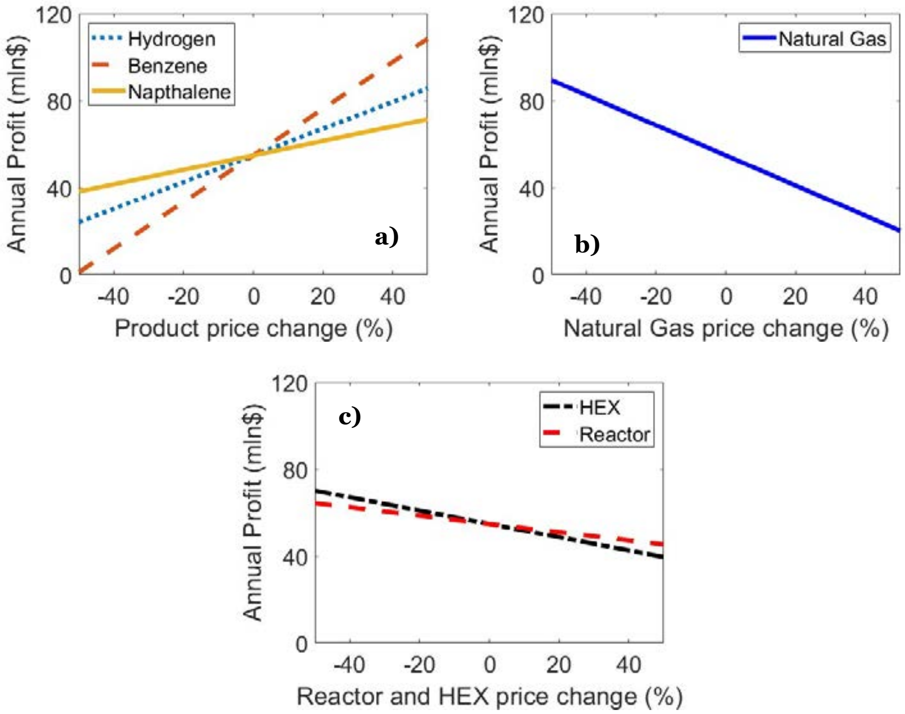

Figure 6.8: The sensitivity of key process factors on the profitability of the catalytic NOCM process: (a) product prices, (b) reactant costs and (c) the main investment cost of the reactor and the main heat exchanger.

6.3 Conclusion

The techno-economic evaluation of a detailed process design for catalytic direct coupling of methane to olefins and aromatics shows significant economic potential to convert cheap natural gas into valuable benzene and hydrogen. Naphthalene is a significant by-product, which is mainly combusted in the current process design for heating the reactor with the consequent emission of CO_2. If electrical heating or hydrogen combustion is used a large quantity of naphthalene will be available, saturating the current market. It is therefore necessary to look for other processes to convert the naphthalene into valuable products, such as mono aromatics. The profitability of the process is mainly determined by the product prices with a dominant role for benzene and hydrogen.

The process also has several challenges such as the integrated heating of the gaseous feed (with the gaseous product) and the heating of the reactor itself with duties of 165 MW and 142 MW, respectively. The excessive heat exchanger area can be reduced by operating at a higher temperature difference and 40°C is estimated to be optimal, increasing the heating and cooling duty. The suggested reactor for this process is a FCC-type reactor operated at a pressure of minimal 5 bar, using the catalyst as the heat transfer medium at the same time. Both the primary heat exchanger as well as the reactor account for more than half of the total investment costs, due to their required capacity and extreme condition (1000°C). Any optimization regarding these units can result in a significant decrease in process costs.

Several critical assumptions are at the basis of the design which need to be validated, for instance the conversion and selectivity at 5 bar and 1000°C, effect of carbon deposition on catalyst activity and the effect of higher concentrations of hydrocarbons (C_{2+}) in the reactor feed on both reactivity and carbon deposit selectivity.

The minimal required reactor pressure is five bar. It is suggested to test reaction performance at increased pressure, as well as concerning impurities in the feed, i.e. C_{2-5} hydrocarbons. Current industrial hydrogen separation techniques are sensitive to fouling and requiring low temperatures. Therefore, deep aromatics removal is required before hydrogen purification. Lastly, the required heat exchangers at the reactor are large and require significant additional heating and cooling, due to the large duty in combination with the low heat transfer coefficient. Overall, an increase in pressure in the reactor will lead to lower heat-exchange area and less compression required for the separation. Experiments should validate if adequate natural gas conversion can be reached at elevated pressure.

6.4 List of abbreviations

FT	Fischer Tropsch
MTO	Methanol to olefins
GTL	Gas to liquids
MDA	Methane dehydroaromatization
OCM	Oxidative coupling of methane
NOCM	Non oxidative coupling of methane
NPV	Net present value
Ktpa	Kilo ton per annum (year)

6.5 Acknowledgements

We acknowledge support from the Dutch National Science Foundation (NWO) and the industrial partners: SABIC, Sasol and BASF.

Keywords: Fe©SiO2 · non-oxidative methane conversion · process design · Naphthalene upgrading

6.6 Supporting information

6.6.1 S.1 Methane conversion calculations

Guo et al. [32] achieved 31% CH_4 conversion at 1000°C, compared to the equilibrium conversion level of 50% [52]. The equilibrium conversion decreases to 35% when increasing the pressure to 5 bar, as shown in Figure 6.4. A conversion of 22% would be achieved if the conversion reported by Guo would decrease to the same extend. Kosinov et al. [63] showed that at higher reactor pressure coking rates diminish significantly, while methane conversion rates increase. Therefore, we assumed that a conversion closer to equilibrium would be achievable at higher pressures. The fractional decrease in coke selectivity reported by Kosinov as function of pressures was used a measure for the fraction closer to equilibrium we could achieve. In this case at 5 bar the coke selectivity was halved compared to atmospheric pressure. Assuming we can also halve the difference between the achieved single-pass conversion and the thermodynamic equilibrium we obtain a single pass conversion of 28%.

Note that when taking into account the conversion of C_{2+} hydrocarbons (explained below) the overall methane conversion drops to 22.3%, based on stream #2 and #7 Table 6.5.

The process performance has been evaluated at pressures between 1-10 bar reactor pressure, Figure S 6.1a shows that the internal stream size significantly reduces up to a pressure of 5 bar, at which point it flattens. The initial decrease is due to the benefits of a compressed stream, the reason for the reduction in this effect is the reduction in methane conversion. The same trend can be seen in Figure S 6.1b, which shows the expected profit per quantity of natural gas used, which also increases up to 5 bar and then flattens off. Thus 5 bar reactor pressure is chosen as an optimized pressure for this system. Although experimental proof is needed to validate this choice.

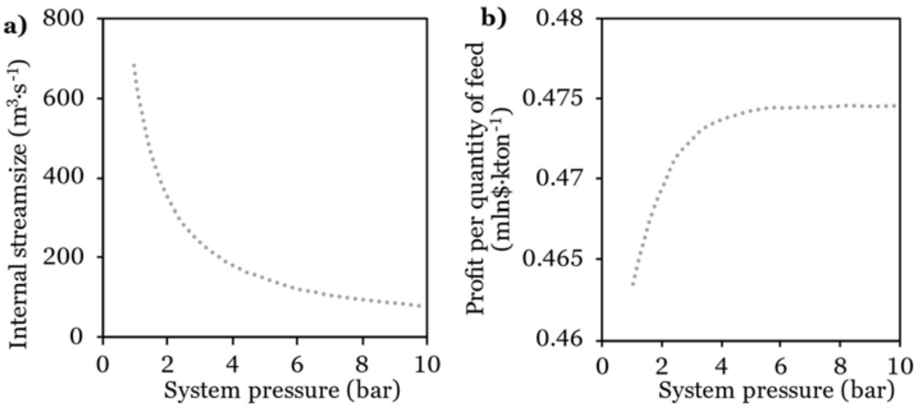

Figure S 6.1: Optimization of reactor pressure; the effect of reactor pressure on (a) the internal stream size in the reactor section ($m^3 \cdot s^{-1}$)) and (b) profit per quantity of methane fed (mln$\$ \cdot kT^{-1}$).

6.6.2 S.2 Product selectivity

For the reactor modelling in Aspen Plus the following approach is applied. The feed stream is split in 4 parallel streams:

1. The first stream is a methane bypass, simulating the unreacted methane.
2. The second stream models the methane conversion in a stochiometric reactor, with the selectivity as described in Table 6.4 in the main text.
3. The third stream contains the higher hydrocarbons as well as hydrogen and inert, excluding C_5. The conversion and selectivity of these reactants are calculated in a Gibbs-reactor where a thermodynamic equilibrium is calculated allowing for the formation of all components listed in Table 6.4, as well as the input reactants, at a T = 1000°C and P = 5 bar. These reactor conditions will be explained later on.
4. The fourth stream converts C_5 to elemental carbon (coke) and hydrogen.

Finally the four product streams are mixed and is assumed to be the reactor product stream.

The assumed selectivity as described in (ii) has been corrected for the variation in pressure, shown in Figure S 6.2. Benzene and naphthalene were corrected according the thermodynamic equilibrium, with ethylene used to close the carbon balance. These theoretical results show the same trend in the MDA reaction as experimentally shown by Kosinov et al. [63].

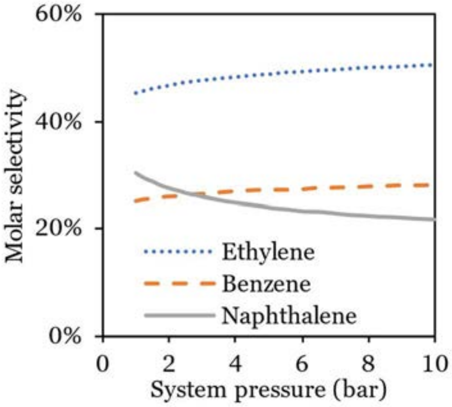

Figure S 6.2: modelled shift in molar selectivity towards ethylene, benzene and naphthalene as function of reactor-pressure.

6.6.3 S.3 Cost analysis of ethylene recovery in the presented NOCM process

The order-of-magnitude calculations concerning the recovery of ethylene using cryogenic distillation are based on Seider and Lewin [115]. The costs for refrigeration are estimated at 50 $\$\cdot GJ^{-1}$ [115] for the cooling needed to reach the 110 K required to liquify ethylene for the separation. Based on the heat capacity of stream #34 in Table 6.5 and the temperature difference of 184 K between 21°C and 110 K, Aspen Thermo Data calculates a minimum energy requirement of 9.3 $MJ\cdot kg_{ethylene}^{-1}$. The real required energy input for cryogenic distillation is estimated at four times the minimum value [116], resulting in 37 $MJ\cdot kg_{ethylene}^{-1}$. This results in a cost of 1900 $\$\cdot ton_{ethylene}^{-1}$ which is nearly twice the current market value of 1000 $\$\cdot ton_{ethylene}^{-1}$ [101]. Note that the value will likely be higher when the required CAPEX is including [117].

6.6.4 S.4 Composition of all streams considered for the process

Table S 6.1 The conditions, molar flows and molar fractions of all process streams represented in Figure 6.5 of the main text.

# Stream	**1**	**2**	**3**	**4**	**5**	**6**	**7**	**8**	**9**	**10**	**11**	**12**	**13**	**14**
T (°C)	20	21	590	1000	600	100	90	90	90	200	90	90	90	218
P (bar)	5	5	5	5	5	5	5	5	5	12.4	12.4	12.4	12.4	35
n (Mmol·hr^{-1})	4.71	20.2	20.2	23.5	23.5	23.5	23.5	0.22	23.2	23.2	23.2	0.05	23.2	23.2
CH_4 (%)	91.0	83.0	83.0	55.5	55.6	55.6	55.6	0.39	56.1	56.1	56.1	1.0	56.2	56.2
C_2H_6 (%)	4.9	1.1	1.1	0	0	0	0	0	0	0	0	0	0	0
C_3H_6 (%)	1.7	0.4	0.4	0	0	0	0	0	0	0	0	0	0	0
C_4H_{10} (%)	0.7	0.15	0.15	0	0	0	0	0	0	0	0	0	0	0
C_5H_{12} (%)	0.5	0.12	0.12	0	0	0	0	0	0	0	0	0	0	0
C_2H_4 (%)	0	2.2	2.2	2.0	2.0	2.0	2.0	0.05	2.0	2.0	2.0	0.13	2.0	2.0
C_6H_6 (%)	0	0.09	0.09	1.3	1.3	1.3	1.3	4.7	1.3	1.3	1.3	11.4	1.3	1.3
$C_{10}H_8$ (%)	0	0.01	0.01	1.2	1.2	1.2	1.2	94.6	0.3	0.3	0.3	87.4	0.11	0.11
H_2 (%)	0	4.1	4.1	32.4	32.4	32.4	32.4	0.01	32.7	32.7	32.7	0.03	32.8	32.8
N_2 (%)	1.3	8.8	8.8	7.5	7.5	7.5	7.5	0.02	7.6	7.6	7.6	0.06	7.6	7.6

Stream	**15**	**16**	**17**	**18**	**19**	**20**	**21**	**22**	**23**	**24**	**25**	**26**	**27**	**28**
T (°C)	90	96	96	174	190	71	210	152	250	91	91	20	20	105
P (bar)	35	35	2	2	0.2	0.1	2	2	2	2	2	2	2	5
n (Mmol·hr^{-1})	23.2	3.7	3.7	3.7	3.3	0.42	0.42	0.68	0.28	0.41	0.41	0.28	0.13	0.13
CH_4 (%)	56.2	2.8	2.8	2.8	0	24.2	24.2	14.8	0	24.9	24.9	0.45	78.3	78.3
C_2H_6 (%)	0	0	0	0	0	0	0	0	0	0	0	0	0	0.04
C_3H_6 (%)	0	0	0	0	0	0	0	0	0	0	0	0	0	0
C_4H_{10} (%)	0	0	0	0	0	0	0	0	0	0	0	0	0	0
C_5H_{12} (%)	0	0	0	0	0	0	0	0	0	0	0	0	0	0
C_2H_4 (%)	2.0	0	0	0	0	3.0	3.0	1.9	0	3.1	3.1	0.29	9.3	9.3
C_6H_6 (%)	1.25	7.6	7.6	7.6	0.2	64.8	64.8	41.6	0	69.6	69.6	99.2	5.0	5.0
$C_{10}H_8$ (%)	0.11	17.3	17.3	17.3	18.8	5.6	5.6	40.3	99.8	0	0	0.01	0	0
H_2 (%)	32.8	0.08	0.08	0.08	0	0	0	0.45	0	0.75	0.75	0	2.40	2.4
N_2 (%)	7.63	0.18	0.18	0.18	0.08	1.6	1.6	0.95	0	1.6	1.6	0.01	5.04	5.0
Sulfolane (%)	0	71.8	71.8	71.8	81.0	0.67	0.67	0.08	0.19	0	0	0	0.01	0.01

Stream	**29**	**30**	**31**	**32**	**33**	**34**	**35**	**36**	**37**	**38**	**39**	**40**	**41**
T (°C)	94	94	94	-2	-1	21	21	21	192	106	90	90	90
P (bar)	35	1	35	5	5	5	5	5	35	35	35	35	35
n (Mmol·hr^{-1})	22.8	7.1	15.7	15.7	15.8	15.8	0.32	15.5	3.3	3.3	3.3	0	3.3
CH_4 (%)	56.8	4.1	80.6	80.6	80.5	80.5	80.5	80.5	0	0	0	0	0
C_2H_6 (%)	0	0	0	0	0	0	0	0	0	0	0	0	0
C_3H_6 (%)	0	0	0	0	0	0	0	0	0	0	0	0	0
C_4H_{10} (%)	0	0	0	0	0	0	0	0	0	0	0	0	0
C_5H_{12} (%)	0	0	0	0	0	0	0	0	0	0	0	0	0
C_2H_4 (%)	2.0	0.08	2.9	2.9	2.9	2.9	2.9	2.9	0	0	0	0	0
C_6H_6 (%)	0.05	0	0.08	0.08	0.12	0.12	0.12	0.12	0.2	0.2	0.2	0	0.2
$C_{10}H_8$ (%)	0	0	0.01	0.01	0.01	0.01	0.01	0.01	18.8	18.8	18.8	0	18.8
H_2 (%)	33.4	95.5	5.4	5.4	5.4	5.4	5.4	5.4	0	0	0	0	0
N_2 (%)	7.7	0.34	11.0	11.0	11.0	11.0	11.0	11.0	0.08	0.08	0.08	0	0.08
Sulfolane (%)	0	0	0	0	0	0	0	0	81.0	81.0	81.0	100.0	81.0

6.7 References

1. Mesters, C., *A Selection of Recent Advances in C1 Chemistry*. Annual Review of Chemical and Biomolecular Engineering, 2016. **7**: p. 223-238.

2. Karakaya, C. and R.J. Kee, *Progress in the direct catalytic conversion of methane to fuels and chemicals*. Progress in Energy and Combustion Science, 2016. **55**: p. 60-97.

3. Taifan, W. and J. Baltrusaitis, *CH4 conversion to value added products: Potential, limitations and extensions of a single step heterogeneous catalysis*. Applied Catalysis B: Environmental, 2016. **198**: p. 525–547.

4. Galadima, A. and O. Muraza, *Advances in Catalyst Design for the Conversion of Methane to Aromatics: A Critical Review*. Catalysis Surveys from Asia, 2019. **23**: p. 149-170.

5. Gao, Y., L.M. Neal, D. Ding, W. Wu, C. Baroi, A. Gaffney, and F. Li, *Recent Advances in Intensified Ethylene Production – A Review*. ACS Catalysis, 2019. **9**(9): p. 8592-5621.

6. Zimmermann, H. and R. Walzl, *Ethylene*, in *Ullmann's Encyclopedia of Industrial Chemistry*. 2009, Wiley-VCH Verlag GmbH & Co. KGaA.

7. Folkins, H.O., *Benzene*, in *Ullmann's Encyclopedia of Industrial Chemistry*. 2000, Wiley-VCH Verlag GmbH & Co. KGaA.

8. *Gas 2020*. 2020, IEA: Paris.

9. Conti, J., P. Holtberg, J. Diefenderfer, A. LaRose, J.T. Turnure, and L. Westfall, *International Energy Outlook 2016* 2016, U.S. Energy Information Administration.

10. McFarland, E., *Unconventional Chemistry for Unconventional Natural Gas*. Science, 2012. **338**(6105): p. 340-342.

11. Abbasi, H., C. Benson, T. Briselden, P. Angelini, and D. Brooks, *Roadmap for Process Heating Technology*. 2001, Industrial Heating Equipment Association.

12. Orella, M.J., Y. Román-Leshkov, and F.R. Brushett, *Emerging opportunities for electrochemical processing to enable sustainable chemical manufacturing*. Current Opinion in Chemical Engineering, 2018. **20**: p. 159-167.

13. Yeh, S., N.P. Lutsey, and N.C. Parker, *Assessment of Technologies to Meet a Low Carbon Fuel Standard*. Environmental Science & Technology, 2009. **43**(18): p. 6907-6914.

14. Wismann, S.T., J.S. Engbæk, S.B. Vendelbo, F.B. Bendixen, W.L. Eriksen, K. Aasberg-Petersen, C. Frandsen, I. Chorkendorff, and P.M. Mortensen, *Electrified methane reforming: A compact approach to greener industrial hydrogen production*. Science, 2019. **364**(6442): p. 756-759.

15. Karytsas, S. and H. Theodoropoulou, *Public awareness and willingness to adopt ground source heat pumps for domestic heating and cooling*. Renewable and Sustainable Energy Reviews, 2014. **34**: p. 49-57.

16. Valancius, R., R.M. Singh, A. Jurelionis, and J. Vaiciunas, *A Review of Heat Pump Systems and Applications in Cold Climates: Evidence from Lithuania*. Energies, 2019. **12**(22): p. 4331.

17. Klerk, A.d., *Fischer–Tropsch Process*, in *Kirk-Othmer Encyclopedia of Chemical Technology*. 2013. p. 1-20.

18. Wittcoff, H.A., B.G. Reuben, and J.S. Plotkin, *Chemicals from Methane*. 2012, John Wiley & Sons, Inc.

19. Kee, R.J., C. Karakaya, and H. Zhu, *Process intensification in the catalytic conversion of natural gas to fuels and chemicals*. Proceeding of the Combustion Institute, 2017. **36**: p. 51-76.

20. Abdulrasheed, A., A.A. Jalil, Y. Gambo, M. Ibrahim, H.U. Hambali, and M.Y.S. Hamid, *A review on catalyst development for dry reforming of methane to syngas: Recent advances*. Renewable and Sustainable Energy Reviews, 2019. **108**: p. 175-193.

21. Wang, B., S. Albarracín-Suazo, Y. Pagán-Torres, and E. Nikolla, *Advances in methane conversion processes*. Catalysis Today, 2017. **285**: p. 147-158.

22. Huang, K., J.B. Miller, G.W. Huber, J.A. Dumesic, and C.T. Maravelias, *A General Framework for the Evaluation of Direct Nonoxidative Methane Conversion Strategies*. Joule, 2018. **2**: p. 349-365.

23. Amghizar, I., L.A. Vandewalle, K.M.V. Geem, and G.B. Marin, *New Trends in Olefin Production*. Engineering, 2017. **3**: p. 171-178.

24. Appl, M., *Ammonia*, in *Ullmann's Encyclopedia of Industrial Chemistry*. 2011.

25. A.Wood, D., C. Nwaoha, and B.F. Towler, *Gas-to-liquids (GTL): A review of an industry offering several routes for monetizing natural gas*. Journal of Natural Gas Science and Engineering, 2012. **9**: p. 196-208.

26. Panahia, M., E. Yasaria, and A. Rafiee, *Multi-objective optimization of a gas-to-liquids (GTL) process with staged Fischer-Tropsch reactor*. Energy Conversion and Management, 2018. **163**: p. 239-249.

27. ExxonMobil Chemicals, *MTG Factsheet*. 2018.

28. Royal Dutch Shell. *Pearl GTL - Overview*. [cited 2021; Available from: https://www.shell.com/about-us/major-projects/pearl-gtl/pearl-gtl-an-overview.html.

29. Tian, P., Y. Wei, M. Ye, and Z. Liu, *Methanol to Olefins (MTO): From Fundamentals to Commercialization*. ACS Catalysis, 2015. **5**(3): p. 1922-1938.

30. Chen, J.Q., A. Bozzano, B. Glover, T. Fuglerud, and S. Kvisle, *Recent advancements in ethylene and propylene production using the UOP/Hydro MTO process*. Catalysis Today, 2005. **106**(1-4): p. 103-107.

31. Ren, T., M.K. Patel, and K. Blok, *Steam cracking and methane to olefins: Energy use, CO2 emissions and production costs*. Energy, 2008. **33**(5): p. 817-833.

32. Guo, X., G. Fang, G. Li, H. Ma, H. Fan, L. Yu, C. Ma, X. Wu, D. Deng, M. Wei, D. Tan, R. Si, S. Zhang, J. Li, L. Sun, Z. Tang, X. Pan, and X. Bao, *Direct, Nonoxidative Conversion of Methane to Ethylene, Aromatics, and Hydrogen*. Science, 2014. **344**(6184): p. 616-619.

33. Mohajerani, S., A. Kumar, and A.O. Oni, *A techno-economic assessment of gas-to-liquid and coal-to-liquid plants through the development of scale factors*. Energy, 2018. **150**: p. 681-693.

34. Rui, Z., P.A. Metz, D.B. Reynolds, G. Chen, and X. Zhou, *Historical pipeline construction cost analysis*. Int. J. Oil, Gas and Coal Technology, 2011

35. Jin, C. and Y. Lim, *Optimization and economic evaluation of integrated natural gas liquids (NGL) and liquefied natural gas (LNG) processing for lean feed gas*. Applied Thermal Engineering, 2018. **149**(25): p. 1265-1273.

36. Stewart, M., *Alternative approach required to contain costs of remote Australian offshore gas fields*, in *Offshore*. 2013.

37. Willyard, K.A. and G.W. Schade, *Flaring in two Texas shale areas: Comparison of bottom-up with top-down volume estimates for 2012 to 2015*. Science of The Total Environment, 2019. **691**: p. 243-251.

38. Sun, K., D.M. Ginosar, T. He, Y. Zhang, M. Fan, and R. Chen, *Progress in Nonoxidative Dehydroaromatization of Methane in the Last 6 Years*. Industrial & Engineering Chemistry Research, 2018. **57**: p. 178-1789.

39. Olivos-Suarez, A.I., A.g. Szécsényi, E.J.M. Hensen, J. Ruiz-Martinez, E.A. Pidko, and J. Gascon, *Strategies for the Direct Catalytic Valorization of Methane Using Heterogeneous Catalysis: Challenges and Opportunities*. ACS Catalysis, 2016. **6**: p. 2965-2981.

40. Kondratenko, E.V., T. Peppel, D. Seeburg, V.A. Kondratenko, N. Kalevaru, A. Martin, and S. Wohlrab, *Methane conversion into different hydrocarbons or oxygenates: current status and future perspectives in catalyst development and reactor operation*. Catalysis Science & Technology, 2017. **7**: p. 366-381.

41. Farrell, B.L., V.O. Igenegbai, and S. Linic, *A Viewpoint on Direct Methane Conversion to Ethane and Ethylene Using Oxidative Coupling on Solid Catalysts*. ACS Catalysis, 2016. **6**: p. 4340-4346.

42. Sakbodin, M., Y. Wu, S.C. Oh, E.D. Wachsman, and D. Liu, *Hydrogen-Permeable Tubular Membrane Reactor: Promoting Conversion and Product Selectivity for Non-Oxidative Activation of Methane over an FeVSiO2 Catalyst*. Angewandte Chemie, 2016. **55**: p. 16149 –16152.

43. Oh, S.C., E. Schulman, J. Zhang, J. Fan, Y. Pan, J. Meng, and D. Liu, *Direct Non-Oxidative Methane Conversion in a Millisecond Catalytic Wall Reactor*. Angewandte Chemie, 2019. **58**: p. 7083-7086.

44. Han, S.J., S.W. Lee, H.W. Kim, S.K. Kim, and Y.T. Kim, *Nonoxidative Direct Conversion of Methane on Silica-Based Iron Catalysts: Effect of Catalytic Surface*. ACS Catalysis, 2019. **9**: p. 7984-7997.

45. Chen, Y., X. Wang, X. Luo, X. Lin, and Y. Zhang, *Non-Oxidative Methane Conversion Using Lead- and Iron-Modified Albite Catalysts in Fixed-Bed Reactor*. Chinese Journal of Chemistry, 2018. **36**: p. 531-537.

46. Okolie, C., Y. Lyu, L. Kovarik, E. Stavitski, and C. Sievers, *Coupling of Methane to Ethane, Ethylene, and Aromatics over Nickel on Ceria–Zirconia at Low Temperatures*. ChemCatChem, 2018. **10**: p. 2700-2708.

47. Xie, P., T. Pu, A. Nie, S. Hwang, S.C. Purdy, W. Yu, D. Su, J.T. Miller, and C. Wang, *Nanoceria-Supported Single-Atom Platinum Catalysts for Direct Methane Conversion*. ACS Catalysis, 2018. **8**: p. 4044-4048.

48. Xiao, Y. and A. Varma, *Highly Selective Nonoxidative Coupling of Methane over Pt-Bi Bimetallic Catalysts*. ACS Catalysis, 2018. **8**: p. 2735-2740.

49. Nishikawa, Y., H. Ogihara, and I. Yamanaka, *Liquid-Metal Indium Catalysis for Direct Dehydrogenative Conversion of Methane to Higher Hydrocarbons*. ChemistrySelect, 2017. **2**: p. 4572-4576.

50. Kim, S.K., H.W. Kim, S.J. Han, S.W. Lee, J. Shin, and Y.T. Kim, *Mechanistic and microkinetic study of non-oxidative methane coupling on a single-atom iron catalyst*. Communications Chemistry, 2020. **3**(58): p. 1-8.

51. Zhao, T. and H. Wang, *Methane dehydro-aromatization over Mo/HZSM-5 catalysts in the absence of oxygen: Effect of steam-treatment on catalyst stability*. Journal of Natural Gas Chemistry, 2011. **20**(5): p. 547-552.

52. Guéret, C., M. Daroux, and F. Billaud, *Methane pyrolysis: thermodynamics*. Chemical Engineering Science, 1997. **52**(5): p. 815-827.

53. Keller, G.E. and M.M. Bhasin, *Synthesis of ethylene via oxidative coupling of methane: I. Determination of active catalysts*. Journal of Catalysis, 1982. **73**(1): p. 9-19.

54. Arakawa, H., M. Aresta, J.N. Armor, M.A. Barteau, E.J. Beckman, A.T. Bell, J.E. Bercaw, C. Creutz, E. Dinjus, D.A. Dixon, K. Domen, D.L. DuBois, J. Eckert, E. Fujita, D.H. Gibson, W.A. Goddard, D.W. Goodman, J. Keller, G.J. Kubas, H.H. Kung, J.E. Lyons, L.E. Manzer, T.J. Marks, K. Morokuma, K.M. Nicholas, R. Periana, L. Que, J. Rostrup-Nielson, W.M.H. Sachtler, L.D. Schmidt, A. Sen, G.A. Somorjai, P.C. Stair, B.R. Stults, and W. Tumas, *Catalysis Research of Relevance to Carbon Management: Progress, Challenges, and Opportunities*. Chemical Reviews, 2001. **101**(4): p. 953-996.

55. Lunsford, J.H., *Catalytic conversion of methane to more useful chemicals and fuels: a challenge for the 21st century*. Catalysis Today, 2000. **63**(2-4): p. 165-174.

56. Luo, L., X. Tang, W. Wang, Y. Wang, S. Sun, F. Qi, and W. Huang, *Methyl Radicals in Oxidative Coupling of Methane Directly Confirmed by Synchrotron VUV Photoionization Mass Spectroscopy*. Scientific Reports, 2013. **3**.

57. Arndt, S., G. Laugel, S. Levchenko, R. Horn, M. Baerns, and M. Scheffler, *A Critical Assessment of Li/MgO-Based Catalysts for the Oxidative Coupling of Methane*. Catalysis Reviews, 2011. **53**(4): p. 424-514.

58. Zavyalova, U., M. Holena, R. Schlögl, and M. Baerns, *Statistical Analysis of Past Catalytic Data on Oxidative Methane Coupling for New Insights into the Composition of High-Performance Catalysts*. ChemCatChem, 2011. **3**(12): p. 1935-1947.

59. Kuo, J.C.W., C.T. Kresge, and R.E. Palermo, *Evaluation of direct methane conversion to higher hydrocarbons and oxygenates*. Catalysis Today, 1989. **4**(3-4): p. 463-470.

60. Wozny, G. and H. Arellano-Garcia, *Oxidative Coupling of Methane: A Design of Integrated Catalytic processes*. Chemical Engineering Transactions, 2010. **21**: p. 1399-1404.

61. Zeng, Y., F.T. Akin, and Y.S. Lin, *Oxidative coupling of methane on fluorite-structuredsamarium–yttrium–bismuth oxide*. Applied Catalysis A: General 2001. **213**: p. 33-45.

62. Nagaki, D.A., Z. Zhao, M.N.Z. Myint, I. Lengyel, A. Mamedov, C.W. Gundlach, K. Sankaranarayanan, and D. Falcone, 2018, *Method for Producing Hydrocarbons by Non-Oxidative Coupling of Methane*, US 9 , 902 , 665 B2

63. Kosinov, N., E.A. Uslamin, L. Meng, A. Parastaev, Y. Liu, and E.J.M. Hensen, *Reversible Nature of Coke Formation on Mo/ZSM-5 Methane Dehydroaromatization Catalysts*. Angewandte Chemie, 2019. **58**: p. 7068-7072.

64. Corredor, E.C., P. Chitta, and M.D. Deo, *Techno-economic evaluation of a process for direct conversion of methane to aromatics*. Fuel Processing Technology, 2019. **183**: p. 55-61.

65. Do, T.N., Y.T. Kim, and J. Kim, *Technical and Economic Feasibility of Direct Methane Conversion for Hydrocarbon Production: Process Design and Techno-economic Analysis*. Computer Aided Chemical Engineering, 2020. **48**: p. 1015-1020.

66. Gattis, S.C. and E.R. Peterson, 2005, *Process for the Conversion of Natural Gas to Hydrocarbon Liquids*,

67. Obradović, A., J.W. Thybaut, and G.B. Marin, *Oxidative Coupling of Methane: Opportunities for Microkinetic Model-Assisted Process Implementations*. Chemical Engineering & Technology, 2016. **39**(11): p. 1996-2010.

68. Zhang, Z.-G., *Process, reactor and catalyst design: Towards application of direct conversion of methane to aromatics under nonoxidative conditions*. Carbon Resources Conversion, 2019. **2**(3): p. 157-174.

69. Ma, S., X. Guo, L. Zhao, S. Scott, and X. Bao, *Recent progress in methane dehydroaromatization: From laboratory curiosities to promising technology*. Journal of Energy Chemistry, 2013. **22**(1): p. 1-20.

70. Salehi, M.-S., M. Askarishahi, H.R. Godini, O. Görke, and G. Wozny, *Sustainable Process Design for Oxidative Coupling of Methane (OCM): Comprehensive Reactor Engineering via Computational Fluid Dynamics (CFD) Analysis of OCM Packed-Bed Membrane Reactors*. Industrial & Engineering Chemistry, 2016. **55**(12): p. 3287-3299.

71. Stünkel, S., H. Trivedi, H.R. Godini, S. Jašo, N. Holst, S. Arndt, J. Steinbach, and R. Schomäcker, *Oxidative Coupling of Methane: Process Design, Development and Operation in a Mini-Plant Scale*. Chemie Ingenieur Technik, 2012. **84**(11): p. 1989-1996.

72. Holmen, A., O. Olsvikb, and O.A. Rokstad, *Pyrolysis of natural gas: chemistry and process concepts*. Fuel processing technology, 1995. **42**: p. 249-267.

73. National Institute of Standards and Technology. *NIST Chemistry Webook, SRD 69*. 2021 [cited 2021; Available from: https://webbook.nist.gov/.

74. Foss, M.M., *Interstate Natural Gas-Quality Specifications & Interchangeability* 2004, Center for Energy Economics.

75. Uniongas. *Chemical Composition of Natural Gas*. 2017; Available from: https://www.uniongas.com/about-us/about-natural-gas/chemical-composition-of-natural-gas.

76. Douglas, J.M., *Conceptual Design Chemical Processes*. 1988: McGraw-Hill Chemical Engineering Series.

77. Barnicki, S.D. and J.R. Fair, *Separation System Synthesis: A Knowledge-Based Approch 1. Liquid Mixture Separations*. Industrial & Engineering Chemistry Research, 1990. **29**: p. 421-432.

78. Barnicki, S.D. and J.R. Fair, *Separation System Synthesis: A Knowledge-Based Approach. 2. Gas/Vapor Mixtures*. industrial & Engineering Chemistry Research, 1992. **31**: p. 1679-1694.

79. Aspen Technology, I., *Aspen Plus*. 2018.

80. Ogihara, H., H. Tajima, and H. Kurokawa, *Pyrolysis of mixtures of methane and ethane: activation of methane with the aid of radicals generated from ethane*. Reaction Chemistry & Engineering, 2020. **5**: p. 145-153.

81. Schneider, I.A., *Über die Rolle des Äthans bei der thermishen Methanzersetzung*. Zeitschrift für Physikalische Chemie, 1963. **223**(1): p. 234-248.

82. Germain, J. and C. Vaniscotte, *Craquage du Methane dans un Reacteur Tubulaire. 3. Effet Iniateur de l'Ethane*. bulletin de la Société Chimique de France, 1958.

83. Rokstad, O.A., O. Olsvik, and A. Holmen, *Thermal Coupling of Methane*. Natural Gas Conversion, 1991: p. 533-539.

84. U.S. Energy Information Administration, *Electric Power Monthly*, in *Monthly Electric Power Industry Report*. 2020.

85. Hub, H. *Hub Natural Gas Spot Price (Dollars per Million Btu)*. 2019; Available from: https://www.eia.gov/dnav/ng/hist/rngwhhdm.htm.

86. Engineering ToolBox, *Fuel Gases Heating Values*. 2005.

87. Technavio, *Global Naphthalene Market 2019-2023*. 2019.

88. Henkel, K.D., *Reactor Types and Their Industrial Applications*, in *Ullmann's Encyclopedia of Industrial Chemistry*. 2000. p. 1-49.

89. Seo, S.-T., W. Won, K.S. Lee, C. Jung, and S. Lee, *Repetitive control of CATOFIN process*. Korean Journal of Chemical Engineering, 2008. **24**: p. 921–926.

90. Alvarado, D. and D.E. Gottschlich. *Membrane Matrimony*. 2018 27-05-2020]; Available from: https://www.mtrinc.com/wp-content/uploads/2018/08/MembraneMatrimony-HydrocarbonEngineering.pdf.

91. Edlund, D., *Hydrogen Membrane Technologies and Application in Fuel Processing*, in *Hydrogen and Syngas Production and Purification Technologies*, K. Liu, C. Song, and V. Subramani, Editors. 2009, American Institute of Chemical Engineers.

92. Zolandz, R.R. and G.K. Fleming, *Gas permeation: Applications*, in *Membrane Handbook*. 1992, Van Nostrand Reinhold. p. 78–85.

93. (MTR)', M.T.a.R. *Hydrogen Purification in Refineries*. 27-05-2020]; Available from: https://www.mtrinc.com/our-business/refinery-and-syngas/hydrogen-purification-in-refineries/.

94. Baker, R.W., *Membranes and Modules*, in *Membrane Technology and Applications, Third Edition*. 2012, John Wiley & Sons, Ltd.

95. Zhang, K. and D. Way, *Palladium-copper membranes for hydrogen separation*. Separation and Purification Technology, 2017. **186**: p. 39-44.

96. David, E. and J. Kopac, *Devlopment of palladium/ceramic membranes for hydrogen separation*. International Journal of Hydrogen Energy, 2011. **36**(7): p. 4498-4506.

97. Yun, S. and T. Oyama, *Correlations in palladium membranes for hydrogen separation: A review*. Journal of Membrane Science, 2011. **375**(1-2): p. 28-45.

98. Khatib, S.J., S. TedOyama, K.R.d. Souza, and F.B. Noronha, *Chapter 2 - Review of Silica Membranes for Hydrogen Separation Prepared by Chemical Vapor Deposition*. Membrane Science and Technology, 2011. **14**: p. 25-60.

99. Sircar, S. and a.T.C. Golden, *Pressure Swing Adsorption Technology for Hydrogen Production*, in *Hydrogen and Syngas Production and Purification Technologies*, K. Liu, C. Song, and V. Subramani, Editors. 2010, American Institute of Chemical Engineers.

100. Ploegmakers, J., Adriaan R. T. Jelsma, A.G.J.v.d. Ham, and K. Nijmeijer, *Economic Evaluation of Membrane Potential for Ethylene/Ethane Separation in a Retrofitted Hybrid Membrane-Distillation Plant Using Unisim Design*. Industrial & Engineering Chemistry, 2013. **52**: p. 6524-6539.

101. Leingchan, R., *Thailand Indusrty Outlook 2019-21 Petrochemical Industry*. 2019. p. 12.

102. Collin, G., H. Höke, and H. Greim, *Naphthalene and Hydronaphthalenes*, in *Ullmann's Encyclopedia of Industrial Chemistry*. 2003, Wiley-VCH Verlag GmbH & Co.

103. Shen, Z., P. He, A. Wang, J. Harrhy, S. Meng, H. Peng, and H. Song, *Conversion of naphthalene as model compound of polyaromatics to mono-aromatic hydrocarbons under the mixed hydrogen and methane atmosphere*. Fuel, 2019. **243**: p. 469-477.

104. IEA, *The Future of Hydrogen*, IEA, Editor. 2019, IEA: Paris.

105. Milligan, D. and J. Milligan. *Matche. Equipment Costs*. 2019 [cited 2019; Available from: http://www.matche.com/.

106. Peters, S.M., K.D. Timmerhaus, and R. E.West. *Equipment Costs: Plant Design and Economics for Chemical Engineers*. 2019 [cited 2019; Available from: http://www.mhhe.com/engcs/chemical/peters/data/ce.html.

107. Towler, G. and R. Sinnot, *Chemical Engineering Design: Principle, Practice and Economics of Plant and Process Design*, 2nd, Editor. 2013, Elsevier. p. 307–354.

108. Vogt, E.T.C. and B.M. Weckhuysen, *Fluid catalytic cracking: recent developments on the grand old lady of zeolite catalysis*. Chemical Society Reviews, 2015. **44**: p. 7342-7370.

109. marketinsightsreports, *Global Sulfolane Market Research Report*. 2018.

110. Venezia, Nicholson, Stevenson, Rangel, Chakravarty, and Lee, *Argus Benzene Annual*, in *Benzene Annual 2018*. 2018.

111. Industry Federation, *China CN: Market Price: Monthly Avg: Organic Chemical Material: Industrial Naphthalene 90% or Above*. 2020.

112. S&P Global, *Platts Hydrogen Assessments*. 2020.

113. Macrotrends.net. *Natural Gas Prices - Historical Chart*. 2021 28-10-2021]; Available from: https://www.macrotrends.net/2478/natural-gas-prices-historical-chart.

114. Barchart.com. *SGX Benzene Historical Prices*. 2021 28-10-2021]; Available from: https://www.barchart.com/futures/quotes/H9G21/historical-prices?orderBy=contractExpirationDate&orderDir=asc.

115. Seider, W.D., J.D. Seader, D.R. Lewin, and S. Widagdo, *Product and Process design principles*, ed. J. Welter. 2009: Donald Fowley.

116. Chorowski, M. and W. Gizicki, *Technical and economic aspects of oxygenseparation for oxy-fuel purposes*. Archives of Thermodynamics, 2015. **36**: p. 157-170.

117. Ulrich, G.D. and P.T. Vasudevan, *How to Estimate Utility Costs*. Engineering Practice, 2006: p. 66-69.

Chapter 7

Alternative synthesis methods for silica supported lattice confined catalyst for use in direct non-oxidative coupling of methane

Abstract

Two graft-synthesis methods are used as alternative synthesis methods for the melt-fusion synthesis of the Fe©SiO_2 catalyst, used in catalytic non-oxidative coupling of methane. The first synthesis method adapts the graft-synthesis method reported in literature for producing an atomically disperse Fe/SiO_2 catalyst used for propane dehydrogenation. This synthesis method is based on grafting a bis(2,4-dimethyl-1,3-pentadienide)Fe(II) (Fe(oCp)$_2$) complex on the silica surface. The second synthesis method is developed inhouse relying on Fe(II) Phthalocyanine (Fe(II) Pht) as metal-organic compound for grafting. The catalyst based on Fe(oCp)$_2$ has highly similar performance to the original melt-fusion Fe©SiO_2 catalyst, whereas the Fe(II) Pht based catalyst caused both higher methane conversion as well as significantly higher coke selectivity. The increased activity and coke selectivity of the Fe(II) Pht catalyst is attributed to Fe nanoparticle formation. In a separate research track, the synthesis of a Ru/SiO_2 is attempted, to evaluate if ruthenium is a more active metal than iron for the methane coupling reaction. Two synthesis routes are attempted, one is based on ball-milling, adapted from the original synthesis method of the Fe©SiO_2 catalyst, the second synthesis method is based on a sol-gel synthesis. The sol-gel based synthesis resulted in a thermally stable Ru/SiO_2 catalyst, whereas the ball-mill based synthesis lead to complete sublimation of RuO_2 during fusion at 1700°C. The Ru/SiO_2 catalyst has a slightly better performance than blank SiO_2, but significantly lower conversion when compared to the Fe©SiO_2 catalyst, it is thus concluded that the Ru/SiO_2 catalyst is significantly less active than their Fe©SiO_2 counterpart. The graft synthesis based on Fe(oCp)$_2$ shows high promise as alternative synthesis method for Fe©SiO_2 and will allow for significant control over the shape and size of the catalyst.

7.1 Introduction

The method employed for the synthesis of the Fe©SiO_2 catalyst [1] is both process-technically intensive as well as difficult to control. Personal communication with Xinhe Bao [2] showed that a zirconia milling jar with de-gassing lid was used in the original work. The Vickers hardness of yttria stabilized zirconia is 1250 $kg \cdot mm^{-2}$ [3] whereas quartz has a hardness between 1103-1260 $kg \cdot mm^{-2}$ [4], it is thus inevitable that zirconia from the milling balls will wear off into the milled powder after 16h of milling. The zirconia content in the catalyst was also observed by Han et al. [5], although no other author working on the Fe©SiO_2 catalyst mentioned it [1, 6-8]. It is proposed that the dots in the STEM-HAADF image presented in Figure 2a by Guo et al. [1] (Figure S 7.1 for quick reference) are more likely Zr atoms in the SiO_2 matrix than the Fe atoms proposed by the author, due to the higher atomic mass of Zr compared to Fe, resulting in the higher contrast seen in the image. Work by Zhang et al. [9] showed that uncoordinated Zr sites can be active in C-H bond activation in a fashion similar to that proposed by Guo et al. [1] for the Fe sites. It can thus be proposed that at least part of the activity of the Fe©SiO_2 catalyst stems from the traces of zirconia. This hypothesis can be tested by changing the Zr concentration in the Fe©SiO_2 catalyst.

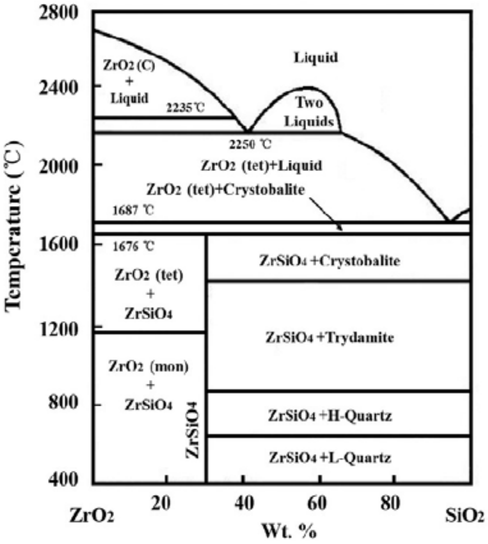

Figure 7.1: Phase diagram of SiO_2 and ZrO_2 [10].

7.1.1 Experimental details concerning the Fe©SiO_2 synthesis

Fusion of the powder was performed in ZrO_2 or corundum crucibles both in this work as well as by Guo et al. [2]. Trials performed for this work showed that corundum crucibles shattered in the oven due to the thermal stress, thus only ZrO_2 crucibles were used during synthesis in this thesis. The zirconia content in the fused powder was found to be a determining factor in the success of the fusion at 1700°C (i.e. fusion into a solid pallet, rather than remaining a powder), which can be understood when looking at the phase diagram of SiO_2-ZrO_2, Figure 7.1. Pure quartz melts only at 1713°C [11], the melting point decreases to 1687°C when adding up to 5.5% ZrO_2, after which it increases again. It is likely that the Fe_2SiO4 also influences the melting point of the mixture, although the effect was clearly not enough to melt Fe_2SiO_4/SiO_2 without ZrO_2, as a pure mixture of Fe_2SiO_4/SiO_2 would remain a powder after fusion at 1700°C. It was found that the crucibles turned from beige to dark brown over extended use, signifying iron oxide penetrating into the crucible. The iron content was found to make the crucibles brittle after about 20 fusions leading to the crucible shattering. Iron content in the final catalyst was slightly reduced by the leaching as can be seen in Table 7.1.

Table 7.1: Elemental composition of the catalyst precursor before and after fusion at 1700°C.

Element	**Fe/SiO_2 power pre-fusion**	**Fused Fe©SiO_2**
Si	45.1	45.4
Fe	0.6	0.5
Zr	2.4	2.1
Y	0.1	0.2
O (rest)	51.4	51.8

It is proposed that the synthesis method, described above, can both be simplified and made more versatile by using metal-organic complexes to deposit the iron on the silica. The silica support can be shaped into the desired form, for example a monolith structure, to optimize mass-transport, heat transport and the free-volume distribution. The iron active sites can be deposited on the desired location using metal-organic complexes, the atomically disperse nature of the iron sites can be obtained by choosing the right complex. The research into this topic has been performed as part of the master assignment of ir. Wouter Lensing.

Chapters 2, 3 and 5 show the importance of a catalyst with a high activity in generating methyl radicals, to maximize the conversion achieved in the catalyst bed, while simultaneously minimizing the required catalyst contact time to prevent deposit formation on the catalyst. The Fe active site shows a very limited increase in methane conversion activity when compared to a blank SiO_2 support as shown by Han et al. [5] and Sot et al. [12]. It is proposed that ruthenium can achieve a higher activity [13, 14] while maintaining similar properties to the Fe©SiO_2 catalyst, due to position of Ru in the period table just below iron. Work concerning the ruthenium catalyst was performed by Patrick Cameron Msc. as part of his master assignment. A recent publication by He et al. [15] showed a theoretical DFT based screening of all transition metal in the *M*©SiO_2 active site configuration. They identified Fe, Mn, Tc, Mo, Ta, W and Re as highest potential candidates, with W©SiO_2 theoretically being the most active methane conversion catalyst. Ru/SiO_2 has lower methane dissection barrier, but is less potent in adsorbing methane compared to Fe according to the DFT simulations [15]. These theoretical calculations have unfortunately not been validated experimentally.

Both the graft-synthesis of the Fe©SiO_2 catalyst as well as the synthesis of a Ru/SiO_2 catalyst will be detailed in sequence bellow.

7.2 Graft-synthesis of Fe©SiO_2

7.2.1 Experimental

Two different metal organic complexes were tested, namely bis(2,4-dimethyl-1,3-pentadienide)Fe(II); (Fe(oCp)$_2$) and Fe(II) Phthalocyanine: (Fe(II)Pht), both shown in Figure 7.2. Synthesis and deposition were aided by dr. M Hempenius in the Materials Science and Technology of Polymers (MTP) group of the University of Twente. The synthesis procedure for the Fe(oCP)$_2$ catalyst was taken from a publication by Hu et al. [16], who used the atomically disperse iron site to non-oxidatively dehydrogenate propylene via hydrogen abstraction similar to the methane activation in this thesis. The catalyst we synthesized was also tested for propane dehydrogenation, giving the same performance as reported by Hu, thus confirming the successful reproduction of the catalyst. The synthesis method for the Fe(II)Pht catalyst was developed in-house. It is proposed that the bulky and flat structure of the phthalocyanine ligand (Figure 7.2b) will hopefully cause a disperse monolayer on the support surface, controlled calcination will subsequently remove the organic ligand, forming atomically disperse iron-sites on the support. Synthesis involved dissolving the Fe(II)Pht in DMSO after which it is mixed with the silica support and kept under agitation overnight. The silica is then washed 2 times in acetone and dried under vacuum at 50°C. The organic ligand is removed via calcination at 650°C in 5%air/N_2 atmosphere, to yield the final catalyst.

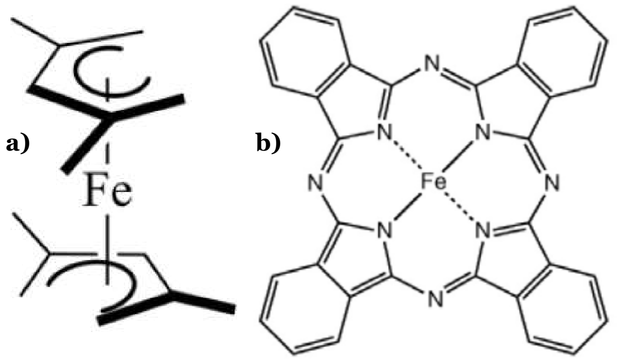

Figure 7.2: The molecular structures of (a) bis(2,4-dimethyl-1,3-pentadienide)Fe(II): (Fe(oCp)$_2$ (b) Fe(II) Phthalocyanine: (Fe(II) Pht).

7.2.2 Results and discussion

The original Fe©SiO$_2$ catalyst is synthesized using ball milling followed by melt-fusion [1], it is most likely that the majority of the iron atoms are buried inside the silica matrix and will not participate in the NOCM reaction. The STEM-HAADF image presented in Figure 2a in the publication Guo et al. [1] allowed to calculate the surface density of the supposed active sites. The STEM-HAADF image is included in the supporting information of this chapter, for ease of reference. For the used particle size fraction of 250-500 μm this amounted to 0.026 wt% Fe on the catalyst surface. This value was used as target for synthesis of both graft-based catalysts. Table 7.2 shows the resulting concentration of iron found on the three different catalysts, i.e. two catalysts synthesized via the grafting methods and the control melt-fusion based catalyst. It proved difficult to control the quantity of iron deposited using the two grafting methods, although the Fe(oCp)$_2$ method based on the work of Hu et al. [16] proved easier to control. No XRD measurements were performed of the Fe(oCp)$_2$ and Fe(II)Pht catalysts, the XRD diffractogram of the Fe©SiO$_2$ is included in **chapter 2**. It is highly unlikely that the XRD diffractograms of the Fe(oCp)$_2$ or the Fe(II)Pht catalysts would show any difference to the diffractogram of pure quartz, due to the very low Fe loading and the non-destructive, low temperature synthesis method, making the formation of a different crystal phase highly unlikely. More measurements are required to prove the claimed single-atom active site. Ideally the catalyst should be characterized by XANES/EXAFS and STEM-HAADF to give definitive proof of the atomic dispersion. An added benefit would be the clearer distinction between Zr and Fe atom in the STEM-HAADF image of the original Fe©SiO$_2$ catalyst, since the graft-synthesized catalyst will contain no zirconia, alleviating the confusion pointed out in the introduction.

Table 7.2: XRF analysis of the Fe/SiO_2 catalysts synthesized using the grafting methods based on Fe(oCp)$_2$ and Fe(II)Pht, compared to the bench-mark melt-fusion Fe©SiO_2 catalyst.

Catalyst	**Target wt% Fe**	**XRF measured wt% Fe**
Fe©SiO_2	0.5	0.5
Fe(oCp)$_2$	0.026	0.051
Fe(II)Pht	0.026	0.19

Figure 7.3 shows a comparison in performance between the two graft-based catalyst described above and the original ball-milled Fe©SiO_2 catalyst. The performance of the melt-fusion Fe©SiO_2 and the Fe/SiO_2 synthesized using Fe(oCP)$_2$ are comparable, showing similar conversion and olefin selectivity. The catalyst based on Fe(oCP)$_2$ does show a lower selectivity to aromatic species, compared to Fe©SiO_2, this is attributed to the different crystal phase of the catalyst. The silica in the Fe(oCP)$_2$ based catalyst is in the α-quartz phase, whereas the silica in the Fe©SiO_2 catalyst is in the β-cristobalite phase. Han et al. [5] showed that cristobalite significantly reduces the coking tendency of the catalyst compared to quartz, leading to higher aromatic yields. The carbonaceous deposits on the spent catalyst were not quantified during this work. The Fe(II)Pht based catalyst shows both a higher conversion and significantly lower product yield compared to both the Fe©SiO_2 catalyst and the Fe(oCP)$_2$ based catalyst. The higher activity can be explained by the higher Fe loading shown in Table 7.2 and lower total hydrocarbon selectivity hints at the formation of Fe nanoparticles. Fe nano-particle/SiO_2 catalyst presented as comparisons in previous literature [1, 5] showed a significantly higher coking tendency due to C-C coupling on adjacent Fe atoms. It is speculated that either the phthalocyanine ligands will stack on top of each-other due to the delocalized pi-structure, and hence bring the Fe ions in close contact with each other during calcination, or the iron atoms agglomerate into nanoparticles during sintering, due to the high surface concentration (Table 7.2).

Note that all measurements presented in Figure 7.3 were measured with and older oven-system, which was later replaced by the oven system first described in **chapter 2** and used for all measurement presented in **chapters 2-5**. Note that there is no insulation between the three zones in the older oven system and there is hence no control over the temperature profile. The Fe©SiO_2 performance shown as comparison in Figure 7.3 was also measured in the old system.

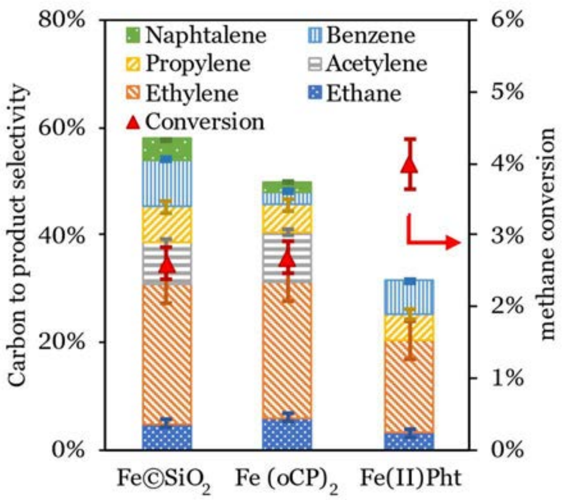

Figure 7.3: Performance comparison between 3 different Fe/SiO2 catalyst; Fe(c)SiO2 synthesized by melt-fusion and both Fe(oCP)2 and Fe(II)Pht synthesized via graft synthesis using different metal organic complexes; reactor temperature: 1000°C; space velocity at 3.2 l·gcat^{-1}·h^{-1}; 1.0 g catalyst 250-500 µm.

The research into this topic was not pursued further. Suggestions for future research involve: testing the synthesis method based on the Fe(oCp)$_2$ with SiO$_2$ in the cristobalite phase, which can be easily achieved by calcining the SiO$_2$ at 1700°C for 6h before Fe deposition. It would be interesting to vary the loading of Fe deposited on the support. It is expected that conversion will increase while maintaining the total carbon to products selectivity, when increasing the Fe loading, as long as the surface concentration of Fe sites is low enough to maintain atomic dispersion. Fe will start sintering into Fe-nano particles once a critical surface concentration is reached, likely leading to a sharp decrease in total carbon to products selectivity, while simultaneously increasing the coke-selectivity, as discussed concerning the Fe(II)Pht based catalyst.

The real benefit of the deposition method lies in the versatility it offers with respect to the shape of the catalyst. Research on coated wall reactors could be continued [7], using the deposition method, and expanded further to monolithic catalysts with controlled channel length, diameter and shape, to optimize catalyst/free-volume distribution and thus optimize reaction performance.

7.3 Ru/SiO₂ catalyst

7.3.1 Experimental

Two methods were attempted for the synthesis of the Ru/SiO2 catalyst. Firstly, a sol-gel method was used [17], dissolving ruthenium triacetylacetinate in acetone which is mixed with tetraethyl orthosilicate (TEOS) dissolved in ethanol. The mixture was brought to 60°C and nitric acid was slowly added to hydrolyze the TEOS. The gel was calcined at 300°C in air, followed by fusion of the resulting powder at 1700°C in air analogues to the Fe©SiO_2 synthesis. The second synthesis for Ru/SiO_2 was based on the original synthesis method for Fe©SiO_2 described by Guo et al. [1]. $RuCl_3$ and quartz powder were ball-milled together overnight. The resulting powder was reduced and dechlorinated with a stoichiometric quantity of sodium borohydride in ethanol followed by consecutive washing with ethanol and milli-q water. The powder was dried overnight at 105°C and then also calcined at 1700°C in air for 6h. The Ru/SiO_2 slabs resulting from the two synthesis methods were crushed to the desired particle fraction (250-500 µm) and leached for 2h in 0.5M HNO_3 to obtain the final catalyst.

7.3.2 Results and discussion

The same molar concentration of Ru to the 0.5 wt% Fe in the original Fe©SiO_2 catalyst was chosen to have a similar concentration of active sites on the catalyst, and thus allow for a fair comparison in activity and performance. This results in a target Ru concentration of 0.9wt% to achieve the same molar active metal concentration as the 0.5wt% Fe©SiO_2 catalyst as shown in Table 7.3. The sol-gel based Ru/SiO_2 catalyst has the desired concentration of Ru, but surprisingly the ball-mill derived catalyst shows the correct concentration of Ru before fusion, but no detectible Ru after fusion at 1700°C. It is likely that the Ru in the ball-milled sample oxidized and sublimated, since the sublimation temperature of Ru(iv)O_2 is roughly 1200°C [18]. The fact that the sol-gel method did not see a significant decrease in ruthenium shows that this synthesis is an effective method to stabilize the ruthenium in the SiO_2 matrix, through chemical bonding that is thermally stable up to at least 1700°C.

Table 7.3: XRF analysis of the Ru/SiO_2 catalysts synthesized using the sol-gel and the ball-mill methods described above.

Catalyst	**Target**	**XRF measured**	
	wt% Ru	**wt% Ru**	**wt% Zr**
Sol-gel	0.9	0.83	0.04
Ball mill; pre-fusion	0.9	0	2.2
Ball mill; post-fusion	0.9	0.84	2.8

The catalyst was furthermore analysed using X-ray diffraction. The diffractograms of the ball-milled and sol-gel based Ru/SiO_2 catalysts are shown in Figure 7.4 compared to the cristobalite reference. It is clear that the cristobalite phase dominated in the two catalyst. The ball-milled Ru/SiO_2 catalyst shows perfect correspondence with the cristobalite diffractogram, a logical consequence of the absence of ruthenium. The sol-gel synthesized Ru/SiO_2 catalyst shows two additional peaks, at 42° and 44° 2θ, as shown in the zoom-in in Figure 7.4, these peaks could be attributed to the 002 and 101 planes of ruthenium respectively [19], hinting at Ru nano particles rather than single atom sites. Although it is also possible that these peaks are causes by a ruthenium silicate, for which there is no literature reference. The proposed atomic dispersion of the Ru active site has not been validated. This would require X-ray adsorption techniques or high-resolution TEM imaging, which could unfortunately not be obtained.

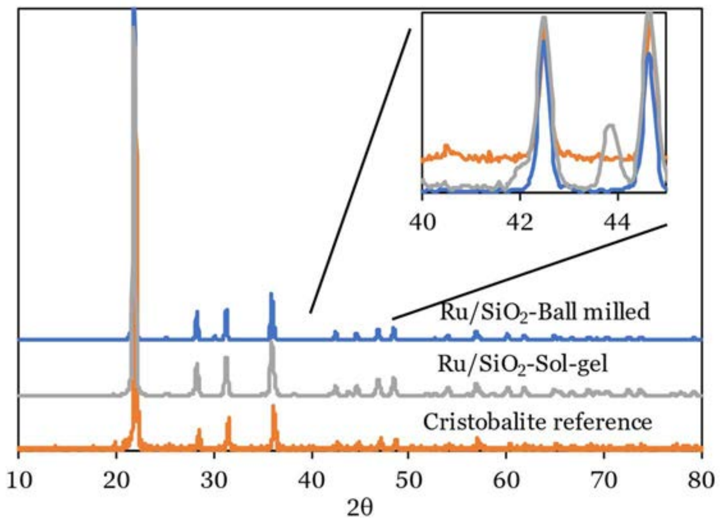

Figure 7.4: XRD diffractogram of the two synthesized Ru/SiO$_2$ catalysts compared to a Cristobalite reference [20].

Figure 7.5 shows the comparison in reaction performance between the two Ru/SiO$_2$ catalyst, with the results for Fe©SiO$_2$ catalyst as benchmark. Conversion is overall lower when using the Ru/SiO$_2$ catalyst when compared to the Fe©SiO$_2$ catalyst, although the product distribution is similar between the 3 different catalyst formulations. The ball-milled catalyst is analogues to a blank support, which is shown to have significant activity in methane conversion [5, 12]. Another explanation for the activity of the ball-milled catalyst is the zirconia (Table 7.3) which can catalyse methane conversion [9]. The sol-gel derived Ru/SiO$_2$ catalyst has a slightly higher activity than the ball-milled catalyst, but significantly lower than Fe©SiO$_2$ (Figure 7.5). It can thus be concluded that Ru/SiO$_2$ is less active in methane activation than Fe©SiO$_2$, although the synthesis method for Ru/SiO$_2$ could not be optimized. Avenues for improvement could be the synthesis of Ru_2SiO_4 prior to ball milling, analogue to the Fe©SiO$_2$ synthesis. It should also be theoretically evaluated if the larger Ru(II) ion can even be incorporated as a single site in a SiO$_2$ matrix. It is thus suggested to revisit this topic in future research.

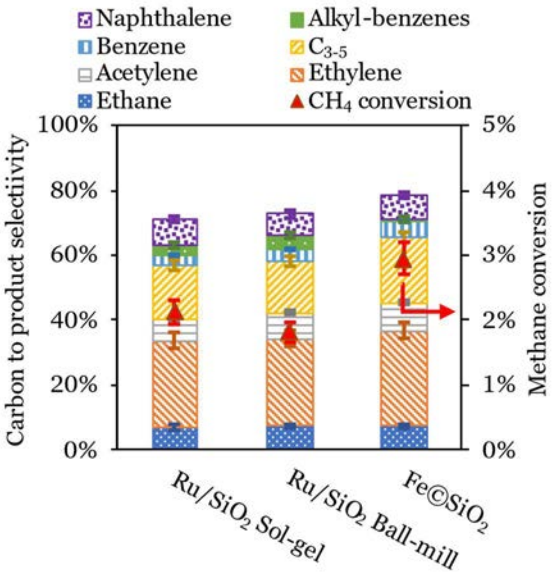

Figure 7.5: Comparison between the Fe(c)SiO2 catalyst and the Ru(c)SiO2 catalyst, synthesized via either a sol-gel or ball-milling synthesis reactor temperature: 1000°C, pre-heater and post-heater at 400°C; space velocity at 3.2 $l{\cdot}gcat^{-1}{\cdot}h^{-1}$; 280 mg catalyst 250-500 μm placed in the top 2 cm of the 6 cm reactor-zone (see **chapter 2** for more details).

7.4 Analysis of other silicon(-oxide) based catalysts for direct methane conversion

A patent filed by Xinhe Bao [21], the scientific leader of the group that first published on the Fe©SiO_2 catalyst [1], details various catalysts for high-temperature non-oxidative coupling of methane. Supports used included SiO_2 $SiOC_{0.5}$, SiC, Si_3N_4 and $SiOC_{0.35}N_{0.2}$, metals included: Fe, Co, Zn, Mn, Pd, Ti, Ce and Sn, with Mg, Ca and K as dopants. Surprisingly, all metal supported on silica catalyst show the same activity under the same condition, i.e. SV and temperature: ~8% CH_4 conversion and no coke formation at 4840 $ml{\cdot}g_{cat}^{-1}{\cdot}h^{-1}$ and 950°C. The addition of alkali metal causes an increase in activity; ~15% conversion at the same conditions, but the alkali metal doping is also shown to cause ~10% deposit selectivity. The best performance reported in the patent was achieved with an Fe©SiC catalyst, which is claimed to achieve 12.5% conversion at 950°C and 15200 $ml{\cdot}g_{cat}^{-1}{\cdot}h^{-1}$, resulting in 4.8 times the specific activity of the Fe©SiO_2 catalyst, while causing no coke formation. Slater [22] showed that SiC is indeed highly active in activating methane, whereas SiO_2 shows very little activity in methane activation. The Fe©SiC catalyst was synthesized by impregnating porous silicon carbide with a aqueous $Fe(NO_3)_3$ solution, which was dried under agitation at 120°C. The powder was fused at 2000°C in vacuum for 6h, followed by a rapid quench in rapeseed oil. These severe conditions prevented attempting this synthesis inhouse, although it would be very interesting to see a detailed analysis disclosing the reason for the high activity of the Fe©SiC compared to the 'benchmark' Fe©SiO_2 catalyst.

It is an interesting observation that there is no discernible difference between any of the metal/SiO_2 catalysts, which are not doped with alkali metal, in terms of performance. It is speculated, based on the results in **chapter 2 and 5**, that the reactor used by Guo et al. [1] in their publication and Bao in the patent [21] is determining for the reaction performance. The catalyst is solely required for reaction initiation and plays a minor role as long as a minimum level of activation is achieved in the catalyst bed. Same mass of catalyst, 0.75g, is used both for Fe©SiO_2 in the original publication [1] as well as for the Fe©SiC catalyst in the patent [21]. Conversion achieved with both catalyst are far from the thermodynamic equilibrium conversion of 44% at 950°C [23]. If the same reactor and reactor loading is used for both tests then the total flowrate is the only difference between the two performance tests. If this assumption is true, this means the gas-phase contribution for the Fe©SiC is minimal and the Fe©SiC catalyst achieves a very significant conversion itself.

7.5 Conclusions

Two organometallic graft synthesis methods were used to synthesize a Fe©SiO$_2$ catalyst. It was found that the grafting method using Fe(oCp)$_2$ gives similar reaction performance results to the original ball-milling derived Fe©SiO$_2$ catalyst. The Fe(II)Pht based grafting method results in both higher methane conversion as well as significantly higher coke selectivity, most likely due to formation of Fe nano particles. Fe(oCp)$_2$ grafting is shown to be a viable alternative to the standard ball-milling synthesis and is proposed as a method for synthesizing a Fe©SiO$_2$ catalytic system with a large degree of shape and size control. Ru/SiO$_2$ catalyst was synthesized via a ball-milling as well as via a sol-gel method. The sol-gel method was effective in thermally stabilizing the Ru-sites, whereas the ball-mill method lead to complete sublimation of the added ruthenium. Reaction performance tests showed lower activity of the Ru/SiO$_2$ catalyst for methane conversion, while hydrocarbon selectivity remained unchanged, in a system with minimal free-volume contribution. It is thus concluded that the synthesized Ru/SiO$_2$ catalyst was less active than the bench-mark Fe©SiO$_2$ catalyst. Analysis of a patent filed by X. Bao showed that the transition metal used in a M©SiO$_2$ catalyst has only very limited effect on performance. Support choice was found to be much more important for determining performance, with SiC supposedly being the best option.

7.6 Acknowledgements

We acknowledge support from the Dutch National Science Foundation (NWO) and the industrial partners: SABIC, Sasol and BASF.

7.7 Supporting information

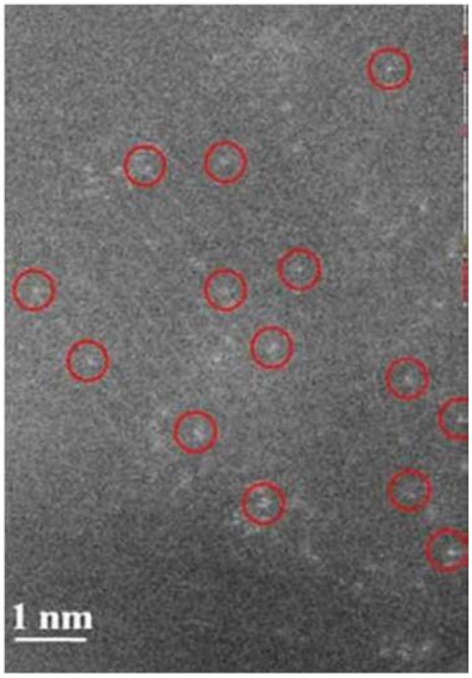

Figure S 7.1: STEM-HAADF image of the Fe©SiO_2 catalyst after reaction; adopted from [1], reprinted with permission from AAAS.

7.8 References

1. Guo, X., G. Fang, G. Li, H. Ma, H. Fan, L. Yu, C. Ma, X. Wu, D. Deng, M. Wei, D. Tan, R. Si, S. Zhang, J. Li, L. Sun, Z. Tang, X. Pan, and X. Bao, *Direct, Nonoxidative Conversion of Methane to Ethylene, Aromatics, and Hydrogen*. Science, 2014. **344**(6184): p. 616-619.

2. Bao, X. *personal communication to:* L. Lefferts, 2016

3. Superior Tehcnical Ceramics, *Material property chart ytzp yttria stabilized zirconia*. 2021.

4. Bauccio, M., *ASM Engineered Materials Reference Book*. 1994: Materials Park, OH : ASM International.

5. Han, S.J., S.W. Lee, H.W. Kim, S.K. Kim, and Y.T. Kim, *Nonoxidative Direct Conversion of Methane on Silica-Based Iron Catalysts: Effect of Catalytic Surface*. ACS Catalysis, 2019. **9**: p. 7984-7997.

6. Sakbodin, M., Y. Wu, S.C. Oh, E.D. Wachsman, and D. Liu, *Hydrogen-Permeable Tubular Membrane Reactor: Promoting Conversion and Product Selectivity for Non-Oxidative Activation of Methane over an FeVSiO2 Catalyst*. Angewandte Chemie, 2016. **55**: p. 16149 –16152.

7. Oh, S.C., E. Schulman, J. Zhang, J. Fan, Y. Pan, J. Meng, and D. Liu, *Direct Non-Oxidative Methane Conversion in a Millisecond Catalytic Wall Reactor*. Angewandte Chemie, 2019. **58**: p. 7083-7086.

8. Kim, S.K., H.W. Kim, S.J. Han, S.W. Lee, J. Shin, and Y.T. Kim, *Mechanistic and microkinetic study of non-oxidative methane coupling on a single-atom iron catalyst*. Communication Chemistry, 2020. **3**(58).

9. Zhang, Y., Y. Zhao, T. Otroshchenko, H. Lund, M.-M. Pohl, U. Rodemerck, D. Linke, H. Jiao, G. Jiang, and E.V. Kondratenko, *Control of coordinatively unsaturated Zr sites in ZrO2 for efficient C–H bond activation*. Nature Communications, 2018. **9**(3794): p. 1-10.

10. Liu, L., Z. Ma, Z. Yan, S. Zhu, and L. Gao, *The ZrO2Formation in ZrB2/SiC CompositeIrradiated by Laser*. Materials, 2015. **8**: p. 8745-8750.

11. Mysen, B. and P. Richet, *Chapter 5 - Silica*, in *Silicate Glasses and Melts*. 2019, Elsevier Science.

12. Sot, P., M.A. Newton, D. Baabe, M.D. Walter, A.P.v. Bavel, A.D. Horton, C. Copéret, and J.A.v. Bokhoven, *Non-oxidative Methane Coupling over Silica versus Silica-Supported Iron(II) Single Sites*. Chemistry—A European Journal, 2021. **26**: p. 8012-8016.

13. Belgued, M., H. Amariglio, P. Pareja, A. Amariglio, and J. Saint-Just, *Low temperature catalytic homologation of methane on platinum, ruthenium and cobalt*. Catalysis Today, 1992. **13**: p. 437-445.

14. Koerts, T., M.J.A.G. Deelen, and R.A.V. Santen, *Hydrocarbon Formation from Methane by a Low-Temperature Two-Step Reaction Sequence.* Journal of Catalysis, 1992. **138**: p. 101-114.

15. He, S.-Y., T.-H. Li, Z.-Q. Huang, Y. Liu, J. Li, and C.-R. Chang, *Screening silica-confined single-atom catalysts for nonoxidative conversion of methane.* The Journal of Chemical Physics, 2021. **154**.

16. Hu, B., N.M. Schweitzer, G. Zhang, S.J. Kraft, D.J. Childers, M.P. Lanci, J.T. Miller, and A.S. Hock, *Isolated FeII on Silica As a Selective Propane Dehydrogenation Catalyst.* ACS Catalysis, 2015. **5**: p. 3494–3503.

17. Ornellana, F., J. Plaza-de-los-Reyes, and S. Urizar, *Ru/SiO2 AND CuRu/SiO2 PREPARED BY SOL-GEL: EFFECT OF pH AND WATER AMOUNT.* Journal of the Chilean Chemical Society, 2003. **48**(2): p. 33-38.

18. Garisto, F., *Thermodynamic behaviour of ruthenium at high temperatures*. 1988, Atomic energy of Canada limited.

19. González-Huerta, R.G., R. González-Cruz, S. Citalán-Cigarroa, C. Montero-Ocampo, J. Chavez-Carvayar, and O. Solorza-Feria, *Development and Electrochemical Studies of Ruthenium Nanoparticles as Cathode in a PEMFC.* Journal of New Materials for Electrochemical Systems, 2005. **8**: p. 15-23.

20. Lafuente, B., R.T. Downs, H. Yang, and N. Stone, *The power of databases: the RRUFF project*, in *Highlights in Mineralogical Crystallography*, T. Armbruster and R.M. Danisi, Editors. 2015, W. De Gruyter: Berlin. p. 1-30.

21. Bao, X., X. Guo, D. Deng, H. Ma, and D. Tan, 2014, *Synthesis of olefins from oxygen-free direct conversion of methane and catalysts thereof*, US 2014/0336432 A1

22. Slater, W.E., *The influence of different surfaces on the decomposition of methane*. Journal of the Chemical Society, Transactions, 1916. **109**: p. 160-164.

23. Guéret, C., M. Daroux, and F. Billaud, *Methane pyrolysis: thermodynamics.* Chemical Engineering Science, 1997. **52**(5): p. 815-827.

Chapter 8

Conclusion and Outlook

8.1 Conclusions

Chapter 1 of this thesis discussed the challenges for 21st century, namely climate change and a shift in hydrocarbon resource demand from mainly fuels to base chemicals. It was argued that natural gas is a prime candidate to take over the role of crude oil as source for olefins and aromatics. Various industrial processes for converting natural gas to higher hydrocarbons were discussed, such as Fischer-Tropsch, methanol-to-gasoline and methanol-to-olefins. These processes all require numerous conversion steps at different conditions, starting from methane steam reforming, making them both costly and viable only at large installed capacity. This leads to a discrepancy concerning the exploitation of smaller gas-fields as well as the natural gas co-produced at smaller oilfields. It was shown that most of this co-produced natural gas is currently either flared or vented, leading to significant unnecessary green-house emissions. Direct conversion of methane to olefins and aromatics is potentially viable at lower installed capacities, and could thus valorise these otherwise wasted natural gas sources. The Fe©SiO_2 catalyst is proposed as the most high-potential candidate for this role.

Chapter 2 demonstrated the importance of temperature profile surrounding the catalyst bed on the overall reaction performance. Residence time at 1000°C downstream of the catalyst was found to significantly enhance the methane conversion, through methane auto-catalysis. This phenomenon was theoretically analysed in the model presented in **chapter 5**. There was, furthermore, a strong relation between the quantity of catalyst in the system and coke selectivity, showing that coke formation on the catalyst surface is the major route for coking. Residence time at 1000°C upstream of the catalyst bed was also found to increase overall coke-on-catalyst yield, attributed to the gas-phase activation of methane prior to the catalyst bed. Product selectivity is determined mainly by gas-phase reactions, although quenching the product mixture directly downstream of the catalyst can cause a significantly higher yield of C_2 hydrocarbons.

The significant increase in methane conversion upon addition of ethane or ethylene (C_2) was shown in **chapter 3**. The effect of C_2 addition was demonstrated to be a purely gas-phase phenomenon. Crucially the product distribution, including coke and deposit selectivity, was found to be independent of the method of methane activation. There was no difference between the effect of ethane or ethylene addition at short residence times, but ethylene proved to be more potent in methane activation at longer residence times. These three results were again all theoretically elaborated in model presented in **chapter 5**. The trends in coke-on-catalyst selectivity as well as deposit selectivity observed in **chapter 3** matched with those previously shown in **chapter 2**, i.e., an increased quantity of catalyst leads to an increased coke-on-catalyst yield, whereas deposit formation can be significantly reduced by maximizing gas-phase methane conversion. Free radical initiation via C_2 addition is highly effective, presence of catalyst does not increase methane conversion at inlet C_2 concentration greater than 2 vol%. Due to the invariance in product selectivity as well as the coking-tendency of the catalyst, it is thus proposed to operate the methane coupling reaction using an excess of 2% C_2 addition in the feed, without any heterogeneous catalyst.

The effect of hydrogen addition on the direct methane coupling reaction was studied in **chapter 4**. Hydrogen addition significantly reduces all reaction rates leading primarily to a significant decrease in methane conversion. The influence of hydrogen addition of product selectivity is proven to be minimal, with methane conversion level being the determining factor for the selectivity distribution, similar to the conclusions for SV change in **chapter 2** and C_2 addition in **chapter 3**. Coke selectivity is highly dependent on the quantity of hydrogen dosed into the reactor. Addition of 10% H_2 leads to an order of magnitude reduction in coke formation on the catalyst, which considering the reduction in methane conversion results in a fivefold reduction in coke selectivity. The chapter shows that dosed H_2 addition can be used as a versatile tool to prevent excessive reactor coking.

The catalytic system is kinetically modelled in **chapter 5**, to gain a theoretical understanding of the autocatalysis and C_2 initiation phenomena experimentally presented in the previous chapters. Micro-kinetic surface reactions were added to an existing gas-phase model. The results from the model can accurately describe the experimental results with respect to methane conversion and product selectivity. Reaction-path analysis shows the importance of the methane autocatalytic cycle in propagating conversion in the post-catalytic gas-phase as shown experimentally in **chapter 2**. Reaction path analysis showed both the reaction path for the methane auto-catalysis in the post-catalytic volume presented in **chapter 2** as well as the methods that ethane and ethylene activate methane as shown in **chapter 3**. The underlying reaction path relies on the generation of excess H· radicals which attack methane molecules to form methyl radicals as well as di-hydrogen. The excess H· radicals are generated through carbon-carbon coupling reactions from C_2 compounds to higher hydrocarbons. The model predicts that maximum acceleration in methane conversion rate is reached at 4% methane conversion, which considering the importance of C_2 species in the auto-catalytic cycle, matches perfectly with the observed decrease in effectiveness for methane activation at higher than 2% ethane or ethylene addition discussed in **chapter 3**. It is thus concluded that the selectivity towards C_2 hydrocarbons is limited at high methane conversion. The only method to achieve high C_2 yields is by having an extremely active catalyst as sole method for methane activation, after which the product mixture needs to be directly quenched. However, the gas phase free-radical propagation reactions are very fast at 1000°C, making high C_2 yields impossible due to formation of higher hydrocarbons.

Chapter 6 presents a detailed process design for industrial application of the NOCM reaction. The process is designed with benzene as main product. Process analysis showed that a minimum reactor pressure of 5 bar is required. The energy requirement for the reactor is high, due to the high reaction temperature (>950°C), high reaction endothermicity and inefficiency of low pressure gas-gas heat exchange between the reactant and product streams. Natural gas is the economically sensible option to accommodate the required heating, although **chapter 6** proposes to use the large amounts of produced naphthalene for this purpose, because of its low price and market size. Both options will, however, lead to excessive CO_2 formation. Electric heating as discussed in **chapter 1** is a potential option, but still deemed too expensive for the moment. Aromatics will firstly need to be removed to prevent fouling in the hydrogen separation step. Aromatics will be removed via absorption by sulfolane, after which distillation recovers both sulfolane and purifies the aromatic species. Hydrogen is subsequently removed from the product stream using polymeric membranes. Ethylene recovery is too costly, due to the required cryogenic distillation and will be recycled. Although the ethylene recycle limits the profitability, it in fact helps reactor productivity as shown in **chapter 3** and theoretically demonstrated in **chapter 5**. The significant naphthalene selectivity limits the profitability of the process, due to its low price and limited market size. It is proposed to hydrocrack naphthalene with co-produced hydrogen to increase the yield of mono-aromatic species.

Chapter 7 describes alternative catalyst synthesis methods. Firstly, graft-synthesis methods using Fe organometallic compounds are evaluated as an alternative for the difficult to control synthesis method based on ball-milling and melt-fusion, used for the original Fe©SiO_2 catalyst. Fe(II) Phthalocyanine as precursor lead to the probable formation of Fe nanoparticles, resulting in both higher methane conversion as well as significantly higher carbonaceous deposit formation. The catalyst based on the grafting of bis(2,4-dimethyl-1,3-pentadienide)Fe(II), however, showed a performance highly comparable to that of the original Fe©SiO_2 catalyst. This graft-method is thus proposed as a viable alternative synthesis method, allowing for a high versatility in catalyst synthesis, with respect to shape and size. A second part of this research focused on the synthesis of a Ru©SiO_2 catalyst, following a ball-mill synthesis comparable to the original Fe©SiO_2 synthesis, as well as a novel sol-gel method. The sol-gel method yielded a thermally stable Ru/SiO_2 catalyst, whereas the ball-milled synthesis lead to sublimation of all ruthenium during fusion. The Ru/SiO_2 catalyst proved to have a lower activity in methane conversion compared to the original Fe/SiO_2 catalyst. The lower activity can be attributed to either a sub-optimal synthesis method, potentially resulting in a non-atomically disperse catalyst, or Ru is less active in high temperature methane activation. Further testing and characterization will be required to prove or disprove either conjecture.

8.2 Outlook

The most significant difference between academically researched conditions and industrially relevant conditions is the reactor pressure as discussed in **chapter 6**. It unfortunately proved impossible to measure at elevated pressures in the experiments performed for this thesis due to safety constraints. It is surprising that pressure was not studied as a variable in the extensive parametric studies concerning methane pyrolysis performed in the 80s and 90s, except for measurements at lower partial pressure of methane. Kosinov et al. [1] showed both a significantly higher methane conversion rate and a lower coke selectivity on increasing the pressure in the MDA reaction. It is possible that these benefits will also translate to the high temperature NOCM reaction, although maximum methane conversion will be reduced at higher pressures as discussed in **chapter 6**. It would be interesting to study the effect of reactor pressure up to 15 bar on fully catalytic system, i.e. the reactor-zone filled with catalyst, as well as the system with extended residence time downstream of the catalyst, i.e. using the post-heater. The best performance from **chapters 3 and 4** should also be evaluated at various increased pressures.

Although a large effort was made in this thesis to manipulate the temperature profile via the oven design, all measurements were performed in single diameter quartz tube. Research presented in **chapter 2** showed that both the heating rate before the catalyst bed, as well as the post-catalytic quench can significantly influence the coke selectivity and product distribution. A custom design reactor will offer more control in maximizing reaction performance. **Chapter 2** showed that rapid heating of the reactant gas upstream of the catalyst bed can significantly reduce coke formation on the catalyst, it is thus proposed to use a thin capillary to feed the reactant gas to the catalyst. Deposit formation on the reactor wall downstream of the catalyst bed proved to be a major source of yield loss. Increasing the reactor diameter downstream of the catalyst bed will likely reduce the deposit formation on the reactor wall, due to the increased volume to surface ratio. A schematic of the proposed reactor design can be seen in Figure 8.1.

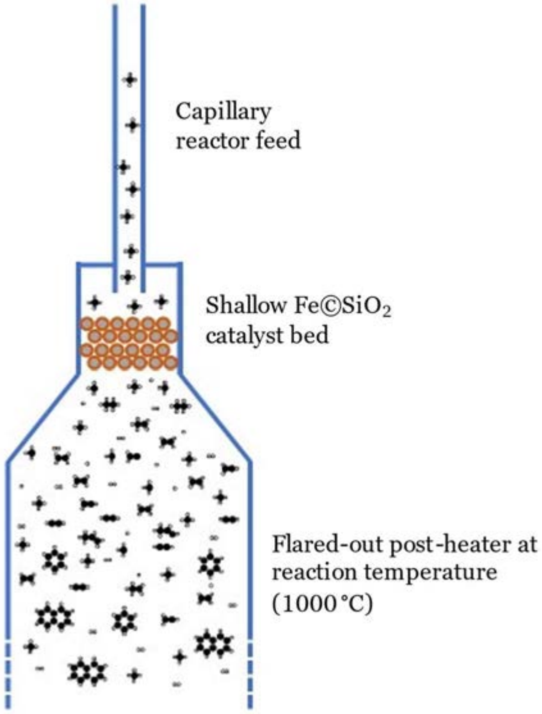

Figure 8.1: Proposed optimal reactor layout for best lab-scale fixed bed performance.

Reactor material choice influences both activity and deposit selectivity in non-oxidative coupling of methane [2, 3]. A more inert reactor material is preferential for minimizing deposit formation. Quartz is one of the more inert materials concerning methane activation [2]. Han et al. [4] showed that the β-cristobalite phase of silica is significantly more coking-resistant than α-quartz when used as catalyst support material. It is postulated that β-cristobalite as reactor material will likely yield the same effect. It should be possible to obtain a silica reactor in the β-cristobalite phase by exposing a quartz reactor tube for an extended time, i.e. 24h+, to a temperature between 1500-1600°C, followed by a rapid decrease in temperature. Cooling rates used for catalyst synthesis show that $2°C\cdot min^{-1}$ should be adequate. A reactor made of SiC could also be an interesting option, as the patent by Bao [5] claims that it is both active in methane activation as well as coking resistant. Although Guéret et al. [6] showed that SiC does cause excessive carbon formation, the reason for this difference is unknown, but it could be explained, among other reasons, by aspects such as a different crystal phase, analogues to the difference between β-cristobalite and α-quartz and impurities in the SiC, particle size. Wang et al. [3] showed that ZrO_2 is also a highly interesting reactor material for NOCM, because of its high resistance to oxidative deposit removal, compared to SiC or Al_2O_3, which tend to suffer from oxidative degradation.

All research into non-oxidative coupling of methane thus far has been carried out in either flow-through, shock-tube, or recently, pulls-compression reactors [7]. It would be highly interesting to evaluate the NOCM reaction in reactors such as a fluidized bed reactor or a vortex reactor [8]. A fluidized bed reactor has shown benefit in oxidative coupling of methane [9], which in essence is comparable to NOCM. Benefits could include a better distribution of heat, more control over the catalyst-free volume ratio, recycling and removal of coked catalysts (as discussed in **chapter 6**) and a potential different temperature between catalyst and gas phase, by preheating the catalyst before it enters the reactor. A vortex reactor is a system similar to a cyclone gas-solid separator, the reactant flow keeps the catalyst particles in a circular suspended motion without letting them flow away with the product mixture. It hence has comparable benefits to a fluidized bed reactor, but at a reduced volume and a larger control over catalyst contact time and post-catalytic residence time. The vortex reactor can theoretically bring a significant improvement to the OCM reaction [10] by minimizing species back-mixing while maximizing thermal back-mixing, which will likely translate well to the NOCM reaction as well for the same reasons stated above.

The process design presented in **chapter 6** shows that the high naphthalene selectivity in NOCM severely hinders its economic potential. It is proposed, in the same chapter, that the naphthalene can be converted into mono-aromatics by hydrocracking. Shen et al. [11] showed that naphthalene can be cracked to olefins and mono-aromatics at 400°C, 40 bar, using hydrogen and methane as cracking agents, using a Zn/HY catalyst. Reaction performance was tested in semi-batch process with a continuous feed of H_2 and CH_4, complete naphthalene conversion was achieved after 1 h. It would be interesting to evaluate this catalyst for direct conversion of naphthalene in the same reactor used for the NOCM reaction in a two-step conversion process as shown in Figure 8.2. It is likely that an elevated pressure is required for the cracking of naphthalene, making the first suggestion of this section even more relevant. A separation step should not be necessary between the methane conversion and naphthalene conversion, because a mixture of 1:4 H_2:CH_4 was used in the original publication [11] and the products are lower olefins and mono-aromatics, thus these species are likely stable at reaction conditions. Catalyst performance should, however, be evaluated in a continuous flow reactor, at lower residence times and lower pressures. A separate, post-purification naphthalene conversion step can always be considered if it proves impossible to match the reaction pressure and residence time between the NOCM reaction and naphthalene cracking.

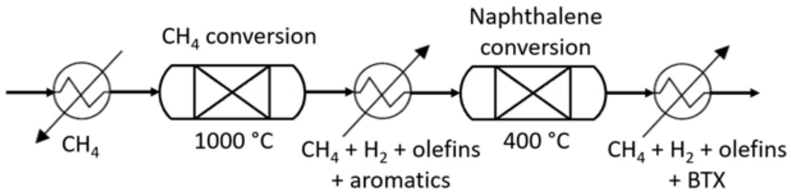

Figure 8.2: Simplified scheme for consecutive methane and naphthalene conversion to achieve high olefin and BTX yields in one reactor.

Chapter 6 furthermore showed the difficulty of the hydrogen purification, both due to the fouling nature of the aromatic species in the product stream, as well as the large pressure difference between the low pressure reactor and high pressures required for PSA or membrane purification of H_2. A potential solution could be proton conducting membrane (P CM) [12, 13]. $BaCeO_3$ based ceramic membranes have high proton conductivity as well as high operating temperature i.e. 600-1000°C [14]. P CMs are capable of actively pumping hydrogen from a low-pressure stream to a high pressure stream. Sakbodin et al. [15] showed that implementing these type of membranes inside the reactor can increase single pass conversion by removing hydrogen in-situ. Alternatively, using these membranes in the beginning of the separation train would significantly reduce the required compression for aromatic purification, due to the reduction of product stream size as well as the increase in aromatic concentration in this stream. Furthermore, a high purity hydrogen stream at high pressure is obtained at the other side of the membrane.

Chapter 5 demonstrated that high olefin yields are difficult to achieve due to the very high gas phase reaction rates at 1000°C. Olefin selectivity can likely be improved when generating either a difference in temperature between the catalyst and gas-phase or a difference in reaction rate between methane activation and the following coupling reactions. In this light it would be potentially interesting to look at various novel methods for methane activation, such as plasma based processes [16], in combination with a tailored temperature profile to maximize ethylene yield. In this concept the plasma would handle the activation of methane, after which the temperature profile will be solely used to steer product selectivity. A similar concept was proposed by Moncada et al. [17], who used a plasma to activate methane and a Pd/Al_2O_3 catalyst at temperatures between 25-200°C to hydrogenate the products to prevent deposit formation. One might think of a similar concept, where the Fe©SiO_2 catalyst is coated on plasmonic particles [18], which could allow for specific heating of the catalyst, while maintaining a much cooler gas-phase temperature in the reactor. This could lead to near 100% ethylene selectivity if the direct formation of ethylene on the Fe©SiO_2 catalyst as proposed by Toraman et al. [19] is indeed the dominant reaction. Although even if the methyl radical production over the catalyst as proposed by Guo et al [20] and Kim et al. [21] is dominant it will still lead to much higher olefin and lower aromatic yields if the temperature difference between the catalyst and gas phase is significant. It is, however, possible that the hot-catalyst will be a nucleation point for coke deposition and reaction parameters should be tuned to prevent this.

8.3 References

1. Kosinov, N., E.A. Uslamin, L. Meng, A. Parastaev, Y. Liu, and E.J.M. Hensen, *Reversible Nature of Coke Formation on Mo/ZSM-5 Methane Dehydroaromatization Catalysts*. Angewandte Chemie, 2019. **58**: p. 7068-7072.

2. Slater, W.E., *The influence of different surfaces on the decomposition of methane*. Journal of the Chemical Society, Transactions, 1916. **109**: p. 160-164.

3. Wang, S., W.J. Lee, C.e. Li, B. Kuan, N. Burke, and J. Patel, *The Pyrolysis of Natural Gas: A Study of Carbon Deposition and the Suitability of Reactor Materials*. Reaction Engineering, Kinetics and Catalysis, 2018. **65**(3): p. 1035-1046.

4. Han, S.J., S.W. Lee, H.W. Kim, S.K. Kim, and Y.T. Kim, *Nonoxidative Direct Conversion of Methane on Silica-Based Iron Catalysts: Effect of Catalytic Surface*. ACS Catalysis, 2019. **9**: p. 7984-7997.

5. Bao, X., X. Guo, D. Deng, H. Ma, and D. Tan, 2014, *Synthesis of olefins from oxygen-free direct conversion of methane and catalysts thereof*, US 2014/0336432 A1

6. Guéret, C., F. Billaud, B. Fixari, and P.l. Perchec, *Thermal Coupling of Methane, Experimental investigations on Coke Deposits*. Carbon, 1994. **33**(2): p. 159-170.

7. Slotbooma, Y., S. Roosjen, A. Kronberg, M. Glushenkov, and S.R.A. Kersten, *Methane to ethylene by pulsed compression*. Chemical Engineering Journal, 2021. **414**.

8. Gonzalez-Quiroga, A., P.A. Reyniers, S.R. Kulkarni, M.M. Torregrosa, P. Perreault, G.J. Heynderickx, K.M.V. Geem, and G.B. Marin, *Design and cold flow testing of a Gas-Solid Vortex Reactor demonstration unit for biomass fast pyrolysis*. Chemical Engineering Journal, 2017. **329**: p. 198-210.

9. Jaso, S., S. Sadjadi, H.R. Godini, U. Simon, S. Arndt, O. Görke, A. Berthold, H. Arellano-Garcia, H. Schubert, R. Schomäcker, and G. Wozny, *Experimental investigation of fluidized-bed reactor performancefor oxidative coupling of methane*. Journal of Natural Gas Chemistry, 2012. **21**: p. 534-543.

10. Vandewalle, L.A., G.B. Marin, and K.M.V. Geem, *CFD-based assessment of steady-state multiplicity in a gas-solid vortex reactor for oxidative coupling of methane*. Chemical Engineering and Processing - Process Intensification, 2021. **165**.

11. Shen, Z., P. He, A. Wang, J. Harrhy, S. Meng, H. Peng, and H. Song, *Conversion of naphthalene as model compound of polyaromatics to monoaromatic hydrocarbons under the mixed hydrogen and methane atmosphere*. Fuel, 2019: p. 469-477.

12. Fontaine, M.L., T. Norby, Y. Larring, T. Grande, and R. Bredesen, *Oxygen and Hydrogen Separation Membranes Based on Dense Ceramic Conductors*. Membrane Science and Technology, 2008. **13**: p. 401-458.

13. Kochetova, N., I. Animitsa, D. Medvedev, A. Demin, and P. Tsiakaras, *Recent activity in the development of proton-conducting oxides for high-temperature applications*. RSC Advances, 2016. **6**(77): p. 73222-73268.

14. Kreuer, K.D., *Aspects of the formation and mobility of protonic charge carriers and the stability of perovskite-type oxides*. Solid State Ionics, 1999. **125**(1-4): p. 285-302.

15. Sakbodin, M., Y. Wu, S.C. Oh, E.D. Wachsman, and D. Liu, *Hydrogen-Permeable Tubular Membrane Reactor: Promoting Conversion and Product Selectivity for Non-Oxidative Activation of Methane over an FeVSiO2 Catalyst*. Angewandte Chemie, 2016. **55**: p. 16149 –16152.

16. Scapinello, M., E. Delikonstantis, and G.D. Stefanidis, *The panorama of plasma-assisted non-oxidative methane reforming*. Chemical Engineering and Processing: Process Intensification, 2017. **117**: p. 120-140.

17. García-Moncada, N., T. Cents, G.v. Rooij, and L. Lefferts, *Minimizing carbon deposition in plasma-induced methane coupling with structured hydrogenation catalysts*. Journal of Energy Chemistry, 2021. **58**: p. 271-279.

18. Jauffred, L., A. Samadi, H. Klingberg, P.M. Bendix, and L.B. Oddershede, *Plasmonic Heating of Nanostructures*. Chemical Reviews, 2019. **119**: p. 8087-8130.

19. Toraman, H.E., K. Alexopoulos, S.C. Oh, S. Cheng, D. Liu, and D.G. Vlachos, *Ethylene production by direct conversion of methane over isolated single active centers*. Chemical Engineering Journal, 2021.

20. Guo, X., G. Fang, G. Li, H. Ma, H. Fan, L. Yu, C. Ma, X. Wu, D. Deng, M. Wei, D. Tan, R. Si, S. Zhang, J. Li, L. Sun, Z. Tang, X. Pan, and X. Bao, *Direct, Nonoxidative Conversion of Methane to Ethylene, Aromatics, and Hydrogen*. Science, 2014. **344**(6184): p. 616-619.

21. Kim, S.K., H.W. Kim, S.J. Han, S.W. Lee, J. Shin, and Y.T. Kim, *Mechanistic and microkinetic study of non-oxidative methane coupling on a single-atom iron catalyst*. Communication Chemistry, 2020. **3**(58).

Summary

This thesis presents a detailed investigation into the reaction performance characteristics of non-oxidative coupling of methane using the Fe©SiO$_2$ catalyst. Natural gas, consisting for 75-99 vol% of methane (CH_4), is seen as a high potential substitute for crude oil in the synthesis of light olefins (ethylene and propylene) and aromatics (benzene, toluene and xylene). Current industrial processes converting natural gas to olefins and aromatics consist of multiple conversion steps starting with methane steam reforming to obtain syngas. For this reason, these processes tend to be energy intensive and require large installed capacity to become economically viable.

Direct conversion of methane to higher hydrocarbons has been investigated for decades as a potential competitive alternative to the indirect routes. The challenges for the direct routes stem from the high chemical stability of methane compared to the intended products (i.e. light olefins and aromatics) and the high endothermicity of the coupling reactions, requiring high reaction temperatures (>800°C) and the undesired formation of carbonaceous deposits, leading to yield loss and system fouling. There are two main methods for tackling this challenge, i.e. oxidative coupling of methane, making the reaction exothermic and significantly lowering the required reaction temperature, and methane dehydroaromatization, which uses a shape selective zeolite catalyst to prevent deposit formation and steer the reaction towards aromatics. Although these two reactions do show high potential, they still operate at too low conversion and yield to become economically interesting. More details concerning these underlying motivations and background to this thesis are given in **chapter 1**.

A recent publication by Guo et al.[1] proposes a high temperature system based around an atomically disperse iron on silica (denoted Fe©SiO$_2$) catalyst, which is capable of converting methane at high conversion levels to a mixture of olefins and aromatic, without deposit formation, at temperature in excess of 950°C. It is proposed that the catalyst activates methane to methyl radicals, which in turn undergo free radical coupling reactions in the gas-phase to obtain the final products. The system is still poorly understood, both

---

[1] Guo, X., G. Fang, G. Li, H. Ma, H. Fan, L. Yu, C. Ma, X. Wu, D. Deng, M. Wei, D. Tan, R. Si, S. Zhang, J. Li, L. Sun, Z. Tang, X. Pan, and X. Bao, *Direct, Nonoxidative Conversion of Methane to Ethylene, Aromatics, and Hydrogen*. Science, 2014. **344**(6184): p. 616-619.

due to the novelty of the system as well as the highly complex gas-phase chemistry that dictates the system performance.

This thesis aims to further the understanding of the catalytic system involving Fe©SiO_2 and to uncover the main parameters which govern the performance of the system. It will furthermore look at the potential challenges for industrial application of the system and propose new and versatile methods for synthesizing the Fe©SiO_2 catalyst. The interaction between the catalytic reaction and the gas-phase chemistry is poorly understood, leading to a reproducibility issue with regards to the performance achieved in the original publication by Guo[1]. A custom 3-zone oven, thermally insulated between each zone, was especially designed to achieve a high level of control over the temperature profile inside as well as up- and downstream of the catalyst bed. **Chapter 2** of this thesis deals with the effect of this temperature profile. The position and amount of catalyst where systematically varied, as well as the space velocity and the temperature upstream and downstream of the catalyst bed. The results show that residence time at reaction temperature (1000°C) downstream of the catalyst bed can significantly increase conversion, without negatively impacting the total hydrocarbon yield. In contrast, residence time at 1000°C upstream of the catalyst causes a significant increase in deposit formation on the catalyst. In addition, achieving higher conversion purely via the catalyst is found to reduce the total hydrocarbon product selectivity, when compared to achieving the same conversion increase by using the post-catalytic volume. It is concluded that that the catalyst is required solely for free-radical initiation, after which the reaction propagates at high activity in the gas phase. Any contact of the catalyst with the activated gas-phase leads to deposit formation.

Ethane is the primary product of the methane coupling reaction with ethylene as secondary product, as shown in the results of **chapter 2** as well as literature. The commonly accepted mechanism for methane activation in the gas-phase concerns an auto-catalytic cycle involving both ethane and ethylene. The addition of these two C_2 hydrocarbons is tested, **chapter 3** shows that ethane and ethylene are highly potent free-radical initiators which significantly enhance methane conversion rate. There is no discernible difference between the effect of ethane or ethylene. Furthermore, C_2 addition does not negatively impact the product selectivity distribution or carbon deposit formation. It is concluded that the C_2 hydrocarbons are solely involved in accelerating the auto-catalytic cycle, analogues to the catalyst (**chapter 2**), after which gas-phase chemistry fully determines the product distribution.

Reproduction of the absence of deposit formation during methane coupling over the Fe©SiO_2 catalyst proved impossible, as also shown by other publications concerning this system. It is proposed that the addition of hydrogen can largely prevent the formation of deposits on the catalyst. Many of the reactions involved in non-oxidative coupling of methane produce hydrogen. Furthermore, the high temperature nature of the reaction studied in this thesis causes most reactions to be reversible, this means that many coupling reactions will be slowed down by hydrogen addition. **Chapter 4** shows that up to 10% H_2 addition can indeed decrease the formation of carbonaceous deposits on the catalyst by an order of magnitude. The methane conversion is simultaneously decreased by a factor of two, while the hydrocarbon product distribution is shown to be mainly determined by the methane conversion level, independent of hydrogen addition.

The system is modelled using a microkinetic gas-phase model in combination with the catalytic cycle as published in the first publication[1] concerning the Fe©SiO_2 catalyst. The results of this model give more quantitative insight into the interaction between the catalyst and the gas-phase and are discussed in **chapter 5**. It is shown that the formation of methyl radicals on the catalyst, followed by gas-phase coupling can accurately predict the performance of the system. Pure gas-phase methane conversion goes through a induction period before the auto-catalytic cycle is fast enough to ensure a high gas-phase methane conversion rate. The catalyst should mainly be used to overcome the induction period, thus significantly reducing the residence time required to achieve decent levels of conversion, as experimentally shown in **chapter 2**. The addition of C_2 hydrocarbons, as discussed in **chapter 3** is also modelled. The model demonstrates that the addition of C_2 can indeed also overcome the induction period, to directly achieve high methane conversion rates. Lastly the model demonstrates that gas-phase chemistry is the sole determinant of the product distribution, both radical and molecule concentration quickly achieve the gas-phase levels downstream of the catalyst.

The high temperatures and low pressures used in the methane coupling reaction with the Fe©SiO_2 catalyst pose significant challenges for industrial implementation. **Chapter 6** in this thesis presents a design concerning industrial implementation of this reaction assuming the performance recorded in the work of Guo[1]. The scope of the design focusses on maximizing the potential profit of the reaction. It is calculated that recovery of ethylene is economically unattractive, due to the low ethylene concentration in the product stream and the cryogenic methods required. The process thus results in a methane to aromatics process, with naphthalene as major product on carbon basis. Although the process shows economic potential as it is, it is advised to upgrade the naphthalene to value added products through a cracking reaction. The minimum pressure in the reactor is calculated to be 5 bars and both the reactor as well as the heat-exchanger over the reactor are determined to be the most significant investment costs. Lastly, hydrogen recovery is costly, due to the low temperatures and high pressures required, clashing with the requirements for the reactor, novel types of hydrogen recovery systems can significantly decrease costs.

The synthesis of the Fe©SiO_2 catalyst is intensive difficult to control, due to the required 16h in a ball-mill as well as a fusion at 1700°C for 6h. **Chapter 7** proposes an alternative synthesis method via grafting the atomically disperse iron sites on the silica surface using a metal organic complex. bis(2,4-dimethyl-1,3-pentadienide)Fe(II) is determined to be a suitable candidate for this graft reaction, with performance matching that of the synthesis method[1]. It is proposed that the grafting method can be used to give a better control over site density and position as well as catalyst shape (i.e. monolithic structures), to optimize mass and heat transport as well as catalyst/free-volume ratio. An alternative Ru/SiO_2 catalyst is proposed to increase the productivity of the catalyst, although this catalyst unfortunately performed worse than the Fe©SiO_2 catalyst.

One of the main omittances in research into the Fe©SiO_2 catalytic system concerns the performance at higher pressures, 5 bars and above as discussed before. It is thus proposed in **chapter 8** to measure the performance of the system at elevated pressured. Another proposed improvement is the tuning of the reactor shape to maximize both conversion and yield, the proposed design involves a capillary tube to feed the catalyst bed, ensuring rapid heating, while extending the diameter downstream of the catalyst to maximize residence time, as discussed in **chapter 2**. More catalyst formulations can tested, following a patent an Fe©SiC catalyst should significantly increase the activity. It is proposed that direct naphthalene upgrading in a dual-purpose reactor can be possible, using the unreacted methane and the produced hydrogen as cracking agents. Lastly a proton conductive membrane is suggested as active hydrogen pump in a potential process, alleviating the need for low temperatures, high pressures and low aromatics concentration for hydrogen recovery.

Samenvatting

Dit proefschrift bevat een gedetailleerd onderzoek naar de reactiekenmerken betreffende non-oxidatieve koppeling van methaan met behulp van een Fe©SiO_2 katalysator. Aardgas, bestaat voor 75-99 vol% uit methaan (CH_4) en wordt gezien als een potentieel alternatief voor ruwe olie bij de synthese van olefinen e.g. ethyleen en propyleen en aromaten benzeen, tolueen en xyleen). Huidige industriële processen voor het omzetten van aardgas in olefinen en aromaten, werken op basis van meerdere omzettingsstappen, beginnende met stoomreforming van methaan om synthesegas te verkrijgen. Deze processen zijn erg energie-intensief en vereisen ze een grote geïnstalleerde capaciteit om economisch rendabel te zijn.

Directe omzetting van methaan naar hogere koolwaterstoffen wordt al tientallen jaren onderzocht als een potentieel concurrerend alternatief voor deze indirecte routes. De uitdagingen voor een directe syntheseroute komt voort uit de hoge chemische stabiliteit van methaan in vergelijking met de beoogde producten (d.w.z. lichte olefinen en aromaten) en de zeer endotherme enthalpieverandering van de koppelingsreacties, leidend tot een zeer hoge benodigde reactietemperaturen (>800°C) en gerelateerde ongewenste vorming van koolstof afzettingen (cokes), wat leidt tot opbrengstverlies en systeemvervuiling. De twee belangrijkste routes voor directe synthese zijn oxidatieve koppeling van methaan, waardoor de reactie exotherm wordt en de vereiste reactietemperatuur aanzienlijk wordt verlaagd of methaan-dehydro-aromatisering, waarbij een configuratie selectieve zeolietkatalysator wordt gebruikt om de vorming van koolstofafzettingen te voorkomen en de reactieselectiviteit richting aromaten te sturen. Hoewel deze twee reacties veelbelovend zijn, worden er tot nu toe nog steeds te lage conversie en opbrengst behaald om deze reacties economisch interessant te maken. Meer details over de onderliggende motivaties en achtergrond van dit proefschrift kunnen in **hoofdstuk 1** gevonden worden.

Een recente publicatie door Guo et al.[1] beschrijft een hoge temperatuur reactiesysteem gebruikmakende van een atomair gedispergeerde ijzer-op-silica katalysator (aangeduid als Fe©SiO_2), dat in staat is om methaan op temperaturen hoger dan 950°C met hoog conversieniveau om te zetten in een mengsel van olefinen en aromaten, zonder vorming van koolstofafzettingen. De publicatie postuleert dat de katalysator methaan activeert tot

---

[1] Guo, X., G. Fang, G. Li, H. Ma, H. Fan, L. Yu, C. Ma, X. Wu, D. Deng, M. Wei, D. Tan, R. Si, S. Zhang, J. Li, L. Sun, Z. Tang, X. Pan, and X. Bao, *Direct, Nonoxidative Conversion of Methane to Ethylene, Aromatics, and Hydrogen.* Science, 2014. **344**(6184): p. 616-619.

methylradicalen, die op hun beurt in de gasfase vrije-radicaal-koppelingsreacties ondergaan om de eindproducten te vormen. Over dit katalyse proces was nog weinig bekend door zijn noviteit, alsmede door de zeer complexe gasfase chemie die de werking van het proces bepaalt.

Dit proefschrift heeft als doel het begrip van het Fe©SiO_2 katalytische proces te vergroten en de belangrijkste parameters te bepalen over werking van het proces. Ook zal er aandacht worden besteed aan de potentiële uitdagingen voor de industriële toepassing van het proces en worden er nieuwe methoden voorgesteld voor de synthese van de Fe©SiO_2-katalysator.

Over de interactie tussen de katalytische reactie en de chemie in de gasfase was weinig verklaard in het originele artikel. Dit heeft de reproduceerbaarheid van de resultaten zoals geclaimd[1] ernstig bemoeilijkt. Een op maat gemaakte oven bestaande uit drie thermisch geïsoleerd zones, is ontworpen om een hoge mate van controle te verkrijgen over het temperatuurprofiel zowel binnenin als voor en na het katalysator-bed. Het effect van dit temperatuurprofiel wordt in **hoofdstuk 2** van dit proefschrift behandeld. Zowel de positie, alsmede de hoeveelheid katalysator werden systematisch gevarieerd, evenals de verblijftijd in het katalysator-bed en de temperatuur voor en na het katalysator-bed. De resultaten laten zien dat de verblijftijd ná het katalysator-bed op reactietemperatuur (1000°C) de conversie van methaan aanzienlijk kan verhogen, zonder de totale koolwaterstofopbrengst negatief te beïnvloeden. Daarentegen veroorzaakt de verblijftijd vóór het katalysator-bed bij 1000°C een significante toename in de vorming van koolstofafzetting. Tevens blijkt het bereiken van een hogere conversie via alleen de katalysator de totale selectiviteit van koolwaterstof-producten te verminderen in vergelijking met het bereiken van dezelfde conversietoename door gebruik te maken van het post-katalytisch volume. Er wordt geconcludeerd dat de katalysator slechts nodig is voor de initiatie van de vrije radicaalreactie, waarna de reactie zichzelf met hoge activiteit in de gasfase voortzet. Elk contact van de katalysator met de geactiveerde gasfase leidt tot vorming van cokes.

De resultaten zoals beschreven in **hoofdstuk 2** alsmede relevante literatuur, laten zien dat ethaan het primaire product is van de methaan-koppeling-reactie met ethyleen als secundair product. Het mechanisme voor methaan-activering in de gasfase, zoals algemeen aanvaard, betreft een auto-katalytische cyclus waarbij zowel ethaan als ethyleen betrokken zijn. De toevoeging van deze twee C_2 koolwaterstoffen werd onderzocht en in **hoofdstuk 3** bediscussieerd. De resultaten laten zien dat ethaan en ethyleen zeer krachtige vrije radicaal-initiatoren zijn, die de omzettingssnelheid van methaan aanzienlijk verhogen. Er is geen waarneembaar verschil tussen het effect van ethaan en ethyleen. Tevens heeft C_2-toevoeging geen negatieve invloed op de product selectiviteit verdeling of op de vorming van cokes. Geconcludeerd wordt dat de C_2-koolwaterstoffen uitsluitend betrokken zijn bij het versnellen van de auto-katalytische cyclus, analoog aan de rol van de katalysator (**hoofdstuk 2**), waarna de productverdeling volledig wordt bepaald door de chemie in de gasfase.

Meerdere vervolg publicaties die gebruik maken van de Fe©SiO_2 katalysator laten zien dat het herhalen van het experiment met een de volledige afwezigheid van koolstofafzetting zoals geclaimd in het oorspronkelijke artikel tijdens de methaankoppelingsreactie onmogelijk is. Mogelijk kan het toevoegen van waterstof de vorming van koolstofafzettingen op de katalysator grotendeels voorkomen. Veel van de reacties met betrekking tot non-oxidatieve koppeling van methaan vormen waterstof als bijproduct. Ook zorgt de hoge temperatuur, van de in dit proefschrift bestudeerde reactie, ervoor dat de meeste reacties reversibel zijn, wat betekent dat veel koppeling-reacties worden vertraagd door waterstoftoevoeging. In **Hoofdstuk 4** wordt aangetoond dat H_2 toevoeging tot 10% inderdaad de vorming van koolstofafzettingen op de katalysator met een factor 10 kan verminderen. Tegelijkertijd wordt de methaanomzetting met een factor twee verlaagd, terwijl de verdeling van het koolwaterstofproduct voornamelijk wordt bepaald door het methaan-omzettings-niveau, onafhankelijk van de waterstoftoevoeging.

Het systeem is gemodelleerd in **hoofdstuk 5** met behulp van een micro-kinetisch gasfasemodel in combinatie met het katalytische proces zoals beschreven de eerste publicatie door Guo[1] betreffende de Fe©SiO_2-katalysator. De uitkomsten van dit model geven een kwantitatief inzicht in de interactie tussen de katalysator en de gasfase. Er wordt aangetoond dat de vorming van methylradicalen op de katalysator, gevolgd door gasfasekoppeling, nauwkeurig het werkelijke proces kunnen voorspellen. De omzetting van methaan in alleen de gasfase doorloopt een inductieperiode voordat de auto-katalytische cyclus snel genoeg loopt en een hoge omzettingssnelheid van methaan in de gasfase genereert. De katalysator dient voornamelijk als overbrugging van de inductieperiode, waardoor de verblijftijd voor het bereiken van een behoorlijke conversieniveaus aanzienlijk wordt verkort, zoals experimenteel ook aangetoond in **hoofdstuk 2**. De toevoeging van C_2-koolwaterstoffen, zoals besproken in **hoofdstuk 3**, is ook gemodelleerd. Het model toont aan dat de toevoeging van C_2 inderdaad ook de inductieperiode kan elimineren, en zodoende direct hoge methaan-omzettingssnelheid geeft. Ten slotte toont het model aan dat de chemie in de gasfase de enige factor is die productverdeling bepaalt, omdat zowel de radicaal- en de molecuulconcentraties snel het gasfaseniveau bereiken na het katalysator-bed.

De hoge temperatuur en lage druk die worden gebruikt in de methaan-koppeling-reactie met de Fe©SiO_2-katalysator vormen een aanzienlijke uitdagingen voor industriële toepassing. **Hoofdstuk 6** van dit proefschrift presenteert een procesontwerp voor industriële toepassing van deze reactie, uitgaande van de gegevens in dit proefschrift. Het doel van het procesontwerp is het maximaliseren van potentiële winst. Er wordt berekend dat het afscheiden van ethyleen economisch onaantrekkelijk is, vanwege de lage partiële druk van ethyleen in de productstroom. Het proces resulteert hierdoor in een methaan tot aromaten proces, met naftaleen als grootste productfractie op koolstofbasis. Hoewel het proces wel economisch potentieel heeft, wordt geadviseerd om het naftaleen op te waarderen tot producten met toegevoegde waarde door middel van kraken van het naftaleen. De minimale druk in de reactor moet 5 bar zijn en zowel de reactor als de warmtewisselaar over de reactor worden als de belangrijkste investeringskosten aangetoond. Ten slotte is waterstofterugwinning duur, vanwege de vereiste lage temperaturen en hoge druk, en is in contrast met de voorwaarden van de reactor. Nieuwe waterstof-terugwinning-systemen zouden de kosten van het proces aanzienlijk kunnen verlagen.

De synthese van de Fe©SiO_2-katalysator is intensief en moeilijk door de vereiste lange duur (16 uur in een kogelmolen en een fusie op 1700 ° C gedurende 6 uur). **Hoofdstuk 7** stelt een alternatieve synthese-methode voor, waarbij het atomair verspreide ijzer op het silicaoppervlak geënt wordt met behulp van een metaal-organisch complex. Bis(2,4-dimethyl-1,3-pentadienide)Fe(II) wordt aangegeven als een geschikte kandidaat voor deze ent-reactie, waarbij de uitkomsten van de reactietest overeen komen met die van de oorspronkelijke synthese-methode[1]. Er wordt voorgesteld dat deze ent-methode gebruikt kan worden om een hogere mate van controle te geven over de dichtheid en positie van de ijzeratomen, evenals over de fysieke vorm van de katalysator (b.v. monolithische structuren), om het massa- en warmtetransport en de ratio tussen katalysator en vrij-volume te optimaliseren. Er wordt een alternatieve Ru/SiO_2-katalysator voorgesteld om de productiviteit van de katalysator te verhogen, hoewel deze ruthenium katalysator helaas slechter presteerde dan de Fe©SiO_2-katalysator.

Een van de belangrijkste tekortkomingen in onderzoek naar het Fe©SiO_2 katalytische proces betreft de prestatie bij hogere drukken, (5 bar en hoger) zoals eerder besproken, daarom wordt in **hoofdstuk 8** voorgesteld om de prestatie van het systeem op hogere drukken te meten. Een andere voorgestelde verbetering is de afstemming van de vorm van de reactorbuis om zowel de conversie als de koolstofopbrengst te maximaliseren. Het voorgestelde ontwerp omvat een capillaire buis voor de toevoer van het gas richting het katalysator-bed, waardoor snelle verwarming wordt gegarandeerd, terwijl de diameter na de katalysator wordt vergroot om de verblijftijd na het katalysator-bed te maximaliseren, zoals besproken in **hoofdstuk 2**. Er kunnen meer katalysatorformuleringen worden getest, volgens een patent zou een Fe©SiC-katalysator de activiteit aanzienlijk kunnen verhogen. Er wordt voorgesteld dat in situ opwaardering van naftaleen in dezelfde reactor als voor de methaan opzetting mogelijk zou kunnen, waarbij het niet-gereageerde methaan met het geproduceerde waterstof als kraakmengsel wordt gebruikt. Ten slotte wordt een proton-geleidend membraan voorgesteld als actieve waterstofpomp in een potentieel proces, waardoor de behoefte aan lage temperaturen, hogedrukken en lage aromatenconcentraties voor waterstofterugwinning wordt vermeden.

Acknowledgements

Dear reader, firstly I want to congratulate you on reaching the end of my thesis and for the attention you have given it, I hope you enjoyed the read and maybe even learned something from it. This work has taken the better part of 5 years to compile. It started with a choice, whether I wanted to continue with ammonia or dabble my feet in the mysterious world of methane conversion. The title of this thesis should shed some light on the eventual choice I made, although many readers will be happy to hear that as of writing this acknowledgement I made the choice to return to ammonia again.

My time in CPM goes all the way back to the beginning of 2015, when I started my master assignment under the supervision of Roger. After half a year of kinetic measurements I packed my bags to spent a semester at Aalto university in the group of Ville Alopaeus, where I had the pleasure of meeting both two great housemates and two great friends, Eric and Stefan. I am happy that we kept in contact and had many awesome encounters both in Germany as well as in the Netherland, let's keep this up well into the future! Back in the Netherlands I first started a so-called TGS-period, performing exploratory research into plasma-catalytic nitrogen fixation. Up-on arrival back in the low-lands I initially lived in a sub-let room on Campuslaan 39, where I had a great time, living with 13 other students there. In the spring I moved to the Paliatievezorgboerderij in Hengelo together with Dennis. Dennis you have always been a great friend! I enormously enjoyed living together with you and spending many a motorcycle holiday traveling around Europe. Dion lived close-by on the Woltersweg, we often dined together and spent many evening enjoying great beers, wines and conversations. Dion eventually moved in with me after Dennis decided to live with his girlfriend. Dion I also want to thank you for being a great friend! I know that we had our ups and downs, but I really appreciate the good times, skiing, horse riding, karting and many other things, we shared together over these years.

CPM was undergoing a lot of change from my time as master student, through my TGS period into my PhD. I want to thank all the 'original' members of CPM for welcoming me with open arms and integrating my seamlessly into the research group. In no particular order: Songbo, Pramod, Seshan, Châu, Kamilla, Marta, Roger, Joline, Tushar and of course Guido. Guido, you have been a great officemate and an even greater friend, I really enjoyed the 'story times' we shared in the beginning, but also you starting a seriously relationship with your lovely fiancé Michaela and the birth and development of your son Alessandro from a baby into an awesome little boy. A lot of people came and went from CPM but Guido appeared to be a constant through it all. Pengyu was one of the first new members to join the group, I remember Pengyu starting as a very shy and honour driven person, who would prefer a 2h midnight bike ride, over being taken home in an inebriated state, but over the course of your PhD you grew into friendly and openminded person, who would not miss the borrel for any reason. Shilpa also re-joined the group as post-doc, I have fond memories of our discussions concerning the grading of the catalysis exams. My very first master student was Wouter, I remember that you approached me during a Alembic barbecue, asking if I had an assignment for you. I really enjoyed supervising you through your thesis, and I am still proud of the proactiveness you showed in your work! Just do not forget to turn off the tap before you leave… Jord, you first started as a master student under my supervision, it was a lot of fun (re-)building your setup together and trying to make some 'cheese' out of your butyric acid results, you are an exceptionally bright and hardworking student, CPM can be proud that you stayed on for your PhD assignment. And last but not least Patrick came from Northern-Ireland to be my master student. I was a great pleasure to see you grow into the project and really evolve into an independent researcher, it is a shame that the pandemic had to cut our time together short, but I am proud of what you achieved in that short time.

Kevin joined the group, in essence taking on the plasma catalytic ammonia project. I really enjoyed our shared corridor in the lab, where we would share well founded criticisms about everything and nothing, and later on our nearly neighbour status where we continued the habit. I am very grateful for the opportunity you gave me to join in with the review you wrote as well as the introduction you did that lead to my first 'real-job'. Shahab, you never really felt like a master student in the group, your level of involvement as well as your stubborn refusion to leave the borrel even after graduating really makes you part of the crew, and a highly respected one at that. I do hope that you didn't forget your promise concerning my graduation present. Pengcheng, you are a hard worker, always present in the lab, but don't neglect your social skills. Erwin shared the office with me and Guido and one might say that I shared the supervisor duty over Erwin with Pengyu. Erwin, I really enjoyed our conversations, borrels and inappropriate Italian lessons. I can of course not forget the Latin gang, Nuria and Pepe, who were the light of party during many karaoke's, borrels and nights out in town. The last member to join CPM in my time was Fernando, who immediately had to prove his worth repairing the pump in the ion chromatograph, on a shoe-string budget with parts sourced from eBay. It is a shame that our time at CPM was cut so short by the pandemic!

Now it is time to deal with the brains of the research group, the academic staff. Firstly I would like to thank Leon from the bottom of my heart, not only for being my promotor and supervisor, but for all the chances and support he gave right from my master to the end of my PhD. You have always been very kind and considerate towards me, even in times when I was struggling with myself and I can honestly say that you shaped me into the scientist I am today. I would of course be amiss if I would not mention all borrels, barbecues and events organized by Leon for the group throughout the years, which helped to make CPM the close and friendly group it is. Jimmy joined the group as new professor, right when I was starting my PhD. Jimmy, you always boom with endless supply of optimism even in the face of adversity, although I do want suggest you start taking some Dutch customs to heart. when in Rome hè? I can of course also not go unmentioned that I do owe you a debt of gratitude for keeping a certain person in the Netherlands, but we will save best for last… Aayan joined CPM at a perfect time for me, right when I was starting my modelling adventure in Ghent. You always had great input when it came to developing the model, with often unique and ingenious insights, which more often than not helped the progress significantly. I also really enjoyed the limited amount of borrels and dinners we shared!

Moving on from the brains to the heart of the group: The technicians and secretaries. In this case 'heart' has a strikingly well-fitting double meaning. Not only are the technicians and secretaries the organ that keeps the group functioning, they also are at the emotional centre of it. First and foremost I want to thank Bert, you have always been there to help me out both inside the lab and outside the lab, whether it concerned work, personal things, or maybe some good old hobby-ing. Although I am still waiting for my official 'Bert's Beunhazen Brevet'. Karin, thank you for the nice times we had both in the lab and on the coffee table, it was fun keeping the lab running streamlined and clean together! Tom, I enjoyed the talks we had in your office and the lab, I still have your CD standing proudly in my collection! And of course Ties, the latest addition to the CPM technicians team, you always have a good discussion up your sleeve, related to science, politics or even TikTok, it is a real shame we were not allowed to have more borrels together. There have been many secretaries that passed the Revu during my time in CPM. Maaike, I was only in CPM for a short time before you left, but I remember you giving me a warm welcome and my office key upon my arrival. Jaqueline, I enjoyed our discussions on dancing, especially concerning the Tango and Salsa. Dorothy, you always worked hard to keep the group together and organize awesome activities, such as Sinterklaas or Chinese hot-pot. And last in this chronology, Anne, you are the real Borrel secretary, always up for some drinks and a good karaoke.

My PhD did not stay contained to CPM only, it involved many collaborations with external people. The first people involved were the technicians at het Hoge Druk Lab, Benno Knaken, Ronald, Erna and Ronald. They helped me along greatly in performing the ball-milling step in my synthesis. On top of this Benno was invaluable in helping me construct the condenser for my experimental setup. After struggling for some time on the topic I was invited for a meeting in Geleen, where Xander introduced me to Dick Nagaki, who gave

me some important directions for my research, which proved to be essential for its success. Louis, I want to thank you for our collaboration in not only one, but two successful Process Plant Design project. I really like your optimism and drive when it comes to guiding the groups and incorporating my suggestions into a the master-course, I am happy that our collaboration has led to a very insightful publication. Although I must also thank the project group, especially Dylan and Bart as well as Henk for their hard work and input in this.

My computational modelling work initially started with Jim Kok in Twente, we had a very nice discussion concerning the system I wanted to model and you very kindly allowed me to use your software package leading to the final chapter and publication. I decided however that proper modelling required some proper expertise, which lead to the fruitful collaboration with Ghent University. I had the pleasure of visiting the LCT two times, where I was perfectly received by Laura. Laura, you are so driven, hard-working and kind, I can safely say that you were the key factor in making both my stay in Ghent and the collaboration successful! Pedro, I really appreciate all the input you gave during our work together, as well as our nice dinner in Ghent, talking about Portugal and the Low Countries. Of course, this collaboration would never have happened if Joris would not have given me the invitation to join his group and for always being open to a discussion and giving quick replies to my question and doubts. Lastly I want to thank all the people in the LCT group, who immediately made me feel at home and included me in the shared activities, such as badminton.

My PhD period did not only involve academic work, I still had time for friend and hobbies, some would say too many hobbies. At the beginning of my PhD I got tricked into joining a table-top RPG group by Edo, I was supposed to be a side character only participating occasionally, but ended up playing nearly every week, together with David, Raoul, Lionel, Finn, Timothy and Bas, a.k.a. the Wardens of the West! I want to thank you all the amazing times we had together! Next to this I also danced for quite some time at 4 happy feet, were I went through too many dance partners to mention here, I want to thank you all for an amazing time! Especially my first dance partner, Belinda, you are still a great friend and I really enjoy our dinners and discussions! The last hobby I picked up during my PhD was horse-riding, were I spent many a Thursday night until deep in the morning at the Barrage drinking more than I should. I want to thank all the member of Hippocampus for the great times we had riding, drinking and during all the activities.

Now it will of course be impossible to finish a PhD without friends and family. There are two members of our Jochies friend group that I haven’t mentioned yet by name, Han and Jan, it is a shame that we haven’t had as close contact during my PhD as we had during the bachelor and master, let’s make sure this changes in the future! Aymerick, our friendship

goes far back, but I am really happy that we still see each other often, either in Brussels, Twente or Lyon, the annual karting and following champagne showers are always the highlight of the year. Jelke, I think I can safely say that you are my oldest friend, sharing our traditional yearly holiday in Lyon together. Lucas, our friendship grew out of a tutorage, but is now much more than that, often playing games or dining and drinking together.

I come from a big and close family and I am thankful for their support and hospitality during my PhD and before. I still want to give special thanks to some of them in particular. In this section I will momentarily switch to Dutch. Als eerste wil ik mijn ouders, Erik en Carla bedanken voor hun grenzeloze liefde, toewijding en hulp. Jullie waren mijn rots in de branding, beiden op persoonlijk, maar ook op wetenschappelijk gebied. Ik ben bevoorrecht met hun hoge mate van ouderlijke steun. Als tweede wil ik mijn grootouders, Pake Sjoerd en Beppe Anne, bedanken voor het geven van een huis weg van huis, hun liefdevol onthaal, zorgzaamheid en alle appeltaart die ik maar wilde. Met een warm hart denk ik ook aan mijn zus Eline en haar vriend Wessel en alle gezellige vakanties samen, in de sneeuw of in de zon, we maakten er altijd een onvergetelijke tijd van! Ik heb het heel fijn gehad bij Theo en Judith. Judith verzorgde de gast-vriendelijkheid en de heerlijke maaltijden, terwijl Theo ten alle tijde in was een discussie of een stevige wandeling. Laura, Wilko, Alex en Lars, wij hebben samen veel mooie momenten gehad, in Frankrijk op de kartbaan en in het zwembad, of in Twente tijdens een gezellige barbecue en bij het sleutelen aan de motoren. In Zwitserland was het heerlijk vertoeven bij Marja en Christoph, of voor het middeleeuws festival, waar de Postma familie in prachtige kledij van de partij was, dan wel samen met Dennis op onze motoren. Tenslotte was ik altijd welkom bij mijn peetouders, Conny en René, voor een genoeglijk etentje, maar eveneens voor hulp bij de aankoop van een auto of motor.

Before my PhD started my family was mainly Dutch, but I am very happy that my current family is largely Portuguese, due to my girlfriend Maria. Teresa, ainda me lembro da primeira vez que nos conhecemos em Sète (França) e onde tive a minha primeira experiência de como preparar bacalhau à moda portuguesa. Tanto na casa do Esteves como em Portugal, eu sempre me senti em casa. Atrevo-me a dizer que ninguém experienciou verdadeira hospitalidade até ser convidado para a casa de uma família Portuguesa. Em Portugal eu também conheci o João Luís, que com igual sentimento me mostrou o que é fazer um churrasco à portuguesa acompanhado com um bom vinho português, à Nossa! Não me poderia esquecer de mencionar a avó Lina, que sempre foi dócil e uma mulher muito especial, sempre me fez sentir em casa e bem-vindo. Fiquei muito feliz ao ver a convicção de que, mesmo com a sua senioridade, foi capaz de visitar a Maria e eu em Hengelo.

Now we have come to the end of this acknowledgement chapter and I am left with only one more person to thank: Maria, embora ainda duvide que uma Grolsch Kanon seja a melhor maneira de seduzir alguém, estou feliz que o tenhas feito. Conhecemo-nos mesmo no início do meu PhD e temos vindo a construir um estável lar desde então. Tivemos os nossos altos e baixos, mas eu amo-te muito e estou muito grato por todo o amor e apoio que me deste durante todo o meu PhD, obrigado.

List of Publications

Per August 2021

Journal articles:

Postma, R.S. & Lefferts, L., *Effect of ethane and ethylene on catalytic non oxidative coupling of methane*, Reaction Chemistry & Engineering, 2021, 10.1039/D1RE00261A

Postma, R.S. & Lefferts, L., *Influence of Axial Temperature Profiles on Fe/SiO2 Catalyzed Non-oxidative Coupling of Methane*, ChemCatChem, 2021, 10.1002/cctc.202001785

Rouwenhorst, K.H.R., Engelmann, Y., Van 't Veer, K., Postma R.S., Bogaerts, A. & Lefferts, L. *Plasma-driven catalysis: Green ammonia synthesis with intermittent electricity.* Green Chemistry, 2020, 10.1039/d0gc02058c

Postma, R.S., Brunet-Espinosa, R., Lefferts, L., *Competitive Adsorption of Nitrite and Hydrogen on Palladium during Nitrite Hydrogenation*. ChemCatChem, 2018, 10.1002/cctc.201800523

Brunet-Espinosa, R., Rafieian, D., Postma, R.S., Lammertink R.G.H., Lefferts, L., *Egg-shell membrane reactors for nitrite hydrogenation: manipulating kinetics and selectivity*, Applied Catalysis B: Environmental, 2018, 10.1016/j.apcatb.2017.10.058

Postma, R.S., Kertsen S.R.A., Van Rossum, G., *Potassium-Salt-Catalyzed Tar Reduction during Pyrolysis Oil Gasification*. Industrial and Engineering Chemistry Research, 2016, 10.1021/acs.iecr.6b01095

Conference presentations:

Postma R.S. & Lefferts, L., *Suppressing carbon formation and enhancing product yield in Methane pyrolysis.* 2021, Oral presentation at NCCC online conference

Postma, R.S. & Lefferts, L, *Ammonia synthesis from hydrogen and nitrogen via chemical looping using non-thermal, atmospheric plasma catalysis.* 2017, Oral presentation at NCCC conference, Noordwijkerhout, the Netherlands

Conference poster presentations:

Postma R.S. & Lefferts, L., Direct non-oxidative coupling of methane over Fe©SiO_2, an investigation into the characteristics of the reactor design. 2020, poster presentation at NCCC conference in Noordwijkerhout, the Netherlands

Postma R.S. & Lefferts, L., Direct non-oxidative coupling of methane over Fe©SiO_2, an investigation into the characteristics of the reactor design. 2019, poster presentation at Europacat conference in Aachen, Germany

Postma R.S. & Lefferts, L., *Effects of catalyst position on the NOCM reaction using Fe©SiO2*. 2019, poster presentation at NCCC conference in Noordwijkerhout, the Netherlands

Postma R.S. & Lefferts, L., *Methane Pyrolysis: Understanding the synthesis of Fe©SiO_2.* 2018, poster presentation at NCCC conference in Noordwijkerhout, the Netherlands

Rolf Sybren Postma was born on 7 January 1992 in Hoorn, the Netherlands. At the age of 6 he moved to Berkel, just north of Rotterdam, where he lived until he was 15. For the last 3 years of high school he moved with his family to Lyon, France, where he was educated at Ombrosa Lycée multilingue de Lyon. In France he developed a keen interest in both history as well as the natural sciences. In 2010 Rolf moved back to the Netherlands to start his bachelor in Chemical engineering. On top of his degree he spent significant time as a student-assistant teaching mainly experimental courses. For his master he decided to specialize in process engineering, finishing an internship on pyrolysis oil upgrading at BTG. The master thesis was joined together with Aalto University in Finland, where Rolf spent 5 months developing a mass transport model for a liquid phase catalytic reaction. After graduating he spent the better part of a year setting up a research track into plasma catalytic nitrogen fixation before starting his PhD in the Catalytic Processes and Materials group, under the supervision of prof. Leon Lefferts, the result of which is this thesis.

9 789036 552950